Ceramic Nanostructures from Block Copolymers

by

Vanessa Zee-Haye Chan

B.S.E. Materials Science and Engineering
University of Pennsylvania, 1994

SUBMITTED TO THE DEPARTMENT OF MATERIALS SCIENCE AND ENGINEERING IN PARTIAL FULFILLMENT OF THE REQUIREMENTS FOR THE DEGREE OF

DOCTOR OF PHILOSOPHY IN POLYMERS
AT THE
MASSCHUSETTS INSTITUTE OF TECHNOLOGY

FEBRUARY, 2000

Signature of Author: _____
Department of Materials Science and Engineering
January 7th, 2000

Certified by: _____
Edwin L. Thomas
Morris Cohen Professor of Materials Science and Engineering
Thesis Supervisor

Accepted by: _____
Linn Hobbs
Professor of Materials Science and Engineering
Chairman, Departmental Committee for Graduate Students

Ceramic Nanostructures from Block Copolymers

by

Vanessa Zee-Haye Chan

Submitted to the Department of Materials Science and Engineering
on January 7th, 2000 in Partial Fulfillment of the
Requirements for the Degree of Doctor of Philosophy in
Polymers

ABSTRACT

The field of nanotechnology has received burgeoning interest in recent years as the characteristic dimensions for many applications (such as integrated circuits and magnetic storage media) become smaller and smaller. In this work, block copolymers are harnessed in order to produce both porous and relief nanostructures. The interest in using these materials is due to the unique morphologies that block copolymers form and the fact that these nanostructures do so by *self-assembly*. With careful selection of the relative volume fraction and phases, nanostructures with highly ordered and complex pore structures with a vast range of different symmetries can be produced; structures that are not attainable by more conventional processing techniques such as lithography.

In this thesis, we have produced porous and relief *ceramic* nanostructures from self-assembling (template free) block copolymer precursors using a one-step, room temperature technique. To accomplish this, a silicon containing block copolymer system was used where upon exposure to an oxidation process the material undergoes two steps 1) the selective removal of the hydrocarbon block and 2) the formation of a ceramic from the inorganic containing block, resulting in nanoporous and nanorelief ceramics. These structures have potential to be used at temperatures far above the T_g of traditional nanoporous or nanorelief polymers. By choosing the appropriate morphologies and parent block copolymers, 3D nanostructured ceramics with interfacial areas of ~ 40 m^2/g, masks for one-step lithography with a density of ~5 x 10^{11} dots/cm^2 or templates for the next generation of nanomagnets can be produced. In addition to these applications, it is envisioned that these structures can be used as photonic band gap materials, high temperature membranes and low dielectric constant materials.

Specifically, the formation of both nanoporous and nanorelief structures from an ABA triblock copolymer system of poly(pentamethyldisilylstyrene) P(PMDSS) with polyisoprene was studied. The focus of this thesis is on the oxidation of the double gyroid and "inverse" double gyroid morphologies using either ozone/uv and oxygen plasma techniques. By transmission electron microscopy (TEM) and atomic force microscopy (AFM), it is shown that the PI can be preferentially removed by oxidation resulting in a nanoporous material in the case of the double gyroid morphology and a nanorelief material in the case of the inverse double gyroid morphology.

Oxidation of the P(PMDSS) homopolymer was also studied chemically using X-ray photoelectron spectroscopy (XPS), Auger electron spectroscopy (AES), Fourier Transform Infra-red Spectroscopy (FTIR), Rutherford Backscattering Spectrometry (RBS) and Forward recoil Spectrometry (FRES) and morphologically by AFM. Through these chemical analysis techniques, it is demonstrated that the ozone + uv and uv only oxidation processes converts thin films of P(PMDSS) to a ceramic, specifically silicon oxycarbide, that is far more stable than the parent homopolymer.

Thesis Supervisor: Edwin L. Thomas
Title: Morris Cohen Professor of Materials Science and Engineering

Table of Contents

List of Figures

List of Tables

Abbreviations

ε	degree of asymmetry in a polymer phase diagram
γ_{AB}	the interfacial energy between A and B
λ	microdomain periodicity
ξ	interface thickness
ρ	density
σ	fraction by which the effective magnetic field is less than the applied field
Σ	area of the IMDS interface per chain
τ	symmetry parameter for multiblock copolymers
ϕ_A	volume fraction of A
χ_{AB}	Flory-Huggins interaction parameter between A and B
a	Kuhn statistical segment length
B	effective magnetic field
AES	Auger electron spectroscopy
AFM	atomic force microscopy
BE	binding energy
C	curvature
CMC	constant mean curvature surface
DSC	differential scanning calorimetry
FFT	fast Fourier transform
F_{LAM}	free energy of lamellae
FRES	forward recoil spectrometry
FTIR	Fourier transform infra-red spectroscopy
fwhm	full-width half-maximum
GPC	gel permeation chromatography
H	mean curvature
IMDS	intermaterial dividing surface
LFR	living free radical polymerization
M_n	number average molecular weight
M_w	weight average molecular weight

N	overall degree of polymerization, ($N=N_A + N_B$)
NMR	nuclear magnet resonance spectroscopy
O_2-RIE	oxygen reactive ion etching
O_3	ozone
ODT	order disorder transition
OsO_4	osmium tetroxide
p.d.	polydispersity (M_w/M_n)
PDMS	poly(methyldisiloxane)
PEO	polyethylene oxide
PI	polyisoprene
PI-DG	double gyroid structure with PI as the matrix
P(PMMA)	poly(methylmethacrylate)
P(PMDSS)	poly(pentamethyldisilylstyrene)
P(PMDSS)11	LFR synthesized P(PMDSS) with a molecular weight of 11K
P(PMDSS)34	anionically synthesized P(PMDSS) with a molecular weight of 34K
P(PMDSS)-*b*-PI	poly(pentamethyldisilylstyrene-block-isoprene)
P(PMDSS)-DG	double gyroid structure with P(PMDSS) as the matrix
PS	polystyrene
q	scattering vector
R	radius of curvature
RBS	Rutherford backscattering spectrometry
RUMP	Rutherford Users Manipulation Program
RuO_4	ruthenium tetroxide
SAXS	small angle X-ray scattering
SEM	scanning electron microscopy
THF	tetrahydrofuran
TEM	transmission electron microscopy
TEMPO	2,2,6,6-tetramethylpiperdinyloxy initiator
TMS	tetramethylsilane
UV	ultraviolet
XPS	X-ray photoelectron spectroscopy

Acknowledgments

The list of people that I would like to thank is long, but I have been fortunate to be surrounded by family, friends and mentors who have been positive inspirations in my life. I have learned a lot from these people and I think it is important to acknowledge them for helping me to define who I am today.

Over the past five years at MIT, I have become much wiser in the ways of the world and this has been due largely to Prof. Edwin (Ned) L. Thomas. From the onset, Ned has given me the perfect balance between guidance and intellectual freedom by allowing me to pursue my thesis into directions that interested me. I would like to thank him allowing me to take multiple productive trips to IBM Almaden Research Center in CA and to openly collaborate with research groups at IBM, University of Athens, University of Pennsylvania, University of Twente and University of California at Berkeley. Through his mentoring, I have learned to become an independent and free thinking researcher, to ask the questions that are important and to tackle problems that will have an impact and for these lessons I am truly grateful.

While at MIT, I established a critical collaboration with various research scientists at IBM Almaden Research Center and was given the opportunity to make several trips to use their research facilities. One of the most important people in my Ph.D. experience is Dr. Robert (Bob) D. Miller, my mentor. I would like to thank him for believing in me, for making sure I talked to the right people and whose dedication to this project helped me through the rough spots. I would also like to thank CPIMA (the Center for Polymer Interfaces and Macromolecular Assemblies) and especially Dr. Charles (Chuck) Wade for allowing these trips to be possible from a financial standpoint.

I am also grateful to Professor Nikos Hadjichristidis at the University of Athens, whose many members of his research group generously synthesized all the block copolymers used in this dissertation. Specifically, I would like to thank Apostolos Avgeropooulos, Hermis Iatrou and Nikos Ekizglou for their synthetic prowess.

I would also like to thank my other thesis committee members, Professor Henry (Hank) I. Smith and Professor Anne Mayes for scientific feedback during my thesis. I am grateful to Anne for her enthusiasm and for spending considerable time and effort on helping me to perfect the document. I am thankful to Hank for giving me the opportunity to spend 6 months immersed in NSL (the Nanostructures Laboratory) where I learned about the different semiconductor processing tools and co-authored a paper on scintillating fudicial grids for electron-beam lithography. I also appreciate his frankness and openness on scientific ideas and people which

has also been invaluable to my development at MIT and for teaching me how to properly throw a softball.

The collaborations that I have had at MIT have been widespread and I am indebted to all the people who have been a part of my scientific development. Professor Russell (Russ) J. Composto, from the University of Pennsylvania was my undergraduate thesis advisor and through him my love for polymers first developed. It was wonderful being able to continue this collaboration when I was in graduate school and to return to the University of Pennsylvania to perform Rutherford Backscattering experiments in his research group with his graduate student Howard Wang.

At IBM, I have interacted with many amazing people and I would like to especially thank Jane Frommer for being a positive role model for women in science and for extending her hospitality and kindness beyond the AFM lab to her home, to Craig Hawker for allowing me as a polymer physicist to explore the realms of polymer chemistry and teaching me to truly appreciate the handiwork of chemists, Victor Lee for also extending his friendship beyond the fumehood by welcoming me into his family and for patiently synthesizing the monomer in my thesis again and again and again. I also would like to mention Dolores Miller, Richard Campbell, Dave Sampson, Mike Tomey, Vaughn Deline and Paul Furuta for their friendships and help while I was at IBM.

I have also been fortunate to interact with Professor Julius Vancso and Rob Lammertink from the University of Twente on ferrocenylsilane polymers. I look forward to the collaboration that Rob and I will have from years to come and hope that the polymers that he synthesizes will always be as interesting as the ones that he has made for his thesis.

The experimental techniques used in this thesis at MIT were taught to me by the staff of the Center for Materials Science and Engineering (CMSE) and the Nanostructures Laboratory (NSL). I would especially like to thank Mike Frongillo, Tim McClure, Jim Daley and Elisabeth (Libby) Shaw for not only patiently teaching me and all the other graduate students the nuances of all these different instruments but also for sharing with me their views on life which were just as valuable.

In the last few months, I have also been fortunate to collaborate with Jim Hoffman from the Mathematical Sciences Research Institute at the University of California, at Berkeley. His computer simulations on the double gyroid morphology were critical in Chapter Six and I would like to acknowledge him for adding this beauty to my thesis.

I would especially like to thank all of the members of Ned's research group who have not only made group meetings interesting but have also shared their two cents with me over multiple caffeinated beverages. Thanks to Jennifer Wagner, my UROP who spent the Spring of 1999 semester learning how to use RUMP to do the RBS and FRES simulations in Chapter Four. Specifically, I would like to extend my thanks to Augustine "the pony" Urbas, Yoel Fink, Stephane Joly and Rob Lescanec for their patient ears and for the invaluable conversations that we have had on life, liberty and justice for all.

I am grateful to all the "behind-the-scenes" people who made everything run so much smoother; Ned's secretaries (Martha, Michelle, Cecilia and Jean), the DMSE graduate administrators, especially Gloria Landahl who made sure I was paid on time and was always there with a smile and a hug when I needed it and Cecil for teaching me that plants need water and whose high spirits that were a Godsend during the wee hours of the morning. I am also appreciative to Professor Linn Hobbs, who in the last few weeks has gone above the call of duty and shown that caring people still exist in this world.

Financially, I am indebted to the National Science Foundation for awarding me with a graduate research fellowship (1994-1997) which gave me independence in my research and for giving me an International Research Opportunity Postdoctoral Research Fellowship (1999-2000) to apply what I have learned in my Ph.D. to the "new" world of cell biology. I am also grateful to IBM for awarding me with an IBM Almaden Center Fellowship (1997-1998), a Cooperative Research Fellowship (1998-1999) and financial support when I was in California. My research at MIT would also not have been possible without the support of the Air Force.

One of the most important aspects at MIT has been the friendships that I have and I am especially grateful to these people for riding with me through the ups and the downs. Ming Ming Liu for sharing her love of food and enjoyment of the good things in life, George Malliaras who always encouraged me to believe in myself and who reintroduced me to the love for books, Chris Conley for his freshly baked chocolate chip cookies, his appreciation of Saturday morning cartoons and for flying out from Arizona for my thesis defense, Simon Karecki who taught me to drink good beer, ski parallel turns and drive a stick shift like every good woman should, Rebecca "BJ" Morss for setting my bar higher (and heavier) and for all the times she held my hand (and hair), Dave Grundy for my poker face and teaching me the finer points of pyromania and bridge, Matthew Dyer for his "conservative" approaches to conversations, bridge bids and life which

often challenged mine, Anne-Valerie Ruzette for the many conversations over our parallel lifelong decisions and Manisha Sood, who from the time we were ten years old has been there whenever I've needed her.

Personally, I would also like to thank the Muddy Charles Pub for the breaks on Thursday afternoons and Beantown and MIT women rugby football clubs for allowing me to release my aggressions on the field rather than in the lab.

I would especially like to thank my following friends who have pulled me through some of my tougher moments here. Martha Harbison, my partner in crime and the other half of 250 lbs of Fury (KSCU 103.3 FM, the Underground Sound) who kept me sane during my many trips out to CA, Karen Willcox, who "spiced" up my life, kept up with my chocolate addiction and kept me sane while at MIT and Mark(o) van der Helm, for the wide spectrum of study breaks in Central Square and for always *selflessly* sharing his Chocolate Sluggo, fondue and time.

Finally, I am eternally grateful to my parents, Charles and Clara who have given so much to me. My dad for showing me by example how to be dedicated to my work, to find strength within myself during tough times and to never forget my sense of humor. My mom for putting her children before herself, for teaching me to appreciate the little things in life and for reminding me to always have compassion for those around me. I hope that one day I can be as good a friend and parent to my children as they have been to theirs. I am also lucky to have the best brothers in the world; Virgil and Ernest have always been an important part of my life and I would like to thank them for always believing in me, for supporting me without fail and for not blabbing to our parents about everything that I do. Without my family's love, support and encouragement, none of this would have been possible.

I dedicate this thesis to my mother, Clara Kit-Yee Chan (nee Fung) who has been with me every step of the way. Thanks for all the trips you made to swimming and piano lessons, for the bedtime stories and especially for the *invaluable* heart-to-hearts during all the critical times in my life.

Chapter One
Overview

1.1 Introduction and Project Motivation

In recent years, there has been extensive research on processes and materials which can yield 3D organic and inorganic structures with pore sizes on the sub-micron size scale. Such materials have burgeoned interest due to their potential use as catalysts and as high temperature membranes. To produce nanostructures, templating routes have been developed to yield mesoporous silica (Monnier 1993) while nanoporous hydrocarbon materials have also been made from block copolymer precursors (Lee 1989, Hashimoto 1997 and Park 1997). In the formation of mesoporous silica, the templating routes either involved many processing steps (Monnier 1993, Morey 1998, Sierra 1999 and Ulrich 1999) or high temperature pyrolysis (Zhao 1998 and Johnson 1999) and the materials produced were either powders or fine grains. In this thesis, an alternative process was developed where conformal *ceramic* coatings were produced from block copolymers through a simple template-free room temperature oxidation route with relatively few processing steps. Conformal coatings can be produced since the block copolymer can be dissolved in solution and shaped materials coated with the solution. For example, a fiber could be dipcoated in a polymer solution, dried and after oxidation the fiber would be coated with a nanoporous or nanorelief ceramic.

The overall concept is to utilize block copolymers to produce nanoporous or nanorelief *ceramic* structures through oxidation. Block copolymers are unique in their ability to self-assemble into nanostructures with 1D, 2D and 3D periodicities. The goal of this dissertation is to harness these morphologies to produce nanoporous and nanorelief ceramics by selectively removing one block through oxidation and converting the remaining block to a ceramic by the same oxidation process. Specifically, the newly discovered double gyroid (Hajduk 1994) is the focus of this thesis since this structure has unique 3D properties and can not be attained by other routes (i.e. lithography) due to the intricacy of the morphology and the small characteristic dimension (tens of nanometers) of the structures.

In the past, block copolymers have been utilized to produce nanoporous hydrocarbon materials through ozonolysis and exposure to an oxygen plasma. (Mansky, 1995, Mansky 1996, Park 1997) These hydrocarbon materials are limited in the etch selectivities that are inherently obtainable and the fact that the materials are still constrained by the Tg of the remaining block.

Through the utilization of silicon containing block copolymers we are able to obtain nanoporous or nanorelief *ceramics* which should result in superior properties. This idea to produce nanoporous ceramics stemmed in part from my undergraduate research project at the University of Pennsylvania where under the guidance of Professor Russell J. Composto, I developed a process to form ceramic thin films from polymer precursors. In my undergraduate research project boron nitride was produced through the high temperature pyrolysis of poly(borazylene) resulting in a ceramic stable to 1250°C. (Chan 1996)

To accomplish this goal of nanoporous and nanorelief ceramics, careful design of the block copolymer precursor was necessary. Silicon containing polymers were chosen since it is well-known in the literature that these materials have the ability to form SiO_x when oxidized by ozone and uv (Koberstein 1997) or an oxygen plasma (Chou 1985). When exposed to an oxygen plasma, such materials can form a thin layer of etch resistant SiO_x which is responsible for their extremely low etching rate relative to polymers containing only C, H, N and O. This etch selectivity provides the basis for most of the multilayer resist schemes involving pattern transfer. However, this selectivity was also shown in this thesis to be useful for the formation of structures in a heterogeneous polymer film where one of the phases contains silicon and the other does not, i.e. in a block copolymer. Since block copolymers can self assemble into a variety of interesting morphologies depending on the structure and composition of the individual blocks, employing silicon containing block copolymers for pattern development and visualization proved to be a promising route for the development of nanostructures. (Lammertink 1999)

The system we investigated was a silicon containing block copolymer, where one block contains silicon (in our case, poly(pentamethyldisilylstyrene)) P(PMDSS)) and the other block is comprised entirely of a hydrocarbon material (polyisoprene). This material self-assembles into the well-known morphologies that have been exhibited in other block copolymer systems and 1-D, 2-D and 3-D periodic morphologies were documented. The hydrocarbon block was then selectively removed using either ozonolysis coupled with uv or an oxygen plasma while the silicon containing block was converted either simultaneously to a ceramic by the same oxidation processes. By carefully selecting the morphology of the block copolymer precursor, either nanoporous or nanorelief structures were produced from the double gyroid morphology. If the matrix is comprised of the hydrocarbon block, then a nanorelief structure as formed, whereas if the matrix consists of the silicon containing block then a nanoporous structure was formed.

The resulting nanoporous and nanorelief ceramics have structural feature sizes that are unobtainable by conventional ceramic processing techniques and have the potential to be used at temperatures far above the glass transition temperatures of traditional nanoporous polymers. (Chan patent pending) It is envisioned that these materials will be used for applications including nanostructured templates, photonic band gap materials, (Fink 1998 and Urbas 1999) high temperature membranes and low dielectric constant materials.(Hendricks 1995)

1.2 Silicon Containing Homopolymers

P(PMDSS) was synthesized by both living free radical and anionic techniques.(Chan 1998) Living free radical polymerization was carried out by myself under the direction of Dr. Craig Hawker at IBM Almaden Research Center, while the anionically polymerized material was synthesized by Drs. Apostolos Avgeropoulos and Hermis Iatrou at the University of Athens in Professor Nikos Hadjichristidis' group. These polymers were used to study the oxidation of the silicon-containing polymer to a ceramic, as detailed in **Chapter Four.**

1.3 Block Copolymers

Various block copolymers of poly(pentamethyldisilylstyrene), P(PMDSS) and polyisoprene, (PI) were synthesized by anionic techniques.(Avgeropoulos 1998) ABA triblock copolymers rather than AB diblock copolymers were synthesized in order to facilitate future processing of the polymer by methods such as roll-casting,(Albalak 1993) where bridging of the midblock chains plays an important role in the achievement of well oriented microdomains.

Among the triblock copolymers synthesized were two which exhibited the double gyroid morphology. One formed PI networks in a P(PMDSS) matrix while the other formed P(PMDSS) networks in a PI matrix; these two samples were the fundamental materials studied in this thesis. Polymers with different molecular weights and volume fractions (relative amount of PI as compared to P(PMDSS)) were also synthesized and their morphologies documented in **Section 3.3.**

A morphology diagram was plotted which was shown to be highly asymmetric for this block copolymer system, with lamellae forming at $\phi_{P(PMDSS)} = 35\%$ and double gyroid at $\phi_{P(PMDSS)} = 53\%$. It was believed that the formation of these morphologies at these unusual volume fractions is due to a combination of the asymmetric architecture of some of these triblocks as well as differences in the Kuhn statistical segment lengths of the two blocks.

1.4 Oxidation of Poly(pentamethyldisilylstyrene) Homopolymer

Before studying the formation of a nanoporous or nanorelief ceramic from the block copolymer system, the conversion of the silicon containing block to a ceramic first needed to be understood. For this reason, the oxidation of P(PMDSS) homopolymer by ozonolysis, uv and oxygen reactive ion etching (O_2-RIE) was studied.

The P(PMDSS) homopolymer used to study the conversion to a ceramic was synthesized at both IBM and the University of Athens. Using the homopolymer, the processing conditions needed to convert P(PMDSS) to a ceramic by the two different oxidation techniques. The conversion was monitored both chemically (by Fourier Transform Infra-Red (FTIR) Spectroscopy, X-ray photoelectron spectroscopy (XPS), Auger electron spectroscopy (AES), Rutherford backscattering (RBS) and Forward Recoil Spectroscopy (FRES)) and morphologically (by atomic force microscopy). RBS was performed at the University of Pennsylvania under the guidance of Professor Russell Composto and with help from Howard Wang. Jennifer Wagner, my undergraduate research opportunity program student carried out the RBS and FRES simulations under my guidance.

It was shown that when ozonolysis is performed at room temperature, conversion to a ceramic does not occur since the resulting material contains primarily hydrocarbons. To obtain an oxidized silicon species in our polymer system, oxidation must occur by 1) ozonolysis in the presence of uv 2) uv only in air or 3) reactive ion etching (RIE). Thus, in order to convert the P(PMDSS) block to a ceramic material, it is necessary to use conditions that are more aggressive than ozonolysis alone. AES studies have shown that with the RIE a thin layer of silicon oxide forms on the surface of the film. RBS and FRES studies were performed in order to collect data on the film composition. When exposed to uv only in air or a combination of uv + ozonolysis, P(PMDSS) converted to a complex oxide with residual carbon in the film; by FTIR and XPS this complex oxide was shown to be silicon oxycarbide.

When the oxidized materials were annealed to 400 °C in a nitrogen atmosphere, it was shown that the samples that were exposed to ozone plus uv remained stable enough to be commercially viable with respect to the refractive index, thickness and chemical profiles as determined by AES. This temperature was chosen since one application of this material is as the low dielectric constant layer in interconnects and in this application, a 400°C anneal in nitrogen is

necessary. When the as-cast and ozone treated materials were annealed to this temperature, the material was unstable with both the refractive index and thickness changing significantly.

In studying the RIE of P(PMDSS), an interesting dewetting phenomenon leading to reticulated microstructures was observed.(Chan,1998) The evolution of this morphology was studied by atomic force microscopy (AFM). From this study it was shown that it is important to perform etching at low temperatures in order to prevent the formation of reticulated structures which otherwise might collapse and/or fill in the formation of the nanoporous structures formed from the block copolymer precursor.

1.5 Formation of Nanoporous and Nanorelief Structures

Using the oxidation techniques investigated in Chapter Four, the oxidation of the triblock copolymers was studied. 3D ceramic nanostructures were produced from P(PMDSS)-PI block copolymers that exhibited the double gyroid and inverse double gyroid morphologies. (space group Ia3d). Depending on the relative volume fraction of the hydrocarbon block to the silicon containing block, either nanoporous or nanorelief structures were fabricated. In this room temperature one-step oxidation process employing ozonolysis and uv irradition, not only was the hydrocarbon block selectively removed, but the silicon containing block converted to a ceramic.

To this effect, a nanoporous structure was formed from the double gyroid material which contains PI networks in a P(PMDSS) matrix by selectively removing the PI by ozonolysis; such processing led to the preservation of both structure and morphology of the parent block copolymer. A nanorelief structure was also formed from the material which forms P(PMDSS) double gyroid networks in a PI matrix. The PI matrix was selectively removed using both ozonolysis and reactive ion etching.

Using this simple template-free, one-step, low temperature oxidation technique, porous and relief ceramic nanostructures were produced. Specifically, a combination of ozone + uv was utilized where the oxidation step performs two simultaneous functions: 1) selective removal of the hydrocarbon block 2) conversion of the remaining silicon containing block to a ceramic (silicon oxycarbide in this case). The resulting nanoporous or nanorelief ceramic materials have either near monodisperse diameter 3D connected pores or 3D connected networks and can be used for applications where high temperature stability and /or solvent resistancy is required.

With careful selection of the relative volume fraction and phases, block copolymers can be used to produce nanorelief and nanoporous materials with a vast range of different symmetries and structures. Commercially this process is significant not only because of the type of materials that are attainable but because of the simplicity and versatility of the method: large area, conformable and continuous films/coatings can be produced, the precursor is a polymer and easily processible, the nanostructures form by self-assembly, so no template is required and the oxidation is done at room temperature with inexpensive equipment. (Chan, patent pending)

Work has also been done in collaboration with Professor Julius Vancso and Rob Lammertink (University of Twente) in the reactive ion etching of poly(ferrocenylsilane)-b-polyisoprene copolymers. (Lammertink 1999) Here, thin films of cylinders were spun onto of silicon and exposed to an oxygen plasma, resulting in the removal of the PI and the formation of dots comprised of a complex iron-silicon-oxide. Due to the presence of an inorganic, one-step lithography was shown to be possible.

1.6 Future Studies

It is possible with careful design of the block copolymer system to produce porous or relief nanostructures by methods other than oxidation. For example, a polymer system can be used where one block can be selectively removed by acid etching (i.e. poly(ethylene oxide), PEO) or by an electron beam (i.e. poly(methylmethacrylate) PMMA) and/or by annealing above the ceiling temperature resulting in depolymerization (PMMA or alpha-methylstyrene.) Also, by controlling the relative volume fraction of the degradable block, nanostructures can be produced from morphologies other than the double gyroid.

Work has recently been initiated in collaboration with Prof. Caroline Ross (DMSE, MIT) on the formation of magnetic nanostructures form block copolymer templates. These templates are formed by selectively removing one phase by methods such as etching, oxidation, selective irradiation and degradation. The nanochannels that are formed are then subsequently back-filled with a magnetic material such as cobalt by electroplating. This work is a direct spin off of the thesis and has great potential to produce a new generation of high density magnetic storage devices.

Chapter Two
Material Synthesis and Selection of Composition

2.1 Introduction

In order to produce nanoporous ceramic materials from block copolymer precursors, careful design and synthesis of the precursor material was necessary. The focus of this chapter is on the synthesis of the homopolymers and block copolymers used in this thesis.

Since block copolymers are an important aspect of this work, an overview on the theory behind the formation of ordered microdomain structures from these materials is first given. A section is then specifically devoted to the work that has been carried out on silicon containing block copolymer systems and their use in lithography.

In our case, the block copolymer that we required needed to perform two functions, namely the selective removal of the organic block and the conversion of the silicon in the silicon-containing block to an oxidized material. To achieve our goals, the block copolymer system was designed with these features in mind and in **Section 2.1.2**, the reasons for choosing the poly(pentamethyldisilylstyrene-block-isoprene) P(PMDSS)-*b*-PI are discussed.

Experimentally, the synthetic procedure for synthesizing the silicon-containing monomer is given. The polymerization of P(PMDSS) by both living free radical and anionic techniques is outlined and the material synthesized by both routes compared by GPC, NMR and FTIR. (Chan, 1998) The anionically synthesized P(PMDSS) was then further characterized by elemental analysis (through flame tasting) and by differential scanning calorimetry (DSC). Living free radical polymerization was carried out under the direction of Dr. Craig Hawker at IBM Almaden Research Center while the anionically polymerized material was kindly synthesized by Dr. Apostolos Avgeropoulos, Dr. Hermis Iatrou and Dr. Nikos Ekizoglou members of Professor Nikos Hadjichristidis' group at the University of Athens. These homopolymers were the basis of the study on the oxidation of the silicon containing polymer, as discussed in **Chapters Four** and **Five.**

Block copolymers of P(PMDSS) and PI were also synthesized anionically at the University of Athens. The synthetic routes for polymerizing these materials anionically is described and a table outlining the various molecular weights, volume fractions and polydispersities given. Eight copolymers were synthesized and their morphologies are documented in **Chapter 3.**

2.1.1 Block Copolymers and Ordered Microdomain Structures

Block copolymers are macromolecules comprised of chemically distinct homopolymer chains that are joined together by covalent bonds. "Block" refers to long sequences in the chain which consist of one monomer type while "copolymer" refers to the presence of two or more chemically distinct monomer species in the chain.(Hajduk 1995) The sequential arrangement of block copolymer structures can vary depending on the number of blocks and their chemical distinction. Diblocks contain only two chemically distinct segments A-B, while triblocks contain three blocks of which two can be chemically distinct, A-B-A or three can be chemically distinct A-B-C. (Noshay 1977) Block copolymers which consist of multiblock $(\text{-A-B-C})_n$ systems with many segments have also been synthesized in the literature. (Breiner 1998 and Sioula 1998)

The properties of block copolymers are often superior to their parent homopolymers since a single block copolymer will have a combination of both parent homopolymers' properties. Thus, block copolymers can be formed where one block, for example, will provide the necessary mechanical properties and the other block the transport properties. (Folkes 1985, Kinning 1987) Block copolymers can be synthesized by a variety of techniques that include anionic addition, ring opening polymerization and step growth polymerization techniques. The important characteristics of a block copolymer, include the Flory-Huggins segment-segment interaction parameter χ_{AB}, the relative lengths of each block, the number average molecular weight, (M_n), weight average molecular weight, (M_w) and the polydispersity (p.d.) defined as M_w / M_n. An ideal polymer would be one where the polydispersity is one, resulting in a single species of the molecular weight distribution. This is desired since a lower polydispersity in molecular weight translates to a more precise control of a polymer's morphology and properties.

The structure of block copolymer systems is governed by self-assembly. By tailoring the relative block sizes, an equilibrium 3-D superstructure with a specific geometry will form as a consequence of thermodynamics. The phase behavior and hence morphology of a bulk block copolymers is controlled by three parameters: N, ($N=N_A + N_B$) the overall degree of polymerization, ϕ, ($\phi = N_A/ (N_A + N_B)$) the volume fraction of the A block (assuming a

diblock copolymer), and the A-B segment-segment (Flory-Huggins) interaction parameter χ. Flory (1953) developed a model for the free energy of mixing of a polymer-solvent system which was then extended to the blending of two polymers. This free energy model is given by:

$$F/kT = (\phi_A / N_A) \ln (\phi_A) + (\phi_B / N_B) \ln (\phi_B) + \chi_{AB} \phi_A \phi_B$$

where ϕ_i is the volume fraction of the polymer i^{th} in the blend and N_X is the number of statistical segments in the homopolymer. The first two terms encompass the ideal contributions of translational entropy to the free energy of mixing and are dictated by the ϕ_i and $1/N_x$. The last term which is governed by χ, represents the enthalpic contribution to the free energy as well as the non-ideal entropic contributions. This drives the system towards phase separation if AB segment pair interactions are unfavorable. χ is defined by the difference in interaction energies between AA, BB and AB segment pairs and follows a temperature dependence which is usually approximated to $\chi(T) \sim \alpha T^{-1} + \beta$ Thus, as temperature is lowered, χ increases thereby favoring a decrease in A-B contacts and at a critical temperature, phase separation will occur. The overall phase state of the system is said to be governed by the product χN since entropy scales as 1/N and enthalpy as χ.

This model can be extended to block copolymers which can be viewed as two different polymers which are covalently linked at one point. Since the blocks are covalently linked, phase separation can only occur on the order of molecular lengths and as a result is described as *microphase separation*. In most block copolymer systems, χ is a positive term since A and B are dissimilar polymers and hence have unfavorable interactions. The transition between a random homogeneously mixed state to one of an ordered microphase separated state is referred to as the order-disorder transition (ODT) or microphase separation transition.

In a block copolymer system, there are different degrees of order. On the molecular length scale, the blocks may be completely amorphous or possess a degree of liquid crystallinity or crystallinity. In the case of block copolymers that possess liquid crystallinity or crystalline blocks, the morphology that forms will depend on whether the material microphase separates first or crystallizes first. The competition between crystallization and ordering will dictate the

type of morphology that forms and there has been extensive work in understanding the relation between processing and equilibrium morphology in these material systems. For all block copolymer systems, below the ODT, the polymer chains will order into different self-assembled structures. If the polydispersity of the system is small, the equilibrium microphase separated structures are arranged onto a lattice resulting in long-range order.

The morphology which forms at the ODT depends on the competition between the enthalpic and entropic terms in the free energy of mixing. Enthalpy drives to minimize the interfacial area which separates the two blocks while entropy favors the blocks to approach random coil configurations.

A symmetrical diblock (i.e. $N_A = N_B$) will yield a lamellar morphology since the coils on either side of the intermaterial dividing surface (IMDS) will have similar dimensions. The IMDS is the surface where the junction of the A and B blocks localizes and in most traditional block copolymer morphologies is closely approximated by a constant mean curvature surface (CMC). (Thomas 1988, Lambert 1996) For a 50:50 diblock AB copolymer, Leibler (1980) showed that the critical χN value is $\cong 10.5$, as derived below:

Let γ_{AB} be the interfacial energy, χ_{AB} the Flory-Huggins interaction parameter between A and B, N the total number of segments, a the Kuhn statistical segment length, λ the microdomain periodicity of the lamellae and Σ the area of the IMDS interface per chain. The interfacial energy is proportional to the interaction parameter, giving:

$$\gamma_{AB} = \frac{kT}{a^2}\sqrt{\frac{\chi_{AB}}{6}}$$

Through volume conservation, this yields for a lamellar structure:

$$Na^3 = \frac{\lambda}{2}\Sigma$$

To calculate the equilibrium domain spacing, use the minimum-maximum principle is used where the free energy of lamellae, F_{LAM}, is given by:

F_{LAM} = Free energy due to the interface + Free energy due to chain stretching

The interfacial free energy is simply $\gamma_{AB}\Sigma$ and by modeling the chains as Gaussian springs, which gives the chains stretching energy as:

$$\frac{3}{2}kT\frac{(\lambda/2)^2}{Na^2}$$

The free energy of the lamellae is then simply given by:

$$F_{LAM} = \gamma_{AB}\Sigma + \frac{3}{2}kT\frac{(\lambda/2)^2}{Na^2}$$

Therefore

$$F_{LAM} = \frac{kT}{a^2}\sqrt{\frac{\chi_{AB}}{6}}\frac{Na^3}{(\lambda/2)} + \frac{3}{2}kT\frac{(\lambda/2)^2}{Na^2}$$

or $$F_{LAM} = \frac{\alpha}{\lambda} + \beta\lambda^2$$

Where

$$\alpha = 2akTN\sqrt{\frac{\chi_{AB}}{6}} \quad \text{and} \quad \beta = \frac{3kT}{8Na^2}$$

Now,

$$\frac{\partial F_{LAM}}{\partial \lambda} = 0 \qquad \rightarrow \qquad \lambda_{optimum} = \frac{-\alpha}{\lambda^2} + 2\beta\lambda$$

Where the optimum period of the lamellar repeat is given by:

$$\lambda = \sqrt[3]{\frac{\alpha}{2\beta}} \cong aN^{2/3}\chi^{1/6}$$

This is the well known $N^{2/3}$ scaling law for strongly segregated block copolymers. Note that the chains are stretched resulting in $N^{2/3}$ dimensions and not $N^{1/2}$.

Therefore the lamellar free energy is given by:

$$F_{LAM}(\lambda_{opt}) = \frac{\alpha}{\lambda_{opt}} + \beta\lambda_{opt}^2$$

Note that the enthalpic contribution to the free energy is approximately two times that of the entropic contribution.

$$F_{LAM} \cong 1.2kTN^{1/3}\chi^{1/3}$$

At the Order-Disorder Transition (ODT):

$$F_{LAM} = F_{DISORDERED}$$

At the disordered state, the chains have their preferred Gaussian shapes so their energy is just the segment-segment contact energy which is given by:

$$1.2\ kTN^{1/3}\chi^{1/3} = N\chi\phi_A\phi_B kT$$

For a 50/50 volume fraction, $\phi_A\phi_B = 1/4$, so:

$$1.2\ kTN^{1/3}\chi^{1/3} = N\chi/4$$

or

$$(N\chi)_c = (4.8)^{3/2} \sim 10.5$$

where $(N\chi)_c$ is the critical value at the order-disorder transition.

If the volume percent of one of the blocks is increased, the volume requirement of each of the coils changes. To relieve this imbalance the interface between the blocks will become increasingly curved towards the block with the smaller volume fraction. The mean curvature (H) of the IMDS increases from zero for flat lamellae to systematically increasing values of H for double gyroid, cylinders and spheres. Where the mean curvature is defined as:

$$H = \frac{1}{2}(C_1 + C_2) \quad \text{where } C_1 = \frac{1}{R_1} \text{ and } C_2 = \frac{1}{R_2}$$

Where C_1 and C_2 are the curvatures and R_1 and R_2 are the radii.

In all cases, the IMDS is always defined by a surface of constant mean curvature (CMC) with the condition for minimization of area at fixed volume fraction, as discussed in **Section 6.1.4.** Thus, the morphology that forms depends on the volume fraction of the blocks and the temperature at which this occurs depends on the degree of polymerization N and the interaction between the two blocks as defined by χ.

In the strong segregation limit, where $N\chi >> 10$ and where the interface thickness, ξ, is small as compared to the domain periodicity, λ, the microdomain morphology changes with the volume fraction of the A block relative to the B block. **Figure 2.1** shows the evolution of morphology with increasing A (i.e. polystyrene) content and decreasing B (i.e. polyisoprene) content in an AB diblock copolymer system.

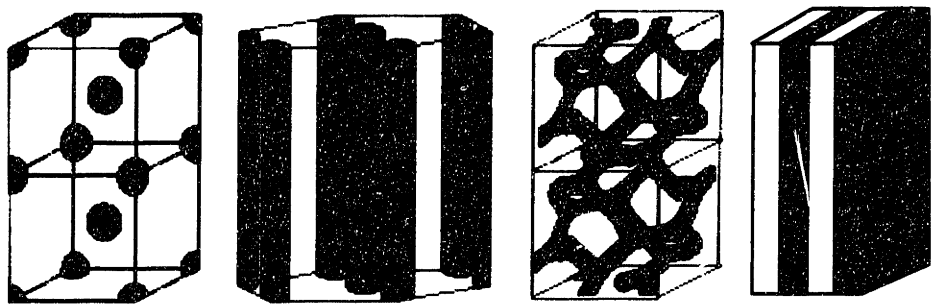

Figure 2.1: Morphology diagram of an A-B block copolymer system with increasing A volume fraction (blue phase region). (After B.J. Dair 1998) As the relative amount of A increases, the morphology changes from A spheres packed on a bcc lattice in a B matrix, to A cylinders packed on a hexagonal lattice in B, to a cubic tricontinuous A structure in a B matrix (i.e. double gyroid) to alternating A-B lamellae. Once the volume fraction of A surpasses 50%, B becomes the minority phase and the above morphologies are inverted (Burke 1973 and Holden 1996).

The block copolymers used in this thesis were triblocks and in our particular material system, it was found that these morphologies often formed at volume fractions that were different to more traditional diblock copolymer systems. This shift in volume fraction could be explained by the asymmetric architecture of some of our polymer samples and/or differences in segment size of the polymer blocks as discussed in **Section 3.3.4.**

Although a wide range of morphologies were obtained in our silicon containing polymer system, the focus of this thesis was on the double gyroid morphology (Hajduk 1994), shown in **Figure 2.2.** This structure was chosen since the 3-D networks provides great technological and commercial utility due to their interconnected nature and intricacy. This coupled with the small characteristic dimensions of block copolymers results in a unique system since structures that are *both* on this size scale and with this level complexity can *not* be produced by more traditional routes such as lithography.

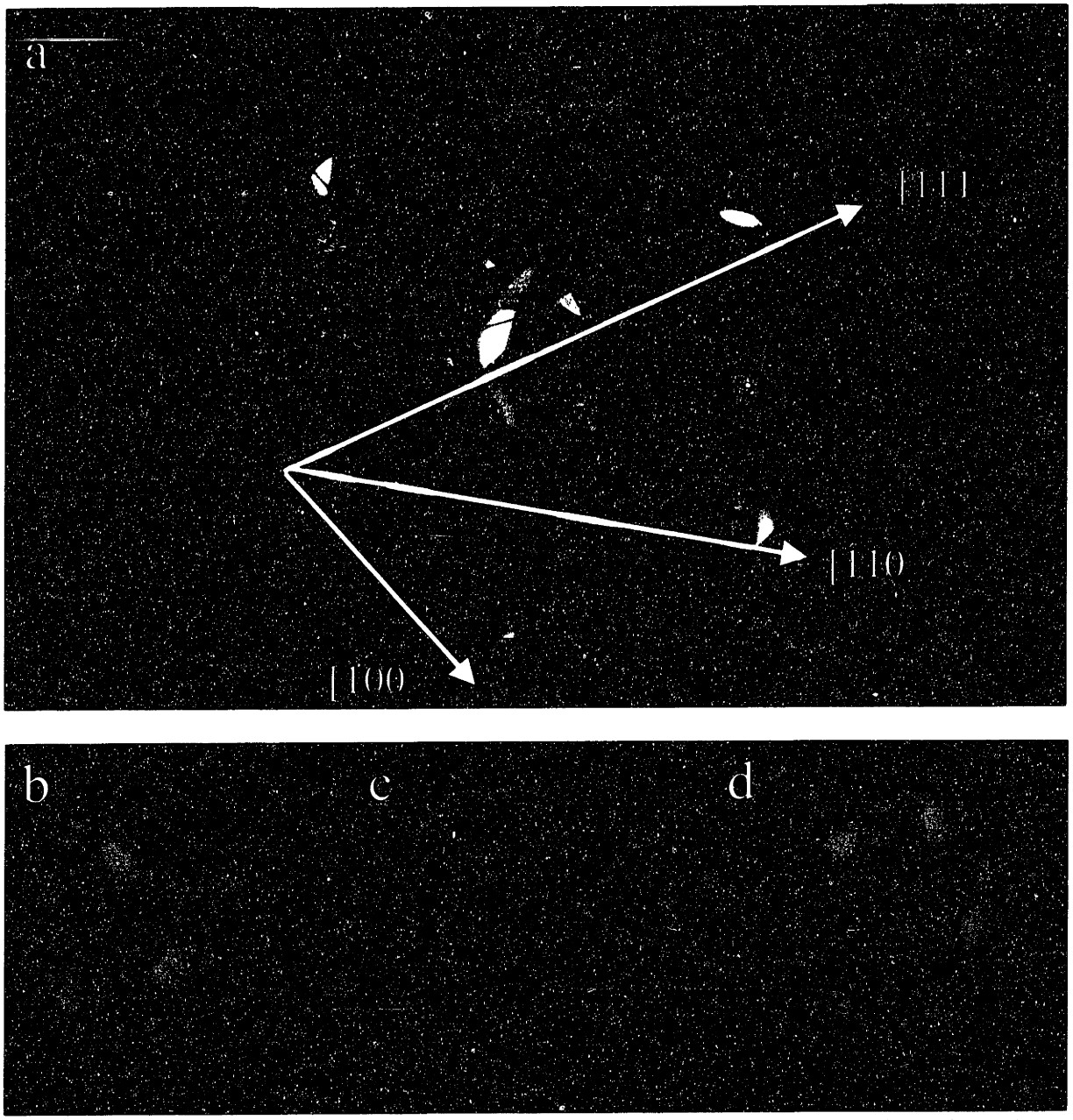

Figure 2.2: Schematic of the double gyroid morphology generated by Jim Hoffman from the Mathematical Sciences Research Institute (MSRI) at the University of California, Berkeley, using a computer simulation program that renders volumes based on constant mean curvatures.[1] The networks are comprised of cylinder-like connectors aligned along <110> directions joining in threes at nodes. There are sixteen triple junction nodes per unit cell. (b) View down the [100], showing 4_1 screw symmetry (c) View down the [110], exhibiting 2_1 and 2 symmetry axes (d) View down the [111], exhibiting 3 fold symmetry. For the P(PMDSS)-DG morphology, the networks are comprised of PI and the matrix P(PMDSS) while for the inverse double gyroid morphology, PI-DG, the reverse is true.

[1] www.msri.org/people/staff/jim

In addition, since the structure is periodic in three dimensions, morphology orientation is not critical, since pathways for oxidation and removal of the hydrocarbon block exist irrespective of the orientation of the morphology with respect to the surface. This is not the case with cylinders, where morphology orientation is crucial. For example, a block copolymer that forms hydrocarbon cylinders in a silicon containing matrix will require that the hydrocarbon cylinders are perpendicular to the surface in order to completely remove the hydrocarbon cylinder by oxidation. If the cylinders are lying in the plane of the substrate, the silicon containing matrix would shield underlying cylinders from becoming oxidized. In order to control the orientation of the cylinder morphology it is necessary to carefully control both film thickness and the interactions of the polymer with both the substrate and air interfaces. By focusing on the double gyroid, these parameters do not need to be controlled since orientation will not affect the removal of the hydrocarbon block from the bulk of the material.

The double gyroid is also an inherently interesting morphology to study because many different commercial applications can be envisioned with this triply periodic structure due to the interconnected nature of the networks. For example, if the material was to be used as a membrane, the networks naturally possess redundant pathways for the filtrate to travel. If one channel or strut were to become clogged, the filtrate can travel back to the triple point and move down an alternative channel or strut. Similarly, if the channels were plated with metal, the conductivity of the metallic network would be robust due to the redundancy of the conduction pathways.

2.1.2 Silicon Containing Block Copolymers

Silicon containing polymers have had widespread interest in the semiconductor industry due to their usefulness as etch resists in multilayer schemes. Traditionally, high resolution 2-D patterns have been generated by microlithographic techniques. However as the complexity of integrated circuits increases so do the problems associated with using single-layer resists over chip topography. For this reason, a variety of multilayer resist schemes have been developed. The simplest of these utilizes a thin imageable layer coated over a thick planarizing polymer. After development, the high resolution images from the top layer are transferred to the underlying layers by oxygen reactive ion etching (O_2-RIE) using anisotropic etching techniques as discussed in **Section 4.12.** Since most organic polymers containing C,H,N,O etc. are rapidly

etched by the aggressive oxygen plasma, considerable effort has been expended on the development of imageable polymers which form refractory oxides in an oxygen plasma (e.g. polymers containing Si, Ge, Sn, B, Ti, Al, etc).(Hirao 1992, Sugita 1992, Gabor 1994, 1995, Chu 1995). Silicon containing polymers are common and inexpensive; therefore this element has received the most attention. (Miller 1994)

A number of studies on the synthesis of siloxane based block copolymers for various applications have been reported. (Chaumont 1981, Gabor 1994, Chu 1995) Chu *et al.*, synthesized diblock copolymers of polystyrene-poly(dimethylsiloxane), (PS-PDMS). They found that the experimentally determined phase diagram was strongly skewed towards low styrene volume fractions due to differences in the Kuhn statistical segment length as discussed in **Section 3.3.4.** Polymers which exhibited PS spheres, cylinders, lamellae and PDMS cylinders were synthesized although none of the materials were exposed to an oxygen plasma.

Gabor *et al.* (1994, 1995) studied the etching of siloxane polymers by O_2-RIE as passive etch barriers for lithography. The utilization of these materials for such an application was novel but since the application was in lithography, 1-D periodic structures, namely lamellae were studied, since the goals were primarily oxygen etch resistance and /or surface modification. One intrinsic problem with these siloxane materials is that they have very low Tg values resulting in poor dimensional stability during processing without crosslinking. (Bushnell 1986) In addition, the low surface energy of the siloxane blocks results in a migration of the siloxane block to the air-film interface resulting in the modification of the surface properties of the film. This would be detrimental in the formation of 3-D structures since an overlying passivating layer of SiO_x would inhibit the patterning of underlying layers.

In addition to the siloxanes, silicon has been introduced into a variety of 1,3-diene block copolymers either through the use of silicon-containing monomers or by post-polymerization functionalization.(Guo 1992) Regarding the latter, Gabor *et al.* (1995, 1996) have investigated the hydrosilylation of a number of poly(styrene)-poly(butadiene) or poly(styrene)-poly(isoprene) block copolymers. The viability of these polymers as electron beam resists was investigated. The O_2-RIE etch rate selectivity of the silylated block relative to polyimide was impressive

(42 : 1). However, the stability of the functionalized butadiene copolymers was limited since the materials would crosslink after a few months while the hydrosilylation of the isoprene phase of the block copolymers could not be driven to completion.

2.1.3 Material Design

Unlike the work of previous research groups in the formation of nanoporous silica materials as discussed in **Section 6.1.1**, we developed a template-free process to form these materials. To achieve these nanoporous and nanorelief *ceramic* structures, the block copolymer system was designed so that it would have the following properties:

1. The two blocks would microphase separate.
2. The block copolymer would have a relatively low polydispersity, so that well-controlled phase separated morphologies would form.
3. The organic block would have a glass transition temperature (Tg) which was significantly below room temperature so that the final polymer could be easily processed.
4. The silicon containing block would contain enough silicon so that SiO_x would form when exposed to an oxygen plasma, ozone and/or uv giving flexibility in the oxidation process.
5. The silicon-containing block would have a Tg significantly above room temperature so that once the non-silicon containing polymer was removed by reactive ion etching, ozone and/or uv, the remaining polymer would retain its structural integrity.
6. The domain size would be tailored through control of the polymer molecular weight and low enough that the viscosity of the polymer in solution would not be too high for processing.
7. The two blocks would have a common solvent in order to facilitate solution processing.

In **Section 2.1.2**, the silicon containing block copolymers that have been previously synthesized for use as bilevel resists by other groups (Gabor 1994, 1995 and Bushnell 1986) were discussed. However, these polymers were not ideal since some had dimensional stability problems due to the presence of the silicon in the low Tg block while others required a post-polymerization process in order to incorporate the silicon and this process was not 100% efficient.

A polymer system was chosen where the silicon would be intrinsic to the high T_g phase. Thus the issue of dimensional stability upon removal of the hydrocarbon block would be overcome and the silicon would not need to be incorporated in a post-polymerization process.

Pentamethyldisilylstyrene, PMDSS whose structure is shown in **Figure 2.3** was chosen because it met these requirements and due to its similarity to styrene, would anionically polymerize. PMDSS also has 24wt% silicon which is significantly more than the minimum necessary silicon content of 10wt% for a continuous silicon oxide etch barrier to form upon exposure to an oxygen plasma, as discussed in **Chapter Four.**

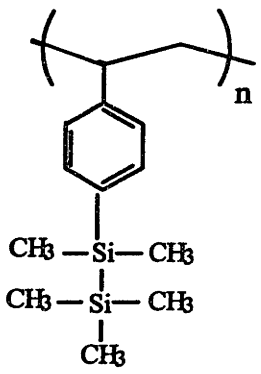

Figure 2.3: Chemical structure of poly(pentamethyldisilylstyrene), P(PMDSS).

The anionic polymerization of p-trimethylsilylstyrene was first reported by Chaumont *et al.* (1982) and Yamzaki *et al.* (1984). More recently, Hirao *et al.* (1992, 1995) studied the anionic polymerization of styrene derivatives containing permethyl oligosilane substituents. These authors prepared triblock copolymers of the ABA type where A is *p*-trimethylsilyl styrene and B is either styrene or isoprene. Recently, the same authors have reported the formation of block copolymers from a variety of oligosilyl substituted styrenes, and styrene. (Hirao 1995) Although diblock copolymers of polystyrene (PS) and poly(pentamethyldisilylstyrene) P(PMDSS) were reported, the total molecular weights were relatively low ($M_w < 29{,}000$) and morphology studies were not described.

For the hydrocarbon block, polyisoprene was chosen because of its low Tg and the presence of double bonds in its structure. The low Tg of PI would enable processing by methods such as roll-casting, (Albalak 1993) where the block copolymer must not be completely glassy in order to facilitate processing. Triblock copolymers rather than AB diblock copolymers were synthesized because in roll-casting, domain-domain coupling by

triblocks helps to achieve long range order of the sample. The triblocks also allow the polymer chains to form bridges and loops which enhance the mechanical properties of the resulting oriented material.

In addition, the double bonds in PI can be degraded by both ozonolysis and oxygen reactive ion etching giving flexibility in the oxidation process. Details of these techniques are discussed later in **Chapter Four.** For the PI itself, it was necessary to synthesize a microstructure dominated by -1,4 and -3,4 type double bonds. If the double bond were in the sidechain rather than in the backbone, ozonolysis would not result in polymer fragmentation since the backbone chain would not be degraded. To promote the formation of -1,4 and -3,4 bonds, the PI was synthesized primarily in a non-polar solvent, benzene.

2.2 Synthetic Experimental Procedures

In this section the synthesis of the materials used in this thesis is discussed. In order to produce these specialized silicon-containing polymers, the monomer was first synthesized and the synthetic procedures for this is outlined. The formation of silicon containing homopolymers is discussed by living free radical polymerization techniques. Halogenated initiators were first attempted but due to the difficulty in removing the copper catalysts, nitroxide initiators were then used. The homopolymer was also synthesized anionically in Greece and this synthesis as well as the anionic polymerization of the block copolymers is discussed.

2.2.1 Monomer Synthesis

p-Pentamethyldisilylstyrene was synthesized by Mr. Victor Lee from IBM Almaden Research Center, according to a modified literature procedure. (Kawakami 1988) In a 500 mL 3-neck flask equipped with mechanical stirring, magnesium turnings (9.14 g, 381 mmol) in tetrahydrofuran, THF, (100 mL) was activated with 10 drops of 1,2-dibromoethane heated to a gentle reflux under nitrogen. *p*-Chlorostyrene (48 g, 346 mmol) was added slowly with efficient stirring until the mixture began to foam and reflux vigorously. Heating was discontinued and the remaining p-chlorostyrene was added at such a rate that continuous refluxing was maintained. After the addition, the mixture was heated to reflux for another 40 min. At 35 °C, chloropentamethyldisilane (36.1 g, 216 mmol) in THF (50 mL) was added and the final mixture was heated at 50 °C for 1 hr. The cooled mixture was diluted with hexane and filtered through

Celite. Solvent was evaporated under vacuum and the crude product was column chromatographed with petroleum ether. The final product was distilled, giving a clear oil 35.6 g (70%): bp 72-74°C, (0.5 mTorr); ^{1}H NMR $\delta(CDCl_3)$ 7.30-7.38 (m, 4H), 6.65 (dd, 1H, J=17.61, 10.87 Hz), 5.71 (dd, 1H, J = 0.94, 17.66 Hz), 5.18 (dd, 1H, J = 0.94, 10.86 Hz), 0.27 (s, 6H), 0.91 (s, 9H); ^{13}C NMR $\delta(CDCl_3)$ 139.4, 137.5, 136.9, 134.0, 125.5, 113.8, -2.3, -4.0.

2.2.2 Homopolymer Synthesis by Living Free Radical Polymerizations

Living free radical (LFR) polymerization was chosen as a synthetic route for the homopolymer P(PMDSS) because of its simplicity as a polymerization technique compared to techniques like anionic polymerization.(Solomon 1993) The synthesis here is the first reported polymerizations of silicon containing monomers by the living free radical route. These polymerizations were carried out at IBM Almaden Research Center under the guidance of Dr. Craig Hawker. As seen in the reaction schemes, **(Figures 2.4-2.5)** the initiators are activated by heating and are deactivated upon cooling. The elegance of this technique is that starting blocks can be produced, cooled to room temperature, characterized without deactivating the initiating end. If a block copolymer is desired, the initiating end on these homopolymers can be reactivated by heating and a block copolymer formed by polymerizing a second monomer type on this active end. Multi-block copolymers can be synthesized through sequential addition of different monomer types. In the past, free radical polymerization has not been a viable pathway for the production of block copolymers because of the high polydispersities of the polymer due to premature termination of the growing end by either disproportionation or combination. In the last few years, there have been advances in controlling this polydispersity by using stable free radicals resulting in a polymerization technique known as living free radical polymerization.(Solomon 1993) However, this technique can not be used for polymerizing the block copolymer system chosen since isoprene can not be initiated by living free radicals so only the homopolymer was synthesized.

Two approaches were taken in trying to synthesize these polymers. In the first, halogenated initiators were used and in the second, nitroxide based initiators.

2.2.2.1 Halogenated Initiators

Living free radical polymerizations using halogenated initiators were based on the following reaction where X is chlorine or bromine:

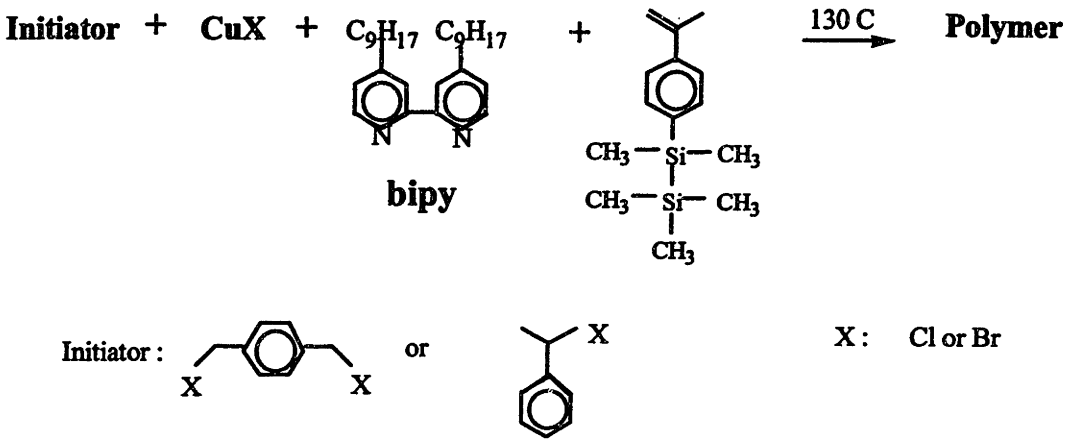

Figure 2.4: Polymerization of P(PMDSS) using a halogenated initiator system.

Matyjasewski *et al.* have demonstrated that this method of polymerization is relatively successful for styrenes and (methyl)acrylates, (Wang *Macromolecules* 1995 and *JACS* 1995, Patten, 1996, Gaynor 1996) producing polymers with polydispersities ranging from 1.1 to 1.5.

The mechanism behind these reactions is based on atom transfer radical polymerization (ATRP). The copper in the copper halide (CuX) complexes with the bi-pyridine (bipy) ligands which then acts as a catalyst for the initiator during the polymerization of the vinyl monomers. The reaction itself is based on a redox cycle with the addition of each monomer unit corresponding to one cycle. The relatively low polydispersities (compared to the lower limit of 2.0 predicted by traditional free radical polymerization theories) are attained due to the minimization of termination reactions during polymerization. Details on the exact mechanism of these polymerizations are given in by Matyjaszewski *et al.* (Wang, JACS 1995)

However, one problem of this polymerization technique was that despite washing and precipitating the synthesized polymer multiple times it was not possible to remove the Cu complexes and the polymer retained a greenish color. In etching this would be very detrimental

since the Cu contamination in the polymer would not be acceptable if this material were to be used as a low dielectric constant layer. For this reason, nitroxide based initiators were pursued.

2.2.2.2 Nitroxide Based Initiators

Nitroxide based initiators were investigated in parallel with the halogenated initiators for the preparation of macromolecules. (Hawker 1996, Veregin 1996) Work was focused on using 2,2,6,6-tetramethylpiperdinyloxy (TEMPO) as an initiator. A typical reaction scheme is shown below:

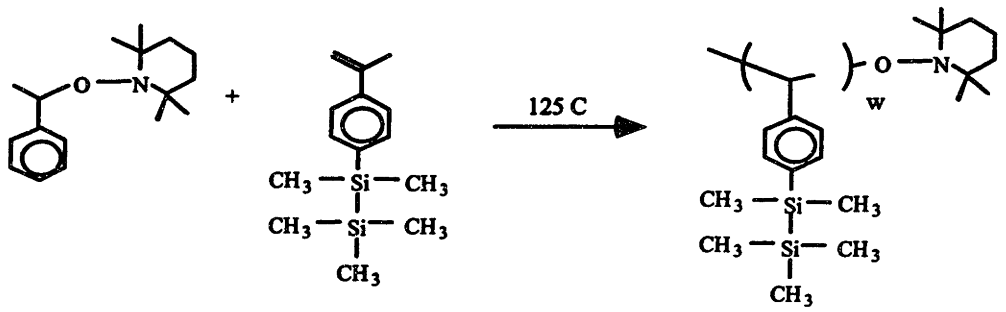

Figure 2.5: Polymerization of P(PMDSS) using a nitroxide initiator system.

With nitroxide based initiators, the low polydispersity of the polymer is due to the stability of the nitroxide free radicals which are thermally activated and are controlled by diffusion of the monomer. Since the polymerization is diffusion controlled and the nitroxide free radicals cannot initiate new chain growth on their own, the polymerization adopts a living nature. (Fukuda 1996, Veregin 1996)

Polymerizations based on TEMPO were found to be more reliable than those using halogenated initiators. TEMPO has been used to polymerize styrene and yields polymers with polydispersities as low as 1.10. (Hawker 1994)

Polymerizations were carried out neat using a 100 ml round-bottom flask equipped with a magnetic stir bar. Pentamethyldisilylstyrene (6 g) was pipetted into the flask with (0.046 g, 1.762×10^{-4} mol) of TEMPO initiator. Based on the ratio of monomer to initiator, this would result in a homopolymer with molecular weight of 35,100. The solution was stirred and put in an oil bath at 125°C. Argon was flowed into the reaction vessel throughout the polymerization process. After 12 hours an aliquot of the solution was removed using a syringe and run through a gel permeation chromatograph (GPC). The reaction vessel was then removed from the oil

bath and allowed to air cool. Dichloromethane was poured into the flask and the product allowed to dissolve. The polymer was then precipitated into methanol and was not fractionated further.

Using this nitroxide based initiator a low molecular weight P(PMDSS) was synthesized with a high polydispersity (Mn ~ 10,800 and p.d. 1.83). This molecular weight was much lower than the predicted molecular weight of 35,100. One concern was that the silicon-silicon bond was unstable at these higher temperatures which would result in crosslinking or side reactions, but NMR and FTIR of the synthesized polymer confirmed the structure as P(PMDSS), as discussed in **Section 2.3**. It was believed that the bulky silicon containing side group may have inhibited the diffusion of the monomer to the active end through steric hindrance, thereby increasing the polydispersity of the sample as compared to styrene polymerizations.

2.2.3 Homopolymer Synthesis by Anionic Polymerization

Due to the high polydispersity of the polymer synthesized by living free radical techniques, P(PMDSS) was also synthesized anionically. All anionic polymerizations were carried out in Professor Nikos Hadjichristidis' group at the University of Athens.

The procedure used for the anionic synthesis of the PMDSS block is very similar to that of Hirao (1992, 1995), as shown in **Figure 2.6**.

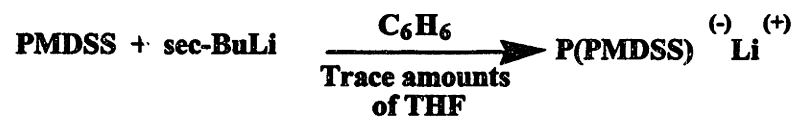

Figure 2.6: Schematic of P(PMDSS) homopolymer synthesis by anionic polymerization using *sec*-butyl lithium initiator.

PMDSS was purified following typical procedures for styrene. Monomer was distilled from CaH_2 to di-butylmagnesium and then to ampoules which were used for the polymerizations. The distillation of PMDSS was carried out at temperatures higher than those used for the distillation of simple styrene monomer, since the boiling point of PMDSS (72°C at 0.5 mm Hg), is higher than that of styrene (~50°C at 0.5 mm Hg). It was found that the monomer behaved identically to styrene during the synthesis, since the polydispersity index of a homopolymer P(PMDSS) was very low (1.06) and the observed molecular weight (M_w) of 38K

was very close to the expected molecular weight of 34K. The difference between the predicted and actual molecular weights is well within the experimental errors of the two characterization methods Low Angle Laser Light Scattering (LALLS) and Gel Permeation Chromatography (GPC).

2.2.4 Block Copolymer Synthesis by Anionic Polymerization

The synthetic procedure described here was also carried out by Drs. Apostolos Avgeropoulos and Hermes Iatrou and follows the sequential addition of the monomers as illustrated below. (Avgeropoulos 1998)

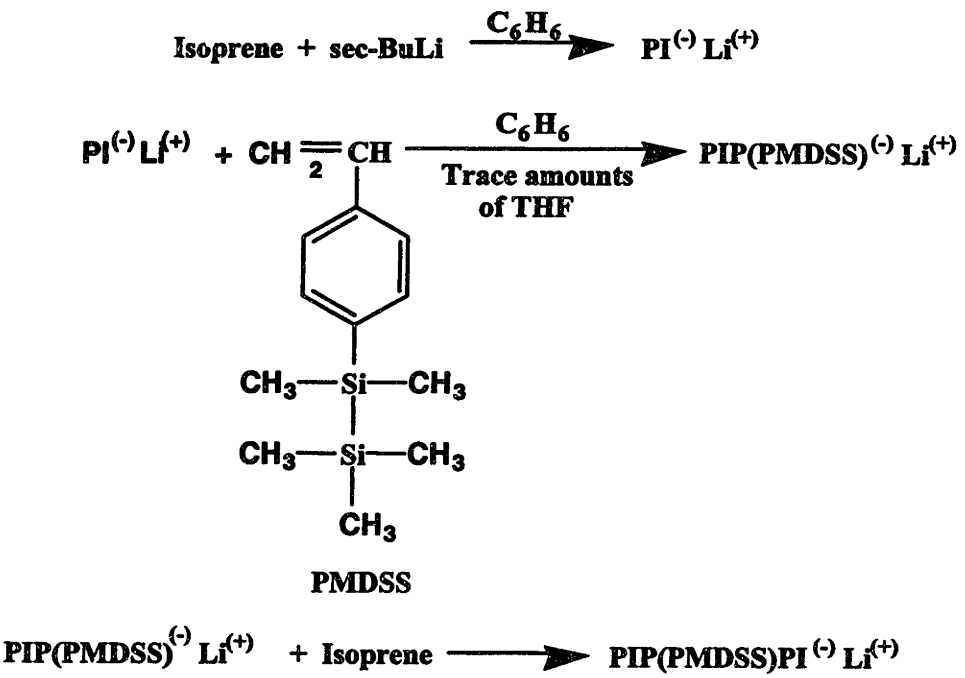

Figure 2.7: Schematic of the anionic polymerization of triblock copolymers through the sequential addition of monomers.

Following the synthesis of the polyisoprenyllithium block, a trace amount of tetrahydrofuran (THF) (0.5ml), was added in order to promote the initiation of the P(PMDSS) block and maintain the narrow molecular weight distribution of the diblock precursor. It should be noted that in the final block copolymer, the two PI end blocks have different molecular weights and different microstructures. The difference in microstructure was determined from ^{1}H-NMR spectroscopy and can be attributed to the small amount of the polar solvent THF that

was added in the synthesis of the second PI block. The first PI block, which was synthesized in pure benzene, has a microstructure that is typical of anionic polymerization of isoprene in a non-polar solvent, (10 wt % 3,4, 70 wt% cis-1,4 and 20 wt % trans-1,4). However, since the second block was synthesized in benzene with a small amount of a polar solvent, the microstructure contains 1,2 microstructure and an increased value of 3,4 microstructure (8 wt % 1,2, 42 wt % 3,4 and 50 wt % 1,4) making the material harder to ozone etch. Since only a small amount of THF was present during the synthesis, the 1,2 content is not as high as isoprene polymers synthesized in strictly polar solvents, but there was a significant increase in the -3,4 component.

The mixture was allowed to react for 3 hours at 40°C to complete the polymerization of the middle PMDSS block. Before adding the third monomer (isoprene), an aliquot of the diblock was taken for characterization by GPC as shown in **Figure 2.8** for the polymerization of the polymer that forms the double gyroid morphology with P(PMDSS) as the matrix. It is known from anionic polymerization of styrene and isoprene that the colors of the living end change during polymerizations, depending on the monomer that is being polymerized. In the case of styrene, a dark red-orange color is normally present (depending on the concentration of the solution), while for isoprene, a yellow to pale yellow color is usually observed. The change from one color to the other, when the appropriate monomer is added should be nearly instantaneous since the initiation and propagation rates are fast in both cases. Despite the fact that in PMDSS the side group on the phenyl ring is bulky (which could contribute to steric hindrance thereby decreasing the initiation rate), the color change from yellow to orange was indeed nearly instantaneous due to the addition of THF. The addition of a small amount of polar solvent before the addition of the second monomer led to a decrease in the degree of aggregation of the solution from 3-4 to 2. It is important to note that when the isoprene monomer was added to the P(PMDSS) living end, it was found that the change in color from orange to yellow was very slow, leading to the conclusion that the P(PMDSS)$^-$Li$^+$ is a poor initiator for the polymerization of isoprene.

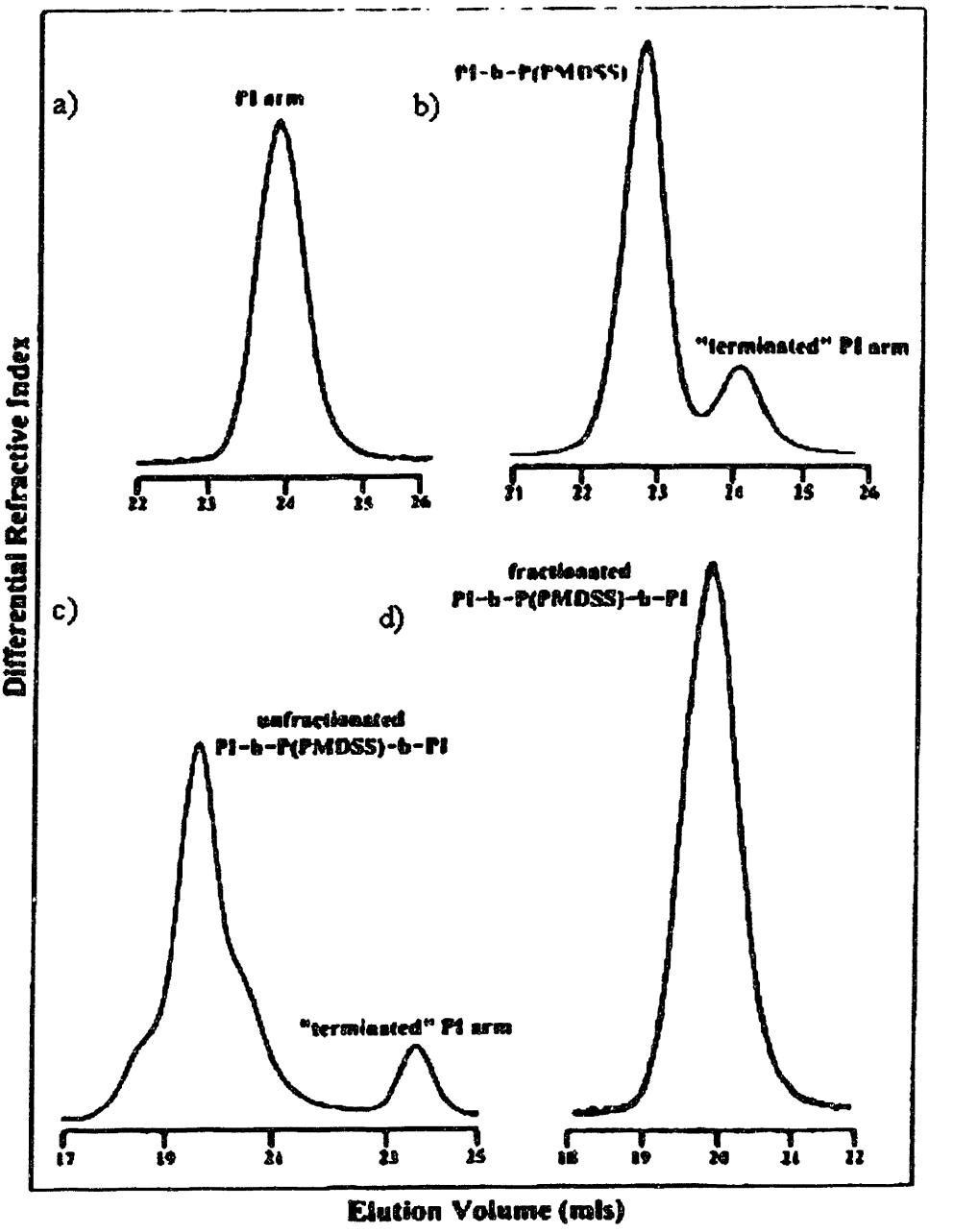

Figure 2.8: Gel permeation chromatographs of the triblock copolymer P(PMDSS)-DG during the polymerization process. a) After the synthesis of the first PI block b) After the synthesis of the P(PMDSS) mid-block. Some of the PI has terminated resulting in a small peak at higher elution volumes. c) After the synthesis of the second PI end block. In order to remove the terminated PI arm and to decrease the polydispersity of the polymer, the material was fractionated, resulting in the GPC spectra in d).

In the P(PMDSS)-DG sample that forms a double gyroid morphology with PI networks, designated P(PMDSS)-DG, a small percentage of the first block, PI$^-$Li$^+$, was terminated due to possible impurities in the PMDSS monomer. This is shown in **Figure 2.8** at the chromatograph of the PI-*b*-P(PMDSS) living end and it is characterized as "terminated" PI block. Fractionation was carried out by adding methanol (non-solvent) to the stirred polymer solution (~0.5% w/v) in toluene (solvent) at room temperature until turbidity was detected. The mixture was then heated and stirred until clear, transferred to a warm separatory funnel and allowed to equilibrate to room temperature overnight. The procedure continued until the undesirable products were no longer present by using GPC.

For the B_1AB_2 PI-rich copolymers, the reactions used were similar to the above reactions, except that the order of monomer addition is reversed. In these polymerizations, the small amount of THF which is needed to enhance reaction kinetics, is added just before the polymerization of the final PMDSS end block, after the middle PI block has been polymerized. For this reason, the microstructure of the PI is characteristic of anionic polymerization of isoprene in a non-polar solvent. In order to overcome this slow initiation and obtain low polydispersity of the final polymer, a small amount of a polar component is typically added to increase the initiation and propagation rate of the isoprene block by the first block, P(PMDSS)$^-$Li$^+$. However we chose not to do that in order to avoid obtaining a PI block with high 3,4-microstructure which is undesirable for ozone etching. It should be noted that the polydispersity of the high molecular weight P(PMDSS)-PI-P(PMDSS) block copolymers is also greater than usual due to the combination of the high molecular weight and high solution viscosity due to a concentration of ~20%.

Since the half-life ($t_{1/2}$) of PI is 1hr and the polymerization is considered complete after $6t_{1/2}$, THF was added after 10hrs to increase the solubility of the solution for the polymerization of the final block. By waiting such a long time, to allow the completion of the isoprene polymerization, the change in microstructure of the PI block would be unaffected by the addition of a polar solvent. From ^{1}H-NMR spectroscopy it was determined that the microstructure adopted by the PI block was typical for the anionic polymerization of isoprene in benzene.

2.3 Characterization of Synthesized Polymers

The molecular weights and structure of the synthesized polymers will be discussed here while the characterization of the morphologies of the synthesized block copolymers is documented in **Chapter Three.**

2.3.1 Molecular Weight Determination

The weight-average molecular weight (M_w) of the final polymers was determined with a Chromatix KMX-6 low-angle laser photometer (LALLS) by Drs. Avgeropoulos and Iatrou. This instrument, equipped with a helium-neon laser, was operated at a wavelength of 633 nm. The refractive index increments, dn/dc in THF at 25° C were measured with a Chromatix KMX-16 refractometer.

The M_w values were obtained from the $(KC/\Delta R\theta)^{1/2}$ vs. C plots ($\Delta R\theta$, excess Rayleigh ratio; K, combination of known optical constants; C, polymer concentration). In all cases the correlation coefficient was better than 0.99.

GPC experiments were carried out at 30°C using a Waters model 510 pump, Waters Model 410 differential refractometer and Waters model 486 tunable absorbance detector. Three Phenomenex (type: phenogel 5 linear, pore size: 50 Å to 10^6 Å) columns were used. THF, distilled over CaH_2 and sodium, was the carrier solvent at a flow rate of 1 mL/min.

The molecular characteristics of the block copolymers synthesized are shown in **Table 2.1.** It can be seen from **Table 2.1** that the polydispersities of the triblocks synthesized ranged from 1.06 to 1.5. Typically 1-2 g of each polymer was synthesized for characterization and experimental work. In the case of the double gyroid materials produced, the P(PMDSS)-DG, (Sample 1), 0.6 g of the material was synthesized and for the PI-DG, (Sample 6), 1.5 g had been synthesized. The specifics with respect to the morphologies that formed and the degree of ordering of the materials is discussed in Chapter Three.

Table 2.1: Molecular and morphological characteristics of homopolymers and block copolymers

Sample ID	Polymer	Molecular Weight	Polydispersity	$\phi_{P(PMDSS)}$	Morphology
P(PMDSS) 38	P(PMDSS) (anionic)[a]	34K	1.06	1	Not applic.
P(PMDSS) 11	P(PMDSS) (LFR)[b]	11K	1.83	1	Not applic.
1	PI-PSS-PI	24K-98K-26K	1.12	0.66	Double Gyroid
2	PSS-PI-PSS	52K-250K-42K	1.24	0.26	spheres
3	PSS-PI-PSS	34K-160K-34K	1.5	0.30	spheres
4	PSS-PI-PSS	43K-167K-46K	1.2	0.35	No apparent periodic morphology
5	PSS-PI-PSS	44K-148K-120K	1.3	0.53	cylinders
6	PSS-PI-PSS[b]	44K-167K-112K	1.06	0.48	Double Gyroid
7	PSS-PI-PSS	44K-167K-46K	1.06	0.35	Lamellae
8	PI-PSS-PI	28K-110K-28K	1.09	0.66	TBA

[a] **P(PMDSS) synthesized anionically** [b] **P(PMDSS) synthesized by living free radical polymerization**

2.3.2 Nuclear Magnetic Resonance

In order to ensure that the P(PMDSS) synthesized by living free radical and anionic techniques were chemically identical, nuclear magnetic resonance spectroscopy (NMR) spectra were recorded at IBM Almaden Research Center. One concern was that the high polymerization temperatures of living free radical techniques would facilitate side reactions in the Si-Si or C-Si bonds in the monomer or polymer, or that oxygen would react with the Si species. ^{1}H-NMR, ^{13}C-NMR and ^{29} Si-NMR determinations of both the composition and the microstructure of the materials were carried out in $CDCl_3$ at 30°C using a Varian Unity Plus 300/54 instrument. All of the ^{29}Si-NMRs were performed by Ms. Dolores Miller at IBM Almaden Research Center.

Nuclear magnetic resonance (NMR) occurs when nuclei of certain atoms are exposed to an oscillating magnetic field within a static magnetic field.[2] The electrons in the atom circulate about the direction of the applied magnetic field, which induces a small opposing magnetic field at the nucleus, called the effective field. The effective field, B is proportional to the applied field, B_o, and is given by:

$$B = B_o (1-\sigma)$$

where σ is the fraction by which the effective field is less than the applied field.

The electron density surrounding the nucleus depends on the element and the bonds in the molecule. As a result, each nucleus will have a characteristic effective field which depends on its chemical environment. Since the applied field, B_o is different from machine to machine, chemical shifts were defined in order to compare NMR spectra. The chemical shift, δ, given in ppm, is the difference between the resonance frequency of the nucleus relative to a standard and is defined as:

$$\delta = \frac{(\nu_{REF} - \nu) \times 10^6}{\nu_{REF}}$$

Typically in NMR spectroscopy, the standard is tetramethylsilane (TMS, $Si(CH_3)_4$). The chemical shift of a nucleus is characteristic to the chemical environment of the atom and from these signature shifts, the chemical composition of the polymer can be determined.

NMR was carried out on the anionic and living free radical synthesized P(PMDSS) homopolymers. The ^{13}C- NMR, ^{1}H-NMR, ^{29}Si-NMR were identical, with all peaks present at chemical shifts which corresponded to groups in the structure of stoichiometric P(PMDSS) as seen in **Figures 2.9-2.11.** When these peaks were integrated, the relative amounts of C, H and Si were in agreement with stoichiometric P(PMDSS). The most important data were those from the ^{29}Si-NMR, since side reactions in the living free radically polymerized polymer would likely have occurred between the Si-Si or the Si-C bonds.

---

[2] www.cis.rit.edu/htbooks/nmr/chap-4/chap-4.html

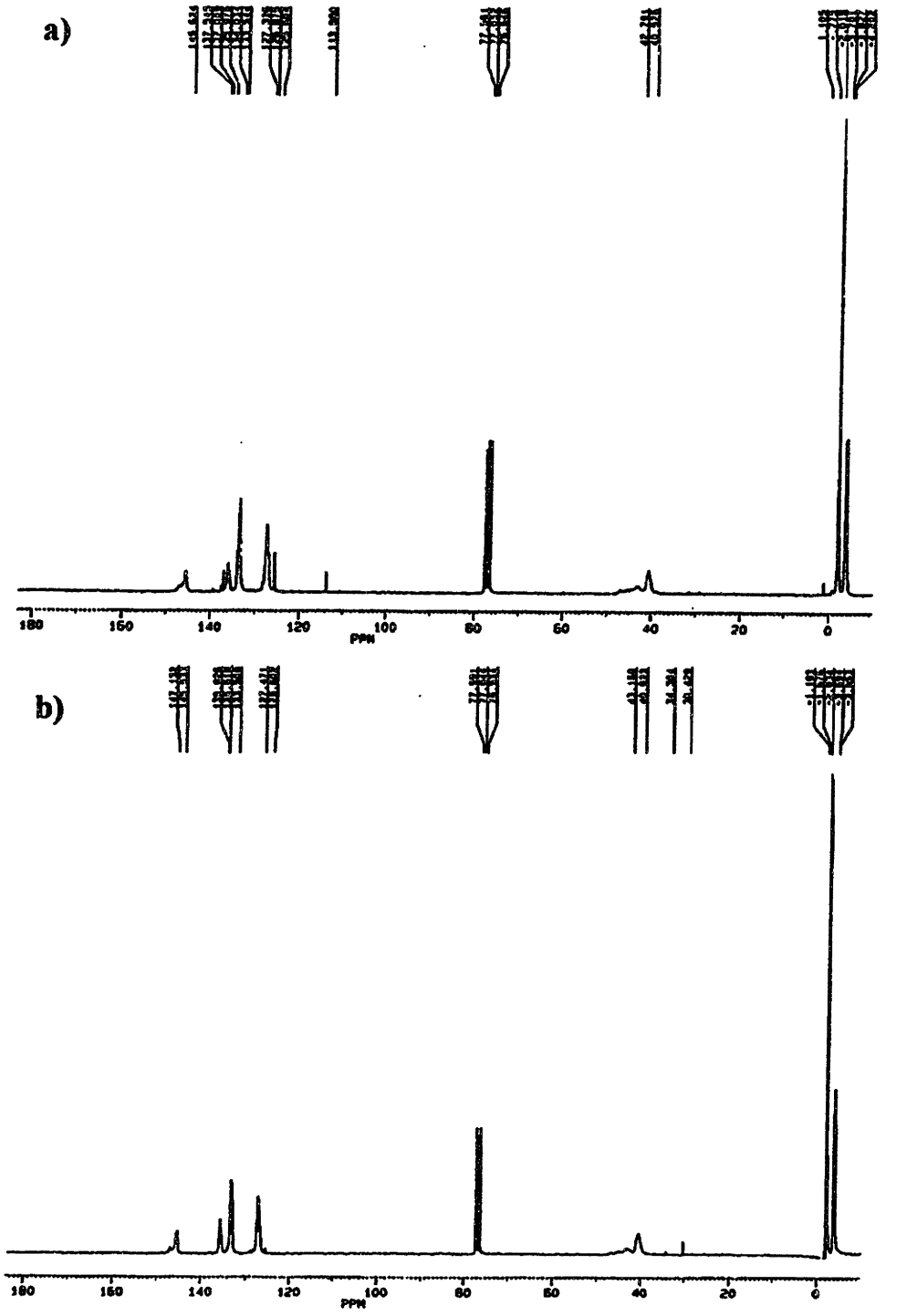

Figure 2.9: ^{13}C-NMR of P(PMDSS) synthesized by a) living free radical polymerization and b) anionic polymerization. The spectra are identical suggesting that the materials synthesized by these two routes are identical despite the high polydispersity of the LFR synthesized material.

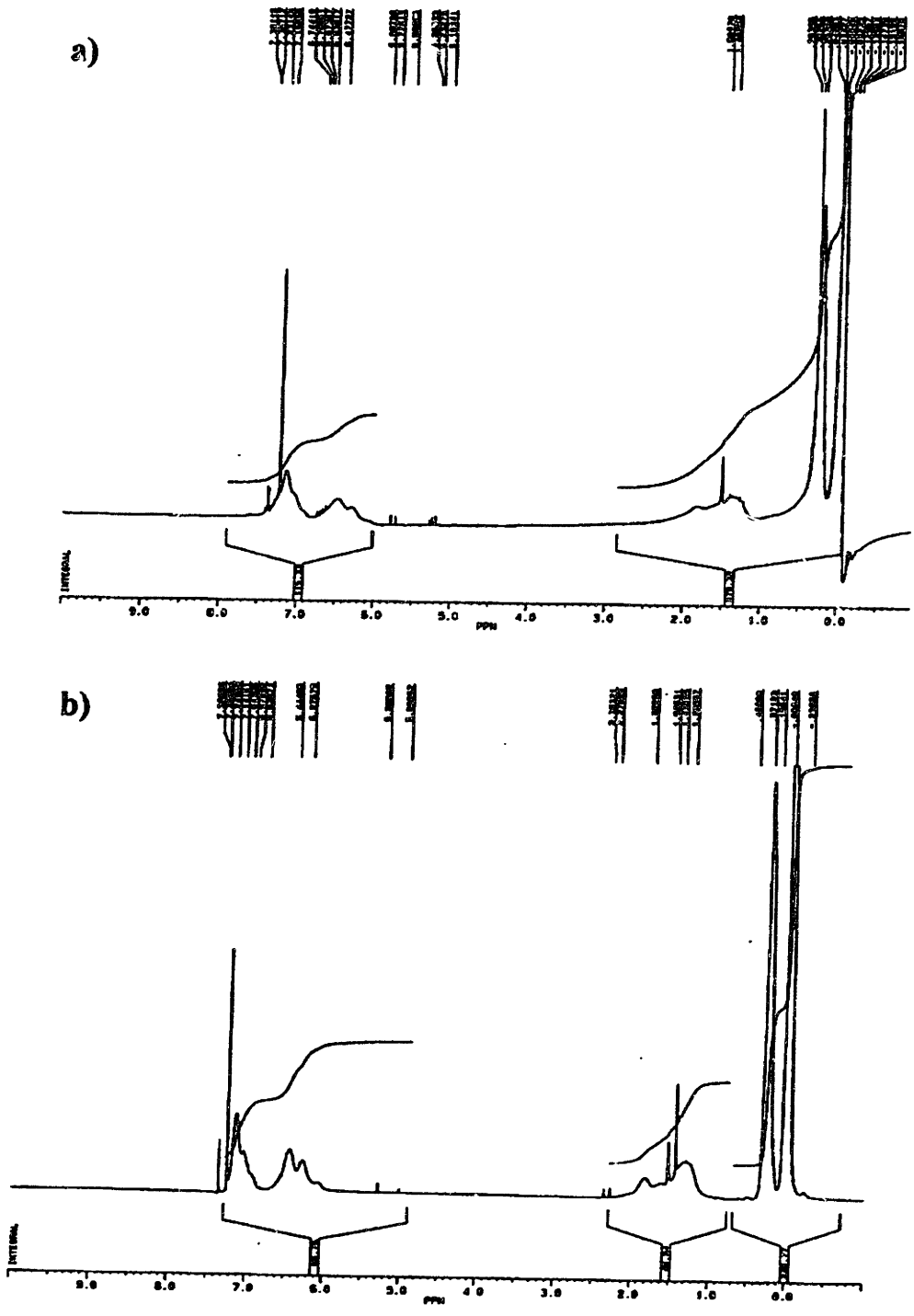

Figure 2.10: ^{1}H-NMR of P(PMDSS) synthesized by a) living free radical polymerization and b) anionic polymerization. The spectra are identical suggesting that the materials synthesized

by these two routes are identical despite the high polydispersity of the LFR synthesized material.

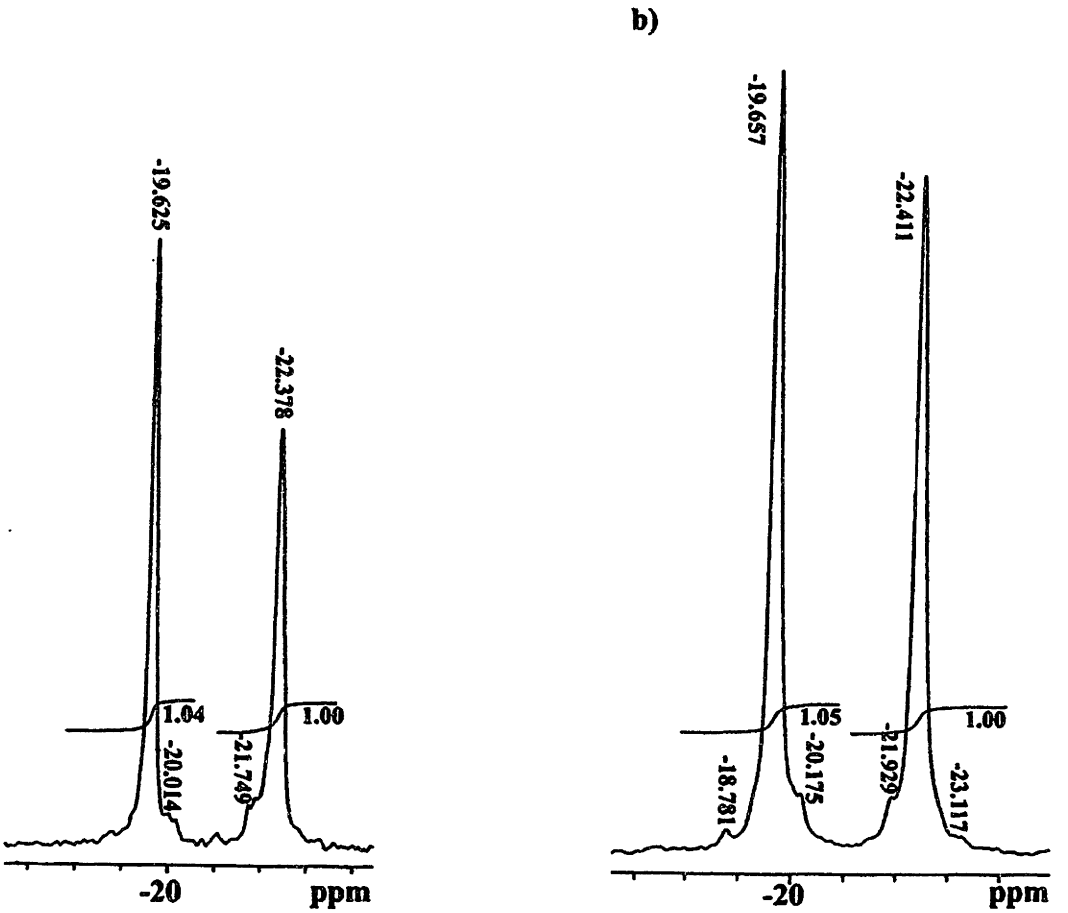

Figure 2.11: ^{29}Si-NMR of P(PMDSS) synthesized by a) living free radical polymerization and b) anionic polymerization. The spectra suggesting that the materials synthesized by these two routes are identical despite the high polydispersity of the LFR synthesized material. Both spectra exhibit 1:1 ratio of the two silicon peaks in P(PMDSS) indicating that the Si-Si bond is intact in both materials. The shift of the two types of silicon at δ -19.7 and -22.4 correspond well to the document shifts of -19.3 and -21.7 reported in the literature by (Marsmann 1981).

As seen from **Figure 2.11**, the ^{29}Si-NMR spectra of both polymers show the presence of two types of silicon, at δ -19.7 and –22.4 in a one-to-one ratio; From literature (Marsmann 1981), the shift for the * silicon $(CH_3)_3$ - Si-Si*-$(CH_3)_2$ - C_6H_5 is assigned to the resonance at –21.70 while the shift for the *silicon $(CH3)_3$ - Si*-Si-$(CH_3)_2$ - C_6H_5 is assigned to the signal at –19.30. Our data are consistent with these literature values proving that side-reactions did

not occur during living free radical polymerization and the broad molecular weight distribution is likely due to steric hindrance which led to a higher polydispersity than desired.

It is recommended in the future that in order to decrease the polydispersity of the silicon-containing block when using living free radical polymerization techniques, random copolymers of PMDSS be synthesized with styrene. This is because very narrow molecular weight distributions of polystyrene can be made by LFR and preliminary studies show that the incorporation of styrene decreases the polydispersity of the resulting polymer. Since PMDSS has 24wt% silicon in the monomer and as discussed in **Chapter Four**, 10 wt% silicon is necessary in order to form an etch barrier in reactive ion etching, a significant amount of styrene monomer can be added to maintain 10 wt% silicon in the random copolymer. In fact, given the molecular weight of the PMDSS monomer is 238 g/mol and a molecular weight of the styrene monomer of 104 g/mol, a random copolymer containing up to 52.3wt% styrene can be synthesized while still retaining an overall 10wt% of silicon in the material.

2.3.3 Fourier Transform Infra-red Spectroscopy

5% by weight solutions of the polymer in toluene were spun onto quartz substrates and Fourier Transform Infrared Spectroscopy (FTIR) spectra taken of the samples to yield chemical composition information of the materials. FTIR was conducted at both IBM Almaden Research Center and at MIT by myself. Sixty-four scans were taken for each spectra and data were recorded in transmission mode.

In FTIR, infrared (IR) light is passed through the sample and the frequencies at which absorption of IR radiation occurs by the sample measured. An interferogram, a plot of intensity versus mirror position, is collected which is a summation of all the wavelengths (cosine waves) emitted from the sample. The interferogram is converted into a spectrum through a Fourier Transform and shows the intensity of sample emission measured as a function of frequency. Intensity is reported either as absorbance (amount of light absorbed) or transmittance (amount of light transmitted), while frequency is reported as wavenumbers. Chemical functional groups absorb light at specific frequencies and from this phenomena, chemical structure can be obtained qualitatively.

The FTIR spectra, **Figure 2.12**, of both the anionically and LFR synthesized polymers exhibit the expected C-H and C-C stretching based on polymerization of the monomer without

any side reactions. There also was no absorption observed between 1000-1050 cm $^{-1}$ wavenumbers, the expected stretching regime for Si-O-Si groups.[3]

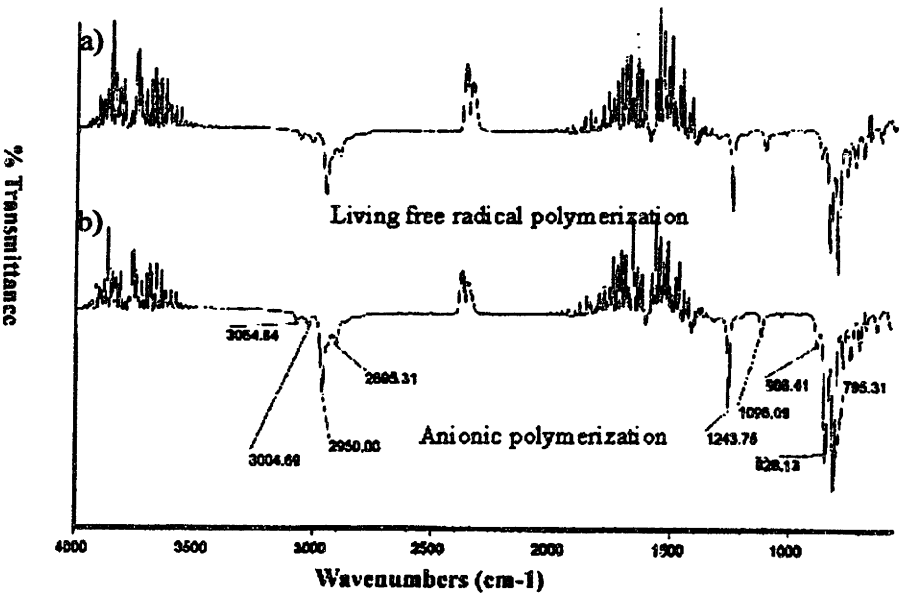

Figure 2.12: Fourier transformation infra-red (FTIR) spectras for P(PMDSS) synthesized by a) living free radical polymerization and b) anionic polymerization.

2.3.4 Elemental Analysis

The polymers were sent to Galbraith Laboratories, Inc.[4] to determine elemental composition. In order to determine the C and H amounts, 10 to 100 mg of the sample were put into a tin capsule to the nearest 0.01 mg and sealed. The sample was then combusted to 1050 °C in a constant oxygen stream. Using a Leco CHN 1000 Determinator, infrared absorptions of CO_2 and H_2O were studied. The samples were calibrated to cyclohexanone-2,4-dinitrophenylhydrazone (%C:H:N of 51.79: 5.07: 20.14), s-2483 acetanilide (% C:H:N, 71.09 : 6.72: 10.36), s-3483 acetanilide (% C:H:N of 71.09 : 61.71: 10.36), s-6483 EDTA (%C:H:N 41.10: 5.52: 9.59) and s-0606 Carbon powder (%C of 100.00). The error of the readings were less than 0.06% for hydrogen and 0.08% for carbon and the method detection limit 0.3%.

[3] Unpublished results from Dr. Robert Miller.
[4] Galbraith Laboratories, Inc., PO Box 51610, Knoxville, TN 37950-1610 (423) 546-1335.

To determine the amount of silicon, the samples were mixed with an appropriate amount of lithium borate flux and fused at 1000°C in a platinum crucible. The resulting melt was dissolved in a dilute nitric acid quenching solution. Scandium was then added to the solution as an internal standard. The solution was then brought to volume to be analyzed by inductively coupled plasma emission spectroscopy (Wallace 1981, ASTM E1479-92) using a Perkin-Elmer P2000. The material was decomposed using a plasma with 15 l/min at 1400 watts and a primary wavelength at 251.611 nm directly read. The detection limit was 0.40 mg/l in solution and the error of the readings less than 1.10%. A summary of the elemental analysis of the homopolymer is shown in **Table 2.2.**

Table 2.2: Experimentally determined and expected weight percentages of carbon, silicon and hydrogen for the anionically polymerized P(PMDSS).

Element	Experimentally Determined Weight Percentage	Expected Weight Percentage
C	66.5%	66.7%
Si	20.5%	23.9%
H	9.7%	9.4%

When the weight percentages of C, H and Si are summated, it can be seen that they do not add to 100% and could be due to experimental error in determining the relative amounts of these three elements as discussed above.

2.3.5 Differential Scanning Calorimetry

Differential Scanning Calorimetry (DSC) is a thermal analysis where transition temperatures are determined by measuring changes in enthalpy.(McNaughton 1975, Bershtein. 1994) The sample is placed in an aluminum pan and is heated simultaneously with a reference sample. In DSC the temperature difference, ΔT, between the sample and the reference pan is monitored and is proportional to the enthalpy change, ΔH, the heat capacity, C and the total thermal resistance R.

The total thermal resistance can be divided into two components: 1) the internal resistance of the instrument and 2) the resistance due to the sample. In DSC the sample and

reference are kept at the same temperature through two control loops which control two independent heaters. One loop eliminates any temperature difference due to a thermodynamic change by increasing/decreasing the power input while the other loop controls the average heating rate of the two samples. The differential power input to the two heaters, dq/dt is recorded and is related to the true heat flux by the equation:

$$\frac{dH}{dt} = -\frac{dq}{dt} + (C_S - C_R)\frac{dT}{dt} - RC_S\frac{d^2q}{dt^2}$$

Where dH/dt is the rate of absorption of heat per unit time, dq/dt is the power input, Cs and Cr are the heat capacities of the sample and reference respectively, (Cs-Cr)dT/dt is the offset of the base line from the zero level, $RCsd^2q/dt^2$ is the slope of the experimental curve and R is the thermal resistance. The second and third terms are normally insignificant. The second term is small if the sample and reference have similar heat capacities while the third term is due to thermal lag which affects the shape of the curve and even the peak temperature. In DSC thermal lag is minimized since R, the thermal resistance is minimized; Ro is small since the sample and reference chambers are identical while Rs is negligible since only small quantities of material, approximately 20 mg are used. This decreases thermal resistance which translates to decreases in the thermal lag. The equation can then be simplified to:

$$C = \frac{dH}{dt} \approx -\frac{dq}{dt}$$

In polymer systems, DSC is normally used to measure the glass transition temperature, a second order transition. However, if the material is a crystalline polymer, it can also be used to measure the crystallization/melting temperature.

Figure 2.13 shows typical experimental data taken by DSC. The important curve in this figure is the black one which represents the differential thermal analysis signal in microvolts. When a thermal transition is detected (e.g. a glass transition temperature), a change in the curve is seen. Normally three runs are taken to ensure the accuracy of the reading. For the P(PMDSS) homopolymer, a glass transition temperature of 107°C was measured using a

Perkin-Elmer DSC. Approximately 70 mg of the sample was placed in an aluminum sample pan and heated to 120°C. A heating rate of 5°C per minute was used in nitrogen.

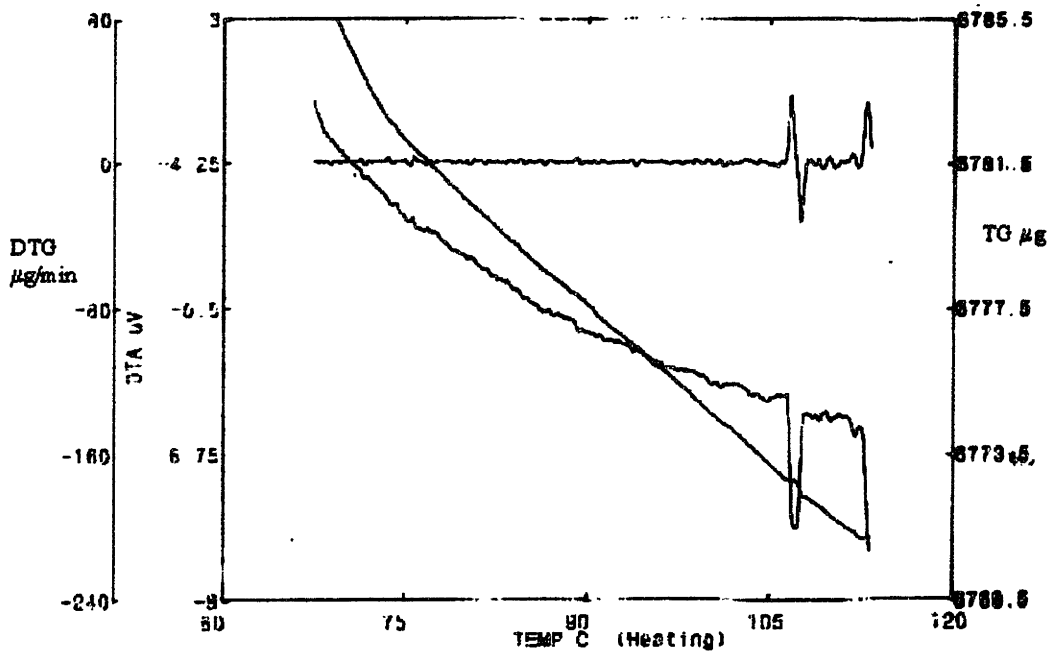

Figure 2.13: Differential Scanning Calorimetry data for P(PMDSS) homopolymer synthesized anionically, showing a glass transition temperature, Tg at 106.8°C.

2.4 Conclusions

It has been shown that P(PMDSS) homopolymer was successfully synthesized both by living free radical techniques and by anionic polymerization. FTIR and NMR spectra exhibited the expected chemical features. The polymer produced by LFR resulted in a lower molecular weight material than that produced by anionic techniques, possibly due to early termination of the living end or steric hindrance of the bulky monomer. This resulted in much higher polydispersities in the polymer produced by LFR as compared to anionic techniques.

Eight triblock copolymers of P(PMDSS) with PI were also successfully synthesized by anionic techniques. Low polydispersity (1.06-1.5) and high molecular weight ABA and BAB copolymers were made. These materials had molecular weights much greater than the 29,000 Daltons reported by Hirao *et al.* (1992, 1995) and morphologies spanning the phase diagram were documented, as discussed in **Chapter Three.**

Chapter Three
Characterization of P(PMDSS)-PI Triblock Copolymer Morphologies

3.1 Introduction

As discussed in **Chapter 2**, P(PMDSS) block copolymers have been previously synthesized by Hirao (1995) but their morphologies were not investigated and only low molecular weight polymers were produced. In this thesis eight high molecular weight triblock copolymers were synthesized of the type ABA and BAB where A is polyisoprene (PI) and B is poly(pentamethyldisilylstyrene) (P(PMDSS)) respectively. The volume fraction of the P(PMDSS) blocks ranged from 0.26 to 0.66. Among the polymers synthesized in this material system, two exhibiting cubic morphologies were produced and are the first documented silicon containing block copolymers which form tricontinuous structures.

In this chapter the triblock polymers whose synthesis was described in Chapter Two are characterized morphologically through TEM and SAXS. From the eight block copolymers that were synthesized by anionic polymerization, a morphology diagram was determined which was found to be asymmetric. It is believed that this asymmetry is due to a combination of the asymmetric architecture of some of the block copolymer molecules and differences in the Kuhn statistical segment length of the two blocks.

3.2 Experimental

3.2.1 Sample Preparation

Samples were static cast in porcelain crucibles by slow evaporation of ~5% w/w solution of the polymers in toluene, for one week at room temperature. (Since the solubility parameter of P(PMDSS) has not been determined, toluene was used. Judging from the microphase separation from the TEM micrographs, it was an appropriate solvent although there is the possibility that toluene could be selective to one phase and future work should be done on determining the solubility parameter of the P(PMDSS) polymer). After casting, the polymer films were approximately 0.7 mm thick. They were then annealed in a vacuum oven at 120°C for 7-14 days.

In order to study the bulk-cast films by transmission electron microscopy, films approximately 50 - 100 nm thick were sectioned at -90°C using a diamond knife equipped

Reichert-Jung 4E cryo-ultramicrotome. The polymer sections were then transferred to both 600-mesh and carbon films on 100-mesh copper grids and the polyisoprene blocks were preferentially stained in vapors of a 4% osmium tetroxide (OsO_4) water solution for 2 hours.

3.2.2 Transmission Electron Microscopy

Unlike scanning electron microscopy, (SEM) which relies on backscattered and secondary electrons, TEM is a transmission method, namely electrons must pass through the sample in order to be imaged. For this reason, samples must be extremely thin, typically less than 50 nm. As a result, extensive sample preparation on bulk samples via microtoming or solvent casting of thin films is needed in order to samples sufficiently thin for imaging. (Thomas 1986) Care must be taken in interpreting results to ensure that data represent the real structure and are not artifacts from the experimental preparation or the imaging process.

TEM was used to examine the local morphology of the microphase separated systems by obtaining 2-D projections of a 3-D structure. Contrast arises from phase and amplitude changes imparted to the electron beam by the sample. However to differentiate between the different blocks and hence image the microphase separated morphology, one block normally has to be stained to increase contrast. For example, in poly(styrene)-poly(diene) systems, the double bond in the diene block is stained with OsO_4 and through atomic density contrast, the diene phase will appear much darker in the bright field images than the unstained poly(styrene) phase.

The films were characterized in the bright field mode using a JEOL 2000FX transmission electron microscope, operating at 200 kV, unless otherwise noted. A goniometer stage with a double tilt holder was used to obtain high symmetry 2-D projections of the morphology. Images were typically taken at magnifications ranging from 14,000 to 60,000.

3.2.3 Optical Diffractometry

Birefringence of samples were examined using an optical birefringence apparatus built by Dr. John Chen. (1997) When light propagates through samples containing microphase separated grains of lamellae or cylinders, the grains behave optically as a uniaxial material. In an anisotropic medium, only two plane waves of orthogonal polarization are allowed to propagate for any given direction. These two waves have orthogonal polarizations and travel at two different velocities since the electric field of each wave experiences different interactions with

the dielectric constants of the sample. In a uniaxial material, there exists a special direction defined as the optic axis, n, where these two velocities are equal. Birefringence, Δn, in a uniaxial material is defined as the difference in the refractive indices for light polarized parallel, n_e, and perpendicular, n_o, to the optic axis n where $\Delta n = n_e - n_o$. Birefringence can be used to measure the orientation of the sample as well as determine whether a disordered homogeneous phase or phase with cubic symmetry is present. Such materials also appear dark under crossed polarizers due to the zero birefringence that both isotropic homogeneous samples and cubic materials exhibit. In cubic materials, the point group symmetry leads to a single scalar index of refraction for this crystal class and since polarizability is a second rank tensor property it is isotropic for materials with cubic symmetry.

The space groups of the cubic microdomain structures were investigated by obtaining diffraction patterns of the TEM negatives using an optical diffractometer equipped with a 5mW polarized UniPhase helium-neon laser with $\lambda = 633$ nm. Extinctions of missing hkl Fourier components help determine the plane group for the particular projection which in turn can help assign the 3d space group. Polaroid film was exposed for 1/16 sec. to record the optical diffraction images. Up to fourth order peaks were seen in the optical transforms of the negatives and these correlated well to the computer simulated Fast Fourier Transforms of the digitized images. Fast Fourier Transforms (FFTs) were made from the TEM images, using a montage of 32x32 unit cells in a 1024x1024 pixel array. A program written by Dr. Robert Lescanec uses the 1024x1024 input and multiplies it by a Hanning window to reduce edge effects in the FFT. This program performs the FFT and outputs the data on a log scale as a 2-dimensional image.

3.2.4 Small Angle X-ray Scattering

SAXS is a very useful technique that can typically provide structural information on the size scale of 100-2,000 Å, as well as quantify the degree and nature of ordering in a phase separated system. In order to accurately interpret morphologies on this size scale, SAXS is used in conjunction with TEM so that a suitable model for the analysis of SAXS data can be chosen. (Gobran 1990)

In SAXS, the X-rays which impinge on the sample are scattered by electrons in the sample, and hence contrast is obtained by electron density differences. Through interference, these scattered X-rays produce a diffraction pattern which can be recorded on electronic

detectors, photographic negatives or image plates. Since the data is obtained over the entire scattering volume (~ $1mm^3$), bulk characteristics of a material are obtained, unlike TEM where only information on the local morphology is obtained. In addition from the anisotropy of a SAXS pattern, texture and overall orientation of microdomains can be determined.

Each morphology will have its own set of characteristic hkl reflections which are related to scattering angle through the Bragg equation:

$$n\lambda = 2d_{hkl} \sin\theta$$

Thus, if the scattering angle is known, the d-spacing can be calculated and from this the morphology determined from the allowed hkl reflections of each structure. Since these are not unique, the real space image from TEM will be a useful starting point for analyzing data.

Numerous studies have been performed by previous researchers in the Thomas group on the use of SAXS as a way to analyze the global orientation of a structure, particularly in deformation experiments.(Honeker 1997, Dair 1999) Models can thus be produced by combining real space data with reciprocal space data.

X-ray diffraction data (SAXS) were acquired at the Time-Resolved National Facility (station X12B) at the National Synchrotron Light Source at Brookhaven National Laboratory (BNL) using a custom-built two-dimensional gas-delay line detector (10x10 cm, 512x512 pixels). A doubly-focused monochromatic X-ray beam (spot size, 0.5x0.5 cm fwhm) with a wavelength of 1.54 Å was used in the optical system. The sample-to-detector distances ranged from 215-260 cm.

The intensity of the scattered X-ray is recorded as a function of the scattering vector q, where:

$$q_{hkl} = \frac{4\sin\vartheta}{\lambda}$$

and λ is the wavelength of the X-rays and θ is half the scattering angle. When combined with Bragg's law:

$$\lambda = 2d\sin\vartheta$$

the following expression can be made to calculate the d-spacings of the scattering hkl planes:

$$d_{hkl}\ (\text{Angstroms}) = \frac{2\pi}{q_{hkl}}$$

Using this relationship, d-spacings were calculated from the equation and for selected block copolymers and are given in **Table 3.1.**

Using the morphology that was determined by TEM, peaks were indexed and compared to the theoretically allowed ratios given in the International Tables for Crystallography. The allowed reflections of the space groups to which the spherical, cylindrical, double gyroid and lamellae morphologies belong are given in **Appendix A.**

Plots of ln Intensity versus q were made and are given in Appendix A along with the indexed peaks and their ratios. It must be noted that the higher order peaks for the SAXS were difficult to distinguish from the background signal and for this reason the SAXS patterns were mainly used to calculate d-spacings.

Although SAXS is a perfect complement to TEM in morphology characterization, microdomain morphology can be determined by combining TEM, optical diffraction patterns and digitized Fast Fourier Transforms and in this thesis, the main purpose of SAXS was to obtain d-spacings for the different morphologies.

3.2.5 X-Ray Reflectivity

X-ray reflectivity was carried out at IBM Almaden Research Center with Dr. Mike Toney. Films of the polymer were made by spincoating a 5% by weight solution of the P(PMDSS), (Mw = 38K) in toluene onto special thick silicon wafers. These thick silicon wafers (~ 0.25 cm) ensure that the film has uniform thickness which is necessary for accurate measurements. In X-ray reflectivity, an X-ray beam is reflected off of the sample and the intensity of the reflected beam is monitored as a function of the angle of reflectance, theta.

For low theta values, (tenths of a degree), the x-ray beam undergoes total external reflection from the silicon substrate. At a critical theta, the beam that penetrates the polymer film will reflect off the polymer/silicon interface. Standing waves are then produced in the film resulting in the formation of interference fringes. From the critical angle where reflection from

the silicon/polymer interface occurs, the refractive index can be calculated and from this the electron density. If the chemical formula of the material is known then mass density can be calculated.

It was found that the densities of the two blocks were extremely similar, differing by only 0.02 g/cm^3. It would be expected that in SAXS there would be poor contrast between the two blocks and therefore very weak scattering since intensity is proportional to the square of the electron density difference. The density for various components (in g/cm^3) is ρ_{PS}=1.04, ρ_{PI}=0.913, as reported in the Polymer Handbook and for $\rho_{P(PMDSS)}$=0.915 (± 0.04). However, despite this small difference in density, SAXS patterns were still obtainable although as seen in Appendix A, the peaks were not as intense as expected for highly ordered materials. In order to try to improve the intensity of the SAXS peaks, the samples were annealed in-situ to 160°C while SAXS data were collected. It was hoped that due to differences in thermal behavior between the contrast between the two blocks would increase as a result of the annealing. This was true only for the P(PMDSS)-DG sample which may be due to the low molecular weight of this sample as compared to the other block copolymers studied.

3.3 Results and Discussion

The molecular weights and polydispersities of the seven block copolymers synthesized anionically are reported in **Table 2.1** and selected d-spacings given in **Table 3.1.** The focus of this thesis is on two double gyroid morphologies. One of which forms PI networks in a matrix of P(PMDSS), referred to as the "double gyroid" or P(PMDSS)-DG **(Section 3.3.1)** and one of which forms P(PMDSS) networks in a PI matrix, designated the "inverse double gyroid" or PI-DG **(Section 3.3.2).**

Table 3.1: d-spacings of selected morphologies as calculated by small angle x-ray scattering.

Sample	Reflection.	q	d Å	Morphology
1	{211}	0.013	490	P(PMDSS)-DG
5	{100}	0.0093	675	Cylinders
6	{211}	0.0101	620	PI-DG
7	{100}	0.0123	510	Lamellae

3.3.1 Double Gyroid : PI Networks Within a P(PMDSS) Matrix

A triblock copolymer of PI-P(PMDSS)-PI, hereby designated P(PMDSS)-DG, with molecular weight 24K-98K-24K was synthesized anionically as outlined in **Chapter 2.** The polymer was static cast from toluene and annealed at 120C for 2 weeks. After cryomicrotoming, the PI networks were selectively stained with OsO_4, and as a result appear dark in bright field TEM images as shown in **Figure 3.1.** All three primary high symmetry double gyroid projections, <111>, <110> and <100> are present. From SAXS, a d-spacing of 570 Å was calculated.

The appearance of "wagon-wheel" structures in the <111> projection has previously caused confusion in the morphological identification of block copolymers with cubic structures. In **Figures 3.1 a-b** the TEM image with p6mm symmetry and the digitized FFT of the TEM image are exhibited. Higher order peaks are evident in the FFTs. There are strong similarities of the image and its FFT to those shown earlier by Avgeropoulos (1997), for a PS-PI-PS triblock of similar composition. The main difference between the two polymers is the position of the PI block. The two Fourier transform patterns each have 12 prominent peaks around the center beam, with an alternating 6-fold pattern of a high-intensity peak next to a lower intensity peak. The higher intensity peaks occur at a smaller q than the lower intensity ones, and the q_2/q_1 ratio is approximately equal to 1.15 in both transforms. The experimental ratio agrees very well with the theoretically determined ratio $1.165 = q_{220} / q_{221} = \sqrt{8} / \sqrt{6}$ for a sample exhibiting double gyroid morphology with Ia3d space group symmetry. The peaks in the FFT are satisfactorily indexed according to the DG model. Symmetry patterns can be determined by indexing the diffraction pattern of the TEM image and comparing them to fast Fourier transforms of appropriate computer simulated projections produced by TEMsim, as discussed in **Section 6.1.4).** The best agreement of simulated images with the TEM data occurs for models with section thickness of about 1 unit cell, consistent with the expected section thicknesses.

Figures 3.1 c-d show a TEM image which exhibits p4mm symmetry, and the digitized FFT pattern. The angle between the first order diffraction peaks was measured to be 89°, indicating that the projection is almost perfectly down the 4-fold axis. The FFT also indexes well according to the DG model, the prominent peaks corresponding to the {220} family.

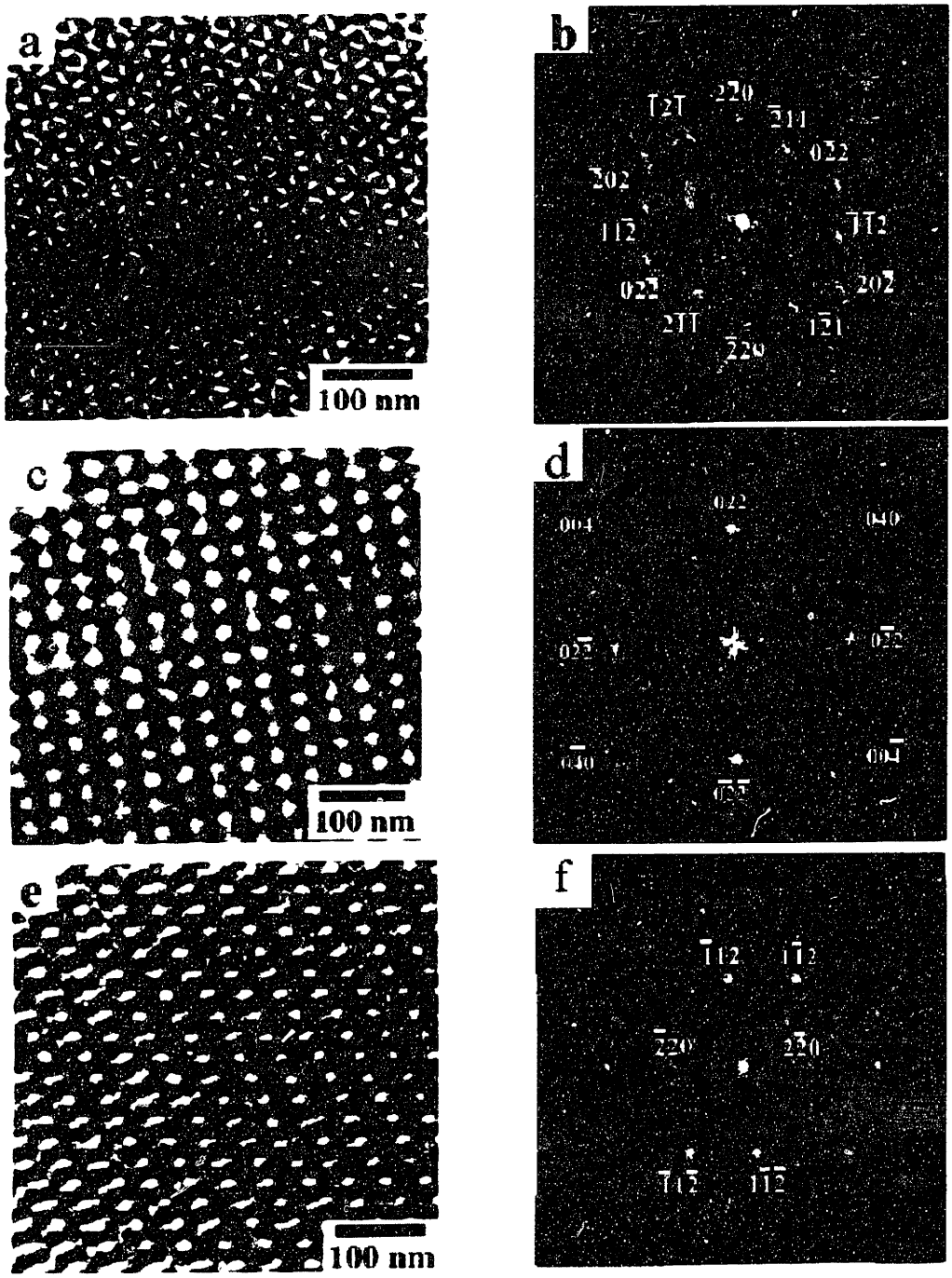

Figure 3.1: TEM Images and diffraction patterns of 24/100/26 PI/P(PMDSS)/PI. The PI networks have been stained dark with OsO_4. (a) Bright-field TEM image exhibiting the [111] projection. (b) Indexed digitized FFT of the TEM image. (c) Bright-field TEM image exhibiting the [100] projection.(d) Indexed digitized FFT of the TEM image. (e) Bright-field TEM image exhibiting the [110] projection. (f) Indexed digitized FFT of the TEM image.

The <110> projections of the DG have c2mm plane group symmetry. **Figures 3.1 e-f** show the TEM image, and the digitized FFT, all exhibiting c2mm symmetry. The 2-fold projections are the elucidative cubic symmetry projections for identifying the DG morphology compared to structures based on other cubic space groups. The resemblance between the present set of images and those obtained in an earlier work (Avgeropoulos 1997) for the PS-rich triblock copolymer, leads to the conclusion that the morphology observed is definitely the DG.

One interesting observation of this material system was the extremely large grains that this block copolymer system forms with static casting. The grain sizes observed in the cubic sample were much larger than those observed in analogous triblock PS-PI-PS polymers[30]. In fact, the block copolymer forms well-ordered morphologies even without annealing. In the case of PS-b-PI-b-PS samples of comparable total molecular weight, the grain sizes varied from 20x20 to 30x30 unit cells, but in this system much larger grains form after annealing, spanning 60 unit cells and several microns as shown in **Figure 3.2.**

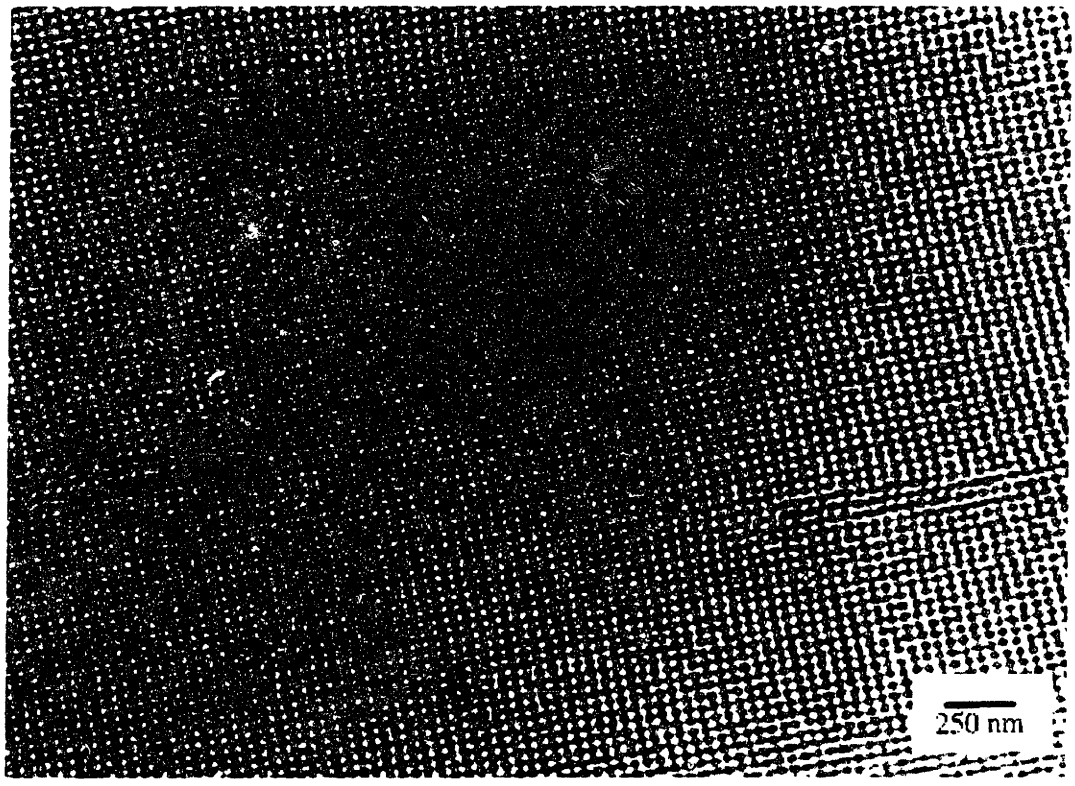

Figure 3.2: Bright field TEM image of static cast 24/100/26 PI/P(PMDSS)/PI exhibiting the [100] projection. Even though the material is static cast it is extremely well ordered resulting in a grain that is several microns in size.

This extremely good order could be due to the fact that the entanglement molecular weight of the P(PMDSS) is likely to be significantly higher than PS. The entanglement molecular weight for P(PMDSS) is crudely estimated to be ~68,000 simply on the basis of the ratio of the molecular weights of the PMDSS monomer and styrene monomer and assuming the entanglement molecular weight of polystyrene is 34,000 g/mole. The monomeric molecular weights of PMDSS and styrene are 234 and 104 respectively. Half of the PMDSS molecular weight results from the silicon containing side group, so its contribution to polymer entanglement is minimal. As an approximation of entanglement molecular weight, it was assumed that the same number of monomer units are needed to entangle P(PMDSS) as PS.

3.3.2 The "Inverse" Double Gyroid: P(PMDSS) Networks Within a PI Matrix

In Section **3.3.1**, a double gyroid morphology with PI networks within a P(PMDSS) matrix was characterized. A block copolymer was also synthesized where the networks and matrix are reversed, namely the networks are comprised of P(PMDSS) and the matrix PI. This material is designated the "inverse" double gyroid and is referred to as PI-DG since its morphology is inverted to the double gyroid characterized in **Section 3.3.1**. The asymmetric triblock copolymer was a PI-P(PMDSS)-PI with a molecular weight of 44K-168K-112K.

It can be seen in **Figure 3.3**, that material is not as well ordered as the P(PMDSS)-DG in **Section 3.3.1** although the tricontinuous structure is evident here. This poorer order is likely due to the high molecular weight of this polymer (total molecular weight of 312K) and the highly entangled PI endblocks. In addition, there is an inversion in contrast between the TEM micrographs of **Figures 3.1 and 3.3** since the PI networks are stained dark with OsO_4 in **Figure 3.1** while in **Figure 3.3**, the matrix is composed of PI and is stained dark by OsO_4.

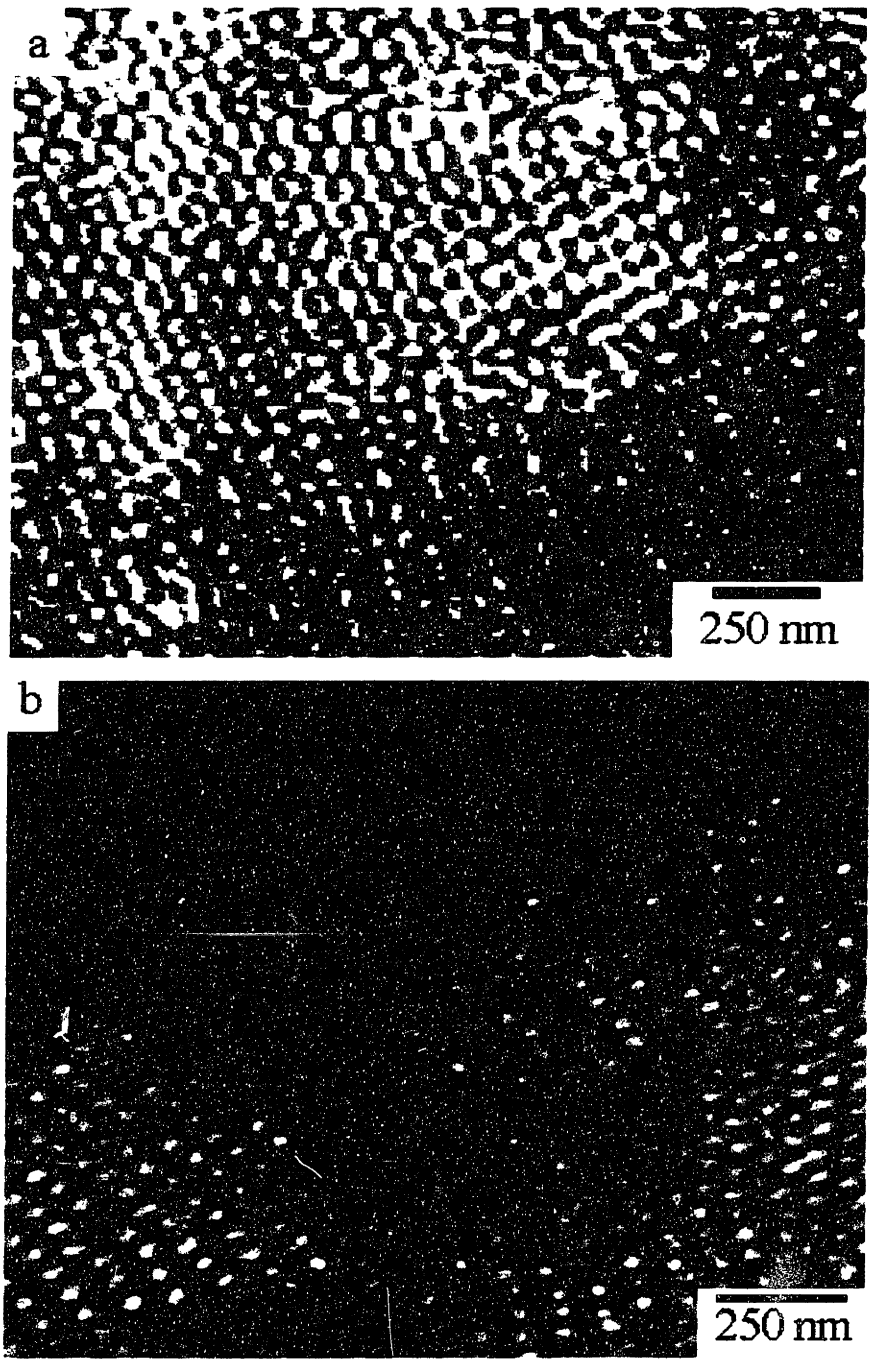

Figure 3.3: Bright field TEM image of 44K-168K-112K P(PMDSS)-PI-P(PMDSS), exhibiting the double gyroid morphology. The PI matrix has been preferentially stained with OsO_4, resulting in an inversion in contrast as compared to Figure 3.2 where the PI forms networks.

Typically with an ~50% volume fraction in a symmetric triblock copolymer system, the material would exhibit lamellae, as discussed in **Section 2.1**, however in this case the polymer forms a tricontinuous morphology of P(PMDSS) networks in a PI matrix, as shown in **Figure**

3.3. The formation of the double gyroid morphology at this volume fraction could be due either to the asymmetry of the triblock copolymer since the two end blocks have very dissimilar molecular weights and/or due to differences in the Kuhn statistical segment length as discussed in **Section 3.3.4.**

3.3.3 Other Block Copolymer Morphologies

The focus of this thesis is on the two polymers that form the double gyroid and inverse double gyroid microstructures, however, block copolymers with different morphologies were also synthesized.

3.3.3.1 P(PMDSS) Spheres Within a PI Matrix

Figure 3.4 shows the P(PMDSS)-PI-P(PMDSS) sample with $\phi_{P(PMDSS)}$ = 26%, 52K-250K-42K which forms P(PMDSS) spheres in a matrix of PI. The spacing between the spheres is relatively large, on the order of the diameter of a sphere, approximately 50 nm. The overall order of the sample is poor due to the relatively high molecular weight of the PI midblock.

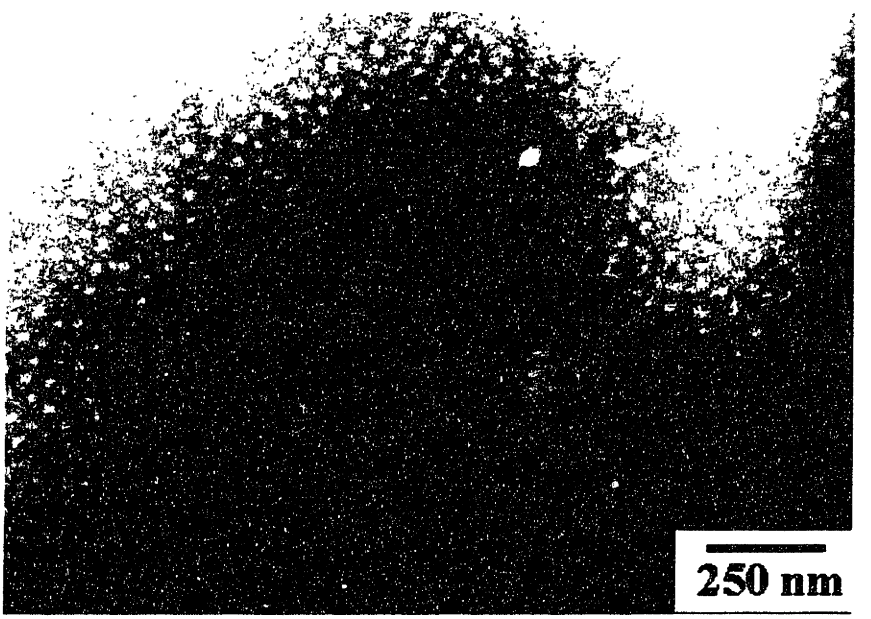

Figure 3.4: Bright field TEM image of static cast P(PMDSS)-PI-P(PMDSS), 52K-250K-42K after staining with OsO_4. Material exhibits P(PMDSS) spheres in a matrix of PI.

Another P(PMDSS) spherical microdomain sample was synthesized, as illustrated in **Figure 3.5.** However, the polydispersity of this sample, P(PMDSS)-PI-P(PMDSS) 34K-160K-34K, was extremely high (p.d. = 1.5) resulting in spheres that were nonuniform in size and

exhibited even poorer order than the sample shown in **Figure 3.4**. In fact, there are micron-sized regions as shown in **Figure 3.5b** where hexagonally packed cylinders have formed indicating that the material is clearly polydisperse.

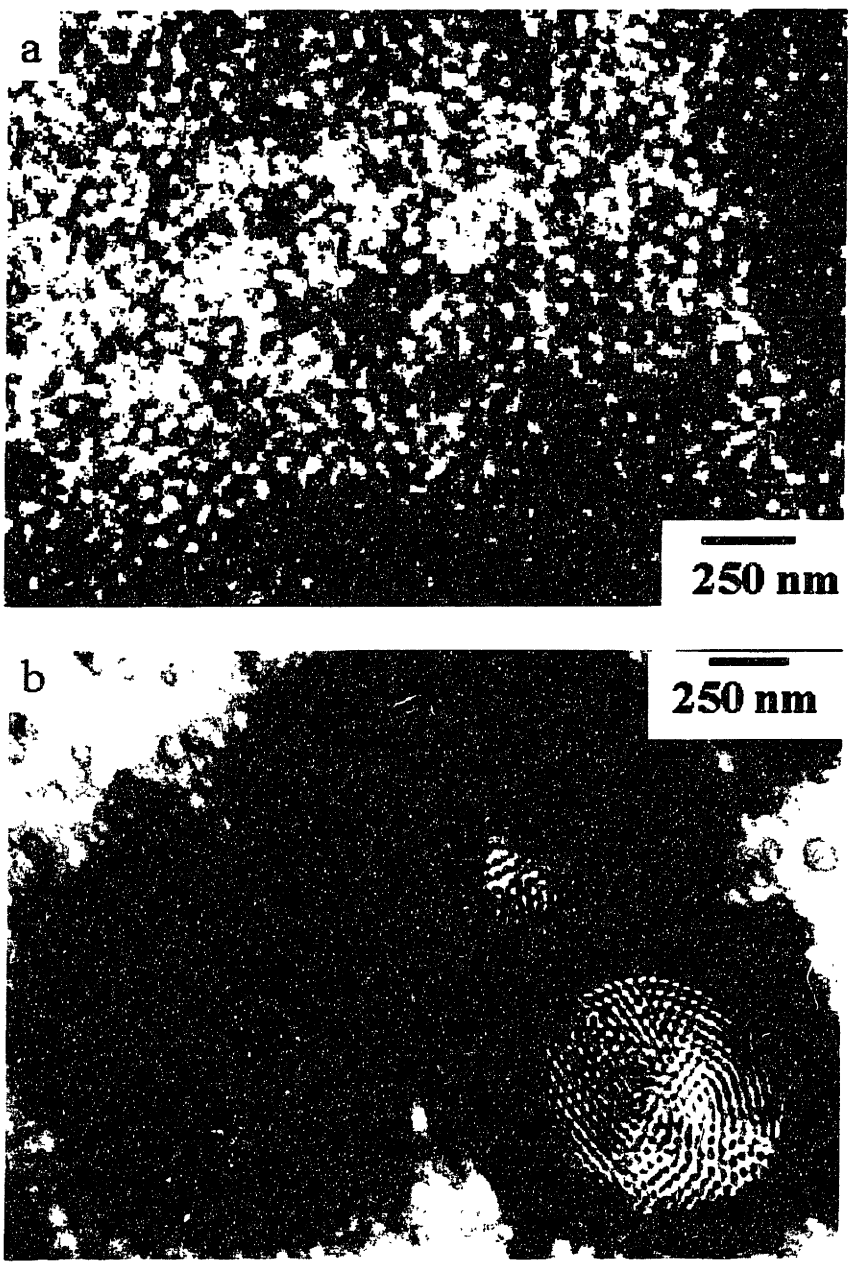

Figure 3.5: Bright field TEM image of static cast P(PMDSS)-PI-P(PMDSS), 34K-160K-34K after staining with OsO_4. In some regions the material exhibits a) P(PMDSS) spheres in a matrix of PI while in other regions b) micron sized spheres containing PI cylinders form within a matrix of P(PMDSS). The spheres are nonuniform in size and at the interface with the spherical morphology there is darker staining. In general the ordering is poor due to the polydispersity of the sample (p.d. = 1.5).

3.3.3.2 P(PMDSS)-PI Lamellae

A symmetric triblock copolymer P(PMDSS)-PI-P(PMDSS), 44K-167K-46K was synthesized and in spite of a P(PMDSS) volume fraction of 35%, the material formed lamellae rather than the expected double gyroid.

It can be seen in **Figure 3.6**, that although the material exhibits lamellae, the P(PMDSS) lamellae are half the thickness of the PI lamellae which confirms the volume fraction of the material. Lamellae may form at this volume fraction for reasons that also explain the formation of the double gyroid morphology at 50% volume fraction as discussed in **Section 3.3.2**.

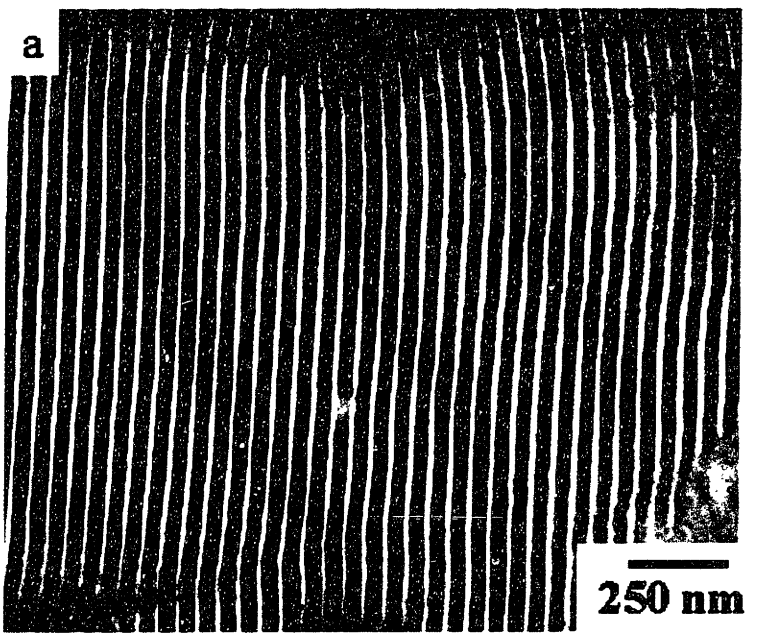

Figure 3.6: Bright field TEM image of static cast P(PMDSS)-PI-P(PMDSS), 44K-167K-46K. Material exhibits a lamellar morphology despite the rather low volume fraction of P(PMDSS) of 35%. The P(PMDSS) lamellae (which appear white) are half the thickness of the PI lamellae (which appear dark since they have been stained with OsO_4), which corresponds well to the 35% P(PMDSS) volume fraction.

3.3.3.3 P(PMDSS) Cylinders Within a PI Matrix.

Figure 3.7 shows the cylindrical morphology of an asymmetric triblock copolymer, P(PMDSS)-PI-P(PMDSS) with a molecular weight of 44K-148K-120K and a $\phi_{P(PMDSS)}$ of 53%. When the material is cast from toluene and stained with RuO_4,which preferentially stains the phenyl group in the P(PMDSS), the cylinders appear dark in a light matrix. Given the volume fraction of the P(PMDSS) of 53%, a cylindrical morphology was not expected.

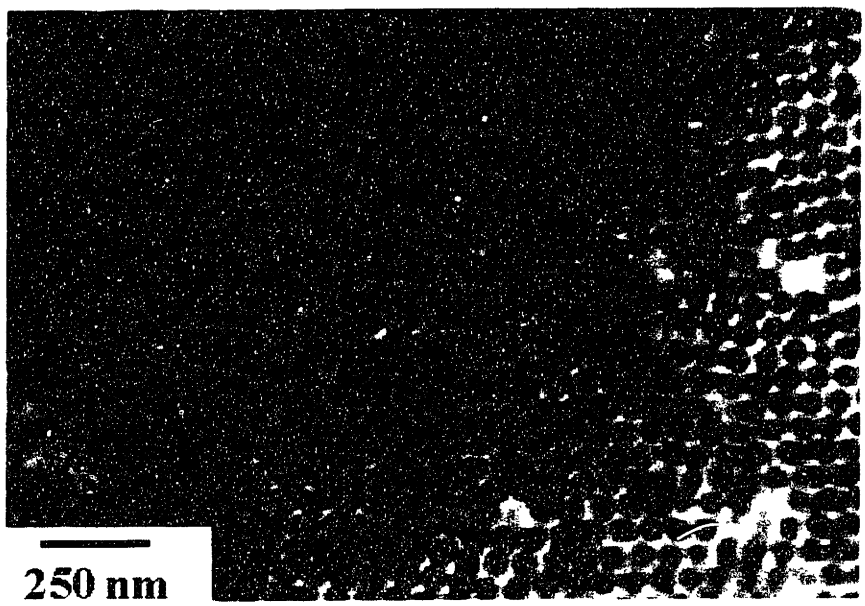

Figure 3.7: Axial view of a bright field TEM image of static cast P(PMDSS)-PI-P(PMDSS), 44K-148K-120K, with a volume fraction of P(PMDSS) of 53% after staining with RuO_4. P(PMDSS) cylinders are stained dark.

When this polymer was stained with OsO_4, two levels of contrast are seen in the transverse view, as shown in **Figure 3.8a** as expected in a cylindrical morphology. OsO_4 preferentially stains the PI regions dark, so one expects the micrograph to show white P(PMDSS) cylinders, surrounded by a darker matrix. However, in the axial view of **Figure 3.8b**, there are three levels of contrast and it appears as if the material is forming concentric cylinders.

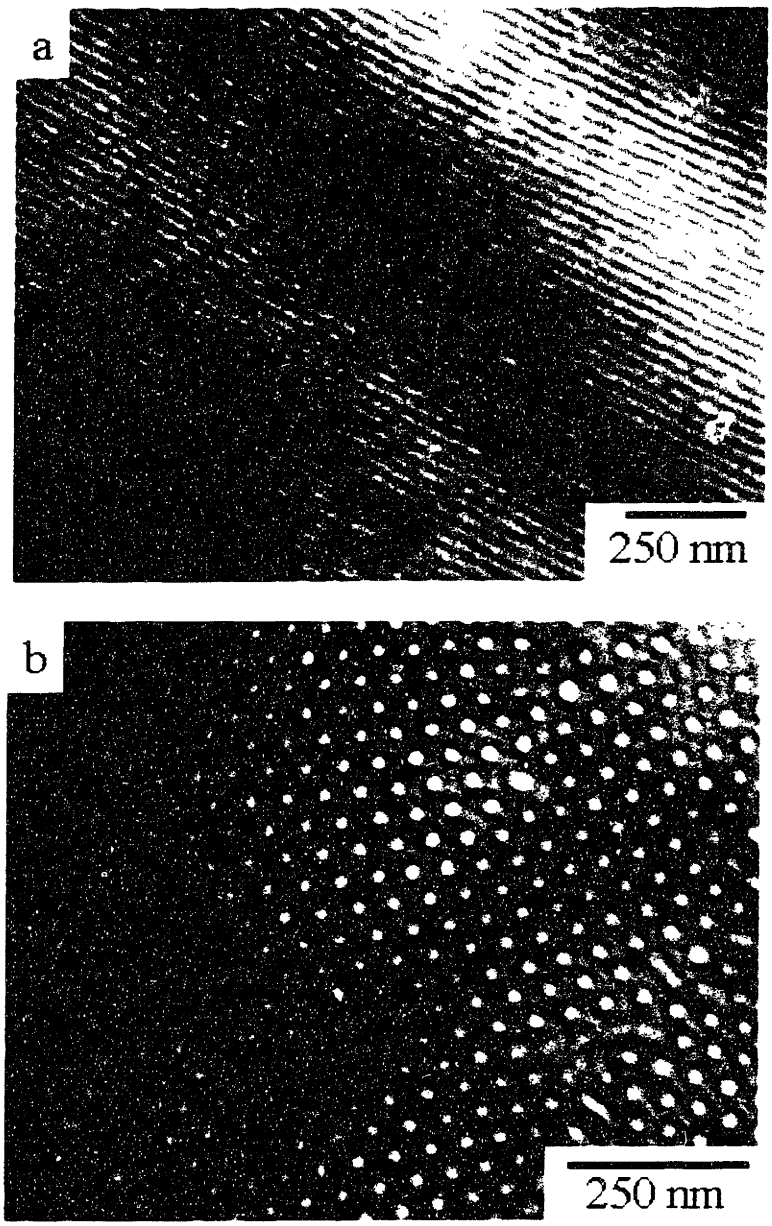

Figure 3.8: Bright field TEM image of static cast P(PMDSS)-PI-P(PMDSS), 44K-148K-120K after staining with OsO_4. a) Transverse view. Material appears to exhibit concentric cylinders with inner P(PMDSS) cores, an outer ring of PI within a matrix of P(PMDSS). The interface is staining darker than either block. b) Axial view. Two levels of contrast are observed here.

Although concentric cylinders are seen in the axial view of the OsO_4 stained polymer, only two levels of contrast are evident in **Figures 3.7 and 3.8a**. Other research groups have also noted that when a block copolymer is stained the interface can be stained darker than either of

the two blocks.[1] It is not known what is the mechanism behind this phenomenon, although it has been observed by others.

3.3.4 The P(PMDSS)-PI Block Copolymer Phase Diagram

After the morphological examination of each of the individual P(PMDSS)-PI block copolymers, it is useful to bring this data together in the form of a morphology diagram. As previously discussed in Chapter 2, simple diblock copolymers exhibit a $N\chi$ vs. ϕ diagram symmetric about ϕ=0.5, with seven different periodic microdomain structures depending primarily on ϕ. These morphologies develop in the order (spheres-cylinders-double gyroid-lamellae-double gyroid-cylinders-spheres) with the majority and minority components reversing at ϕ=0.5.

The morphology diagram of the P(PMDSS)-PI materials synthesized for this thesis is given in **Figure 3.9.** The molecular weights and polydispersity of these materials can be found in **Table 2.1.**

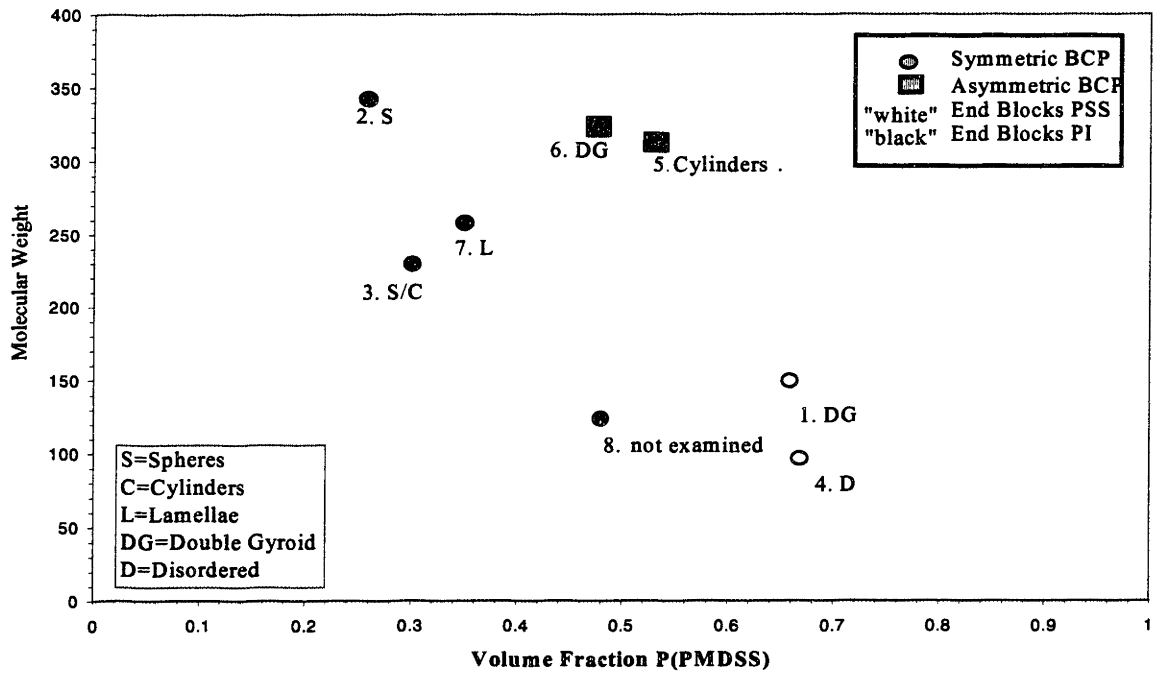

Figure 3.9: Experimentally determined morphology diagram for P(PMDSS) and PI triblock copolymers

[1] Personal communication T. Hashimoto and C.K. Ober.

This diagram is the superposition of several phase diagrams since the polymers plotted have different architectures, including asymmetric triblock copolymers and polymers with ABA and BAB sequences. The different diagrams can be isolated through the legend where symmetric triblock copolymers (i.e. the two end blocks have the same molecular weight) are given the diamond symbol and asymmetric triblock copolymers (i.e. the two end blocks have very dissimilar molecular weights) are given a square symbol. If the polymer has P(PMDSS) as the end blocks the symbol is colored blue. If the polymer has PI as the end blocks, the symbol is colored pink.

It can be seen that when P(PMDSS) are endblocks, there appears to be a large shift in the volume fractions for the order-order boundaries compared to the simple diblock morphology diagram. For example, lamellae form at $\phi_{P(PMDSS)} = 0.35$ while double gyroid is exhibited at $\phi_{P(PMDSS)}=0.48$.

Asymmetry in the morphology diagram of diblock copolymer systems is known and in the PS-PI block copolymer system the order-order boundaries of the morphology diagram bias towards low volume fraction PS. For example, with a volume fraction of 20% PS, cylinders form, whereas with a volume fraction of 20% PI, spheres form. (Vavasour 1993) This asymmetry in the morphology diagram has been explained due to differences in the Kuhn statistical length, $b_{A/B}$, and or the density between the two pure components, $\rho_{A/B}$. Specifically, the asymmetry can be characterized through the quantity ε, where ε is given by:

$$\varepsilon = \frac{(\varphi_A/\varphi_B)}{(R^2_{A,g}/R^2_{B,g})}$$

$$\varepsilon = \frac{\varrho_{oB} b_B^2}{\varrho_{oA} b_A^2}$$

where R_g is the radius gyration of the pure block and f_i the volume fraction of the block. It can be seen that asymmetry is due to differences in either the Kuhn segment length or the density, but if $\rho_{0B}b_B^{\,2} = \rho_{0A}b_A^{\,2}$ then the conformational asymmetry is cancelled due to the balancing of these two effects. The location of the order-order morphology boundaries is dependent on the value of ε and is a direct result of the chemical nature of the copolymer species. Vavasour and

Whitmore showed that if ε is varied from 0.1 to 1, the order-disorder boundary is not greatly affected although the order-order boundaries change substantially. In the case where $\rho_{0B}b_B^2 < \rho_{0A}b_A^2$ the order-order boundaries are shifted toward the higher A content. In other words, the lower bounds for the transition to a new morphology shifts to higher values of A. Physically, the asymmetry is a direct result of the unequal chain stretching of the two blocks with respect to their unperturbed dimensions. Thus, in the case of $\varepsilon < 1$, the B blocks are more stretched than the A blocks and in order to reduce this difference, the spacing of the A lamellae is increased relative to the spacing of B lamellae and thus the morphology diagram skews towards the A volume fraction. In fact, it can be seen that for $\varepsilon < 1$, the lamellae region in the morphology diagram can be extended in the volume fraction $0.52 < f_A < 0.68$. Although this self-consistent mean field theory predicts this skewing, experimentally, Kuhn lengths are difficult to measure/calculate and there are large discrepancies between the various research groups even on values for the well-studied PS-PI system.

Similar shifts in the volume fraction of the morphology diagram have been seen in another silicon containing polymer system, namely in polystyrene-polymethyldisiloxane diblock copolymers. Chu *et al.* (1995) found that in the PS/PDMS system, the morphologies skew towards an even lower styrene volume fraction as compared to PS/PI. In this case, lamellae were found at a $\phi_{PS} = 0.35$ and cylinders at $\phi_{PS} = 0.56$. An attempt was made to corroborate this data to the theory of Vavasour and Whitmore but ε was calculated to be 1.04 which is much too low to explain the skewing. However, as mentioned previously, statistical segment lengths are difficult to calculate therefore it is difficult to discount this theory entirely. Another alternative explanation is that the polymers made by Chu *et al.* (1995) were cast from toluene which may be slightly selective towards PS, although this was unlikely based on the intrinsic viscosities of the homopolymers which would indicate that toluene was a neutral solvent. Domain sizes were also found to be larger for a given molecular weight which would indicate that the χ value should be significantly greater than for the PS/PI system.

In the case of the P(PMDSS)-PI system, it was shown in **Section 3.2.6** that the density of the P(PMDSS) and PI were nearly identical. It is likely that the Kuhn segment length of the two blocks is very dissimilar since the bulky pentamethyldisilyl side group would lead to significant steric hindrance as compared to PI. Thus, it is expected that $\rho_{oB}b_B^2 \neq \rho_{oA}b_A^2$. Due to this steric

arrangement, it is expected that the skewing of the P(PMDSS)-PI morphology diagram should be greater than the PS-PI morphology diagram. When we compare our materials to those synthesized by Chu *et al.* (1995), we find that we have the formation of lamellae at $\phi_{P(PMDSSS)}$ = 0.35, cylinders at $\phi_{P(PMDSS)}$ = 0.53 and the "inverse" double gyroid (PI-DG) at $\phi_{P(PMDSS)}$ = 0.48. This shift is in the *opposite* direction that we would expect if we believe that Kuhn statistical segment lengths are responsible for the shift in the volume fraction. However, it must be noted that in our system we have *triblock* copolymers and as a result comparing the data with diblocks may not be useful since there may be other dominating factors which affect the morphologies in triblock copolymer systems.

One important characteristic of two of the polymers which experience this shift in volume fraction is their asymmetric nature. Polymers **5** and **6** which form the "inverse" double gyroid and P(PMDSS) cylinder morphologies respectively have a structure where the molecular weight of the A_2 end block is three times the molecular weight the of A_1 end block. This asymmetry could be the reason for the shift in the volume fraction of the morphologies observed at these unusual volume fractions.

The effects of asymmetric architectures was studied by Mayes and de la Cruz (1989) who found that the morphology diagram behavior for ABA triblock copolymers with varying architectures was examined following the mean-field theory used by Leibler (1980) for diblock copolymer melts. Mayes and de la Cruz defined a symmetry parameter, τ for triblock copolymers which is given as:

$$\tau = \frac{f_1}{f}$$

where f_1 is the fraction of A monomers in the first block and f is the total fraction of A monomers in the chain. Thus, in our case for the asymmetric polymers, **5** and **6** of Table 2.1, τ is approximately 0.25, since the molecular weight of one block is ~ three times the size of the molecular weight of the other end block, namely $M_{A2} \sim 3M_{A1}$.

Mayes and Olvera de la Cruz (1989) found that as τ increased, the morphology window of the morphology diagram was strongly affected. For a 50/50 volume fraction diblock copolymer, it was predicted that the material forms lamellae directly from the disordered state. If a symmetric triblock copolymer with the same composition is studied, morphology windows for

body centered cubic (bcc) spheres and hexagonally packed cylinders (hpc) are predicted. If the copolymer is made asymmetric at the same composition, with $\tau = 0.25$, (i.e. the molecular weight of one end block equal to three times the molecular weight of the other end block) the bcc and hpc windows are stable over larger regions. In addition, the volume fraction at which the melt orders from the disordered state to a microphase separated morphology also shifts with τ, in other words, the morphology diagram becomes highly asymmetric. Thus, in the case of these asymmetric triblock copolymers synthesized here, the formation of double gyroid and cylinders at these unusual volume fractions could be due to the asymmetry of the end block molecular weights since the shift is in the correct direction. In our case, we expect lamellae at $\phi_{P(PMDSS)} = 0.48$ but obtain double gyroid and expect lamellae at $\phi_{P(PMDSS)} = 0.56$ but obtain cylinders. This could be because the stability window of the lamellae and double gyroid is widened due to the asymmetric architecture. If these two polymers were isolated data points this would be quite a strong argument, however, it is unusual though that cylinders of P(PMDSS) in a matrix of PI are found at a *higher* volume fraction than P(PMDSS) double gyroid networks in a PI matrix. This observation can not be explained.

In addition to these theories, when studying block copolymer morphologies, the question of whether or not equilibrium has been reached needs to be addressed. First of all, the degree of segregation between the two end blocks is not known and it is only assumed that the sample was annealed long enough to achieve equilibrium. Secondly, the solubility parameter for P(PMDSS) has not been determined before and as a result, it is not known whether or not toluene is a neutral solvent for the PI and P(PMDSS). If toluene was a preferential solvent for one of the blocks, this could result in a shift in the volume fraction of the expected morphologies since this would result in one block coming out of solution before the other block. If this were the case though, the volume fraction that we see the other double gyroid morphology, P(PMDSS)-DG should also be shifted. However, we do see the formation of this morphology at the expected volume fraction, $\phi_{P(PMDSS)} = 0.66$. The difference with the P(PMDSS)-DG to the PI-DG, lamellae and cylinder samples though is that the PI are the endblocks in the former and the P(PMDSS) are the endblocks in the latter set. It could be possible that when P(PMDSS) exists as the end blocks rather than the midblock, the affect of steric hindrance on the morphology is greatly increased due to the higher degree of freedom that the end blocks possess as compared to the midblock. This could explain why the order-order boundaries are skewed towards the P(PMDSS) volume

fractions for the triblock copolymers when P(PMDSS) blocks are on the end. However, in order to completely elucidate this, equivalent triblock copolymers with P(PMDSS) end blocks as well as PI end blocks must be synthesized and separate morphology diagrams determined.

In order to fully understand the reasons for the shift in the volume fraction of some of the morphologies, a more systematic study needs to be carried out on this system. Namely, two sets of triblock copolymers should be synthesized. One set should consist of symmetric triblock copolymers with a systematic change in the volume fraction. If the resulting morphology diagram is asymmetric, than this must be due to differences in the Kuhn statistical segment length of the two blocks. In the second set, asymmetric triblock copolymers, all of which share the same symmetry factor should be synthesized and compared to the morphology diagram in the first set. If the morphology diagram is skewed by the same amount than it can be said that the asymmetry of the polymer molecule does not contribute to the shift in the volume fractions of the morphology diagram. However, it is likely that in the second set of polymers, the asymmetry of the morphology diagram will be even greater based on the theoretical work of Mayes and de la Cruz.

3.4 Conclusions

The synthesis and the morphology of various triblock copolymers of the type ABA and BAB, where A is polyisoprene and B is poly(pentamethyldisilylstyrene) has been shown. Through TEM images and their Fast Fourier Transforms as well as SAXS materials exhibiting P(PMDSS) spheres, cylinders, lamellae and double gyroid have been documented and d-spacings calculated. When the triblock copolymers have the P(PMDSS) block at the ends, the order-order boundaries of the morphology diagram shift towards the low volume fraction of P(PMDSS), opposite to what is seen in the PDMS-PS system. This could be due to asymmetry in the architecture, non-neutral solvents, kinetic effects or non-equilibrium conditions. In order to elucidate this, more systematic studies need to be carried out.

Chapter Four
Oxidation of Silicon Containing Homopolymers: A Compositional Study

4.1 Introduction

In the formation of a ceramic nanostructure from a block copolymer precursor, it is first important to understand the conversion process of the inorganic containing block into a ceramic. A ceramic as defined by Kingery, Bowen and Uhlmann are "solid articles which have as their essential component, and are composed in large part of, inorganic nonmetallic materials." (Kingery 1976) To determine the extent of conversion of our silicon-containing block to a ceramic, the oxidation of the *anionically* synthesized poly(pentamethyldisilylstyrene), P(PMDSS) homopolymer by both oxygen plasmas and ozonolysis/uv was studied both chemically (this chapter) and morphologically (Chapter 5).

Chemically, the oxidation of P(PMDSS) homopolymer was investigated using five different characterization techniques. Atomically, the materials were studied by X-ray photoelectron spectroscopy (XPS) which determined the nature of the chemical environment of the different atomic species (Si, C and O) before and after oxidation. The thickness of the ceramic upon conversion was studied by Auger electron spectroscopy (AES), and Rutherford backscattering and forward recoil spectroscopies (RBS and FRES) were used to determine the bulk stoichiometries of the materials after oxidation. Bond stretching was studied by Fourier Transform Infra-Red (FTIR) spectroscopy in order to identify the different types of chemical groups present, while the refractive indices and thicknesses of the oxidized materials were characterized by ellipsometry.

In the beginning of this chapter an overview is given on ozonolysis and oxygen reactive ion etching – the two different oxidation techniques used in this thesis. In contrast with oxidation, it is possible to form similar ceramic materials through high temperature pyrolysis which is discussed in **Section 4.1.3**. The work in the formation of silicon oxycarbide and silicon carbide by the pyrolysis of silicon containing polymeric precursors is important since our materials can be directly compared to those made by this processing route.

The five experimental techniques used to study compositional changes are also outlined in detail in this chapter with an explanation of how data was obtained and the type of data

acquired by these techniques. The data obtained using these techniques is then used to compare and contrast the chemical changes that occur in the material when oxidized by various methods. The temperature stability of these converted materials is then investigated at the end of this chapter since this property is desired in ceramic materials.

4.1.1 Ozonolysis of Organic Materials

Ozone is a powerful oxidizing agent that is generated when an atomic oxygen or oxygen-containing free radical reacts with gaseous molecular oxygen (Horvath 1985):

Figure 4.1: The equilibrium reaction between ozone and oxygen/atomic oxygen and oxygen containing free radicals.

Ozone can be generated by various techniques, depending on the method used to create the atomic oxygen. Oxygen radicals can be produced by thermal dissociation at high temperatures, by photochemical dissociation under the influence of uv light, through electrolysis of oxygen-containing compounds, through radiochemical radiation of oxygen, or by applying a large electric field across air or pure molecular oxygen. The application of a large electric field creates an electric discharge which results in the formation of atomic oxygen radicals which combine with molecular oxygen to form ozone.

The kinetics and mechanisms of ozone reactions with different polymers have been studied by Razumovskii *et al.* (1971). In their studies, ozone was generated through an electrical discharge yielding concentrations between 2.5 $x10^{-3}$ to 0.5 $x10^{-5}$ mole/l. Polymer samples were in powder form and of known surface area. The gas output of the reaction vessels was analyzed by a spectrophotometric device and during the reaction, polymer samples were removed for infra-red analysis.

Razumovskii *et al.* found that ozone reacts with polymers mainly at the surface since the reaction rate and the concentration of intermediate peroxy-radicals is proportional to the surface area and is independent of the molecular weight of the polymer.

When a polymer containing unsaturated double bonds in the backbone is exposed to ozone, oxidative cleavage of the double bond occurs by the following mechanism:

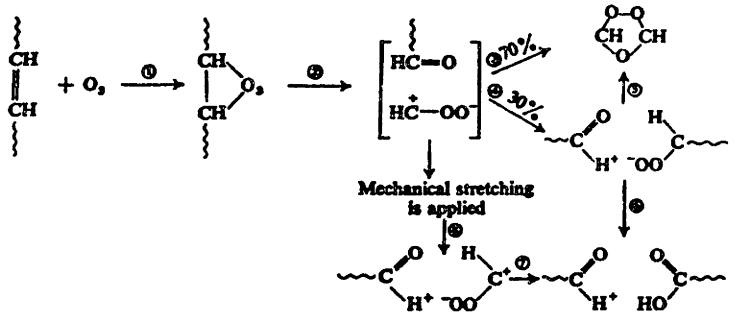

Figure 4.2: Mechanism by which polymers with double bonds degrade when exposed to ozone. (After Razumovskii, 1971).

When a polymer containing a double bond, **a**, (such as polyisoprene or polybutadiene) is exposed to ozone, the ozone opens the unsaturated bonds and forms a primary molozonide, **b**. This ozonide then rearranges to form intermediate products such as aldehydes, **c**. There is a 70% probability that this molozonide rearranges to form the end-product ozonide, **d** while 30% of the time, the bipolar ion and carbonyl group separate, **e**, and rearrange to form a cross ozonide or isomerize with chain breaking, **f**.

Polymers which have totally saturated aliphatic chains react with ozone via a free-radical mechanism. As an example, the reaction mechanism of polyethylene can be represented as follows, where the degradation of the polymer occurs through the decomposition of peroxy-radicals :

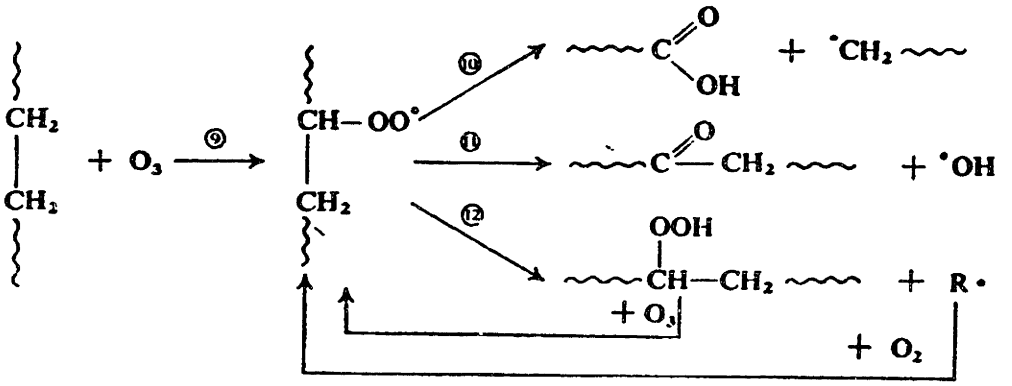

Figure 4.3: Degradation of polyethylene using ozone. (After, Razumovskii, 1971).

In this case, the ozone replaces a proton in the main chain, forming lower molecular weight groups such as carboxylic acid, carbonyl groups and radical species. The rate of attack of ozone on saturated bonds is much lower as compared to unsaturated moieties resulting in a lower rate constant for the ozonolysis of saturated polymers.

Rate constants for reaction of polymers with ozone are given in **Table 4.1.** Note that the reaction rate of ozone with PB and PI is 6 orders of magnitude greater than for PS. Such a comparison of reaction rates is directly analogous to etch selectivity of these polymers in reactive ion etching, as discussed in **Section 4.1.2.** It is this difference in rate constants that allows the selective removal of the poly(diene) block to polystyrene.

Table 4.1: Rate constants of reaction and number of disintegrations per event of O_3 with different polymers. (After Razumovskii, 1971.)

No.	Polymer	Structural link of chain	K ($l/mole^{-1}$ sec^{-1})	Number of disintegrations per event
1.	Polyphenyl	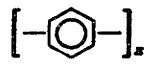	5×10^{-3}	—
2.	Polynaphthalene	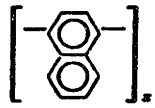	2×10^{3}	—
3.	Polycarbonate	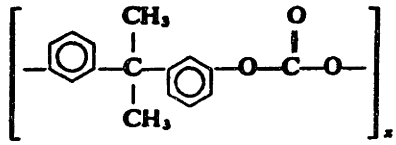	3·0	—
4.	Poly*iso*butylene	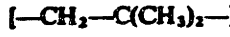	0·012	0·05
5.	Polythene*	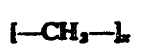	0·046	0·1
6.	Copolymer of ethylene with propylene	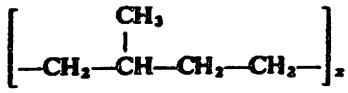	0·06	0·06
7.	Polypropylene	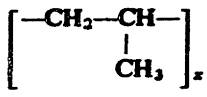	0·08	0·1
8.	Polystyrene	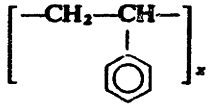	0·12	0·01
9.	Polyvinylcyclohexane	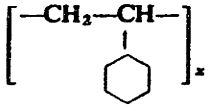	0·8	—
10.	Polyphenylacetylene	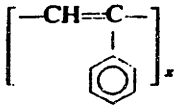	1·4	—
11.	Polybutadiene	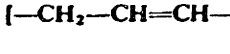	8×10^{4}	0·001
12.	Poly*iso*prene	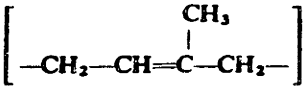	10^{5}	0·03

* The rate constant and the number of disintegrations of chain for polythene insoluble in CCl_4 were calculated from its low-molecular analogues such as polymethylenes C_{30} and C_{40}.

If a block copolymer such as PS-PI, is exposed to ozone, the diene block will undergo oxidative cleavage much more rapidly than polystyrene block since there are no unsaturated bonds in the PS backbone. PS reacts with ozone but at a much lower rate since the aromatic carbon-carbon bonds present are much less reactive to ozone than olefinic double bonds and the backbone is composed of aliphatic bonds. (Horvath 1985) Similarly, fluorinated polymers have been shown to be resistant to attack by ozone. (Horvath 1985)

Rate constants were also determined for certain polymers as a function of the functional groups attached to the polymer main chain as shown in **Table 4.2.**

Table 4.2: Rate constants of reaction of O_3 with different functional groups. (After Razumovskii, 1971).

Functional groups		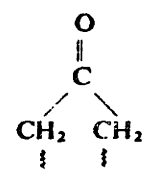						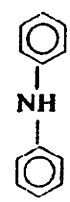
K_i l/mole sec	0·03	0·14	13	15	50	360	10^5	2×10^6

The conversion of Langmuir-Blodgett layers of silicon-containing oligomers to ultra-thin silicon oxide films using a combination of ozonolysis and uv light has also been studied. (Mirley 1995, Koberstein, US Patent 1997) They studied the formation of SiO_x from the oxidation of diacid terminated poly(dimethylsiloxane). FTIR and XPS, demonstrated that up to 90% of the methyl side groups in carboxylic acid-terminated poly(dimethylsiloxane) (diacPDMS) are oxidized by this process leading to the formation of hydroxyl and bridging oxygen species. In the final film, the material consisted of 75% SiO_2 while the remaining film consisted of incompletely oxidized $-CH_3$, Si-OH groups and O-Si-C bonds. Despite the high residual carbon left behind in the film after uv + ozone exposure, the film was still regarded as an oxide. FTIR spectra shows the presence of residual methyl groups with symmetric bendings at 7.9, asymmetric stretching at 3.4 and rocking at 12.1 (μm) wavelengths. By XPS It was shown that the C/Si ratio in (diacPDMS) dropped from 2.2/1 in the native polymer to 0.22/1 after ozone-uv

exposure; hence 90% of the carbon atoms were evolved. After exposure to ozone and uv, the 38 Å sample of diacPDMS lost over 60% of it's thickness and decreased to 15Å . The oxide layer could not be made thicker because the formation of the oxide layer hindered transport of the ozone to underlying unreacted oligomers.

4.1.2 Reactive Ion Etching of Silicon Containing Polymers

An alternative oxidizing agent to ozone is an oxygen plasma which is comprised of highly reactive oxidizing species. A plasma is created when a large electric field is applied across a volume of gas resulting in the production of electrons, ions and a variety of charge neutral species such as highly reactive atoms and molecular fragments. It is these reactive species which are responsible for reactive ion etching. Most conventional reactive ion etchers use a 13.56 MHz radio-frequency (rf) electric field to excite the low pressure glow discharges. Such plasmas have pressures of 0.1 mTorr - 10 Torr with electron densities of 10^8 - 10^{13} cm^{-3}. (Mucha 1994) A reactive ion etcher is shown schematically in **Figure 4.4.**

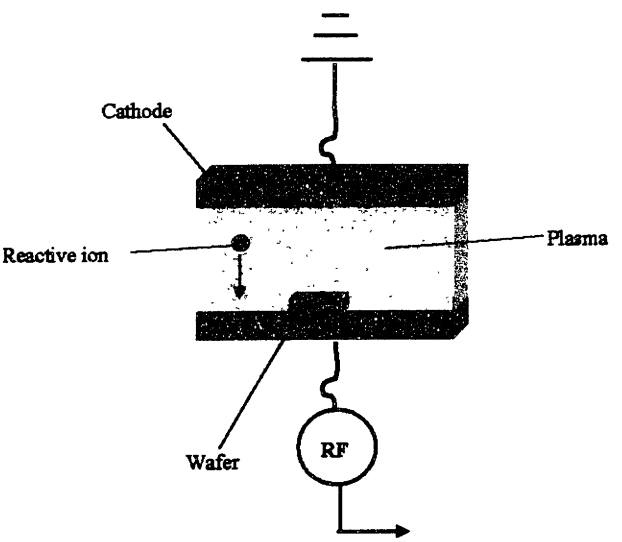

Figure 4.4: Schematic of a parallel-plate reactive ion etcher.

After the reactive species are produced in a parallel plate reactive ion etcher, they are accelerated to the substrate which is placed on the powered electrode. The bias voltage across

the plasma can be controlled, which in turn controls the acceleration and energy of the reactive species that bombard the surface.

In reactive ion etching, the role of the plasma is twofold. First of all, the accelerated electrons create reactive species by colliding with gas molecules and breaking bonds. Since this process is not thermally activated, not only can the etching temperature be kept low, but there are no kinetic limitations. Secondly, as the discharge occurs, energetic radiation in the form of ions, neutral species, electrons and photons will alter the surface chemistry of the sample.

Reactive ion etching is shown schematically in **Figure 4.5.** After the reactive species have been generated **(1)**, they must diffuse through the plasma to the surface of the sample **(2)** and adsorb onto a surface site **(3)**. With free radicals which chemisorb, reaction with the surface can also occur **(4)**. The adsorbed species can also diffuse along the surface of the sample. Eventually, the product which has formed as a result of the reactive species interacting with the sample must desorb from the surface **(5)**. If one of these steps does not occur, etching can not occur. After desorption, the by-products then diffuse into the bulk of the gas **(6)**.

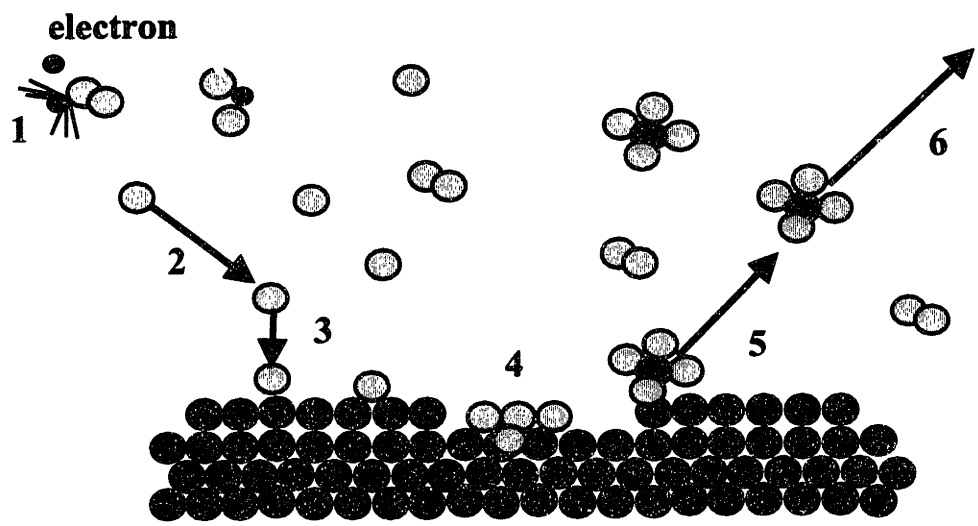

Figure 4.5: Schematic of the chemical component of the reactive ion etching of a surface which does not form a protective layer after exposure to the plasma (After Mucha 1984).

Overall, reactive ion etching can be defined by two mechanisms; chemical and physical. Physical etching refers to positive ion bombardment of the sample which breaks surface bonds and is responsible for sputtering. The positive ion bombardment is a direct result of the fact that the species in the plasma with the highest mobility are electrons which results in a negative

potential on the sample surface relative to the plasma. The positive ions in the plasma are then accelerated to the sample surface and upon impact break surface bonds resulting in physical etching. Chemical etching is defined by the chemical reactions which occur on the surface of the sample. As an example, a carbon-hydrogen bond can be dissociated thereby producing a radical site on the polymer. An oxygen molecule can react here and form a peroxide radical which can then form a hydroperoxide by abstracting a hydrogen from a radical species. (Hartney 1989) The reaction product then desorbs from the sample surface and diffuses into the bulk of the plasma gas.

The process parameters which govern reactive ion etching are all interrelated resulting in a very complex system. Externally controlled operating parameters are gas pressure and gas composition, which dictate the amount and type of plasma gas in the reactor, power which refers to the power of the plasma, excitation frequency, which in this case was fixed to 13.56 MHz, flow rate of the feed gases and sample temperature. (Mucha 1984)

The parameter space for reactive ion etching is expansive which results in significant differences in the behavior and nature of the plasma for etching depending on the precise values of the parameters chosen. By changing these variables, (which include plasma gas chemistry, plasma power, the particular etching machine used and flow rates) the nature of the plasma can be significantly altered allowing the extensive control of the etching conditions of different materials. For this reason, etch selectivity between two different material systems can be widely varied. However, it is well-documented that the incorporation of inorganics to a polymer increases its etch resistance. (Sugita, 1992, Miller 1994) The reason for this is that if the inorganic is present in a sufficient weight percentage it will form a protective oxide layer when exposed to an oxygen plasma thereby preventing further etching. In the case of silicon exposed to an oxygen plasma, silicon is converted to silica which cannot be chemically etched but can be sputtered by high-ion-energy bombardment. However, physical sputtering occurs at a much slower rate than chemical etching.

In the last ten years there has been extensive research on the development of new polymers for microlithographic patterning. One focus of this research, particularly for bilayer applications in photoresist technology, as shown in **Figure 4.6**, has been on silicon-containing polymers that form a protective oxide layer when exposed to an oxygen plasma. (Reichmanis 1984, Miller 1994)

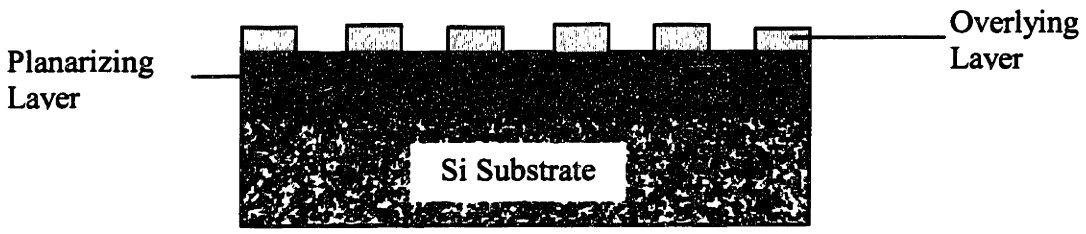

Figure 4.6: Schematic of a bilayer resist configuration.

In a bilayer resist configuration, the resist consists of a top layer which when exposed to radiation is able to delineate a pattern and has an etch resistance that is at least five times greater than the planarizing layer. (Reichmanis 1984) The planarizing layer is of sufficient thickness to planarize the underlying substrate whose surface is normally not perfectly flat. The pattern delineated in the overlying layer is then replicated to the planarizing layer through a dry developing technique (such as by O_2-RIE). For this reason, the planarizing layer is normally an organic material, such as polymethylmethacrylate (PMMA) or novolac. The etch-resistance of the top oxide layer to the oxygen plasma provides the selectivity needed for subsequent lithographic image transfer. For this reason, considerable effort has been devoted to understanding the mechanism behind the formation of this protective oxide coating.

Various silicon-containing polymers have been investigated, including silicon substituted novolacs, methacrylates, olefinsulphones and styrenes as well as polysilanes, silylated organic resists and siloxane copolymers.[11] These studies have focused mainly on the lithographic properties such as imaging, pattern transfer and etch selectivity. Characterization techniques have included Auger electron spectroscopy (AES), X-ray photoelectron spectroscopy (XPS), Rutherford backscattering (RBS), and scanning electron microscopy (SEM). Relatively little work has utilized atomic force microscopy (AFM) as a technique to study the evolution of surface morphologies upon etching and our work in this area will be discussed in **Chapter Five**. (Petri 1994)

Chou *et al.* investigated the elemental composition of surfaces of plasma etched silicon-containing polymers by AES and XPS and found that a 10 Å thick oxide layer persists throughout the reactive ion etch (RIE) process. (Chou 1985) This steady state layer formation results from the competing processes of oxide growth vs. ion sputtering ; the resulting oxide is not chemically etched by the oxygen plasma. It is this characteristic that produces the important etch selectivity for silicon-containing polymers versus those without silicon.

Gokan *et al.* studied organosilicon polymers and found that the etch resistance increased with increasing silicon content in the polymer. They found that if a minimum of 1 $x10^{16}$ Si atoms/cm^2 were present on the polymer surface, etching ceased after the formation of the oxide layer which typically was at least 10 Å thick. (Gokan 1986) Similarly, other researchers (Macdonald 1983, Reichmanis 1984, Ohnishi 1985) have found that the O_2-RIE resistance rapidly improves with increasing silicon content, leveling off at a critical concentration of approximately 10-15 wt % silicon.

Models have been developed for the growth of this oxide layer in an oxygen plasma where the growth rate follows a steady state process. Watanabe *et al.* (1986) showed that the etching rate becomes constant after an initial rapid decrease in thickness. If the amount of silicon present in the material is less than 10 wt%, than the resulting SiO_2 or SiO_x is porous. In these models, the growth rate was diffusion-limited, inversely proportional to oxide thickness, and limited to a maximum oxide thickness, after which further growth of the oxide layer ceased. Other researchers have expanded this steady-state model, (Jurgensen 1988, Dijkstra 1991) and found that there were at least two regimes for the oxide formation. In regime I, the transition regime, the etch rate is positive, since the carbon moieties in the polymer are removed before a contiguous protective SiO_X barrier is formed. Regime II, the steady state regime, follows, where an effective SiO_X barrier has been formed and the etch rate becomes essentially constant; i.e., the rate of oxide removal by ion sputtering equals the rate of oxide growth with a typical oxide thickness of 1 nm as shown by Chou et al.[15] Hence, if a silicon containing polymer with more than 10 wt% is exposed to O_2-RIE, a thin oxide layer forms which protects the remaining underlying film from becoming oxidized thus preventing complete conversion of the film to an oxide.

This oxide barrier that forms in the silicon-containing polymers results in etch selectivity in the block copolymer between the inorganic containing block and the organic containing block, and is further discussed in **Section 6.1.2.**

4.1.3 Pyrolysis of Silicon-Containing Polymers

In addition to utilizing oxidizing species to produce ceramics from inorganic polymers, it is possible to obtain these materials by traditional high temperature pyrolysis routes. In my undergraduate research, I studied the formation of boron nitride from polyborazylene, ($B_3N_3H_6$) a polymer precursor. By pyrolyzing the material to 900°C boron nitride with a residual hydrogen concentration of 10% was produced.(Chan 1996) Conceptually the idea is the same as the pyrolysis of organosilicon precursors to form silicon oxycarbide; by heating the material to very high temperatures, a ceramic is formed through the rearrangement of the bonds and the removal of volatile species such as hydrocarbons.

The disadvantage of this method over ozonolysis or reactive ion etching in producing *oxide* ceramics is the fact that very high temperatures are necessary; temperatures which are oftentimes higher than the degradation temperatures of most polymers. This technique could not be used to produce ceramic nanostructures from block copolymers because it would be necessary to heat the material above the T_g and order-disorder transition temperature of the block copolymer resulting in a disordered structure from which an ordered nanoporous material could not be made. However, it is important to mention the ceramics that are formed by such high temperature treatment of inorganic polymers and to compare these materials to those produced by low temperature oxidative routes.

In the studies on the pyrolysis of organosilicon precursors, metastable silicon oxycarbide (termed black glass due to the excess carbon), is produced upon heating to temperatures above 600°C. (Belot 1994) Ideal silicon oxycarbide consists of silicon that is bound to both carbon and oxygen while the carbon is bound only to silicon (i.e. CSi_4). However, the definition of silicon oxycarbide has expanded to include materials that also include carbon-oxygen bonds, carbon-oxygen-silicon bridges and residual hydrogen since the majority of the materials produced using a silicon containing polymeric precursor contain these moieties. The chemical route of the pyrolysis was characterized by a combination of nuclear magnetic resonance spectroscopy (NMR), Fourier transform infra-red spectroscopy (FTIR) and thermal gravimetric analysis coupled with mass spectrometry (TGA-MS). In a typical reaction scheme, at 600°C, the Si-O and Si-C bonds undergo redistribution reactions resulting in SiO_xC_{4-x} at 900°C with the loss of hydrocarbons and hydrogen. Reported weight losses ranged from 14% (Belot pp 287-297, 1992) to 25% (Renlund Part I 1991) These glasses were stable up to temperatures ranging from 1000°-

1350°C above which the silicon oxycarbide rearranged to a mixture of SiO_2 and SiC. Above 1350°C, SiO and CO are evolved resulting in the formation of SiC.

This pyrolysis route is useful since silicon oxycarbide glasses have been shown to have superior mechanical properties and chemical stability over silica. (Renlund Part II 1991) The substitution of a percentage of the bivalent oxygen atoms by tetravalent carbon atoms improves the properties in two ways. It is believed that the carbon atoms both tighten the silica network and prevent crystallization at higher temperatures resulting in improved temperature stability.

The material systems used in these studies were typically polysiloxane and disilane precursors formed using a sol-gel process. One disadvantage of the sol-gel route is the suppression of the formation of free carbon which would compromise the Si-C bonds in the glass network. The majority of the polysiloxane precursors used resulted in ceramics with O/Si ratios close to 1.5 and by careful design of the precursors, ratios approaching 1.1 have been attained. In these cases, crosslinking reactions were utilized in order to bind the Si to the matrix. (Belot, pp 52-55, 1992 and Michlczyk 1993)

The binding environment of the Si, C and O atoms can be studied by X-ray photoelectron spectroscopy (XPS) as a function of pyrolysis temperature.(Bouillon 1991, Renlund 1991, Chaudhry 1995, Harris 1995 and Soraru 1996) The XPS peaks of the modified silicon precursors are very broad due to the wide range of chemical environments in the processed materials.

Soraru *et al.* (1996) studied the formation of silicon oxycarbide glasses from the high temperature pyrolysis (1000°C in argon) of silicon containing sol-gel precursors. The temperature stability of the resulting material was investigated by heating to 1500°C in argon to measure the temperature stability. By XPS (after sputtering the surface for one minute in order to reduce C contamination) it was shown that Si2p spectrums obtained were extremely broad spanning from 98eV to 107 eV suggesting the formation of intermediate mixed silicon oxycarbide species (SiO_4, $SiCO_3$, SiO_2C_2, SiC_3O, SiC_4) in decreasing binding energies. The C1s spectrum showed the presence of CSi_4, CH_2 , O-C-Si and C-O bonds at 283 eV, 284.5-285 eV , 285.5 eV and 285-289 eV binding energies respectively. The overall stoichiometry of the material produced was found by XPS to be $SiO_{1.44}C_{0.3}$, although hydrogen concentrations could no be determined.

Renlund *et al.* (1991) studied the production of silicon oxycarbide by the pyrolysis of silicone resins at temperatures below 900°C. The silicon oxycarbide glasses that form which are composed primarily of silicon-oxygen tetrahedra with carbon atoms acting to bridge different

silicon-oxygen tetrahedra. The material was annealed to 1600°C and above 1400°C the networks rearrange to form free carbon in the form of graphite and SiC crystals as observed by TEM diffraction. This can only be accomplished at extremely high temperatures because silicon-oxygen and silicon-carbon bonds must be broken which require significant amounts of energy. XPS on the silicon oxycarbide produced at 900°C showed the presence of C-C, C-O and C=O bonds at 284.6 eV, 286.3 eV and 286.4 eV respectively. The Si2p peak indicated that 70% of the silicon was bound at 102.9 eV (SiO_2C_2) and 30% at 100.7 eV (Si-C). FTIR of the silicon oxycarbide showed peaks at the following wavenumbers: Si-O-Si stretching at 21.3, Si-O-Si rocking at 9.2, Si-C (at a lesser intensity) at 8.7, 11.7, 12.0 with the peaks at 11.7 and 12.0 splitting which suggests that the silicon are bound to at least 2 carbon atoms and C=O vibrational bands between 5.6 and 6.3. The atomic composition of the material was determined by nuclear magnetic resonance spectroscopy (NMR) with atomic concentrations ranging from 64% for silicon, 13-42% for oxygen and 11-23% for carbon.

Harris *et al.* (Chaudhry 1995, Harris 1995) investigated the pyrolysis of 0.1 μm thick films of silsequioxane materials. It was found that up to 600°C, the C, O and Si ratios remain constant due to the formation of –[$MeSi(O)_{1.5}$]. Between 600°-800°C, silicon oxycarbide is formed. At 1000 °C the material begins to mineralize to form SiO_2 and free carbon in the form of amorphous graphite. By XPS, the atomic concentrations were determined. The amount of silicon was 19-25% at all temperatures, the amount of carbon dropped from 44% to 27% and the amount of oxygen increased from 35% to 49%. The silicon existed as O-Si-C groups as evidenced by peaks between 101-102 eV and as SiO_2 due to a peak at 104 eV. Auger electron spectroscopy of the films indicated that throughout the film thickness there were significant amounts of carbon. At the first 50 nm of the film, the amount of carbon was less than further into the film, with a steady state of oxygen, carbon and silicon present after the first 100 nm into the film. Unfortunately the AES data was reported as derivative peak heights and not as atomic concentrations so absolute amounts could not be compared. The problem with derivative peak height data is that it is a function of the number of sweeps that taken for that element. For example, if a film has the same amount of carbon and oxygen but two times the number of sweeps are taken for the carbon as compared to the oxygen, it will appear from the derivative height data that there is two times as much oxygen in the film. Thus, it is difficult to use this data to compare to data in this thesis.

FTIR indicated the presence of sharp peaks at wavenumbers of 3.3-3.6 (C-H), 7.9 (Si-C) and 4.5-4.7 (Si-H). Above 800°C, the sharp peaks broaden indicated featureless bands between 8.0-11 and 12.5-16.7 indicating the presence of SiO_xC_y.

Finally, Bouillon *et al.* (1991) studied the formation of silicon oxycarbide through the pyrolysis of polycarbosilane. Between 550-800°C, silicon oxycarbide, amorphous hydrogenated species, silicon carbide and silicon dioxide were formed. Between 1000-1200°C, the material transforms to silicon carbide. FTIR spectra indicate stretching at wavenumbers of 12.5 (Si-C), 9.1 (Si-O), 3.4 (C-H), 4.8 (Si-H), 7.1 ($Si-CH_3$), 7.4 ($Si-CH_2-Si$). Between 550-700°C the intensities of the stretches due to organic bonds decease significantly and at 700°C only faint traces of the organic compounds are present. XPS demonstrates the formation of Si-C, Si-O and C-Si-O bonds at 100.8 eV, 103.5 eV and 101.8 eV respectively for the Si2p peak. The C1s peak further confirms this with peaks at 282.8 eV (C-Si) and peaks at binding energies above 284.2 eV (Si-C-O, phenyl groups, C-O and C=O moieties).

The research reported here on the high temperature pyrolysis of silicon containing polymers to form silicon oxycarbide and silicon carbide is important in order to compare the oxidized polymers formed by our oxidation techniques. However, it must be noted that none of the researchers did RBS or FRES studies so hydrogen concentrations could not be determined and ellipsometry data also was not taken. In addition, atomic concentrations were often determined from XPS which is only a surface sensitive technique and only one research paper, that by Chaundhry *et al.* (1995) performed AES depth profiling on their samples in order to monitor composition changes throughout the film.

4.2 Experimental

4.2.1 Sample Preparation

Solutions of P(PMDSS), synthesized anionically as described in **Section 2.4**, were prepared by dissolution in toluene (5 wgt%) at room temperature. Films were made by spincoating onto 1" diameter (100) silicon wafers with a native oxide. The silicon substrates were cleaned with toluene prior to spinning and the polymer solution was deposited onto the Si wafers using a syringe tipped with a 0.45 μm filter. Films were prepared by spinning first at 500 rpm for 15 seconds and then at 2000 rpm for 40 seconds. All film samples were baked in a vacuum oven at 70 °C for at least 12 hours to remove any residual solvent. Final film

thicknesses for all samples was measured by both ellipsometry and mechanical profilometery and found to range between 200 and 300 nm. 5-10 data points were taken on different areas of the sample, depending on the consistency of the data.

4.2.2 Ozonolysis Plus Ultraviolet Exposure

The ozone used was produced by a Pacific Ozone Technology Inc. Ozone Generator, Model L21 and the experiments performed at MIT. In this apparatus, ozone is generated by a high voltage discharge between ceramic and metal electrodes. Either dry air or oxygen is flowed into the corona discharge gap, the area between the electrodes. A high voltage is then applied across this gap at high frequencies which breaks down oxygen molecules leading to the formation of ozone, as discussed in **Section 4.1.1.** The concentration of ozone produced can be varied by changing either the carrier gas used, the flow rate into the gap, the voltage applied across the gap and/or the resident pressure of gas inside the gap. In our studies, 2 wt% ozone was used in an oxygen carrier gas; identical to what other researchers in this field have been using.(Mansky 1996) The generator can produce ozone ranging from 0% to 100% and ozone concentration curves are provided in **Appendix B.**

The output of the ozone generator was fed into a glass horizontal tube containing the samples to be exposed. The ozone was exhausted into a glass bubbler containing 2 wt% potassium iodide (KI) solution as shown schematically in **Appendix B.** Upon exposure to ozone, the iodide transformed to iodine resulting in the transformation of the solution from colorless to an orange-red as shown below.

$$2K^+ + O_3 + 2I^- \longleftrightarrow I_2 + O_2 + O^{2-} + 2K^+$$

Figure 4.7: Formation of iodine from potassium iodide upon exposure to ozone.

In conjunction with ozonolysis, the samples could be heated or exposed to uv light simultaneously. At one end of the tube, a ground-glass connector equipped with an ultra-violet light source[1] was inserted allowing the samples to be exposed to ozone and uv simultaneously.

[1] UVP Pen-ray PCQ Lamp. Part number 90-0049-03. Lamp emits 8mW/cm2 1.9 cm away from the light source

This uv light source produced 254 nm wavelength light with a power of 8mW/cm^2, 1.9 cm away from the light source.

4.2.3 Reactive Ion Etching

Plasma etching was performed on two different parallel plate machines, a Plasmatherm located in the Nanostructures Laboratory at MIT and a Magnetron located at IBM Almaden Research Center, San Jose CA. The main difference between these two machines is that the plasma in the Magnetron is magnetically enhanced thereby creating a plasma with a higher electron density. As a result, etching rates in the Magnetron will be much greater than in the Plasmatherm.

The etching experiments were carried out in a low pressure, magnetically enhanced, inductively coupled, plasma etcher. Etching was performed with a base pressure of 10 mTorr and an oxygen flow rate of 40 sccm. The top radio frequency (rf) generator was set at 250 W and the bottom rf generator at 50 W. Etching was performed at either ambient plasma temperature or 0^{o}C. It was estimated that the *minimum* sample temperature was 70^{o}C in the ambient plasma; the actual temperature could be much higher. More details are given in **Section 5.2.3.** Etch rates were calculated by measuring film thickness before and after etching using a profilometer.

4.2.4 Ellipsometry

When P(PMDSS) is oxidized, the material undergoes densification and chemical changes with a reduction in the percentage of carbon and hydrogen and an increase in the percentage of oxygen. With this oxidation, there is a change in the refractive index of the material which can be monitored using ellipsometry.

In ellipsometry, a laser impinges on the surface of a reflective sample, as shown in **Figure 4.8.**

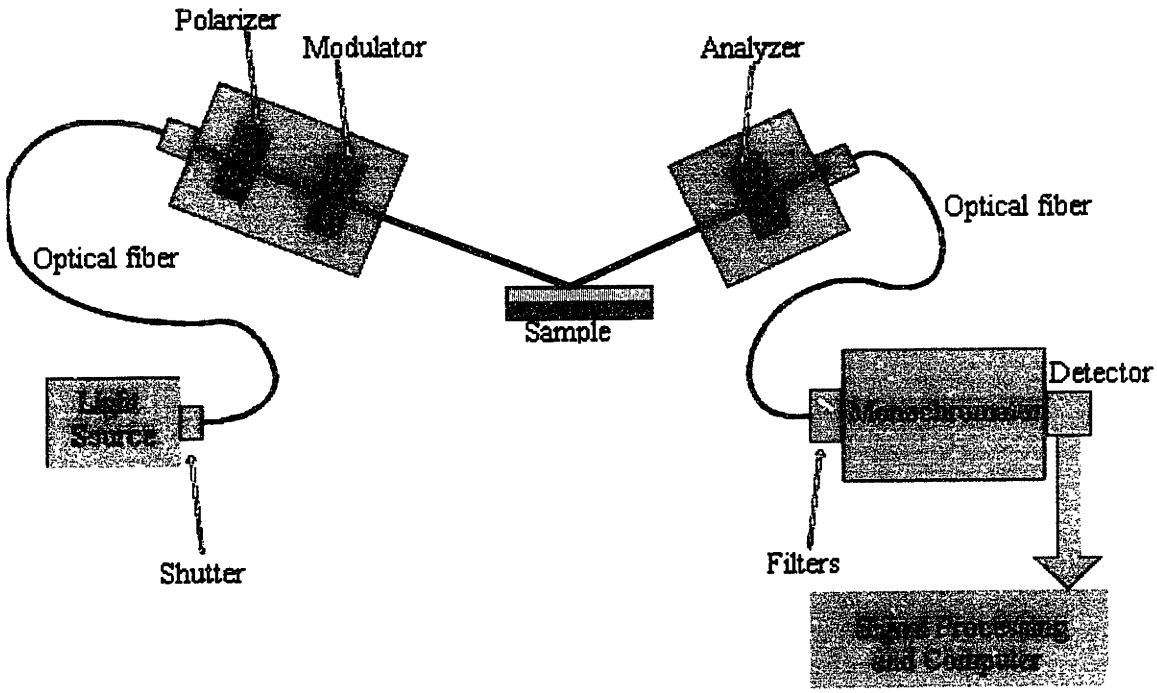

Figure 4.8: Schematic of the experimental set-up for ellipsometry. After http://www.isainc.com/Ellip/descrip/setup.htm

The polarization of the light before and after interaction with the sample is measured and from this information optical constants of the sample can be determined. The light comes through a polarizer and compensator which elliptically polarizes the light. This light is then reflected from the sample surface into a rotating analyzer. The reflected light intensity, I(A) is monitored through a photodetector and is expressed as :

$$I(A) = \bar{I}[1 + 2\alpha\cos 2A + \beta\sin 2A]$$

where α and β are Fourier coefficients of the transmitted intensity and I bar is the average detected signal over one full rotation of the analyzer. Using α and β the ellipsometric angles Ψ and Δ are calculated through the equation:

$$\tan\Psi e^{i\Delta} = \frac{(1+\alpha)}{\beta \pm i\sqrt{(1-\alpha^2-\beta^2}} \text{x} \frac{\text{tanC} + \rho_c \tan(P-C)}{1 - \rho_c \tan C \tan(P-C)}$$

where P and C are the fixed angles of the polarizer and compensator and ρ_C is the relative transmittance of the compensator.

Film thicknesses and refractive indices before and after processing were determined using a Gaertner ellipsometer equipped with a 633 nm wavelength laser and located in the Center for Materials Science and Engineering at MIT. Ten data points were taken and measured thicknesses and refractive indices were within 2%. A schematic of ellipsometry is seen in **Figure 4.8.** Thicknesses were confirmed by profilometry using a TENCOR instrument with a stylus force of 1 mN.

4.2.5 X-Ray Photoelectron Spectroscopy

The atomic concentrations of silicon, carbon and oxygen were estimated by X-ray photoelectron spectroscopy (XPS), is shown schematically in **Figure 4.9.**

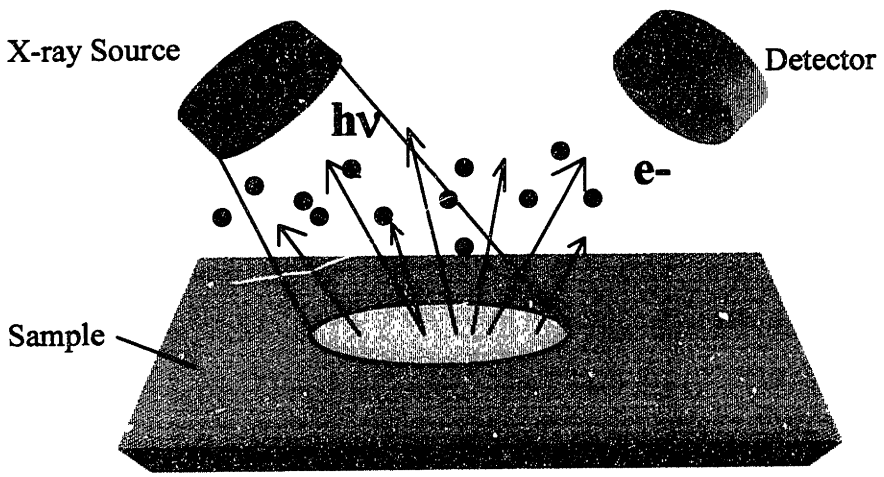

Figure 4.9: Schematic of the experimental set-up for XPS (After Ratner 1997).

In XPS, X-rays are impinged on the sample surface resulting in energy transfer from the photons to a core-level electron of the sample resulting in photoelectron emission, as shown in **Figure 4.10.** (Ratner 1997)

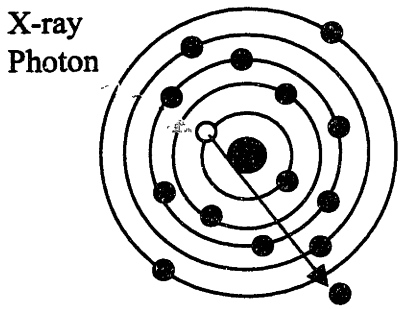

Figure 4.10: When an X-ray photon impinges the sample, energy from the X-ray photon is transferred to a core-level electron resulting its ejection. It is these photoejected electrons which are counted in XPS. Here the ejection of a C 1s electron is illustrated.(After Ratner 1997)

These photoelectrons are separated according to energy and counted. The process on which XPS is based can be simply stated by the Einstein equation:

$$BE = h\nu - KE$$

Where BE is the binding energy of the electron and is directly related to the atomic number of the parent atom and its surrounding environment, hν, is the energy of the X-ray source and KE the kinetic energy of the ejected electron. In XPS, since hν is known and KE is measured, BE can be easily calculated. Since the binding energy is directly correlated to the atomic environment of the emitted electron, careful analysis of the surface chemistry can be made. As the oxidation state of the element increases, the BE of the ejected photoelectrons increases. From this technique not only can the chemical environment of the atom be identified but atomic percentages calculated since the number of photoelectrons emitted is directly correlated.

It must be noted though that XPS is a surface sensitive technique since the escape depth of the photoelectrons is very small, only up to 10 nm for data taken at a sample detector angle of almost 90°. Different thicknesses can be probed by a technique known as variable angle XPS. In this method the angle of the sample (ϑ) is changed relative to the X-ray source and detector which are kept fixed by rotating the sample. As the angle is increased, the sampling depth decreases by $\cos\vartheta$, since the direction of travel of the primary beam will become more and more parallel to the substrate itself, therefore the depth of penetration of the beam decreases. If the

specimen was rough, this would result in data being taken at different heights in the sample as the X-ray beam would be penetrating different areas at different depths depending on the angle of the surface with respect to the primary beam. (Ratner 1997) Fortunately for spin-cast samples, the surfaces are very smooth (approximately 1.0 nm as determined by AFM in Section 5.3) and surface roughness can be neglected.

For non-conducting samples such as polymers, as photoelectrons are emitted, the sample surface becomes positively charged. As a result, photoelectrons originating from a charged surface will have a smaller measured KE than those emitted from a neutral surface. From the Einstein equation this translates to a calculated binding energy that is larger than the true environment from which the photoelectron was emitted. Charging can be compensated using a negative ion gun. However, the XPS machine that was used at MIT was not equipped with a charge compensator so all binding energies were corrected by referencing the lowest energy C (1s) peak to 284.6 eV (the value for native C) and offsetting all binding energies by this shift. The shift factor depended on the chemical nature of each sample since some samples charged more than others and the factors ranged anywhere from 0.2 eV to 2.5 eV. Although these shifts could be very large, *any* material that has been exposed to air will inevitably contain native carbon contamination (in fact, this is even seen in freshly sputtered gold coatings[2]) allowing the referencing of data to 284.6 eV to be routine.(Mirley 1995, Belot 1992)

An XPS spectra, as shown in **Figure 4.11**, is comprised of counts or yield plotted as a function of binding energy. As mentioned above, the binding energy of the atom is related to the bonding environment of the atom from which the photoelectron is ejected. However, there is a full width half maximum (FWHM) associated with an XPS photoelectron peak. The main factors that contribute to the peak width in a polymer sample are the resolution of the instrument, the chemical environment of the atom and the lifetime of the core shell hole.

Instrument resolution is affected by the energy spread of the incident X-ray beam used, the resolution of the analyzer and whether or not a charge compensating gun is used. The X-ray source used at MIT was not a monochromatic source resulting in a broadening of the photoemission peak. In addition, since no charge compensating gun was used, the peak width

[2] Personal communications with Elisabeth Shaw, CMSE, MIT and Dolores Miller, IBM Almaden Research Center.

would also be broader due to the charging that occurs in non-conducting samples resulting in a wider distribution in the measured binding energies of the ejected photoelectrons.

In this study, XPS was used as a complementary technique to determine *qualitatively* whether the polymer had converted to an oxide by the various oxidation techniques. The shift in the binding energies of the elements is determined through the value of the primary binding energy and for this reason, peak widths are not critical since it is the primary binding energy of the peaks that is of interest.

The chemical composition of both P(PMDSS) before and after oxidation was examined by monitoring the binding energy of the Si2p peak closely, as it reflects the chemical environment of the silicon. From literature, it is known that the binding energy of Si in a hydrocarbon environment lies between 100.5-101.8 eV. In an environment of SiO_2, the Si2p peak is centered at 103.5 eV. (Greiner 1971) A typical XPS spectra of the P(PMDSS) after exposure to an O_2-RIE is shown in **Figure 4.11.**

Analysis was done on an XPS spectrometer at both IBM Almaden Research Center with Dolores Miller and at MIT's Center for Materials Science and Engineering (CMSE) Analytical facilities with Elisabeth Shaw. At MIT a nonmonochromatic Mg Kα source was utilized with data collected at 45°. The analysis area was approximately 1mm x 2mm and spectra were taken with a pass energy of 17.9 eV (analyzer resolution of 0.179 eV) resulting in an instrumental resolution of 0.72 eV. At IBM data were taken using a monochromatic Al Kα source. 1000 eV survey spectra were recorded at 150 eV pass energy with a 1000 μm spot size for each sample. High resolution spectra (50 eV pass energy, 20-30 eV window) were recorded for carbon, oxygen and silicon.

Variable angle XPS studies of the samples were conducted at IBM Almaden Research Center in order to estimate possible surface contamination in the O_2-RIE samples. Data were taken at two detector-to-sample angles as shown in **Figure 4.11** a)10° and b)60°. The 10° data provides information on approximately the top 15 Å of the film while the 60° data sample the top 75 Å, assuming a mean free path of about 25 Å for the ~1400 eV kinetic energy Si2p photoelectrons throughout the polymer film. This estimate also assumes a flat sample surface.

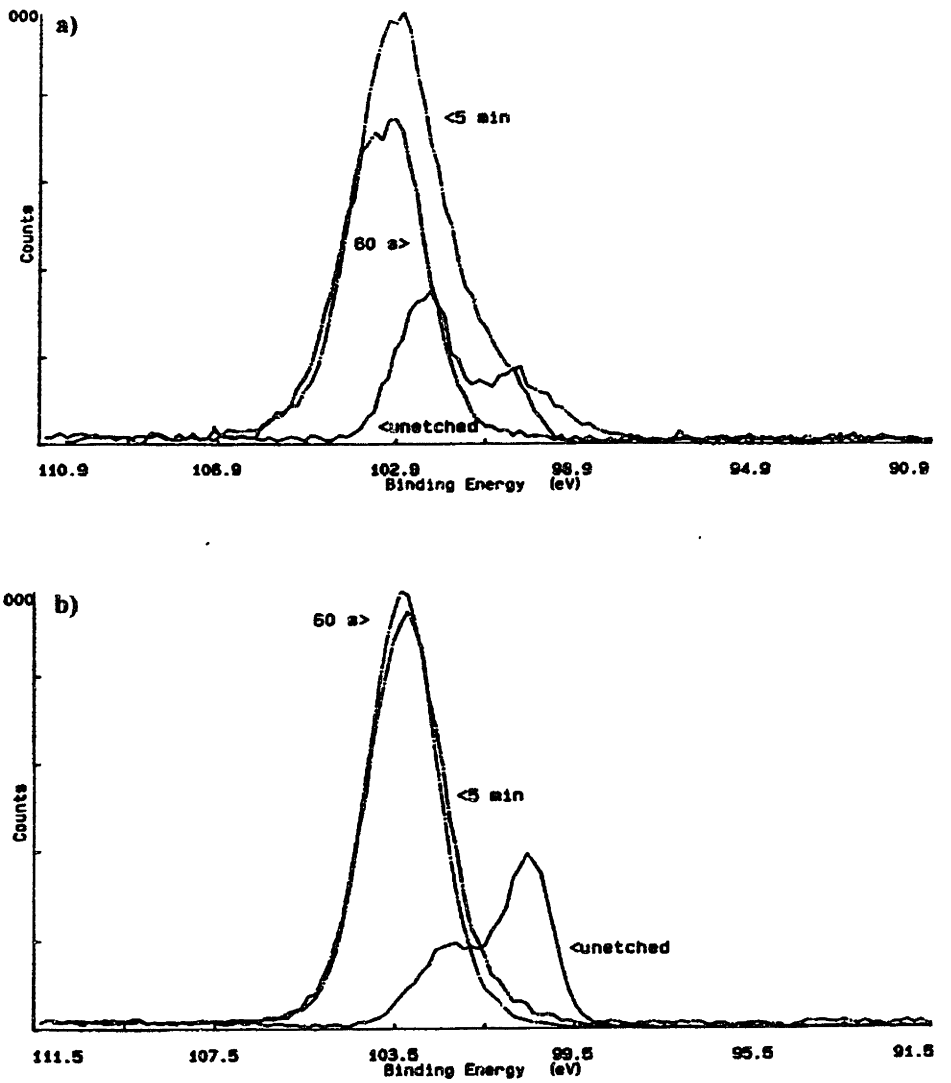

Figure 4.11: Typical XPS spectras showing yield versus binding energy. This figure shows data for as-cast (unetched) P(PMDSS) and for P(PMDSS) exposed to O_2-RIE for 60 seconds and 5 minutes respectively. The areas under the curves and peak heights are different because the peaks were not normalized to the number of sweeps that were taken per cycle. Data were taken at two different sample-to-detector angles a) 10° and b) 60° to monitor surface contamination of the as-cast material. It can be seen that a portion of the as-cast material has been oxidized but that the oxidation only occurred at the surface since the relative amount of Si2p bound at 100 eV (Si bound to hydrocarbons) versus 102 eV (Si bound to a single oxygen) is greater in the 60° than the 10° data. The oxidation of silicon containing polymers at the surface is a common phenomenon due to the greater stability of the Si-O bond as compared to the Si-Si bond.[3]

[3] Personal communication with Dr. Robert D. Miller of IBM Almaden Research Center.

4.2.6 Auger Electron Spectroscopy

Auger electron spectroscopy (AES) is a surface sensitive technique that is used to determine the elemental composition for the uppermost 20-50Å of the sample near-surface region. In AES a sample is bombarded with primary electrons with energies between 3 and 30 keV resulting in the emission of secondary Auger electrons which possess a characteristic energy depending on the element the electrons were emitted as shown in **Figure 4.12.**

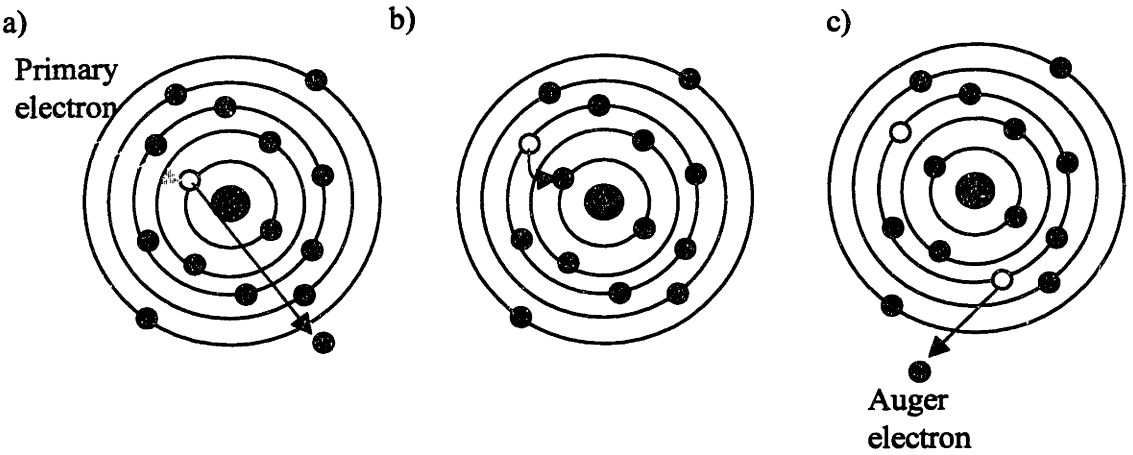

Figure 4.12: Schematic of the emission of an Auger electron. In order to produce these secondary emission electrons, interactions between three different electron levels are necessary. a) An electron is ejected from a core level state by a primary electron. It is these electrons which are detected in XPS. b) Rearrangement of the atom can take place by dropping an electron from a higher energy state to the vacancy created by photoemission. c) An Auger electron can then be ejected from the atom from a higher energy level in order to rid the atom of excess energy. (After Ratner 1997)

Auger electrons typically have low kinetic energies, 2000 eV or less resulting in a shallow escape depth so only the surface composition of the sample composition is probed. Since the emission of an Auger electron requires the transition of three electrons, chemical shifts are not as sensitive as XPS (as shown in **Section 4.2.5)** where the emitted electrons are primary emissions. For this reason, AES and XPS are complementary techniques. AES can be used to obtain depth profiles of the sample by sputtering the sample using an argon ion gun and acquiring AES data as a function of sputtering depth as shown in **Figure 4.13.**

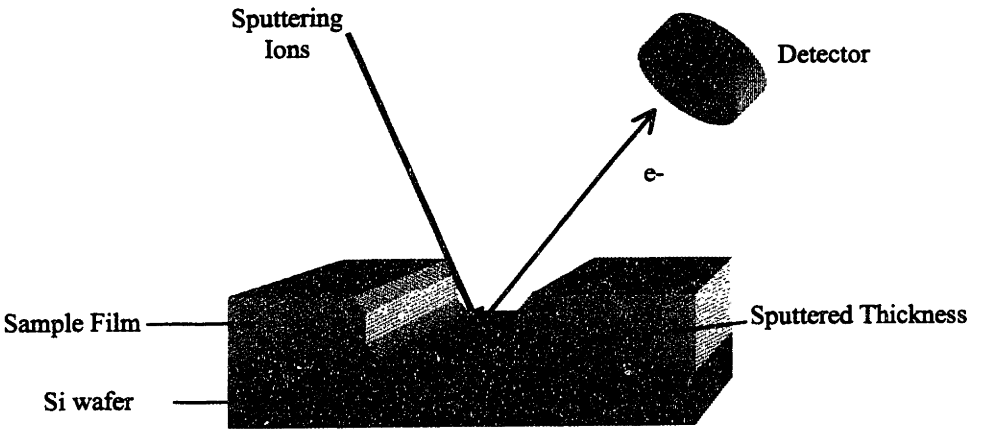

Figure 4.13: Schematic of an AES experiment with depth profiling using a sputter gun.

A typical AES spectra is shown in **Figure 4.14.** Data is given as plots of atomic concentration versus depth. Often the first two data points are ignored due to surface contamination which is extremely common. Typically this contamination is in the form of carbon but if it is humid increases in oxygen can also be evident.[4] Thus, changes in composition can be seen within the sample and in this case an approximate relative thickness of the oxide to the film thickness can be reported as a percentage. These materials are likely to be graded in composition thus an exact oxide thickness can not be given, since the sputtering rate is dependent on the material being sputtered. If the composition is changing than it is difficult to correlate sputtering time with thickness.

[4] Personal communication with Elisabeth Shaw, CMSE, MIT.

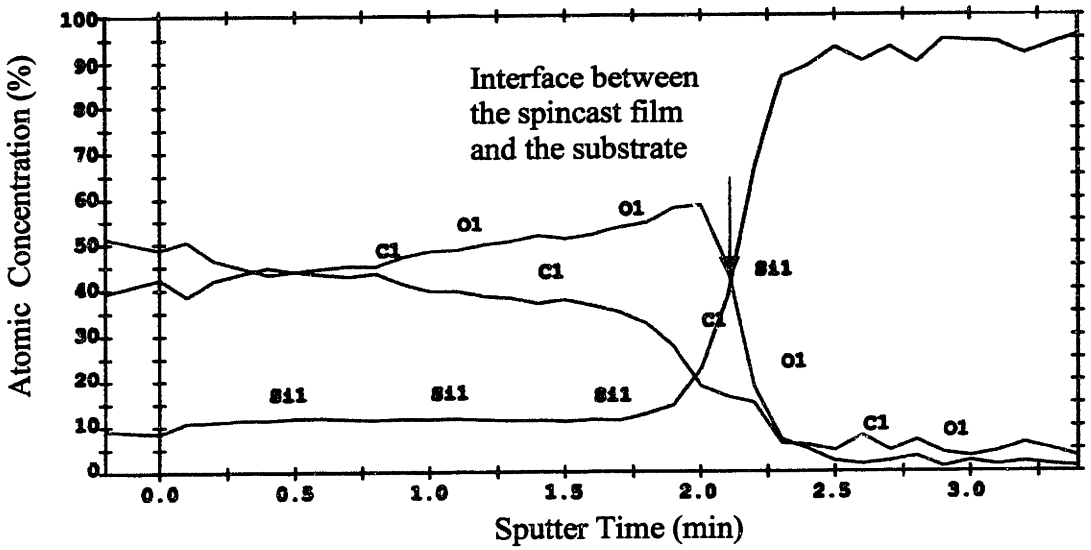

Figure 4.14: A typical AES spectra showing atomic concentration as a function of sputtering time. The sputtering rate is a function of the energy of the argon sputtering ions and the beam current. This sample is for P(PMDSS) that has been exposed to both ozone + uv for one hour. The film thickness changes from approximately 200 nm to 70 nm after oxidation. It can be seen that the oxycarbide that forms is relatively uniform throughout the depth of the film. At the arrow, the sputtering gun has reached the interface between the spincast film and the substrate.

In addition, as shown in **Figure 4.15**, plots of binding energy versus sputtering depth can also be given which illustrates changes in chemistry throughout the sample. This technique is extremely useful in the system studied here since the type of oxide that forms (continuous versus a thin film) can be determined. It must be noted that shifts in kinetic energy are difficult to quantify or compare since it is highly dependent on the angle that the sample has to the detector and only large shifts (20 eV) or more can be qualitatively evaluated between spectra.[4] Any shifts less than this may not be due to chemistry but due to artifacts. In the case of the elements that are studied in this system, the most reliable energy profile is that for silicon since significant shifts in the binding energy are evidenced when it is bound to oxygen.

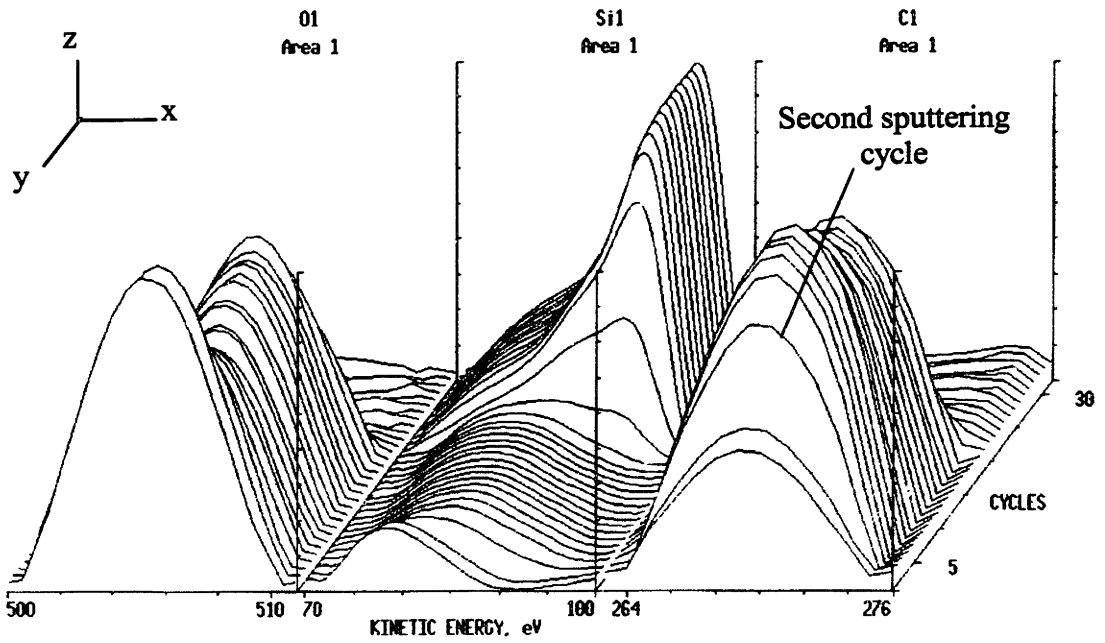

Figure 4.15: Typical composition profiles obtained by AES for P(PMDSS) exposed to ozone and uv for one hour. Data presented here is *undifferentiated.* Counts or yield is plotted on the z-axis, the kinetic energy of the Auger electrons plotted on the x-axis and the number of the sputtering cycle from which data is taken given on the y-axis. Thus, the y-axis represents a depth profile into the sample. From this 3-D plot changes in the chemistry of the sample as a function of depth can be investigated. In this case it can be seen that for the second sputtering cycle, the carbon, silicon and oxygen peaks undergo a slight shift in their kinetic energies. The relative amounts of carbon and oxygen in the film respectively increase and decrease dramatically while the relative amount of silicon stays constant.[5]

Depth profiles of the C, Si and O concentrations were obtained by Auger electron spectroscopy (AES) (Mathieu, 1997) with the help of Elisabeth Shaw at MIT in the Center for Materials Science and Engineering using a Physical Electronics 660 Scanning electron microprobe. The instrument was operated using an electron beam with 5 keV electrons and 25

[5] It must be noted that the software in the AES system automatically scales the data for the profiles to full scale so the area under the curves can not be directly compared. Thus, depending on the upper and lower values chosen for the kinetic energy window, data can be misleading since it may appear more symmetric or smoother if a smaller window is chosen around the maximum peak.

nA current. Sample sputtering for depth profiling was accomplished with a 2 keV argon ion beam using a sputtering current of 30 $\mu A/cm^2$.

4.2.7 Rutherford Backscattering Spectrometry

Bulk chemical compositions were determined by Rutherford Backscattering Spectrometry (RBS). In RBS, a primary ion beam, typically He+ with energies ranging from 100 keV to several MeV is directed onto the sample, as shown in **Figure 4.16**. When ions from the primary beam collide with atoms from the sample, various collisional and excitational processes occur. Part of the primary ions will be backscattered from the nucleus of the target atoms through elastic nuclear collisions. By measuring the energies of these backscattered ions, information on the mass of the target can be determined by modeling this interaction as a two-body collision.

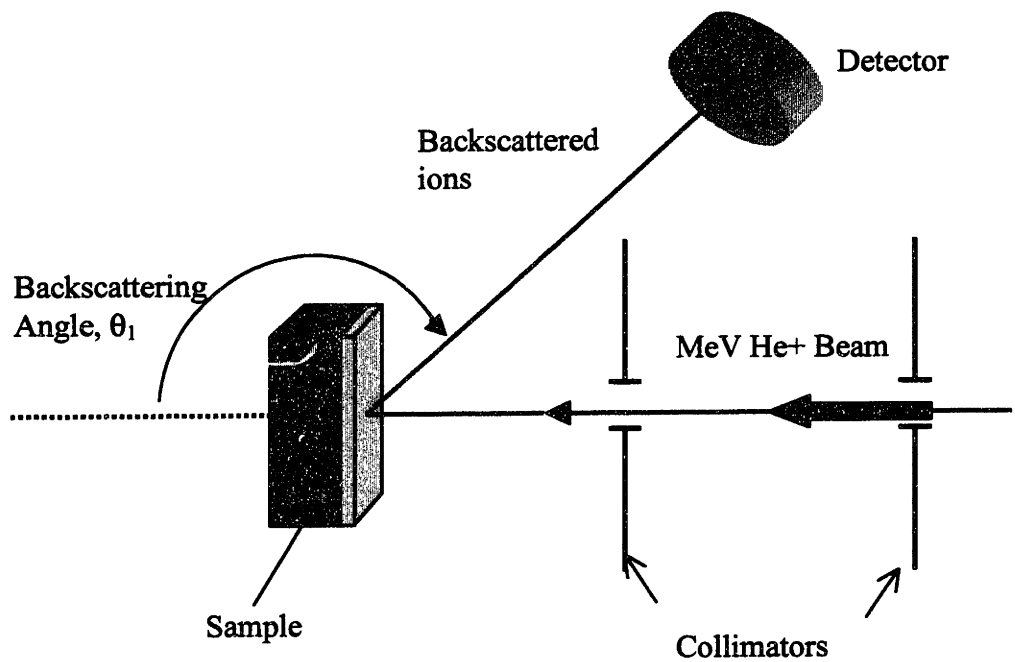

Figure 4.16: Schematic of a Rutherford Backscattering experiment

This two-body collision can be described by M_1 and M_2 where M_1 possesses an initial energy of E_0 while M_2 is at rest. If these two masses collide, they interact through a centrosymmetric potential V(r) and through conservation of energy and momentum the particle energies are calculated as a function of the scattering angle θ_1 and θ_2 through the relation:

$$K = \frac{E_1}{E_o}$$

where K, the kinematic factor is defined as :

$$K = \left(\frac{\cos\theta_1 \pm \sqrt{(A^2 - \sin^2\theta_1)}}{1+A} \right)^2$$

and depends only on the mass ratio $A=M_2/M_1$ and the scattering angle. Hence, if the scattering angle is known (which experimentally is the angle between the incident ion direction and detector), the mass from which the ion was scattered from can be determined by measuring the energy of the backscattered ion, E_1.

In RBS, the detector records the final energy of the backscattered ion. Some of the ion's original energy is lost by ineleastic collisions with electrons as the ion is entering and exiting the sample. Ions that backscatter from atoms near the surface will have a higher energy than those that backscatter from atoms deeper in the sample. This is because the deeper the target atom is from the surface, the higher the probability that the backscattered ion will undergo inelastic collisions and hence the lower the energy of ions backscattered from atoms deeper in the sample compared to those backscattered near the surface. Thus, an RBS energy spectrum, as shown in **Figure 4.17** is comprised of both two-body collision kinematics and the distribution of backscattered ions from atoms that lie in different depths throughout the sample. Data is collected using a silicon solid state detector which detects particles and their kinetic energies.

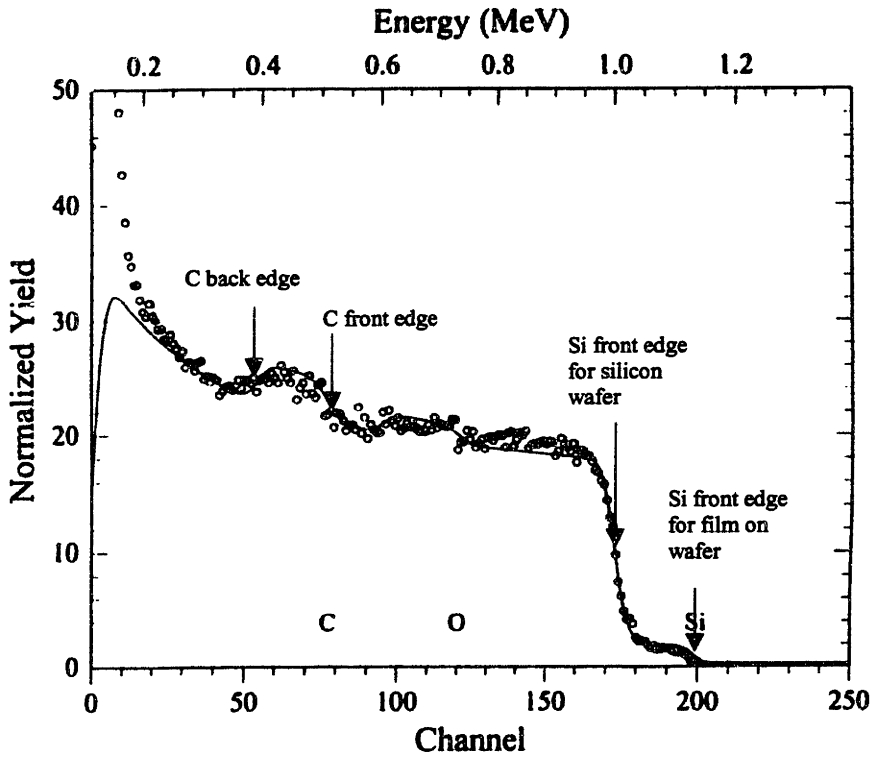

Figure 4.17 : A typical RBS spectra taken at 3.0 MeV for P(PMDSS) exposed to ozone for one hour. Counts or yield is plotted as a function of channel or energy of the backscattered ion. In this case, Si, O, and C yields from the film are present in the spectra. The edges of a peak are defined at half height.

For example, as indicated by the red arrow in **Figure 4.17** for the carbon peak, there exists a surface 'edge' which is due to backscattering of the ions from carbon atoms on the surface. At lower energies, the yield is due to ions that were backscattered from carbon atoms deeper in the sample which have undergone more inelastic collisions and hence will lose more energy than those ions that were backscattered from the surface of the sample. Thus, the carbon peak will be a distribution of scattering events from the surface to approximately 100 nm into the sample. To account for the distribution in the scattering peak due to inelastic collisions, data collected by Ziegler *et al.* on the energy loss per unit length or stopping power for interactions of various ion beams with different elements is utilized.(Ziegler 1977) Quantitatively, each atom has an energy loss factor, S [eV/(atoms/cm^2)], which is defined as :

$$S = -\frac{dE}{dx}\frac{1}{N}$$

where -dE/dx is the energy loss per unit length or the stopping power, given in eV/Å and N is the atomic density. By utilizing this stopping power, the depth distribution of the elements can be calculated and coupled with the kinematic factor, the energy spectra transformed to a mass spectra.

Similarly in the case of the silicon peak, the front edge, as seen in **Figure 4.17**, is due to scattering events from the spincoated film while the background front edge is the interface of the film with the substrate.

Rutherford Backscattering Spectrometry (RBS) was performed at the University of Pennsylvania with Professor Russell J. Composto and Howard Wang using a mini-tandem ion accelerator. Data was collected using 2.0 MeV and 3.4 MeV He++ ions and a geometry where the sample and incident ion were in the same plane and the detector 10° about the sample normal. The detector solid angle is 1.59 mstr. (Chu 1978)

After RBS measurements were recorded for each sample, a computer simulation program called RUMP (Rutherford Universal Manipulation Program or Random Utility for Making Pictures[6]) was used to determine film stoichiometries and thicknesses. The Rutherford cross-sections at the different ion beam settings produced a model of the various elements in a graph of counts versus energy. Using this information, compositional simulations were produced to form the best-fit line for each model. Within the simulations, a substrate layer with stoichiometry of Si 1 is created with an arbitrarily large areal density since the thickness of the substrate is much greater than the thickness of the spincoated film. A second layer is then generated, and its stoichiometry and thickness adjusted until the simulated data matches the collected spectra. A typical RBS spectra is shown in **Figure 4.17** with counts or normalized yield exhibited on the y-axis and channel or energy plotted on the x-axis. Using RUMP the collected data of counts versus energy is converted to stoichiometries through simulations. RUMP utilizes known Rutherford scattering cross-sections of various elements and energies to model the data of counts versus energy as explained in **Appendix C**.

Data for RBS was collected at 2.0 MeV and 3.4 MeV. This was necessary in order to optimize the differing sensitivities of the elements in the thin films. For example, the Rutherford

---

[6]http://www.genplot.com/doc/rump.htm

cross-section for carbon is more sensitive at the 3.4 MeV ion beam energy while the Rutherford cross-section for silicon is more sensitive at the 2.0 MeV ion beam energy.

4.2.8 Forward Recoil Elastic Spectrometry

Forward Recoil Elastic Spectrometry (FRES) operates on the same premise as RBS, namely an energetic ion beam is impinged on the sample and stoichiometry determined by measuring the energy and yield of scattered particles. In FRES however, the detector is placed in a forward position so that forward recoiled particles rather than backscattered ions are detected. Helium ions incident at a glancing angle cause hydrogen atoms to recoil since they are lighter and the energy associated with the recoiled hydrogen recorded by the detector. Thus, FRES is a complementary technique to RBS because it allows the measurement of hydrogen concentrations, since hydrogen is lighter than helium it cannot be backscattered and only forward recoiled.

Typically, a $^{4}He^{2+}$ beam with a 2.7 MeV particle energy is impinged on the sample 75° to the normal. In FRES, a stopper foil is also placed in front of the energy detector (in this case a 10.6 μm aluminum foil was used). This foil only allows lighter recoiled particles, namely hydrogen and deuterium to enter the detector since heavier particles such as He^{2+} are absorbed. FRES was performed at the University of Pennsylvania in collaboration with Professor Russell J. Composto and Howard Wang. A typical FRES spectra of counts versus channel or energy is shown in **Figure 4.18.**

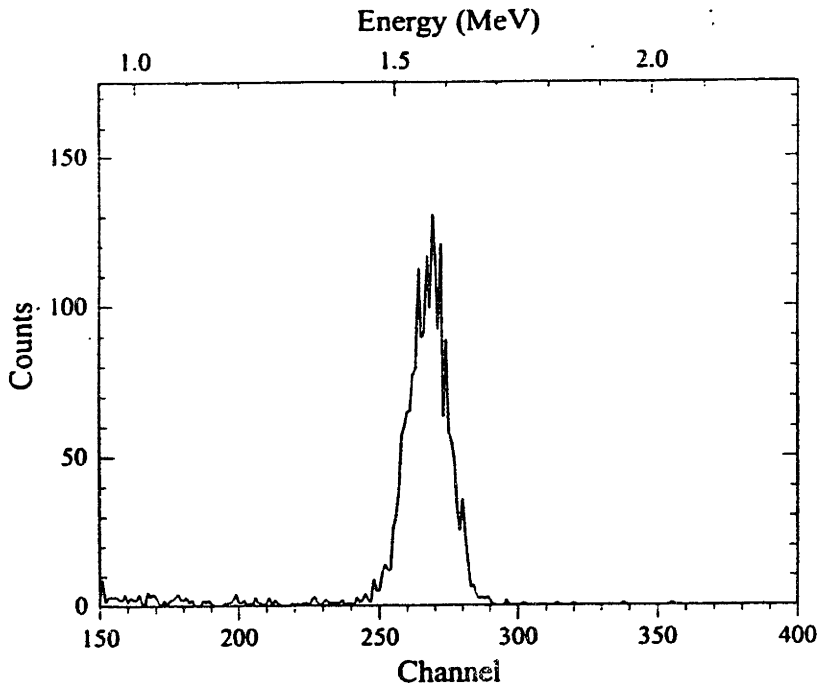

Figure 4.18: A typical FRES spectra for P(PMDSS) exposed to ozone for one hour. Data is given as counts or yield as a function of channel or energy.

The amounts of non-hydrogen elements were determined by RBS and the final stoichiometry of the samples was determined by using FRES to measure the amount of hydrogen. The total number of counts , A, is given by :

$$A = \sigma \Omega Q N t$$

where σ the Rutherford cross-section (known from tables and is a database within RUMP), Ω the solid angle , Q is the charge and Nt is the number of H atoms per cm^2 in the film.

In order to correlate the data from the FRES experiments to the RBS experiments, a polystyrene (PS) standard was used as explained in **Appendix D.**

4.3 Results and Discussion

In the formation of nanoporous or nanorelief ceramics, it is first important to understand the conversion of P(PMDSS) to a ceramic by the oxidation techniques studied in this thesis. To do this, the compositional changes of 200 nm thick films of P(PMDSS) after exposure to ozone only, uv only in air, ozone + uv and O_2-RIE were studied using various chemical analysis techniques and the results are summarized in **Tables 4.3, 4.5 and 4.6.** The spectra for the XPS Si2p, O1s and C1s peaks, AES, RBS, FRES and FTIR data are given in **Appendix E.**

Table 4.3: The binding energies in eV of as-cast and oxidized films as measured by XPS with a sample to detector angle of 45° unless otherwise specified. The percentages in bold represents the atomic percentage of that element on the surface of the film. All data was normalized by assigning the C1s peak to 284.6 eV. The number in parentheses next to the binding energy (BE) of the C1s data represents the magnitude of the shift in order to normalize the data to 284.6 eV. For the other elements, the first BE represents the normalized BE and the BE in parentheses represents the raw binding energy. In the case where there are multiple peaks the percentage next to the normalized and raw BEs represents the proportion of the peak that is constituted by atoms with that binding energy.

Peak	As-cast	Ozone	uv in air	Ozone + uv	O_2-RIE [a]
C1s	**75.6%** 285.4 (0.8)	**67.4%** 286.5 (1.9), 76.6% 286.8 (288.7), 8.6% 288.9 (290.8), 14.8%	**14.2 %** 287 (2.4)	**23.5%** 286.5 (1.9) 94.4% 289.3 (287.4) 5.6%	**19.1%** 284.8 (0.2)
O1s	**8.8%** 530.8, (531.6)	**25.6%** 533.7 (535.4), 8% 532.6 (534.3), 31.5% 531.1 (532.8), 60.5%	**62.8%** 532.8 (535.2)	**56.3%** 532.9 (534.8)	**56.5%** 532.6 (532.8)
Si2p	**15.6%** 99.5 (100.3), 55.8% 101.1 (101.9), 44.3%	**7.0 %** 100.8 (102.7), 47.5% 101.6 (103.5), 19.2% 101.8 (103.7), 33.2%	**23.0%** 103.3 (105.7)	**20.2%** 103.0 (104.9)	**24.4%** 103.4 (103.6)

[a] Experiments were performed on the XPS at IBM where a monochromatic x-ray source was used. Data reported here are for a sample-to-detector angle of 60°.
The stoichiometry of neat P(PMDSS) is Si = 24%, C = 67%, H=9%. Hydrogen concentrations can not be determined by XPS.

As described in **Section 4.2.5** XPS was used to study the chemical environment of Si, C and O before and after oxidation by determining the binding energy of these elements. Extensive

XPS studies have been done on the formation of silicon oxides from silicon containing polymers and oligomers by uv + ozone, O_2-RIE and pyrolysis although there has been no report on the oxidation of P(PMDSS) by these methods. **Table 4.5** shows the binding energies of C1s, O1s and Si2p as reported by these research groups and the chemical species that these binding energies are associated with and will be used to interpret the XPS data.

Table 4.4: Binding energies of C1s, O1s and Si2p as reported by various research groups and the associated chemical species.

C1s	Species	O1s	Species	Si2p	Species
282.8[B]	C-Si	531.6[K]	O-C	99.4[R]	Si-Si
284.2[B]	C in phenyl $C-H_X$	532.5[K]	O-Si-O	100.8[B, S]	Si-C
284.6[B, R]	C-C	533.2[K]	Si-OH	101.8[B, S] 101-102[H]	O-Si-C SiO_xC_y
285.5[S]	Si-O-C			102 [S]	SiO_2C_2
286.3[B, R]	C-O			103.5[B, K, S]	O-Si-O
286.4[B,R]	C=O			104 [S]	SiO_3C
286.3-289.3[K]	-COOH -COH			104 [H]	O-Si-O

[B] Data from (Boullion 1991) [K] Data from (Mirley 1995 and Koberstein 1997) [S] Data from (Soraru 1996) [R] Data from (Renlund, 1991) [H] Data from(Harris 1995)

Table 4.5: Characteristics of as-cast and oxidized films as determined by ellipsometry, Auger electron spectroscopy and Rutherford backscattering and forward recoil spectrometries.

Processing	As-cast	Ozone only	uv in air	Ozone + uv	O_2-RIE
Thickness (nm) [1]	220	150	55	65	200[a]
Refractive Index [1]	1.56	1.51	1.42	1.42	N/A[b]
Stoichiometry [2]	$Si_1C_8O_1H_{11}$	$Si_1C_{11}O_3H_9$	$Si_1C_{0.5}O_2H_{0.5}$	$Si_1C_1O_2H_1$	N/A[b]
Oxide Thickness [3]	N/A[c]	N/A[c]	100%	100%	10%
%C [4]	38% (63%)	46% (61%)	13% (9%)	20% (16%)	78% [5]
%Si [4]	5% (19%)	4% (12%)	25% (42%)	20% (38%)	15% [5]
%O [4]	5% (11%)	13% (23%)	50% (48%)	40% (44%)	7% [5]
%H [4]	52% (7%)	38% (4%)	13% (1%)	20% (1%)	

[1] Refractive index and thickness were calculated by ellipsometry. [2] Stoichiometry was determined using RBS and FRES. [3] The relative oxide thickness was calculated using AES. [4] These values are calculated from the changes in the stoichiometry as measured by FRES and RBS. The first number is the atomic concentration and the second number in parentheses is the weight percentages. [5] Since the O_2-RIE material is a graded material, RBS and FRES measurements were not performed. The C, Si and O atomic concentrations were determined by taking an average across the AES spectra. However, hydrogen can not be detected by AES and is thus omitted. [a] Measured by profilometry. [b] Refractive index and stoichiometry can not be reported for samples exposed to oxygen reactive ion etching since the material is graded resulting in differences in the refractive index and stoichiometry throughout the film thickness. [c] An oxide thickness is not reported for the samples which are as-cast or exposed to ozone only since the majority of the material is comprised of hydrocarbons.

Individual FTIR spectra are given in Appendix E while all the spectra are compared in **Figure 4.19.** A summary of the peaks is given in **Table 4.6.** It should be noted that for the FTIR spectra, absorptions from stretching due to water and carbon dioxide are superimposed on all the spectra. A background was taken as shown in **Figure 4.19** but due to the differences in intensities between the background and the sample spectra, background subtractions were not taken. It can be seen that the spectrum between 7.8-8.2 is difficult to interpret due to speaks from water molecules which are present in this region. Typically FTIR spectra are presented in wavenumbers but wavelengths were chosen here since the important regions were at low wavenumbers (cm^{-1}) and high wavelengths (μm) allowing the expansion of these regions when plotting the data using wavelengths rather than wavenumbers.

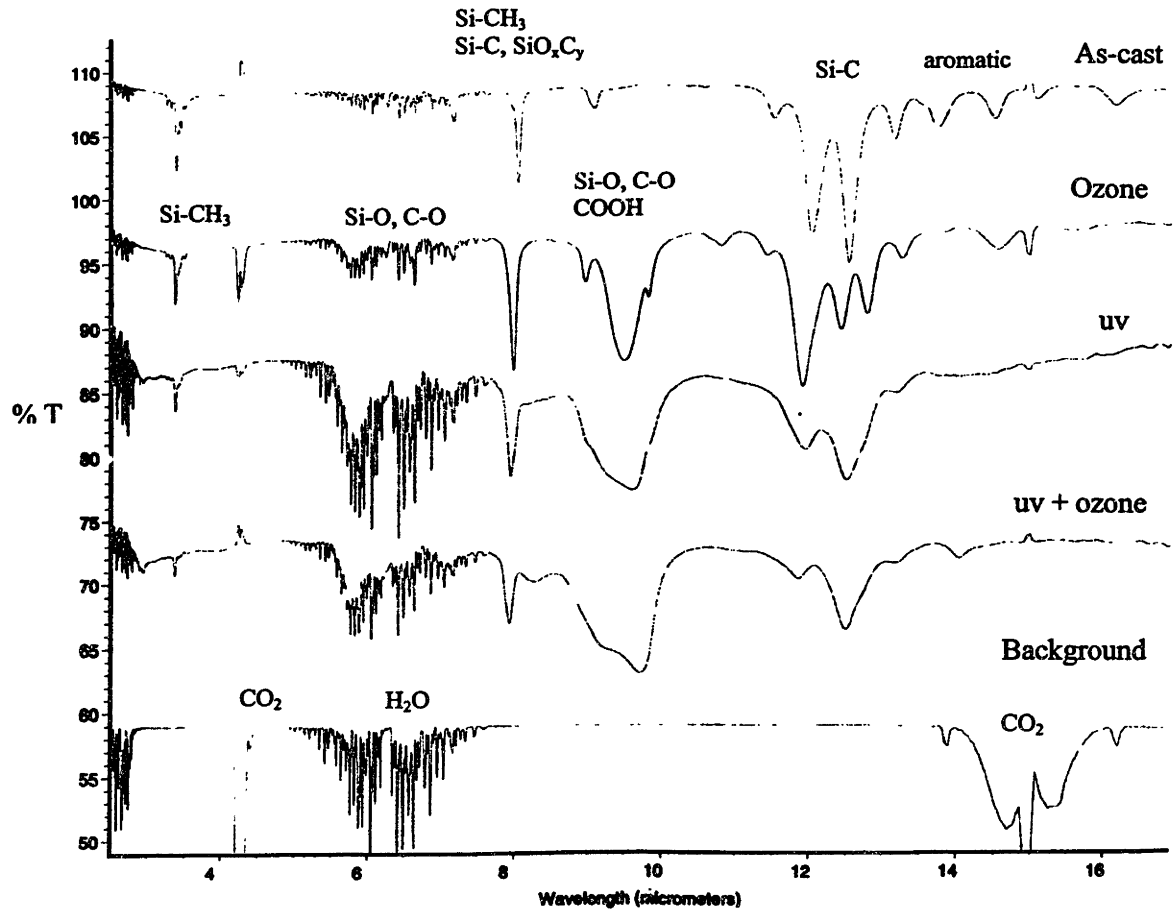

Figure 4.19: FTIR spectra for the background, and P(PMDSS) films that were as-cast, exposed to ozone for one hour, exposed to uv in air for one hour and exposed to uv + ozone for one hour. It can be seen that for the region between 5.6-8.0, sharp lines are seen due to the presence of water and stretching from the carbon dioxide peak is also present.[7] Although the sample chamber was purged with nitrogen the presence of a water peak could be due to the fact that the substrates are NaCl which are hydrophilic and therefore can absorb water.

[7] Personal communication with Dr. Carl Zimba.

Table 4.6: Stretching peaks in wavelengths, (μm) for organosilicon groups.(Belot 1992, 1994, Renlund Pt I and Pt II 1991 and Bouillon 1991) Peaks from FTIR spectra of P(PMDSS) before and after oxidation. Ranges indicate the limits of broad peaks with the numbers underneath indicating the position of the apex of the peak.

Wavelength	Group	As-cast	Ozone Treated	uv in air	Ozone and uv
2.9-3.2	Si-OH			2.7	2.9
3.2-3.3 3.4 3.4-3.6	(CH_3-Si, Aromatic) CH_3 ,CH_2 Si-O	3.4	3.4	3.4	3.4
4.5-4.7	Si-H		4.2	4.3	
5.5-6.3 6.8-7.0	C-O Si-O		5.2-7.8	5.0-7.2	5.0-7.6
7.7-7.8 7.9 8.0-11.1	CH_3-Si Si-C SiO_xC_y	7.8-8.2 8.0	7.8-8.2 8.0	7.8-8.2 7.9	7.8-8.2 7.9
8.8-9.6 9.0-9.7 10.3-10.9	Si-O-Si C-O COOH	8.9-9.1 9.0	8.5-10.5 9.0 9.4 10.6-11.3 10.8	8.2-10.5 9.6	8.8-10.7 9.2 9.7
11.4-12.5	Si-C	11.6-12.8 12.0 12.5	10.8-13.3 11.9 12.4 12.8 13.3	11.0-13.0 11.9 12.5	11.0-13.0 11.8 12.5
14.0-15.3	Aromatic CO_2 SiO_xC_y	13.0-15.0 13.2 13.8 14.5	14.0-15.0 14.5 15.0		14.0
		15.8-16.4 16.2			
17.0-20.0	Polystyrene	16.8-18.1 17.9	17.0-18.5 17.8		

4.3.1 As-Cast P(PMDSS)

Spectra for the as-cast P(PMDSS) is given in **Appendix E, Section E.3.1.** From RBS and FRES, the stoichiometry was experimentally determined to be $Si_1C_8O_1H_{11}$ which is close to the actual stoichiometry of $Si_1C_{6.5}H_{11}$. Consistent with the XPS Si2p peak shown in Figure 4.11, there is some oxygen contamination in the as-cast polymer likely due to oxidation in air since the

sample had not been directly analyzed after spincoating. The amount of oxygen is small though, less than 5 atomic percent as determined by RBS. The oxygenated species appears to be surface-localized as the relative amount of Si in this environment measured at lower detection angles (10°) is larger than that at higher detection angles (60°) **(see Section 4.2.5)**. The XPS data taken at a 45° sample-to-detector angle **(Figure E.1.1)** also indicates a small shoulder at the higher binding energies. This higher binding energy is at ~102 eV which is indicative of Si bound as O-Si-C.

For freshly spincoated polymer, XPS shows that the silicon exists mainly in a carbon-rich environment, as seen by the atomic concentration of the silicon species with a binding energy peak centered at 100 eV as seen in **Figure E.1.1** . Furthermore, elemental analysis was also carried out on the bulk homopolymer and as discussed in **Section 2.3.3** the stoichiometry is also confirmed.

By AES it can also be seen that there is significant oxygen content at the surface as noted by the O peak of **Figure E.1.3** in the first two sputtering cycles which is consistent with the XPS data of **Figure E.5.1**. The remaining kinetic energy data in **Figure E.1.3** is extremely noisy due to the little oxygen in the film. Except for the first two sputtering cycles, the chemistry of C, Si and O also appear constant throughout the sample with the C and Si showing smooth Gaussian peaks. From the depth profile of **Figure E.1.2**, the atomic concentration of C, O and Si is also constant throughout the sample and is consistent with the RBS data with oxygen given as 7% by XPS and 5% by AES. The refractive index and the thickness of the as-cast P(PMDSS) was found to be 1.56 and 220 nm respectively.

The FTIR spectra of the as-cast P(PMDSS) is shown in **Figure E.1.8**. It can be seen that there are prominent peaks at wavelengths (μm) 8.0, 12.0, 12.5, 13.2, 13.8, 14.5, 15.8-16.4 and 16.8-18.1. When compared to the groups in Table 4.7, it can be seen that these peaks correspond to stretching, bending and rocking from CH_3-Si, Si-C, phenyl and polystyrene species.

4.3.2 Ozonolysis

An overview on ozonolysis is given in Section 4.1.1 and the experimental procedures followed described in Section 4.2.2. RBS shows that there is a significant amount of C and H when the material is exposed to ozone with a final film stoichiometry of $Si_1C_{11}O_3H_9$. In fact, the relative amount of C increases with respect to Si. This decrease could be due to the volatilization

of some of the Si during ozonolysis. After processing, the hydrocarbon content is significant, representing 84 atomic percent or 65 weight percent as compared to 90% and 70% respectively for the as-cast material. The refractive index is seen to slightly decrease from 1.56 to 1.51, with the thickness decreasing from 220 nm to 150 nm. Since there is not a significant amount of oxygen in the material, an oxide thickness could not be reported.

It can be seen from the AES depth profile in **Figure E.2.4**, that the atomic concentration of C, Si and O is constant throughout the majority of the film. The amount of silicon in the film is extremely small as seen in the depth profile, corroborating the data obtained from RBS. The composition profile **(Figures E.2.3-E.2.4)** indicates that only the very top surface has a slight shift in kinetic energy of the O and C and that the majority of the film has the same chemical composition. This shift at the surface is similar to the shift seen in the as-cast P(PMDSS). The kinetic energy profile of these materials show that there is very little silicon in the film and significantly more oxygen as compared to the as-cast P(PMDSS). The carbon peak in the kinetic energy profile indicates that it is slightly skewed toward lower kinetic energy values which could be due to the formation of C-O bonds creating a more electronegative environment for the Auger electron resulting in a lower kinetic energy of the ejected electron. This is corroborated by the XPS and FTIR data which indicate different binding environments for these elements compared to the as-cast P(PMDSS).

At the surface of the film, it can be seen by XPS that there is an extremely complicated distribution in the bonding environment of the silicon atoms, resulting in a complex Si2p peak that can better be described by three peaks, as seen in **Figure E.2.1**. As summarized in **Table 4.4,** approximately half of the silicon is bound as Si-C while half is bound as O-Si-C. The O1s peak is also asymmetric and contains contributions from three different atomic species. The majority of the oxygen (60%) is bound as O-C while 30% is bound as O-Si-C and 10% bound as Si-OH. The C1s peak exhibits a bimodal peak with the majority of the carbon still bound as C-C and the remaining C existing alcoholic and carboxylic acid groups.

After exposing the P(PMDSS) to ozone, the spectra by FTIR as shown in **Figure 4.19** became much more complex compared to that of the as-cast P(PMDSS). Most notably, peaks (in μm) were seen to develop with a sharp peak at 4.2, a broad split peak between 8.5-10.5 and a symmetric peak at 10.8 appearing. These are due to Si-H, Si-O and C-O moieties respectively. It can also be seen that the relative intensity of the peaks at 8.0 and 11.85 increased while the

relative intensity of the peaks at 12.4, 13.3, 17.8 were seen to decrease. Since the film thicknesses of the oxidized and unoxidized films are different, absolute intensities can not be compared. In addition, the peaks at 13.8 and 16.2 that were present in the as-cast P(PMDSS) are now missing. This suggests that the aromatic groups are beginning to be oxidized and that with exposure to ozone, oxygen is being incorporated into the structure through the formation of C-O and Si-O bonds. However, the majority of the polymer is still intact since strong stretching is seen from the aromatic groups and polystyrene peaks. This is corroborated by the XPS data of the C1s peak which is comprised of three peaks as outlined in **Table 4.4** and the RBS data that indicates significant amounts of C and H are still present in the film.

4.3.3 UV In Air

When P(PMDSS) is exposed to uv in air, the largest amount of carbon is removed from the film as compared to the other oxidation techniques. It is likely that the exposure of oxygen molecules in the air to 254 nm uv light results in the production of oxygen reactive species which is now able to react with the polymer. From RBS and FRES, it can be seen that the majority of the C and H is removed (as seen in **Figures E.3.6 and E.3.7**) and the material has a final stoichiometry of $Si_1C_{0.5}O_2H_{0.5}$. The C and H retain a stoichiometry of 1:1 in the film but the atomic percentages of C and H decrease from 38% and 52% respectively to 13% while the atomic concentrations of Si and O increase from 5% to 25% and 50% respectively. Thus, 75% of the converted film is comprised of silicon and oxygen while 25% of the film is comprised of hydrocarbons. If this is converted to weight percentages, the changes are even more dramatic with the amount of C and H decreasing from 63% and 7% to 9% and 1% respectively after conversion. In addition, the O and Si weight percentages increase from 11% and 19% to 48% and 42% respectively. Thus, after exposure to uv in air, the P(PMDSS) which originally contained 70% hydrocarbons by weight now contains less than 10% hydrocarbons and the other 90% is comprised of inorganic silicon and oxygen.

Ellipsometry shows that the thickness of the film drops dramatically and the refractive index of the material decreases from that of the P(PMDSS) homopolymer, 1.56, to 1.42. Coincidentally, this is the refractive index of SiO_2 although the oxidized material contains 25 atomic percent C. The FTIR resembles that of silicon oxycarbide as discussed below but unfortunately, no refractive index has been reported for this material.

By FTIR, (Figure **E.3.8**) it can be seen that after exposing P(PMDSS) to uv in air, a significant amount of the C is removed. The regions of stretching due to aromatic groups (14.0-15.3) and polystyrene (17.0-20.0) which were present in the as-cast and ozone exposed P(PMDSS) are no longer present. The spectra indicates the strong presence and development of the following groups: C-O and Si-O (5.2-7.8), Si-C and some $Si-CH_3$ (7.8-8.2), Si-O, C-O, COOH, (8.2-10.5) and Si-C (11.0-13.0). The amount of $Si-CH_3$ is extremely small since the peak at 3.3 is not very intense. Thus, it is likely that the intense peak at 8.0 is due to Si-C or SiO_xC_y since the corresponding $Si-CH_3$ asymmetric stretch at 3.3 is so weak.

When compared to P(PMDSS) that has been exposed to ozone it can be seen that the peaks between 8.2-10.5 and 11.0-13.0 have significantly broadened and in the case of the peak between 8.2-10.5, it is no longer a split peak . The peak centered at 8.0 coupled with the peak between 11.0-13.0 indicates the formation of Si-C bonds and the fact that the peak is split indicates that the silicon is likely to bound to at least 2 carbon atoms.(Renlund Pt II, 1991) This suggests that the residual carbon in the film is due to the formation of a complex Si-C-O material and is not due to the crosslinking of aromatic groups or polystyrene since the stretching from these moieties is not present. If this spectra is compared to those obtained by Harris (1995) and Belot (1992) it can be seen that these two major peaks are also present in their spectra and are indicative of silicon oxycarbide.

From the XPS peak, it can be seen that the Si2p, C1s and O1s peaks are all symmetric which further suggests that upon oxidation by uv in air, the P(PMDSS) forms a uniform and complex silicon oxycarbide.

The AES depth profile **E.3.2** demonstrates that there is a significant amount of oxygen throughout the film, with the final O, C and Si atomic concentration percentages leveling to 55%, 35% and 15% respectively. At the surface of the film, the relative amounts of these three elements are different than in the bulk with surface percentages of O, C and Si of approximately 75%, 15% and 10%. The amount of C increases and the amount of O decreases dramatically for the first two sputter cycles, while the amount of silicon remains relatively constant. From the kinetic energy data, (Figures **E.3.3 and E.3.4**) it can be seen that the chemistry of the O, C and Si changes slightly after the second sputtering cycle but remains constant throughout the rest of the thickness. As mentioned in **Section 4.2.6**, this could be due to surface contamination from adsorbed water on the surface due to high humidity.

The carbon peak appears to be more complex than that of the as-cast P(PMDSS) as seen by the asymmetric shape of the carbon peak for the P(PMDSS) exposed to uv. However, it must be noted that the carbon peak has a higher signal to noise ratio than the silicon and oxygen peaks as evidenced by the background in the latter sputtering cycles for the carbon peak resulting in a peak that is not as smooth as the other peaks. The oxygen and Si peaks appear to have relatively uniform chemistries throughout the film thickness.

When compared to the as-cast P(PMDSS), it can be seen that the kinetic energy peaks for silicon and carbon are centered at a lower energy for the P(PMDSS) exposed to uv. This is likely due to the formation of silicon oxycarbide species through uv exposure. When some of the silicon-carbon bonds are replaced with silicon-oxygen bonds or carbon-oxygen bonds, the electrons in the silicon and carbon are in a more electronegative environment. As a result, the ejected Auger electron will have a lower kinetic energy since it is more tightly bound to its parent atom. This leads to a shift in the peak to a lower kinetic energy value.

Unlike the sample exposed to ozone only, the Si2p XPS peak is symmetrical, with the binding energy indicating that the silicon is bound as O-Si-O. This is corroborated from the O1s peak which shows that the oxygen that is present is also bound as O-Si-O. In the case of the C1s peak it also is symmetric although an extremely small second peak which is barely distinguishable from the background noise can be seen at 289.4 eV which is the binding energy for –COOH and –COH moieties. However, it must be noted that XPS is a surface sensitive technique and as shown by the AES data, the composition further into the film is not the same as at the surface.

4.3.4 Ozonolysis and uv

When the material is exposed to ozone and uv as compared to uv in air, the amount of active oxygen species that the sample is exposed to is greater. The P(PMDSS) retains twice the amount of hydrogen and carbon than when exposed to uv in air resulting in a final stoichiometry of $Si_1C_1O_2H_1$. Once again, the C:H ratio is 1:1. The amount of hydrocarbons in the film has decreased significantly after exposure to ozone and uv with the amount of carbon decreasing from 38 atomic percent and 63 weight percent to 13 atomic percent and 9 weight percent. Similarly, the amount of hydrogen decreases from 52 atomic percent and 7 weight percent to 20 atomic percent and 1 weight percent.

The Si2p XPS peak of the ozone + uv exposed P(PMDSS) **(E.4.1)** is also much more symmetric than in the case of the P(PMDSS) exposed to ozone only **E.2.1.** The binding energy of both the O1s and Si2p data suggest that these two atomic species are once again bound as O-Si-O. The C1s peak indicates a bimodal distribution in the C species with 94% bound as C-C and 6% bound as –COOH or –COH. When compared to the ozone data with a trimodal peak, the C1s peak indicates the presence of more homogenous species. Once again, it must be noted though that XPS provides information only on the surface of the sample and for this reason AES is used to compliment this data.

AES shows that chemically, the silicon concentration is constant throughout the film thickness, **(Figure E.4.2).** In the case of the carbon and oxygen, the composition does change slightly with film thickness but for both these atomic species there are significant amounts all the way through the film. The amount of carbon decreases approximately 15% in the bottom half of the film, while the amount of oxygen increases 15%. However, it would be expected that the changes in the oxygen and carbon concentrations would be significantly greater than 15% throughout the film thickness since the ozone must diffuse into the film. It is possible that the uv radiation crosslinked the hydrocarbons in the top half of the film more than the hydrocarbons in the bottom half of the film. Thus, the hydrocarbons in the bottom half of the film could be oxidized more efficiently by the ozone which would result in a decrease in the amount of carbon in the latter half of the film.

It can be seen in the kinetic energy profile in Figure E.4.5, that there is significantly more oxygen as compared to the as-cast P(PMDSS). One important difference though in these peaks is the shift in the silicon and carbon kinetic energy peaks to lower values for material that has been exposed to uv and ozone as compared to the as-cast P(PMDSS). The reason for this is given in Section 4.3.3 where a similar shift was seen for P(PMDSS) exposed to uv in air.

When the kinetic energy profiles are compared between the P(PMDSS) exposed to uv in air and exposed to ozone + uv, the shapes of the oxygen, carbon and silicon peaks are very similar after the first two sputtering cycles.

FTIR (Figure D.4.7) shows that the aromatic groups (14.0-15.3) and polystyrene (17.0-20.0) are not completely present as in the case of P(PMDSS); a small peak at a wavelength of 14.0 (μm) is evident which is likely due to carbon dioxide if compared to the background spectra. It is possible that in the presence of ozone, the carbon groups are not as completely removed

because the ozone when it attacks the hydrocarbons results in the formation of a crosslinked network. In the case with uv in air, there are less reactive oxygen species so the system is material limited, therefore any oxidized hydrocarbons will be more easily removed since fewer bridges can be formed. The presence of hydrocarbons would appear to conflict the kinetic energy profile data which suggests a uniform material throughout the film but due to the weakness in these peaks relative to other peaks, these aromatic groups may not have been detectable by AES.

A peak with a shoulder at higher wavelengths is seen between 8.8-10.7 and there is a significant increase in the stretching is between 5.0-7.6, both of which are due to the presence of Si-O, C-O, COOH groups. Si-C moieties also exist as seen by the stretching between 11.0-13.0. When compared to the FTIR spectra of the P(PMDSS) exposed to uv in air, it can be seen that the peaks for the uv and ozone exposed sample are more asymmetric , the stretching between 10.3-10.9 (COOH groups) is more intense that there is some residual aromatic groups present. In addition, the split in the peak between 11.0-13.0 is less pronounced with the peak at the lower wavelengths have a much lower relative intensity as compared to the peak at the higher wavelengths. This corroborates the smooth peaks seen in the AES kinetic data.

Ellipsometry showed that the refractive index of the film decreased to 1.42 and that the film thickness also decreased significantly to 65 nm.

4.3.5 Oxygen Reactive Ion Etching

An overview of the O_2-RIE process is given in **Section 4.1.2.** Once the films are exposed to O_2-RIE, the amount of carbon at the surface decreases significantly as expected since carbon in the polymer is readily removed by the oxygen plasma as explained in **Section 4.1.2.** The most obvious change in the silicon XPS spectra **(Figure E.5.1)** upon etching is the shift in the Si2p binding energy from 100.5/101.8 to 103.5 eV, indicating that the silicon near the surface of the film is converted to SiO_2 for a take off angle of 60°.

The AES data obtained for P(PMDSS) etched for 60 seconds at 0°C are consistent with the XPS results. Depth profiling (argon ion sputtering) reveals that the ratio of silicon to oxygen decreases from that of SiO_2 to the elemental distribution of the as-cast polymer, as shown in **Table 4.6.**

The AES data obtained for P(PMDSS) etched for 60 s at 0°C are also consistent with the XPS results. Depth profiling (argon ion sputtering), reveals that the oxygen-to-silicon ratio

decreases from its highest value of approximately 2 at the surface to nearly zero for the as-cast P(PMDSS) homopolymer (**Figure E.5.2**) with the oxide thickness constituting only 10% of the film thickness. Since the material formed from O_2-RIE is graded (i.e. the oxide is <10 nm thick and the composition changes) RBS, FRES and ellipsometry measurements were not taken since these measurements assume a film with uniform composition. FTIR data also was not taken since it is likely that the film will have stretches similar to that seen in the as-cast P(PMDSS) since the oxide thickness is only 10% of the film. In addition, since the goal of this thesis is to study the formation of nanoporous and nanorelief ceramics from a 3D structure, reactive ion etching would not be the ideal oxidation technique due to the directionality of plasmas as discussed in **Section 4.1.2.** Thus it is unlikely that reactive ion etching would be useful for the goals set out in this thesis and for this reason high temperature studies of the reactive ion etched materials were not investigated.

4.3.5.1 Oxygen Reactive Ion Etching of Hydrocarbons

For O_2-RIE, it is also important to calculate the etch rates of PI relative to P(PMDSS) in order to determine the etch selectivity of the block copolymer. The O_2-RIE etch rates of films of the PS and P(PMDSS) homopolymers in the Magnetron (for the conditions of 10 mTorr, an oxygen flow rate of 40 sccm, a top radio frequency (rf) generator power of 250 W and a bottom rf generator power of 50 W) were approximately 800 nm/min and 15 nm/min respectively, resulting in an etch selectivity of approximately 50 : 1. Etch rates were measured by measuring thicknesses before and after etching. It should be noted that etch times longer than sixty seconds could not be carried out because the PS would be completely removed by the oxygen plasma. PS rather than PI was used for the homopolymer etching studies because of the low glass transition temperature of PI, which would prevent the use of profilometry for the calculation of etch rates. Crosslinking of the PI using an electron beam could also have been used but since this was not available, polystyrene was used instead. Since the oxygen plasma reacts with the carbon atoms, the etch rate of PS and PI will be on the same order of magnitude. In fact, Taylor and Wolf (1980) have shown that the etching rate of crosslinked PI relative to PS is approximately 5 : 1. This difference in the etch rates between PI and PS is due to the fact that the presence of the aromatic group in the PS stabilizes the polymer against etching. The etch selectivity between uncrosslinked PI and PS should even be higher than 5:1 because of the high reactivity of

unsaturated bonds in the polymer backbone. Thus, the etch selectivity of the P(PMDSS):PI should be far greater than 50:1 and we can estimate it to be 250:1 given the results of the study by Wolf & Taylor.[50] It should be noted though, that this relative rate is calculated using different etching conditions and on a different reactor than used in our studies and as discussed in **Section 4.1.2** etching conditions vary widely across the parameter space of reactive ion etching.

For the Plasmatherm, a reactive ion etching machine without any magnetic field enhancement, the etch rates of P(PMDSS) and PS were calculated to be 7 nm/min and 165 nm/min respectively, resulting in an etch selectivity of 1:24. If we apply the same data from Wolf & Taylor, this would translate to an etch selectivity of at least 1:100. This etch selectivity is considered to be extremely high as discussed in **Section 6.1.3** where reported etch selectivities in other block copolymer systems were reported to be between 1:2 and 1:42.

4.3.6 High Temperature Stability

One of the primary applications for the materials developed in this thesis would be as low dielectric constant layers in interconnects. In order to be used for these applications, it is necessary that the converted material is stable to 400°C in a nitrogen atmosphere due to a post-fabrication anneal. For this reason, the stability of these converted materials was studied under these conditions.

To investigate this, 200 nm thick spincoated samples of P(PMDSS) homopolymer was oxidized and the resulting material was heated to different temperatures in a nitrogen atmosphere and held at each temperature for one hour with a ramp rate of 20°C per minute. The refractive index and film thickness was subsequently determined by ellipsometry as shown in **Figures 4.20 and 4.21** and the chemistry of the material also investigated by AES for the stable materials. The refractive indices of the P(PMDSS) after processing by ozonolysis, ozonolysis + uv, oxygen reactive ion etching are given in **Table 4.6.**

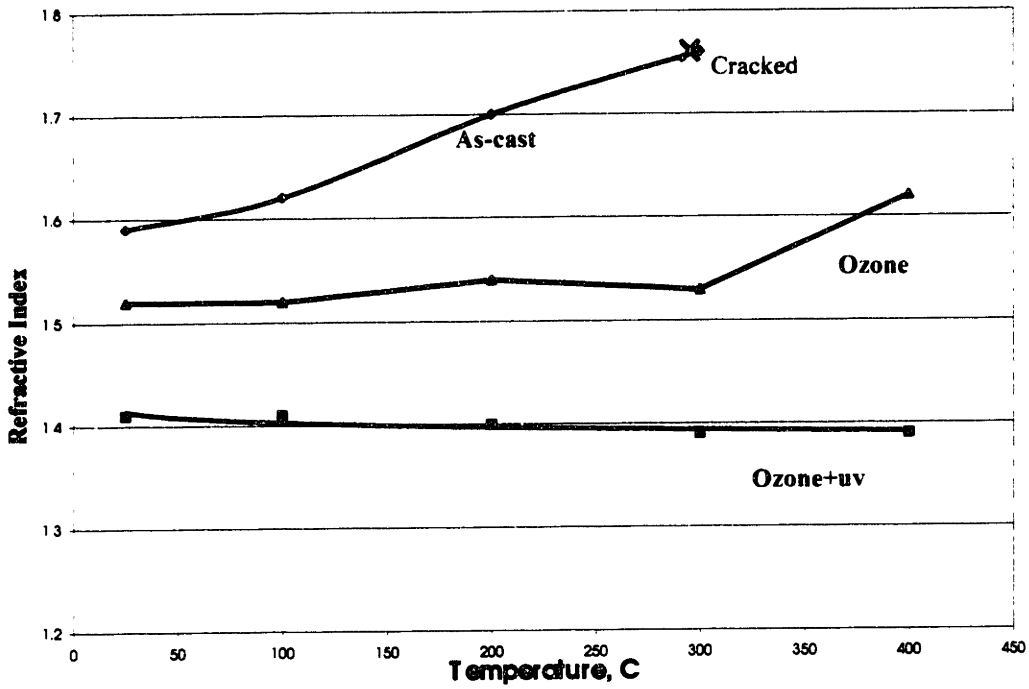

Figure 4.20 : Plots of refractive index vs. annealing temperature for as-cast P(PMDSS), P(PMDSS) exposed to ozone for one hour and P(PMDSS) exposed to ozone and uv for one hour.

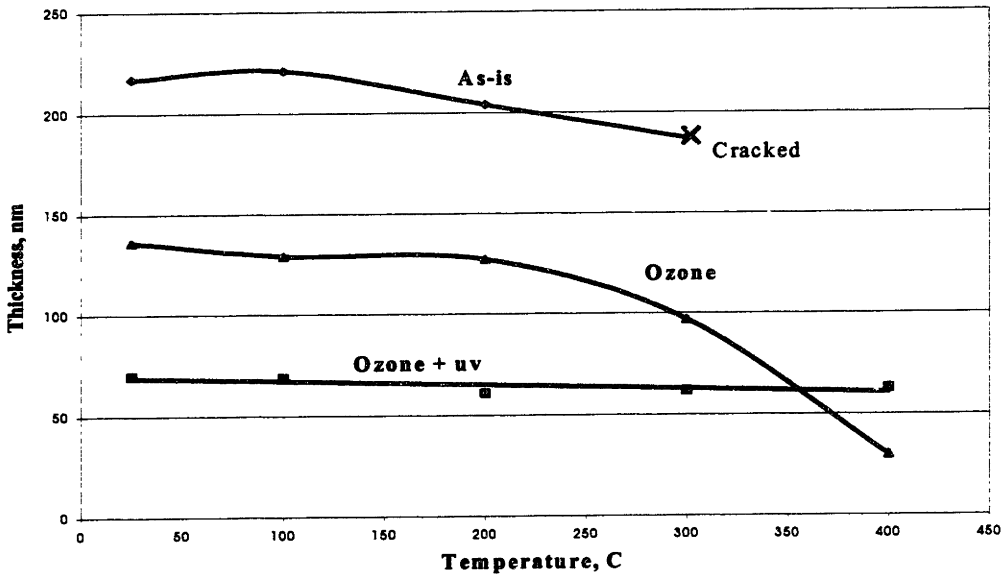

Figure 4.21 : Plots of thickness vs. annealing temperature for as-cast P(PMDSS), P(PMDSS) exposed to ozone for one hour and P(PMDSS) exposed to ozone and uv for one hour.

Figures 4.20-4.21 show that when P(PMDSS) has been exposed to ozonolysis + uv resulted in an oxide film the refractive index and thickness do not change very significantly after annealing to 400°C for 1 hour in nitrogen. A very small but steady decrease is seen in both the refractive index and the thickness. In contrast, the P(PMDSS) which has only been exposed to ozone remains stable to approximately 300°C after which the material's refractive index increases dramatically and the thickness decreases significantly. For P(PMDSS) that was exposed to uv only, the refractive index also was 1.42 and the thickness of the film was 55 nm as outlined in Table 4.5. After annealing to 400°C, these values also did not change significantly.

For as-cast P(PMDSS) homopolymer, the refractive index also increases upon heating and at 300°C the film cracks and degrades resulting in a non-uniform and mottled surface. The uneven surface prevented the measurement of refractive index or thickness since measured values varied greatly depending on where the measurement was taken.

AES studies were done on the P(PMDSS) exposed to uv + ozone and uv in air after annealing to 400°C for one hour in nitrogen since these two materials' refractive index and thickness did not change significantly after heat treatment. In order to determine whether or not annealing changed the chemistry of the film, chemical analysis was performed.

Figure E.6.1 shows the atomic concentration profile and **Figure E.6.2** the kinetic energy profiles for P(PMDSS) after exposure to ozone + uv and annealed to 400°C for one hour in nitrogen. The signal to noise ratio of the carbon peak is much greater than that for the unannealed film as seen in the background signal at higher sputtering cycles. Despite this, it can be seen that the profiles before (**Figures E.4.4 and E.4.5**) and after annealing are almost identical. In fact, it takes the same amount of time to sputter to the interface in both cases (approximately 2.2 minutes) and the shapes of the kinetic energy profiles are also identical (allowing for the high signal to noise ratio in the carbon peak for the annealed sample.)

Similarly, if the profiles for P(PMDSS) exposed to uv in air are compared before (**Figures E.3.4-E.3.5**) and after annealing (**Figures E.7.1-E.7.2**) the spectra are also seen to be almost identical. In this case though the sputtering times are different because for the unannealed sample which was exposed to uv in air, a different sputtering current density was used (30 $\mu A/cm^2$) versus (15 $\mu A/cm^2$) and as a result less time is taken to reach the interface.

4.3.7 Discussion

Four oxidation techniques were studied here : ozonolysis, uv in air, ozone + uv and O_2-RIE. In the case of ozonolysis-only processing, a complete oxidation to an oxycarbide is not observed and there are substantial amounts of residual carbon in the film which remains unoxidized. Although Si-O-C bonds form as evidenced by the FTIR, networks do not appear to form and as a result, when the material is annealed, high temperature stability is not observed.

It was found that in the case of P(PMDSS) exposed to O_2-RIE, a thin film of SiO_2 formed on the surface and the underlying polymer was not oxidized. This could be attributed to the dense oxide that forms through O_2-RIE which protects the underlying P(PMDSS) from oxidation. Etch selectivities of 1:50 were determined between the P(PMDSS) and PS. From Taylor & Wolf, (1980) the etch selectivity between PS and PI is shown to be approximately 1:5 so this would result in P(PMDSS) and PI in having an etch selectivity of 1:250. Such an etch selectivity is significantly better than those determined by Gabor *et al.* (1994) of 1:42 and by Park *et al.* (1997) of 1:2 as discussed in **Section 6.1.3.**

When P(PMDSS) is exposed either to uv only in air or to ozonolysis coupled with uv, we observe the formation of a complex silicon oxycarbide network. Significant amounts of carbon are removed in both cases, resulting in the formation of a denser and thinner material as observed by ellipsometry.

By RBS and FRES, it was documented that there is a significant reduction in the amount of carbon and hydrogen in the film after treatment with ozone + uv or with uv in air. The resulting films had 17 wt% and 10 wt% hydrocarbons respectively after processing as compared to the as-cast film which contains 70 wt% hydrocarbons. The carbon content is similar to the types of materials made through high temperature pyrolysis, which typically contain 12-23% carbon as discussed in **Section 4.1.3.** The amounts of hydrogen were never reported since techniques were used which were not sensitive to hydrogen concentrations.

In the other treatments of ozonolysis only, uv only, uv + ozone, it can be seen by AES that the chemical composition remains relatively constant throughout the thickness of the film with the formation of a continuous oxide in the cases where the material is exposed to uv. However, this is contrary to what was seen by Koberstein *et al.*(Mirley 1995 and Koberstein 1997) where only 15 Å thick silicon oxide layers were formed from silicon containing oligomers after exposure to ozone + uv as discussed in **Section 4.1.1.** One reason for this difference could

be the fact that Koberstein *et al.* used oligomers of polydimethylsiloxane (PDMS) while we used a polymer of P(PMDSS). The molecular weight (M_n) of their oligomers was 2100 g/mol as compared to our molecular weight (M_n) of 34,000 g/mol. PDMS also contains oxygen in the backbone, has less carbon than our material and does not contain any aromatic groups. As a result, the chemistry of our two material systems is very different and it could be expected that the two materials would result in different materials upon ozone and uv exposure. It is possible that in their case, since there is less carbon in the starting precursor, the oxide that forms is too dense to allow the diffusion of oxygen reactive species into the underlying film thereby limiting the thickness of the oxide layer. In our system it was found that a much thicker, 60 nm thick silicon oxycarbide material could be formed by ozone + uv or uv in air exposure.

When our materials are compared to those formed by high temperature pyrolysis, it can be said that the formation of an oxidized material from ozonolysis coupled with uv, uv only in air, or O_2-RIE, results in a final material with fewer chemical species at the surface. This is evident in the symmetrically shaped Si2p peaks with narrow full width half max profiles as compared to the peaks obtained by the researchers mentioned in **Table 4.5.** (Renlund Pt II 1991, Bouillon 1991, , Harris 1995, Soraru 1996, Koberstein 1997).

Soraru *et al.* (1996) observed the formation of a wide distribution of oxidized Si-O-C species independent of the pyrolysis temperature while Renlund *et al.* (1991) and Boullion *et al.* (1991) also both had significant amounts of residual carbon in their films which at extremely high temperatures. In most cases, the materials would first form silicon oxycarbide (usually at temperatures between 600-800°C) and at higher temperatures (T > 900°C), would rearrange to free graphite and SiC.

AES was also used to determine the chemical profile in our films since XPS measures only the bonding at the surface. Only one other research group, Harris *et al.*(1995) studied their materials by AES and only derivative peak height data was presented. Unfortunately we can not compare our atomic concentration data to their derivative peak heights since derivative peak height data does not normalize to the number of sweeps that are taken for an element, as discussed in **Section 4.1.3.**

By comparing FTIR data taken by these research groups we were able to conclude that through a room temperature oxidation process (e.g. uv in air or uv + ozone) we were able to form

silicon oxycarbide with some residual methyl groups. This is indicated by the broad peaks seen at 8.5-10.5 and 11.0-13.0 (μm) wavelengths which is indicative of silicon oxycarbide.

The high temperature stability of P(PMDSS) exposed to ozone + uv and uv in air was studied up to 400°C in a nitrogen atmosphere. By ellipsometry, it was found that the refractive index and thickness did not change significantly and by AES the chemical profiles were nearly identical. By contrast, the film exposed to ozone had significant changes in both the thickness and the refractive index and the as-cast material cracked and degraded.

4.4 Conclusions

We show using XPS, AES, RBS, FRES, FTIR and ellipsometry that it is possible to form a ceramic material using a room temperature one-step oxidation route. This ceramic is considerably more stable to temperatures up to 400°C (the temperature needed for this material to be used in low dielectric constant applications) in a nitrogen atmosphere. Using uv exposure or uv coupled with ozone, P(PMDSS) was converted to silicon oxycarbide as evidenced by the symmetric XPS peaks, FTIR spectra and AES depth profiles. This route could be a possible alternative to pyrolysis in the formation of inorganic ceramics which could have utility as high temperature ceramic coatings. However, exposure to ozonolysis alone does not result in the formation of an oxide and the resulting material is not stable to higher temperatures. Thus the low temperature ozone + uv process produced an inorganic oxycarbide with thermal stability properties far superior to the parent homopolymer.

It was also found that when P(PMDSS) is exposed to O_2-RIE, a surface oxide forms which prevents the underlying material from being oxidized. In addition, it was shown that in our system and for our processing conditions, etch selectivities greater than 100:1 should be realizeable allowing the formation of high aspect ratio structures.

Chapter Five
Oxidation of Silicon Containing Polymers By Oxygen Plasmas : A Morphology Study

5.1 Introduction

Thin films of silicon-containing polymers were studied to investigate changes in surface composition and morphology on exposure to an oxygen plasma. Three different chemical structures were studied, poly(pentamethyldisilylstyrene) (P(PMDSS)), poly(phenylmethylsilane) P(PMS) and poly(p-trimethylsilylphenylmethylsilane) P(PTMSPMS). For low molecular weight poly(pentamethyldisilylstyrene) (P(PMDSS)), a reticulated structure was observed by atomic force microscopy (AFM) that could limit future lithographic applications of these materials. The reticulations were of approximately 1 μm in width and 5 μm in length, though polymer with 3 times the molecular weight resulted in 25% smaller feature sizes. In polysilane polymers, P(PMS) and P(PTMSPMS) containing silicon in the backbone and molecular weights significantly larger than the entanglement molecular weight, the feature dimensions were even smaller. Films etched at lower temperature (0°C) displayed none of the reticulated morphology, retaining instead the smooth appearance of pre-etched films. It was found by X-ray photoelectron spectroscopy (XPS) and Auger electron spectroscopy (AES) that a thin (< 10 nm) layer of SiO_X is formed on the surface of all polymer films irrespective of composition and etching temperature, as shown in **Chapter 4**. Appearance of the reticulated morphology required the combined presence of heating by the plasma (i.e. no temperature regulation), the oxygen plasma, and the presence of silicon in the polymer. The reticulated structures are believed to result from the destabilization of the thin films as they undergo the transition from a nonpolar organosilane to a polar oxide.

5.1.1 Oxygen RIE of Silicon Containing Polymers: Temperature Effects

As outlined in **Section 4.1.2**, there has been extensive work in the development of new photoresists from silicon containing polymers due to their formation of a protective silicon oxide barrier upon exposure to an oxygen plasma. In addition to the study of oxide growth mechanisms, researchers have also examined the effects of substrate temperature on the etching of silicon-containing resists. Durandet *et al.* (1990) have shown in certain cases, due to ion

bombardment, that the substrate can reach temperatures of above 200°C if there is not near-perfect thermal contact between the substrate and substrate holder since essentially only radiative thermal losses occur. In non-silicon-containing novolac resins, Joubert *et al.* (1991) explored resist degradation in both oxygen and argon plasmas and showed that substrate cooling prevents degradation of the resist throughout the bulk by preventing self-diffusion of polymer chains which otherwise would renew the surface with fresh chains . However, it should be noted that the molecular weights of the polymers used in this study were extremely low (1000-2000 g/mol), leading to accelerated diffusion. Joubert *et. al* (1992) have also investigated O_2-RIE processes in silicon-containing resists, and found that an increase in the substrate temperature to ~100°C results in a liquefaction of the top surface areas. This resulted in redistribution of the silicon throughout the bulk resist due to diffusion of the silylated chains, thereby preventing the formation of a contiguous solid etch resistant mask. Various investigators have also found that wafer temperature strongly influences the etch rate of resists and depending on the thickness of the film the etch rate can either increase or decrease the etch rate. In some cases, cooling the substrate results in a higher etch rate. (Bobbio, 1989 and Gokan ,1997) This was attributed to either the decrease in reactivity between Si and reactive oxygen species or the decrease in the mobility of the Si during RIE. However, it should be noted that all these experiments were performed on relatively thick (0.5 - 1 μm) resist layers. With thin (< 0.5 μm) films the opposite effect is noted: cooling reduces the amount of material removed before an effective oxide barrier layer is formed. (Dijikstra, 1991) It has also been shown in low-Tg novolacs that with higher substrate temperature, the etch rate increases in a step-like manner due to higher mobility of the polymer system.(Dijikstra, 1991 and Paniez 1991)

The following discussion reports the formation of an unusual reticulated surface morphology observed by AFM in three silicon-containing polymers on exposure to an oxygen plasma at ambient plasma temperatures. The percent silicon in these polymers varies from 23 to 29% with the silicon situated in either the backbone or in a pendant group, or both (see **Figure 5.2**). Surface roughening of organosilicon polymers during etching has been reported by others. However, no extensive AFM studies have been reported with structures similar to the ones in this discussion, perhaps due to differences in polymer structures, reactive ion etch tools, and varying etching parameters such as gas pressure, oxygen flow rate, etching times, magnetic enhancement and RF power.

Our observations are relevant for the high-resolution etching of photoresists where side wall and edge uniformity are important for accurate pattern transfer. To meet the demanding lithographic requirements for future devices with very small features, it is necessary to minimize sources of surface and pattern roughening in pattern-transfer lithography.

5.1.2 Atomic Force Microscopy of Polymers

The atomic force microscope (AFM) which was developed in 1986 by Binnig *et al.*, has become a successful commercial tool for the study of microstructures of materials, including polymers. The success of this tool for imaging polymers can be attributed to the fact that it is far less damaging (Stimm 1992) than more traditional techniques such as scanning electron microscopy (SEM) and transmission electron microscopy (TEM), since AFM samples do not need to be dried for preparation, coated, exposed to vacuum, microtomed, stained or irradiated with high energy charged particles which can dramatically affect polymer microstructure by crosslinking and scission.

In polymer physics the understanding structure-property relations requires examination over a wide range of size scales; from the monomeric repeat unit, to the polymer chain, to the microphase separated structure in the case of block copolymers, to the micron scale where fibrils, spherulites, cracks, domains in blends, defects and crystallites can exist. AFM is a very useful tool because it can be used to study the hierarchy of ordering within polymers since imaging is possible at length scales ranging from angstroms to hundreds of microns while maintaining a resolution in the z-direction of < 0.1 nm. It is the combination of the nondestructiveness of this technique with its ability to image over a wide range of length scales that makes AFM an extremely useful tool for the study of polymers. (Goh, 1995)

The fundamental AFM imaging mode operates on a very basic premise. A probe tip (typically made out of silicon or silicon nitride coated with gold) is mounted onto a cantilever. The tip is lowered to the surface of the sample and the interaction of the tip with the sample causes a deflection of the cantilever in the z-direction that is measured by a laser that reflects off the cantilever surface. This optical signal is modulated by the cantilever movement and the modulation is measured by a photodetector. The sample is mounted onto a piezoelectric scanner which allows raster scanning in the X and Y directions, so topographical maps of the surface can be made, as shown schematically in **Figure 5.1.**.

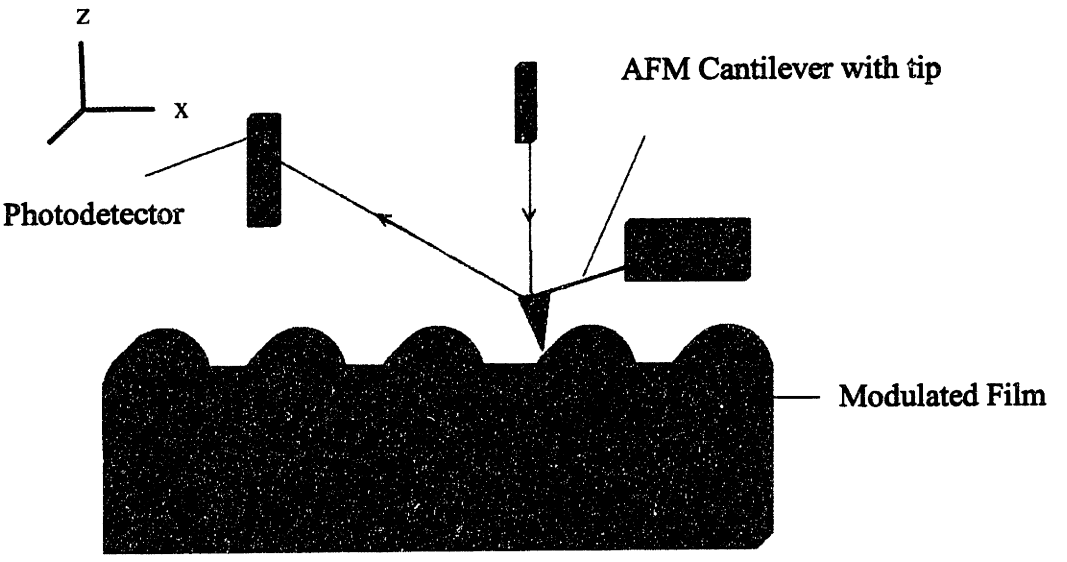

Figure 5.1: Schematic of an AFM experiment.

Since the force between the sample surface and the tip can be monitored in different ways, it is possible to utilize different imaging modes in AFM. The mode that is utilized depends on the type of sample being imaged. Imaging can be performed under contact, noncontact or tapping modes. In the contact mode, the tip is in continuous direct contact with the sample, thereby exerting a vertical and a lateral force on the surface. For soft polymers, this is not advisable since the tip can cause the surface to undergo deformation. In noncontact mode, the tip is oscillated at approximately 100 kHz. Since polymers are "soft" materials, the tapping mode is normally employed. In tapping mode, the cantilever is oscillated at a certain frequency and only van der Waals interactions between the tip and the sample surface are felt. In force modulation microscopy (FMM), an additional sinusoidal modulation with an amplitude of ~20 nm, is applied to either the cantilever position (Pethica, 1987) or to the sample position (Maivald, 1991) while scanning the tip across the sample surface. This applied modulation translates to a modulation of the applied contact force and as a result of the cantilever deflection that is detected by the photodiode. This average deflection is then fed back to the input signal thereby maintaining a constant average applied force. The sample surface is mapped by measuring the rms amplitude at each (x, y) point. Thus, image contrast is achieved through the mapping of the elasticity differences which is based on the mechanical properties of each block.

This force modulation technique will be extremely useful in characterizing block

copolymers with dissimilar elastic moduli at room temperature; for example, poly(styrene)-poly(diene) block copolymers. This modulus difference corresponds to the glass transition temperatures (T_g) of the relative blocks. For high molecular weight poly(styrene), the T_g is about 100°C and for poly(butadiene), about -100°C. (Brandup, 1989) Thus, poly(styrene) will have an elastic modulus which 10 times higher than poly(butadiene) at room temperature and this difference can provide excellent contrast in the FMM.(Chen, 1996) However, FMM can only be applied to flat surfaces. Once one of the block copolymer phases has been removed, image contrast will be from topography and not elastic moduli differences.

As reported by Dietz *et al.*, (1992) AFM can be used to image porous materials such as the surfaces of UF (ultrafiltration) membranes. Line profiles can be taken from the surface scans and from these pore diameters determined. Similar studies have also been done by Fritzsche *et al.* (1992) on poly(vinylidene fluoride) microfiltration membranes, polyethersulfone UF membranes, (Fritzsche,1992) and poly(acrylonitrile) UF membranes.(Fritzsche, 1993) In fact, AFM is superior to both SEM and TEM in the characterization of the skin surface layer of membranes since it does not entail extensive sample preparation and has lateral resolution of 0.1-0.2 nm and depth resolution of <0.1 nm. Furthermore, AFM can be performed with a fluid present, which is a widely-used technique to minimize surface adhesion of AFM tips to samples.

5.2 Experimental

5.2.1 Polymer Synthesis

Three different polymers were studied in this chapter but the principal polymer employed in this thesis poly(pentamethyldisilylstyrene) P(PMDSS). In this chapter, the focus is on the P(PMDSS) that was synthesized by "living" free radical polymerization, as discussed in **Section 2.3**. This polymer is designated P(PMDSS)-11 and was synthesized by myself at IBM Almaden Research Center in 1996. The polymer structure is shown in **Figure 5.2** and its properties are tabulated in **Table 5.1**. The polymer was prepared by free radical initiation in the presence of nitroxides. (Hawker, 1996) The polymerization was performed at 125°C without solvent under an argon atmosphere for approximately 24 hours. The polymer was then precipitated in methanol and was not further fractionated.

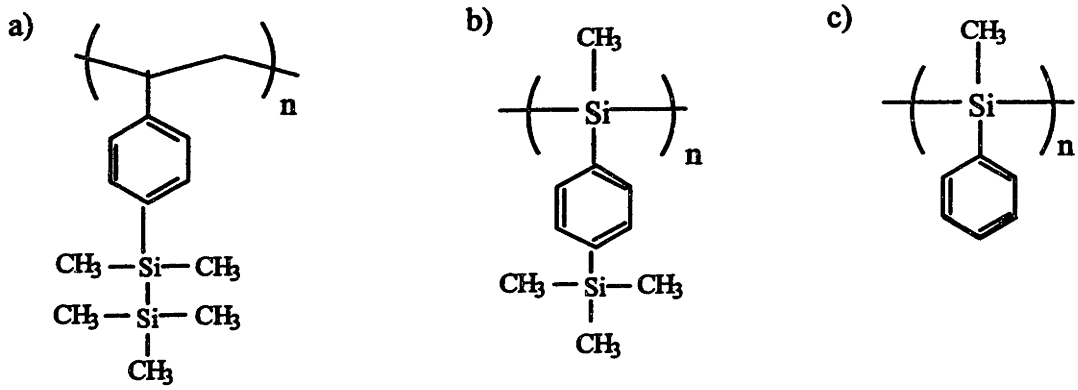

Figure 5.2: Chemical structures of poly(pentamethyldisilylstyrene) P(PMDSS), poly(p-trimethylsilylphenylmethylsilane) PTMSPMS, and poly(phenylmethylsilane) PPMS.

P(PMDSS) was also prepared by anionic polymerization, by Dr. Apostolos Avgeropoulos in the University of Athens, and is designated P(PMDSS)34, as discussed in **Section 2.4**, and the resulting material compared to that prepared by living free radical (LFR) techniques. The ^{1}H NMR, ^{13}C NMR, ^{29}Si NMR and Fourier Transform Infrared Spectroscopy (FTIR) spectra of the free radical and anionically prepared P(PMDSS) samples were identical as shown in **Section 2.4.** However, the material produced by anionic polymerization had a higher molecular weight and a lower polydispersity than that synthesized by LFR. The elemental analysis of P(PMDSS)34 was consistent with the proposed structure as shown in **Section 2.3.4.**

For comparison, two other silicon-containing polymers with very different structures were also investigated, and their polymer properties are reported in **Table 5.1.** Poly(*p*-trimethylsilylphenylmethylsilane), PTMSPMS and poly(phenylmethylsilane), PPMS were both prepared via Wurtz-coupling polymerization by Bob Miller. (Miller, 1989) Their chemical structures are also shown in **Figure 5.2.**

Table 5.1: Characterization of silicon-containing polymers used in this chapter: molecular weight, polydispersity and glass transition temperature (Tg).

Sample	Molecular Weight, Mn	Polydispersity	Tg,°C
Poly(pentamethyldisilylstyrene) (PMDSS)			
Anionic P(PMDSS)34	34,000	1.06	107
Living Free Radical P(PMDSS)11	10,800	1.83	80
Poly(p-trimethylsilylphenyl-methylsilane) PTMSPMS	223,000	2.6	120
Poly(phenylmethylsilane) PPMS	262,000	3.2	117

5.2.2 Sample Preparation

Solutions of P(PMDSS)11 and P(PMDSS)34 were prepared in toluene (5 wt%). The other silane polymer solutions were adjusted to lower concentrations in xylene (1.5% - 3% by weight) due to the much high molecular weight of the samples. Polymer films were made by spincoating onto 1" (100) silicon wafers with a native oxide. The silicon substrates were cleaned with toluene prior to spinning and the polymer solution was deposited onto the Si wafers using a syringe tipped with a 0.45 μm filter. Films were prepared by spinning first at 500 rpm for 15 seconds and then at 2000 rpm for 40 seconds. All film samples were baked in a vacuum oven at 70 °C for at least 12 hours to remove any residual solvent. Final film thicknesses for all samples were measured with a mechanical profilometer and found to range between 200 and 300 nm. As a control, 800 nm thick films of polystyrene were also spincoated to determine relative etch rates.

5.2.3 Reactive Ion Etching

The etching experiments were carried out in a low pressure, magnetically enhanced, inductively coupled, plasma etcher. Etching was performed with a base pressure of 10 mTorr and an oxygen flow rate of 40 sccm. The top radio frequency (rf) generator was set at 250 W and the bottom rf generator at 50 W. Etching was performed at either ambient plasma temperature or by cooling the substrate to 0°C. The wafer temperature was estimated by placing liquid crystal temperature dots on a silicon wafer, covering them with Kapton tape to protect the chamber from etching products, and exposing them to the same etching conditions as used for the polymers for 60s. Polymer etching times were 10s, 20s, 30s, 60s or 5 minutes. Using these temperature dots,

it was estimated that the *minimum* sample temperature was 70°C in the ambient plasma; the actual temperature could be much higher. (Maivald, 1991)

For samples etched at 0°C, the backside of the wafers was first coated with In-Ga in order to improve the thermal contact of the samples to the cold chuck. The sample chuck sits above a reservoir of liquid nitrogen above which a stream of helium passes which conducts heat away from the wafer backside. The temperature of the system is regulated by a thermocouple sitting on the sample chuck that is equipped with a feedback loop to a resistive heater. The wafers were backside cooled by the helium gas and the temperature was allowed to equilibrate for 15 minutes before etching. Since the polymer samples are thin films and the silicon substrate is a relatively good heat conductor, the temperature difference between the chuck and the sample should be minimal.

5.2.4 Atomic Force Microscopy

The atomic force microscopy images were collected using a Digital Nanoscope III at MIT or a Digital Nanoscope 2000 at IBM Almaden Research Center employing optical deflection detection. Standard silicon cantilevers were used for tapping mode. Data were acquired on frames ranging from 250 nm x 250 nm to 50 μm x 50 μm having 1024 x 1024 data points. Images were recorded using both height and phase-shift channels. AFM measurements yielded surface feature dimensions and the root mean square (RMS) surface roughness. (Digital Instruments Manual, 1996) RMS results were compared between images of equal scan size (50 μm x 50 μm) to minimize scan size dependencies.

5.3 Results

All of the as-deposited polymers studied were determined by AFM to be smooth before etching, with a RMS roughness of ~ 0.7 nm. As a control for the profilometry and AFM experiments, a 70 nm thick polystyrene (PS) film was spun onto a silicon wafer and etched under the same ambient plasma conditions as the silicon-containing polymers. After short etching times (< 60s) AFM indicated there was no roughening of the surface. After 60 s, the PS film was removed entirely, corresponding to an etch rate of at least 80 nm/min, as discussed in **Section 4.3.5.**

As a control for determining the effect of heating on the polymers, samples of as-

deposited P(PMDSS)11 were heated to 120°C for 1 hour in either nitrogen or air. No significant surface roughening was observed by AFM: RMS surface roughness of both unetched films and unetched heated films was 0.7 nm.

Figure 5.3 shows the evolution of morphology with etch time in the lower molecular weight P(PMDSS)11. At short etch times, **(Figure 5.3a)**, the origin of the reticulated surface morphology is more obviously seen as an alignment of neighboring hemispherical structures that grow in height with an increase in etch time **(Figure 5.3b)**. This vertical growth is manifested as an increase in RMS roughness with etch time **(Table 5.2)**.

Table 5.2: RMS Roughness (nm) of P(PMDSS)11 for different etch times.

Etch Time (seconds)	RMS Roughness (nm)
0	0.7
10	15
30	26
60	37

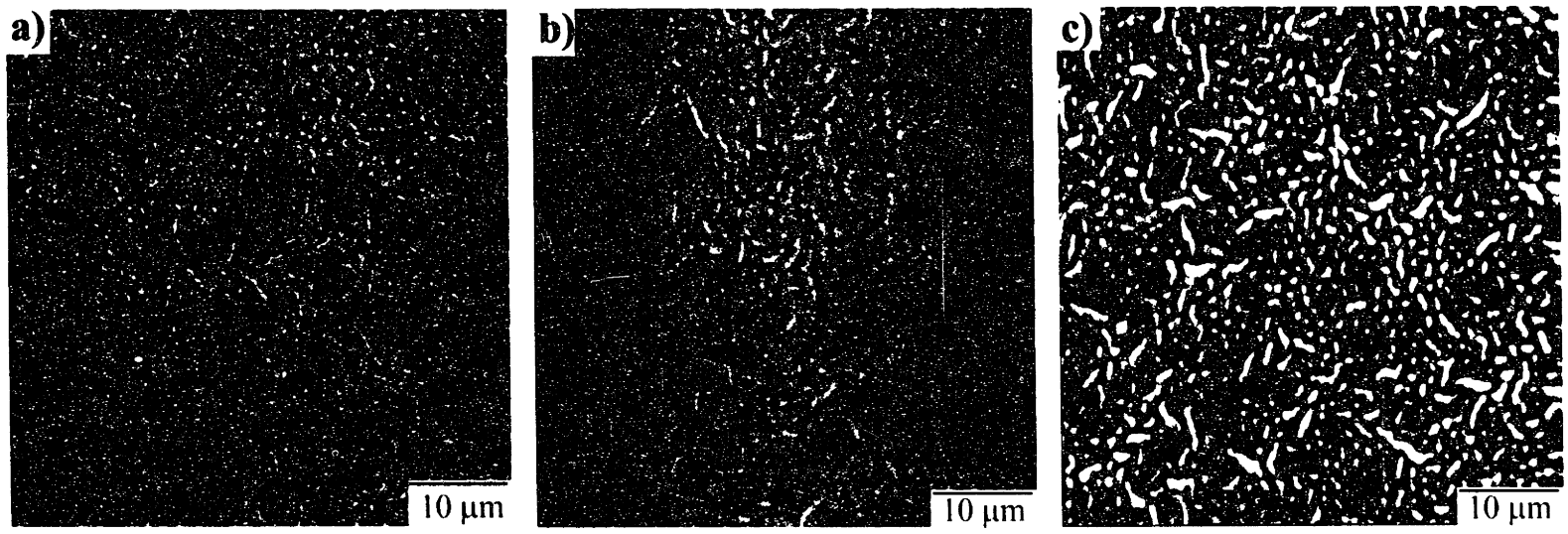

Figure 5.3: AFM images taken in height mode for P(PMDSS)11 after exposing to O_2-RIE for a) 10 seconds b) 30 seconds c) 60 seconds. The roughness increases with etch time as seen in Table 5.2. Maximum height is 100 nm.

As seen from **Figure 5.4**, a substructure *within* the reticulated morphology is composed of particles 0.05-0.25 μm in diameter. The higher molecular weight P(PMDSS)34, also develops a morphology after etching for 60s at ambient plasma temperature **(Figure 5.5a)**. However, instead of the formation of elongated structures as in the case for P(PMDSS)34, this sample produces only small spherical features of approximately 0.5 μm in diameter. The RMS roughness is similar to that of the earlier stages of etched P(PMDSS)11, when the small hemispherical structures were most prominent **(Table 5.2)**. This difference in morphology between P(PMDSS)11 and P(PMDSS)34 is attributed to differences in sample molecular weight. The molecular weight of P(PMDSS)34 is three times that of P(PMDSS)11, and hence the polymer chains are expected to be much less mobile during reactive ion etching. The polydispersity is lower for P(PMDSS)34, another possible contributing factor to the size difference in the surface morphology.

The molecular weights of both P(PMDSS) samples are probably below the entanglement molecular weight. The entanglement molecular weight for P(PMDSS) can be crudely estimated to be ~68,000 simply on the basis of the ratio of the molecular weights of the PMDSS monomer and styrene monomer and assuming the entanglement molecular weight of polystyrene is 36,000 g/mole. The monomer molecular weights of PMDSS and styrene are 234 and 104 respectively. However, over half of the PMDSS molecular weight results from the silicon containing side group, so its contribution to polymer entanglement is minimal. As an approximation of entanglement molecular weight, it was assumed that the same number of monomer units are needed to entangle P(PMDSS) as PS.

Since the molecular weights of P(PMDSS)11 and P(PMDSS)34 are both believed to be lower than the estimated entanglement molecular weight, alternative silicon-containing polymers with higher molecular weights **(Table 5.1)** were also studied. Poly(p-trimethylsilylphenylmethylsilane) PTMSPMS and poly(phenylmethylsilane) PPMS were etched at ambient plasma temperature for 60 s. As seen from **Figure 5.5b,c**, the striking reticulated morphology is not immediately apparent to the eye. However, as seen from the higher magnification inserts of 1 μm scans, the reticulated morphology *does* develop in these samples, albeit at smaller dimensions than in polymer P(PMDSS)11 : ~0.4 μm in diameter and 1 μm in length for polymers PTMSPMS and PPMS compared to ~1μm in diameter and 5 μm in length for P(PMDSS)11.

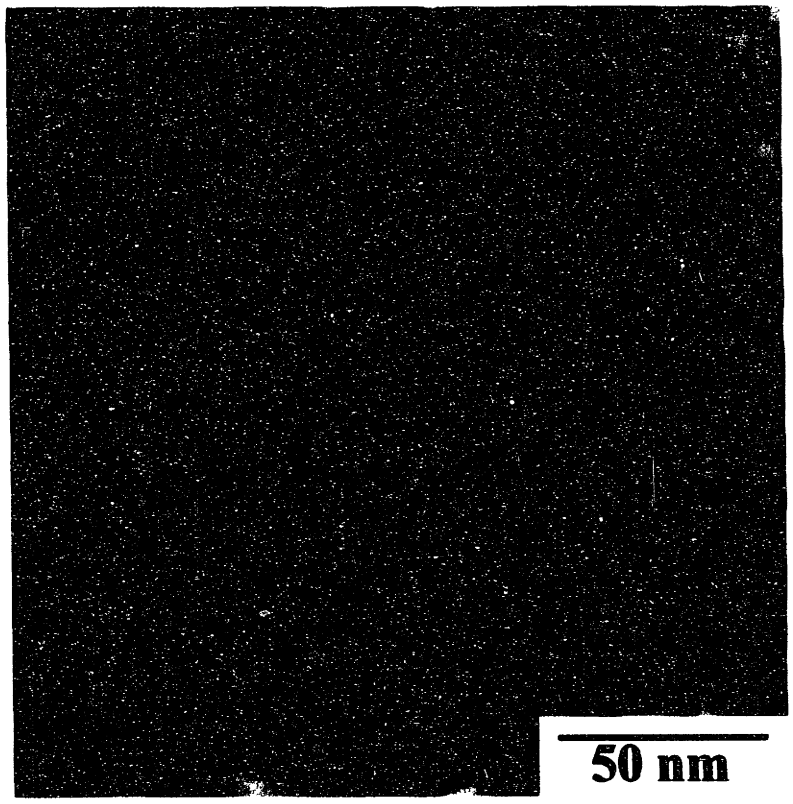

Figure 5.4 : AFM image of the substructure *within* the reticulated morphology. It can be seen to be comprised of particles 0.05-0.25 μm in diameter. Maximum height is 20 nm.

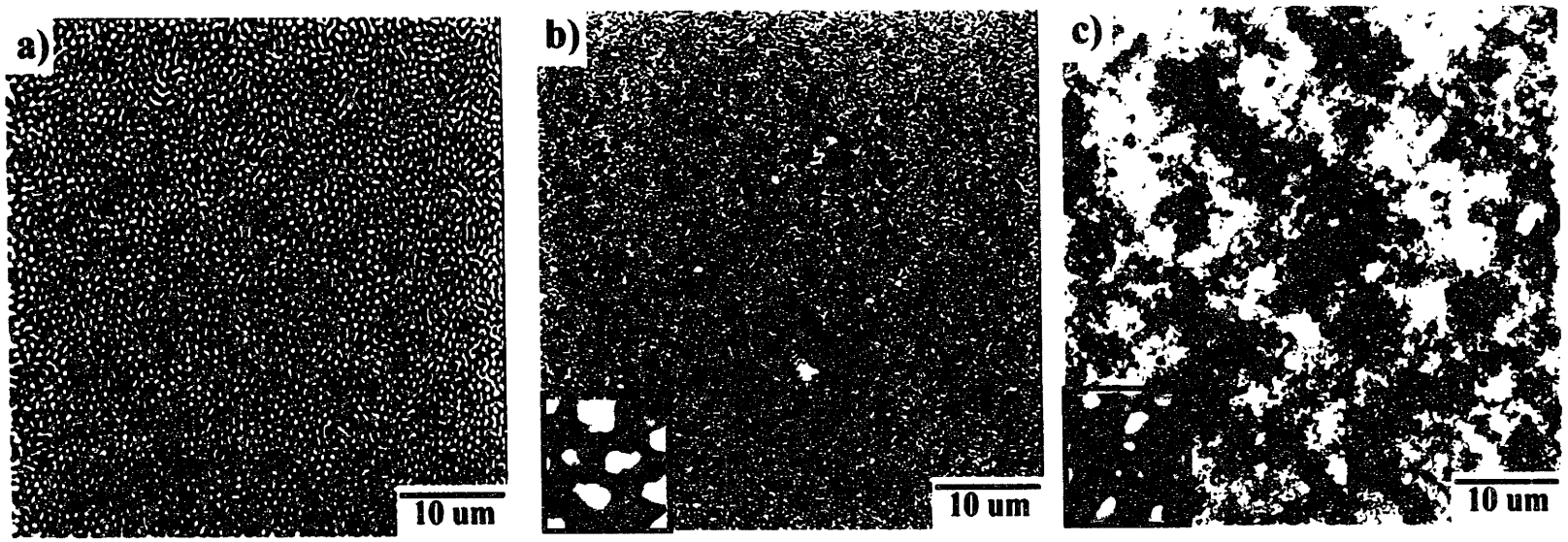

Figure 5.5: AFM images taken in height mode of different silicon containing polymers after exposing to identical etching conditions for 60 seconds. a) P(PMDSS)34 b) PTMSPMS c) PPMS. A substructure is also seen in these materials after etching, as seen in the insets of Figures 5.4b and 5.4c. Maximum height is 100 nm.

The smaller feature size for polymers PTMSPMS and PPMS may be caused by their higher initial molecular weights - lower chain mobility would prevent the full development of the reticulated morphology. The silicon is also present in the backbone of the polymer rather than as a side group that could result in a more rapid conversion to SiO_x during O_2-RIE. Finally, cross-linking reactions in aryl substituted polysilanes PTMSPMS and PPMS could lower chain mobilities. The cross-linking of such polymers upon irradiation has been reported elsewhere. (Miller 1989)

Since it is believed that the mobility of the polymer and its oxidized species may influence morphology, P(PMDSS)11 and P(PMDSS)34 were cooled to 0°C during etching, well below the T_g of the native polymer. The intention was to determine the effect of etching temperature on the resulting surface morphology. AFM images revealed no reticulated features in the final films; the surfaces were comparable to the unetched films with a RMS of 0.7 nm. The absence of a notable surface topography in the samples etched at 0°C indicates that the formation of surface morphology is a thermally driven process. Ongoing experiments by IBM researchers on subsequent heating of these cold-etched films support the differentiation between oxidation and mobilization processes.

5.4 Discussion

5.4.1 Reaction Pathway: The Interplay Between Temperature, Formation of an Oxide and Dewetting

The reaction of the silicon-containing polymers during RIE is explained in terms of chemical reaction pathways and interfacial phenomena, as seen from **Figure 5.6**

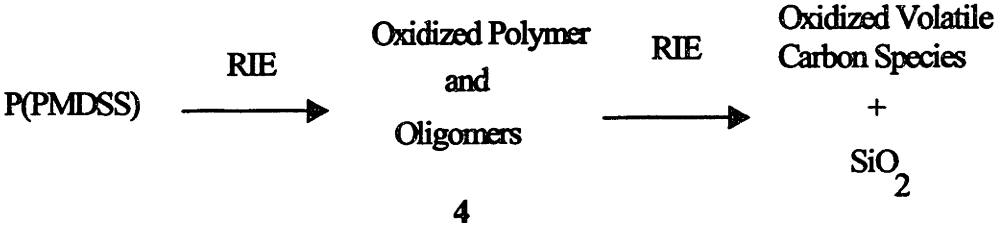

Figure 5.6: Proposed reaction pathway for the oxidation of P(PMDSS).

In the initial step, the native silicon-containing polymer reacts with the oxygen plasma to

form a complex mixture of oxidized oligomers and polymers, designated generically as **4** (**Figure 5.6**). In addition to collision-induced bond cleavage, initial reaction products result from oxygen radical and ion attack, forming various C-O and Si-O species. Hence **4** can be initially described as composed of more polar oxygenated species that lie atop unetched nonpolar starting material. Silanols and siloxanes, for example, have been observed as reaction products of silanes exposed to RIE conditions. Carbon substituents produce intermediates such as alcohols, aldehydes, ketones and acids.[22] The newly created polar species are likely to be of lower molecular weight than the starting material due to concomitant backbone chain cleavage processes.

The creation of this polar-nonpolar interface leads to interfacial energies that drive phase separation between the two species. Dewetting phenomena have been observed in other systems with AFM techniques. (Overney, 1996) The top, higher surface energy species strives to assume spherical morphologies (**Figure 5.3a**) to minimize surface area, aided by the increased mobility of the lower molecular weight products.(Joubert, 1991 and Paniez 1991) An alternate explanation for the appearance of surface structure is spinodal decomposition, driven by strain release as the initial film undergoes the transition to a new inorganic species. These two mechanisms are currently under consideration in further experiments by IBM researchers. Ultimately, the globules and reticulated features become more continuous and increase in height (**Figure 5.3b**), leading to the increase in film roughness (**Table 5.2**). (Reiss, 1992)

In previous literature studies[22] polysilanes such as **2** have been shown to form lithographically imageable in situ hard masks for lithographic image transfer under O_2-RIE conditions, resulting ultimately in a thin coating of etch-resistant SiO_X in the exposed areas. In those studies, various siloxane-containing oligomers and polymers were reported to be formed in the initial etch stages, leading to softening and perhaps even liquefication at the surface, with subsequent conversion upon further exposure to the plasma, to a hard SiO_X mask.

Continued oxygen plasma exposure further oxidizes **4**, driving the reaction coordinate in two directions : (i) volatilization of carbon-containing fragments and (ii) immobilization of silicon-containing domains through formation of SiO_X (**Figure 5.6**). This process continues for the silicon-containing polymers until the formation of a contiguous film of SiO_X hardens the surface, restricting surface mobility and protecting the underlying polymer from further

oxidation. The continuous SiO_X film is detected in the phase shift channel of the AFM. The lack of contrast in the AFM phase shift image indicates a surface homogeneously coated by a single species. (Tamayo, 1997) The chemical composition of the final silicate product is confirmed by Auger and XPS data as being SiO_X.

Support for the proposed reaction scheme is provided by the system's response to changes in the reaction parameters of temperature and atmosphere. Oxygen etching at 0^oC removes carbon-containing moieties and produces SiO_X, yet yields no reticulated morphology – apparently additional thermal energy is needed to form the morphology. Furthermore, heating of the starting material P(PMDSS)11 or P(PMDSS)34 alone produces no reticulated morphology when performed in the absence of oxygen. Thus, we conclude that both heating and oxygen are required to produce the final surface pattern in the silicon-containing polymers.

5.4.2 The Role of Silicon

In the formation of the reticulations a thermally activated step is required and it is believed that this results in an increase in mobility of the intermediate oxidized fragments 4 of the original silicon-containing polymer P(PMDSS). This thermally promoted mobility is enhanced by the decrease in molecular weight of the polymer fragments on etching.

What is the role of the silicon in the RIE of the organosilane polymers? As mentioned earlier, hydrocarbon polymers etch under RIE conditions to the point of complete volatilization. Furthermore, in our study, application of the RIE conditions to polymers that contain no silicon results in no reticulated structures. The incorporation of silicon moieties as silicate precursors alters the reaction pathway on etching, or at least introduces additional routes. To better understand the role of silicon in the RIE of organosilanes, several other silicon-containing polymers have been synthesized and subjected to the same reaction conditions as the title disilane polymer P(PMDSS).

Polymers PTMSPMS and PPMS, silicon-backbone polymers with significantly higher molecular weights than P(PMDSS)11 and P(PMDSS)34, both yield the reticulated geometry of P(PMDSS) on etching, though on a smaller scale **(Figure 5.5b,c)**. This is consistent with the silicon being present (1) as a higher percentage of the polymer stoichiometry and (2) in the backbone rather than just in a pendant group. Both of these factors would lead to a more rapid

solidification (demobilization) of the SiO_X surface species. The presence of silicon in the starting material also provides a precursor for a *nonvolatile* oxidation product, silicon oxide. This is in contrast to the *volatile* products of carbon oxidation such as aldehydes, alcohols, and acids. Polystyrene, a non-silicon containing polymer, shows no notable surface morphology on etching under our RIE conditions.

Comparison of the etching results for the four polymers (parent disilane, two silicon backbone polymers, and polystyrene) leads to the conclusion that the role of silicon is critical in producing the reticulated geometry. When the other studied parameters of temperature and atmosphere are taken into account, it is reasonable to conclude that it is the combined processes of oxidation, dewetting and finally immobilization that lead to the final reticulated surface morphology.

5.5 Conclusions

We have found that exposing a number of silicon-containing polymers to an oxygen plasma at ambient plasma temperature results in the development of reticulated structures with a size scale on the order of micrometers. With shorter etch times, a hemispherical morphology forms which fills out and increases in height with longer etch times.

It was found that by cooling the wafers to 0°C during reactive ion etching, the reticulated morphology does not develop. We suggest that the formation of surface morphologies requires higher temperatures to facilitate the mobility of silicon-containing polar intermediates as they dewet from the underlying polymer surface to form these reticulated structures.

By XPS and AES, as discussed in **Chapter 4**, it was found that the silicon in these polymers is converted to SiO_X during oxygen reactive ion etching and that the oxide is localized on the surface.

In the etching of block copolymers to form nanoporous and nanorelief ceramics, it will be necessary to etch at low temperatures in order to ensure that the reticulation found in this chapter is not reproduced in the block copolymer system.

Chapter Six
Formation of Nanoporous and Nanorelief Structures

6.1. Introduction

In this chapter the preparation of ceramic nanostructures from an inorganic containing block copolymer precursor is investigated. The objective here is to produce porous and relief ceramic nanostructures from block copolymer precursors by a simple template-free, one-step, room temperature oxidation technique. To accomplish this, the oxidation performs two simultaneous functions: 1) selective removal of the hydrocarbon block 2) conversion of the remaining silicon containing block to a ceramic (a silicon oxycarbide in this case) With this method, intricate ceramic nanostructures have been produced with periodicities in all three dimensions – structures that can not be obtained by conventional lithography techniques due to the small size scale and the complexity of the patterns formed. Specifically, in this chapter, 3D ceramic nanostructures have been produced from a silicon containing triblock copolymer system exhibiting the double gyroid and inverse double gyroid morphologies (space group Ia3d), as shown schematically in **Figure 2.2.** Depending on the relative volume fraction of the hydrocarbon block to the silicon containing block, either nanoporous or nanorelief structures were fabricated with calculated interfacial areas of 40 m^2/g, as outlined in **Appendix F.** This value of the interfacial area is significant since zeolites, which have smaller holes and smaller unit cells, have an interfacial area which is only an order of magnitude greater.(Eckert, 1999)

The resulting nanoporous or nanorelief ceramic materials have either nearly monodisperse diameter 3D connected pores or 3D connected networks and can be used for applications where high temperature stability and/or solvent resistancy is required. With careful selection of the relative volume fraction and phases, block copolymers can be used to produce nanorelief and nanoporous materials with a vast range of different symmetries and structures allowing nanostructures with highly ordered and complex pore structures to be prepared. For example, a linear ABC tercopolymer exhibits a "knitting pattern" structure with c2mm symmetry (Breiner, 1998) and a star ABC tercopolymer displays a 2D structure with an intricate tessellation of p6mm symmetry defined by triangles, rectangles and circles.(Sioula, 1998) In addition, feature sizes, pore sizes and spacings are also readily tailored either through blending of

homopolymer(s) with the block copolymer or through molecular weight control since the domain spacing D, is related to total number of monomer units N ($N=N_A+N_B$) through the equation:

$$D \cong aN^{2/3}\chi^{1/6}$$

where a is the monomer length, N the total number of segments and χ the Flory-Huggins interaction parameter. The advantages of this material over those used by previous researchers (Park 1997 and Hashimoto 1997) is their potential to be converted to a ceramic due to the silicon present in the pentamethyldisilylstyrene, P(PMDSS) block. Since the silicon is intrinsically present in the monomer, the etch selectivity is also intrinsic in the block copolymer, so no post-polymerization chemistry is necessary, unlike the materials used by and Park *et al.* (1997) and Gabor *et al.* (1994) as discussed in **Section 6.1.3.**

6.1.1 Formation of Mesoporous Ceramics

In 1993 Monnier *et al.* reported the formation of mesoporous silica utilizing surfactant templates (MCM materials). This approach has allowed access to various mesoporous structures but generally involves multi-step processes and does not allow simple production of large area continuous films.(Morey 1998, Kim 1999 and Sierra 1999) Non-surfactant templates employing block copolymers or complex sugars have also been utilized, but these processes again either involve multi-step preparations, (Ulrich, 1999) long processing times such as drying for 15-20 days (Wei, 1998) and/or high calcination temperatures (between 400-800 °C). (Zhao, 1998 and Johnson, 1999)

For example, some groups have been using nanoporous organic block copolymers as templates for a subsequent sol-gel process in order to produce ceramic structures. Not only does this method require high temperatures, but the process requires many steps; namely the nanoporous template must be produced, then infiltrated with the sol-gel and then finally converted to a ceramic by high temperature pyrolysis. (Ulrich, 1998) As another example, other groups have been investigating the use of silicon containing homopolymers to produce *non-ordered* polydisperse pores in silicon oxide materials (e.g. spin-on glasses) for low dielectric constant applications. (Hedrick 1998) In this case does this technique not only require high temperature pyrolysis but the pores that form are not monodisperse in size and are not periodic.

The approach developed in this thesis has many advantages over existing processes, since no template is required, the process is done at room temperature, the precursor since it is a polymer can be processed in solution (allowing for spincoating and dipcoating of substrates) and through a single oxidation process, the inorganic containing block can be simultaneously converted to a ceramic while the nanopores or nanostruts are produced. The combination of these properties results in many potential commercial applications.

1.2 Ozonolysis of Block Copolymers

The formation of nanoporous structures from block copolymers by oxidative means, namely ozone and reactive ion etching, has been investigated by many groups recently. This is possible due to the very high selectivity of ozone between the polydienes and polymers which do not contain double bonds in the backbone as discussed in **Section 4.1.1.** This selectivity has been used to not only produce nanoporous materials but in conjunction with GPC as a way to determine the sequence distribution of styrene-butadiene copolymers. (Tanaka 1987, 1993 and Patuelli 1994) In the case of the sequence distribution, since the ozonolysis was followed by chromatography, all these experiments were performed in solution.

However, in these studies, the polymers under investigation did not contain any inorganics and as a result only nanoporous *polymeric* structures could be produced. Specifically, polystyrene-polydiene block copolymers have been studied, where the polyisoprene is selectively removed by ozone (Mansky 1996 and Hashimoto 1997) or the double bond in the polyisoprene block is reacted with a heavy metal to provide etch selectivity with the polystyrene block to an oxygen plasma. (Park 1997) These researchers have been investigating the use of block copolymers as nanolithographic templates and as templates for nickel catalysts.

Extensive work has been done on utilizing ozone to produce nanoporous materials from block copolymers.

The use of ozone to produce nanoporous structures has been reported by various investigators. (Lee 1988,1989 and Hashimoto 1997) Lee *et al.* were the first to make porous membranes from poly((4-vinylphenyl)dimethyl-2-propoxysilane)-poly(isoprene) block copolymers. Five compositions of this block copolymer system were studied, four of which formed a lamellar system and one which formed spheres. Samples were solvent cast and the (4-vinylphenyl)dimethyl-2-propoxysilane block crosslinked prior to ozonolysis in order to

immobilize the microdomain. This produced films that were 15-25 μm thick and brittle to ductile depending on the amount of polyisoprene in the block copolymer. Samples were then immersed in a dichloromethane solution of ozone (5.0 mmol/L) for 2-8 hours at -40°C. This ozonide which was produced was then decomposed with trimethyl phosphite in methanol at -30°C for 2 hours after which the reaction temperature was raised to 20°C.

The membranes made by Lee *et al.* yielded pore widths ranging from 7 nm to 28 nm in several different lamellar samples. The widths depended on the size of the polyisoprene domain and the original lamellar structure was reflected in the microstructure of the membranes made from them. This indicates that by controlling the block lengths, the membrane microstructure can be controlled. In order to attain uniform pores, a small molecular weight polydispersity is desirable. Through nitrogen permeability and surface area determination, it was found that the hollow domain was continuous throughout the membrane.

Mansky *et al.*, (1996) have also examined ozonolysis as a way to remove polybutadiene (PB) for nanolithographic applications. In this work, a 23/10 diblock copolymer with cylindrical polybutadiene domains was cast onto deionized water from a 2 wt vol% concentration solution in toluene. Sample thickness was judged to be between 100-150 nm as observed by interference colors on the surface of the water. The samples were then exposed to a room-temperature oxygen atmosphere containing about 2% ozone for 4 hours. Ozone in this machine was generated through microwave discharge. After exposure, the samples were soaked in DI water for 12 hours to leach out the PB fragments. Ozone etched and as-cast samples were examined under bright field TEM and the phase removal was found to be successful since the phase contrast inverted between these two samples. For the as-cast samples, the PB phases which have been stained with OsO_4 appeared dark, while for the ozone treated samples, the cylinder phases are lighter, since the PB has been removed. While some etching of the diene phase certainly occurred, it is not known for certain if the ozone reacted completely across the thickness of the film, though, since no cross-sectional TEM was performed.

Simultaneously while the work at MIT was performed, Hashimoto *et al.* (1997) studied the formation of nanoporous polymers from block copolymers that formed the double gyroid. In this work, a blend of PS-PI block copolymer with homopolystyrene was made resulting in the formation of the double gyroid morphology (PI networks in a matrix of PS) with an overall volume fraction of PS = 0.66. 100-300μm thick samples were static cast from toluene and dried

until a constant weight was attained. The films were then exposed to ozone (no weight percentage was given) for 24 hours and soaked in ethanol at room temperature for 24 hours. This resulted in the complete removal of the PI block by the ozone. The nanochannels were then filled with nickel using a nonelectrolytic plating technique. Although nanoporous polymers were produced, personal communication with Hashimoto has revealed that it is not possible to produce nanorelief polymeric structures. This is likely due to the fact that the networks are extremely fragile and as polymers would likely collapse.

6.1.3 Reactive Ion Etching of Block Copolymers

Researchers have also investigated the use of silicon-containing polymers as bilevel resists for lithography as discussed in **Section 4.1.2.** (Gabor, 1995) In this case, Gabor *et al.* have investigated the hydrosilylation of a number of poly(styrene)-poly(butadiene) or poly(styrene)-poly(isoprene) block copolymers. The O_2-RIE etch rate selectivity of the silylated block relative to polyimide was impressive (42:1). However, the stability of the functionalized butadiene copolymers was limited and the hydrosilylation of the isoprene phase of the block copolymers could not be driven to completion. No 2D or 3D morphologies were investigated

Extensive work has been continued at Princeton University by Harrison *et al.* on the formation of nanoporous structures from hydrocarbon block copolymers using both reactive ion etching and ozonolysis. (Harrison 1997, 1998) The systems utilized here were either PI or PB spheres or cylinders in a PS matrix. Nanoporous structures were made by either removing the PI or PB using ozonolysis or by staining the PI or PB with OsO_4 and removing the PS using a fluorine/oxygen based reactive ion etch process.

In this work, the block copolymer was used as a positive or negative resist and the pattern replicated to underlying silicon, silicon nitride and germanium. Patterns with a hole density of 3 x 10^{12} holes on a three inch wafer were produced. (Park 1997 and Harrison 1997, 1998) Diblock copolymers were spuncoat from toluene directly onto the substrates to be patterned, resulting in film thicknesses ranging from 30-70 nm. Positive masks were made by selectively removing the PI or PB using ozone, resulting in the formation of voids in a PS matrix. An ozone concentration of 4 wt% in oxygen was used and bubbled into a glass reactor cell filled with deionized water. The materials were indirectly exposed to the ozone bubbles for four minutes (i.e. the stream of ozone bubbles did not directly contact the materials). This pattern of voids in a matrix of PS was

then replicated to the underlying substrate through a CF_4 RIE and O_2 RIE process using the parameters of 2 mTorr, 0.08 W/cm^2, and flow rate of 10 sccm of CF_4 and 10 mTorr, 0.08 W/cm^2 and flow rate of 30 sccm of O_2 respectively. The CF_4 RIE step was used to transfer the pattern to the underlying substrate while the O_2 step was used to strip the remaining polymer residue from the template. Negative masks were made by selectively staining the diene block with OsO_4 and exposing the etch resistant stained material to an O_2-RIE process. In this case, the posts would be replicated into the underlying substrate, resulting in a negative mask. However, the etch selectivity of the stained diene block to PS was only 1:2 which would limit the aspect ratio of the underlying pattern to 1:2.

RIE has also been used by Harrison to depth profile block copolymer structures. Here, underlying polymer microstructure was determined by selectively removing layers of the material through exposure to RIE. PS-PB block copolymers were depth profiled by exposing the as-cast material to a non-selective fluorine based reactive ion etching process. After etching for different times, the sample was examined in a high resolution low voltage scanning electron microscope and the internal structure of the material imaged. (Harrison, 1998)

The work done at Princeton University is a significant step in the utilization of block copolymers for non-traditional applications. However, this work only considered organic block copolymers, which do not possess an inherent etch selectivity and must be chemically modified in order to produce an etch selectivity between the two blocks. This was done by preferentially reacting the double bond in the PI with OsO_4. Unfortunately, such materials are not ideal for the semiconductor industry, since the use of heavy metals would be undesirable and large etch selectivities are not attainable which limits aspect ratio of the structures.

During this Ph.D. thesis work, a collaboration was set up with Professor Vancso and Rob Lammertink from the University of Twente to study the use of iron-silicon containing polymers as one-step masks for lithography (Lammertink to appear in *Advanced Materials).* In this work, a block copolymer comprised of poly(ferrocenyldimethylsilane) (PFS) with polyisoprene (PI) was investigated, shown schematically in **Figure 6.1.**

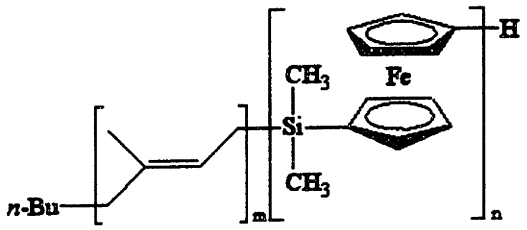

Figure 6.1: Schematic figure of poly(ferrocenyldimethylsilane)-*b*-polyisoprene.

The polymer used had a molecular weight of PI-PFS of 36/12 and formed hexagonally arranged dots with a lattice spacing of 29 nm and a domain spacing of 33 nm. When the material was spincoated to form a film with a thickness (30 nm) that approximated the domain spacing, the iron-silicon containing cylinders oriented perpendicularly to the surface. This block copolymer was then exposed to an oxygen plasma for 10 seconds resulting in the preferential removal of the polyisoprene and the formation of a complex iron-silicon-oxide from the PFS block as shown in **Figure 6.2.**

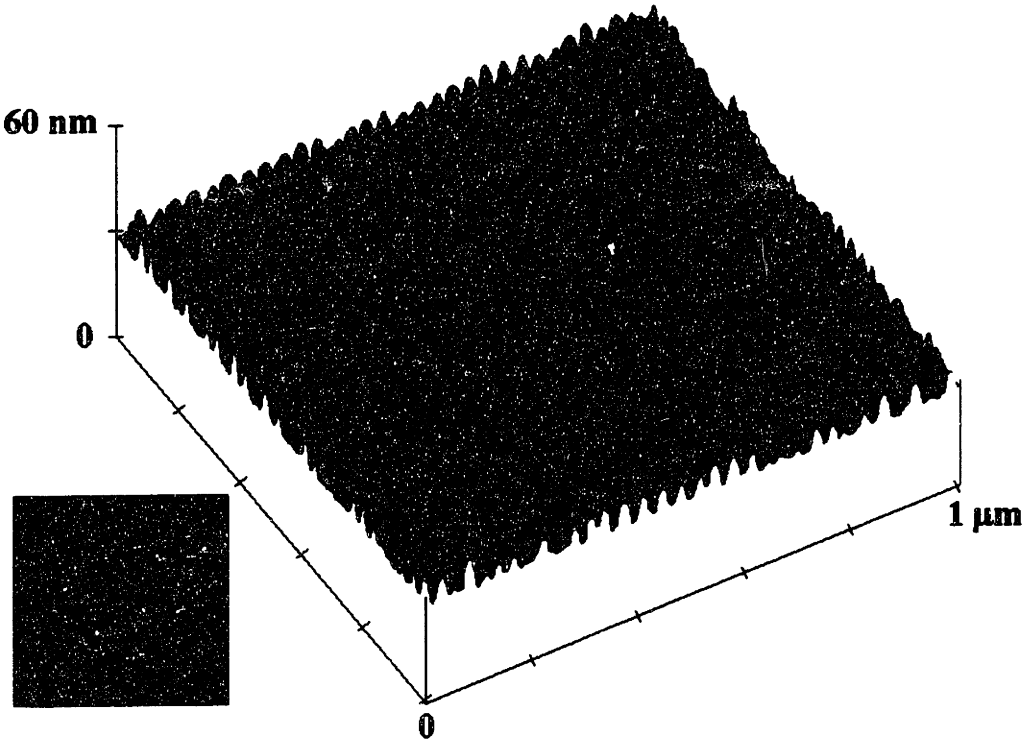

Figure 6.2: AFM image of PFS-PI, 36/12 after exposure to O_2-RIE for 10 seconds. (Lammertink to appear in *Advanced Materials*).

Reactive ion etching of the PI and PFS homopolymers showed that the etch selectivity between the two blocks was approximately 40:1 allowing the use of this material as a negative mask for cylindrical domains. Similar to the approach used in this thesis, since the inorganic is inherent in the inorganic containing block, no post-polymerization chemistry is necessary unlike work done by Park *et al.* (1997) and Gabor *et al.* (1994).

6.1.4 Mathematical Simulations of the IMDS by Level Surfaces

The microphase separated morphologies that form in block copolymers are a consequence of the balance between enthalpic and entropic forces, as discussed in **Section 2.1.1.** In order to lower the overall free energy of the system, the materials self-assemble into intricate periodic morphologies as illustrated in **Figure 2.1.** The continuous interface between these two blocks is called the intermaterial dividing surface (IMDS) and can be approximated by a constant mean curvature surface (CMC).

In the case of the double gyroid morphology which is the focus of this thesis, the structure is periodic in all three dimensions, as shown in **Figure 2.2.** In this system, the CMC surface that is adopted by the IMDS can be approximated using triply periodic level sets defined by trigonometric functions. Level surfaces are surfaces that are solutions to the scalar-valued functions with three independent variables, in this case x, y and z coordinates in Euclidean space. In the case of the "gyroid" morphology, this triply periodic level surface is the solution to the equation:

$$\cos x * \sin y + \cos y * \sin z + \cos z * \sin x = \pm 1$$

The gyroid can also be defined as a minimal surface, namely one that locally minimizes area. Minimal surfaces are subsets of constant mean curvature surfaces since minimal surfaces are defined by the fact that the mean curvature everywhere is zero where the mean curvature, is defined as the average of the 2 principal curvatures at a point on the surface.

In the case of A-B block copolymers, one of the documented morphologies is based on the gyroid minimal surface. For certain compositions, the double gyroid morphology which consists of two non-intersecting but interpenetrating networks of the A block embedded in a

matrix of the B block. Since the two gyroid networks are not connected, the system is known as the double gyroid morphology.

In order to determine the morphology of block copolymers, one tool that is often used is transmission electron microscopy (TEM), as discussed in **Section 3.2.2**. In TEM, thin microtomed sections are imaged resulting in the recording of 2-D projections of 3-D objects. Due to the complexity of the morphologies that block copolymers can self-assemble into, it is often difficult to identify the morphologies based on TEM images alone since the 2-D projections vary widely depending on the viewing axis. For this reason, TEMsim[1] was developed at the Mathematical Sciences Research Institute at the University of California, at Berkeley. Using this tool, periodic structures can be generated and 2-D projections down specific viewing axes and structure thickness created.

With the collaboration of Jim Hoffman at MSRI, various simulations of the double gyroid morphology were made using the hybrid volume /surface rendering component of TEMsim. In the case where a nanoporous material was being simulated, the networks were made transparent and the matrix opaque. In the case where nanorelief materials were simulated, the matrix was made transparent and the two networks made opaque but with two different colors to aid with the visualization.

6.2 Experimental

6.2.1 Sample Preparation

Two materials were studied in this chapter – both are triblock copolymers of the type A_1BA_2 where A is polyisoprene (PI) and B is poly(pentamethyldisilylstyrene), P(PMDSS). (Avgeropoulos, 1998) The monomer, (PMDSS) contains 24 wt% Si, which is much higher than the critical 10wt% needed to form a coherent oxide when exposed to an oxygen plasma.(Reichmanis 1984) Since the silicon is intrinsically present in the monomer, the etch selectivity is also intrinsic in the block copolymer, so no post-polymerization chemistry is necessary, unlike hydrocarbon materials used previously by other groups. (Gabor 1994, 1995, Park 1997 and Harrison 1998) The synthesis of these materials is discussed in **Chapter Two** and the characterization of these two morphologies discussed in **Sections 3.3.1 and 3.3.2**. One material has a composition of 24/100/26 (kg/mol) and forms a double gyroid morphology of PI

networks (ϕ_{PI} = 33%) in a matrix of P(PMDSS) [referred to as the P(PMDSS)-DG] while the other material has a composition of 44/168/112 (kg/mol) and forms the inverse double gyroid morphology of P(PMDSS) networks ($\phi_{P(PMDSS)}$ = 51%) in a matrix of PI [designated PI-DG]. If the PI component forms the matrix, then nanorelief structures are produced, whereas if the P(PMDSS) component forms the matrix, nanoporous structures result.

Samples of the triblock copolymers that were one mm thick were cast from toluene and cryo-microtomed at –90°C. The approximately 50-100 nm thick sections were then picked up either onto 600-mesh Cu grids or onto ultrathin amorphous carbon films on 100-mesh copper grids and the polyisoprene blocks preferentially stained in vapors of a 4% osmium tetroxide-water solution for 2 hours. These sections were then characterized in the bright field mode using a JEOL 2000 FX transmission electron microscope, operating at 200 keV. Imaging of the unannealed as-cast material revealed that highly ordered microphase separation occurs in this system even without annealing. Annealing the 1 mm thick samples for 1 week at 120°C in vacuum resulted in single grains that were several microns in area.

In order to produce large area nanoporous or nanorelief ceramic thin film samples, 700 nm thick films of the block copolymers were also made by spincoating at 4000 rpm, 4-6wt% polymer solutions in toluene onto of Si(100) wafers coated with native oxide. Since these films have thicknesses much greater than the unit cell of the polymer, the bulk polygranular DG morphology was obtained for each copolymer. The spuncast films were annealed for 2 days at 120°C and exposed to stronger oxidation conditions (ozonolysis coupled with uv irradiation) since their greater thickness (as compared to the microtomed sections) and their adhesion to the Si wafer substrate provides more stable support.

6.2.2 Ozonolysis

Unstained sections of the PI-P(PMDSS)-PI 24K-98K-26K as prepared by microtoming, were exposed to a flowing 2% ozone atmosphere for one hour at room temperature in order to preferentially oxidize the polyisoprene block. The PI-oxidized fragments were then removed by soaking the samples in deionized water overnight and the samples examined under TEM at 200 keV.

---

[1] http://www.msri.org/publications/sgp/jim/software/temsim/index.html

For the PI-P(PMDSS)-PI 44K-168K-112K, unstained microtomed sections could not easily be imaged because upon soaking in deionized water, the film broke apart since only P(PMDSS) networks were left behind which were damaged very easily due to the small thickness of the film. However, it was possible by using clam-shell TEM grids to preserve the microstructure of several samples after oxidation.

Both the spincoated P(PMDSS)-DG and PI-DG samples were exposed to a flowing 2% ozone atmosphere and 254 nm ultraviolet light[2] simultaneously for 1 hour and then soaked in deionized water overnight. These films were too thick for TEM so the morphologies were characterized by AFM.

6.2.3 Reactive Ion Etching

Etching experiments were carried out in a low pressure, magnetically enhanced inductively coupled plasma etcher. Etching was performed with a base pressure of 10 mTorr and an oxygen flow rate of 40 sccm. The top radio frequency generator was set at 250 W and the bottom radio frequency generator at 50 W. Etching was carried out at 0° C on thin microtomed sections of the P(PMDSS)-DG for time spans ranging from 10 seconds to 5 minutes.

6.3 Results and Discussion

Thin films of the block copolymers after staining, reactive ion etching or exposure to ozonolysis were examined by TEM, operating at 200 keV. The morphologies of the spincoated materials were documented using atomic force microscopy (AFM) using intermittent contact mode. Imaging of polymers using AFM is discussed in detail in **Section 5.1.2.**

The morphologies of these materials were then compared to computer simulations of the double gyroid made by Jim Hoffman using TEMsim, as discussed in **Section 6.1.4.** Both porous and relief double gyroids were made using the hybrid volume /surface rendering component of TEMsim. Through the comparison of the real data to different viewing axes of the double gyroid morphologies, the formation of nanoporous and nanorelief structures was demonstrated.

---

[2] UVP Pen-ray PCQ Lamp. Part number 90-0049-03. Lamp emits 8mW/cm^2 1.9 cm away from the light source.

6.3.1: The Double Gyroid : PI-P(PMDSS)-PI, 26K-98K-24K

Figures 6.3aand 6.3b are experimental TEM images of the double gyroid morphology for the P(PMDSS)-DG sample oriented such that the viewing direction is approximately [110]. In **Figure 6.3a,** the PI networks are preferentially stained with OsO_4 and appear darker than the surrounding P(PMDSS) matrix. In **Figure 6.3b,** the thin film of the bulk sample has been exposed to ozone resulting in the preferential removal of the PI networks which now appear lighter than the matrix, resulting in an inversion of the image contrast. Despite mass loss which was expected based on the homopolymer studies in Chapter Four, the image periodicity of the ozone treated sample is approximately the same as that of the unetched sample. This contrast inversion is similar to that reported by Hashimoto *et al.* (1997) in a nanoporous all hydrocarbon *polymer* system.

The program, TEMsim[3] was used to simulate a projection of the morphology shown in **Figure 6.3c** employing a level set surface structure with 34 volume percent network component. (Lambert 1996) The good correspondence of the TEM image (**Figure 6.3a**) and simulation (**Figure 6.3c**) allows the PI network strut diameter to be estimated as 20 nm. By SAXS as discussed in **Chapter 3,** the lattice parameter of the material was found to be 120 nm. The specific surface can be estimated by assuming that the intermaterial dividing surface which defines the microdomain structure can be approximated by a member of the gyroid level set family of surfaces with Ia3d symmetry and appropriate volume fraction and using TEMsim to compute the area per crystallographic unit cell, then scaling the dimensionless area $S/V^{2/3}$ to the actual size of the block copolymer unit cell, as outlined in **Appendix F.** The interfacial area per gram of the nanoporous P(PMDSS)-DG material is thus estimated as 40 m^2/g about an order of magnitude smaller than that of common zeolites (Monnier, 1993) but quite high for a mesoscopic structure with a much larger interconnected pore size. By varying the molecular weight, a range of pore sizes and specific areas can be obtained, presenting opportunities for separation and catalysis applications where larger component molecules are involved.

[3] http://www.msri.org/people/staff/jim

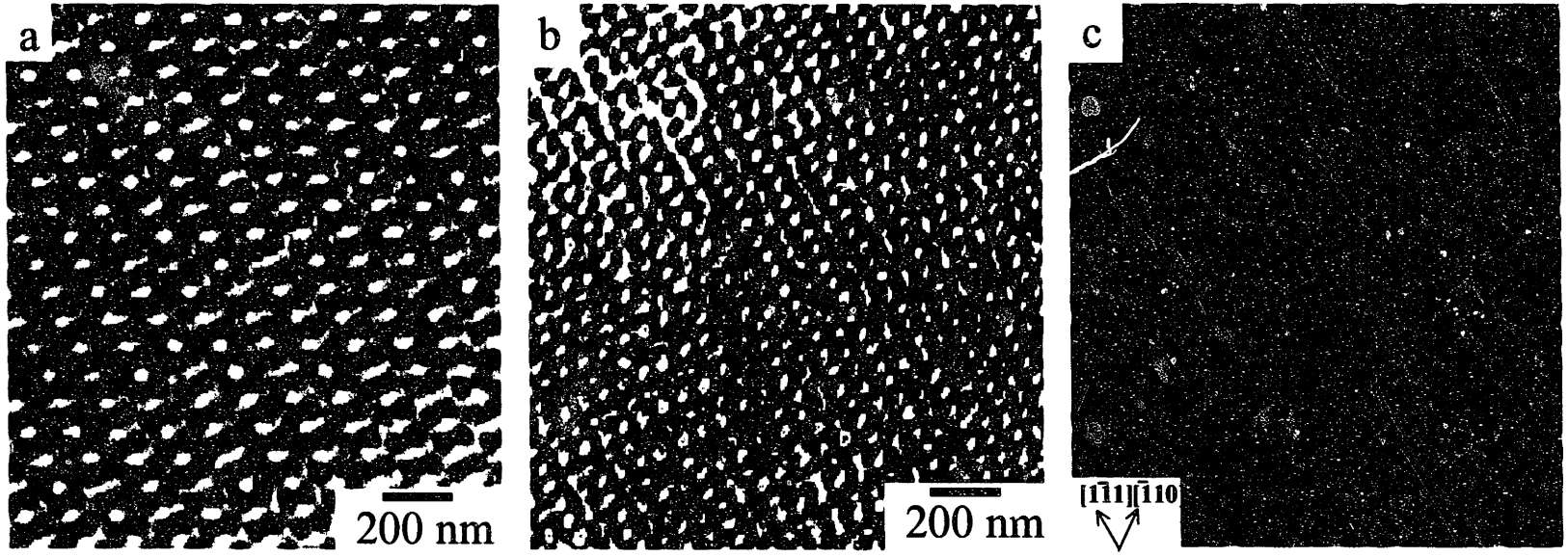

Figure 6.3: Views along the [110] direction of the P(PMDSS)-DG sample. (a), (b) Bright field TEM images of P(PMDSS)-DG (a) OsO_4 stained PI networks appear dark. (b) PI networks have been removed using ozone and as a result, the contrast has inverted and the networks appear light. (c) TEM simulation of a projection down the [110] exhibiting 2-fold symmetry. The networks are assigned a density of 1 and the P(PMDSS) matrix a density of 0. Section thickness is 40% of the repeat in the [110] direction.

Preliminary etching work was also carried out on both block copolymer samples under the experimental conditions used to etch the homopolymers, as discussed in **Section 4.2.3**. A nanoporous double gyroid morphology is also evident in the O_2- RIE samples, **Figure 6.4**, although the images are less well defined than for the ozone etching, as shown in **Figure 6.3b**.

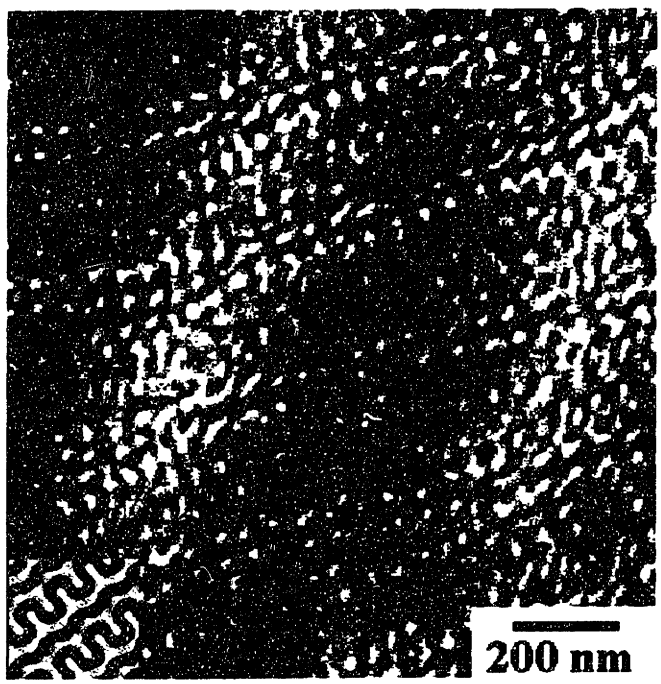

Figure 6.4: P(PMDSS)-DG after exposure to O_2-RIE. Contrast in this image is not as strong as in **Figure 6.3b** due to the incomplete removal of the PI networks. It can be seen that the image seen here has a resemblance to the inset [112] view of the double gyroid morphology at 0.05 height, with the undulating structure apparent in both the simulation and the inset.

It could be expected that in order to form a nanoporous structures from the tortuous double-gyroid morphology ozonolysis would be easier than RIE since RIE is generally an anisotropic process, as discussed in **Section 4.1.2.** Thus, the directionality of reactive ion etching appears to be problematic for the 3D tortuous double gyroid structure since the reactive ions must go around corners in order to remove the polyisoprene. Since nanoporous and nanorelief structures were possible through ozonolysis, the process parameters for O_2-RIE were not further optimized. However, it is possible to promote a more isotropic etching process in RIE by controlling different process parameters. This could be achieved for example, by utilizing lower bias voltages or higher gas pressures. A lower bias voltage would decrease the anisotropy of the plasma since a lower bias would decrease the directionality of the plasma ions. Higher gas pressure would result in more gas phase collisions of the plasma species, thereby

increasing the random walk of these ions resulting in a less directional plasma. Another possibility would be to use a plasma asher which does not contain a forward bias at higher gas pressures. With such process optimization, it is believed that nanoporous and nanorelief structures could be produced through RIE. Furthermore, it was shown in **Chapter Four** that exposure to an oxygen plasma converts the P(PMDSS) to silicon dioxide, allowing the formation of a ceramic.

The nanoporous structures of the spincoated block copolymers subjected to ozone + uv were studied by atomic force microscopy (AFM) using intermittent contact mode. For the P(PMDSS)-DG, the PI has been selectively removed by oxidation leaving an interconnected tortuous porous network within a silicon oxycarbide matrix as shown in **Figure 6.5**. The characteristic pore size of this nanoporous structure is approximately 20 nm. This porous network corresponds well to the feature sizes in the TEM micrographs of **Figure 6.3.**

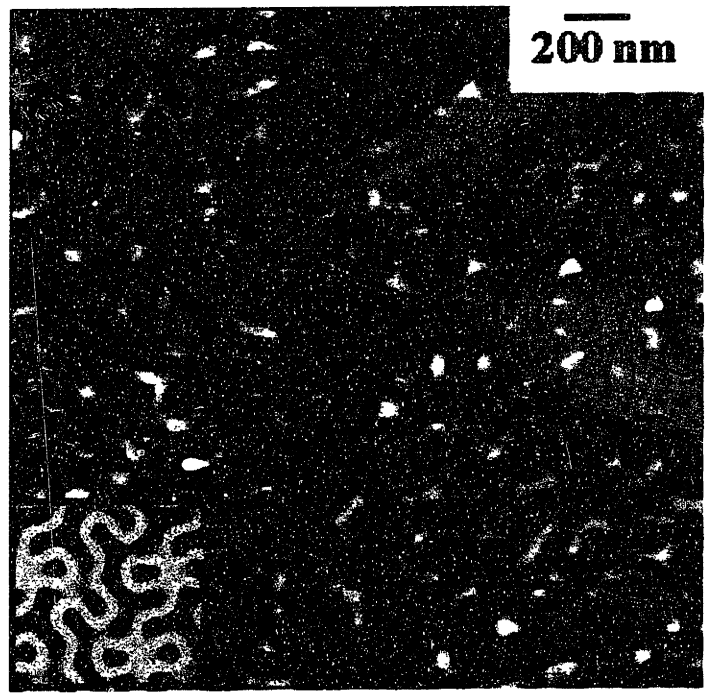

Figure 6.5: AFM image of surface topography of P(PMDSS)-DG after ozonolysis and uv exposure. The PI networks have been removed resulting in the formation of ordered tortuous pathways within a SiO_x matrix. Bright regions are highest, dark regions are empty. The maximum height on the image is 10 nm. Inset: [012] view at zero height of a volume rendered surface of the double gyroid structure with empty strut networks which appear dark.

Using TEMsim, simulations of a porous double gyroid were made. It can be seen from the inset of **Figure 6.5** that the porous ceramic structure possesses a morphology similar to that of the double gyroid morphology viewed along the [012] direction at zero height. In this simulation, the networks have been made dark and the matrix yellow.

We envision the use of the silicon oxycarbide-DG nanostructure as a high temperature membrane with tailorable monodisperse interconnected pores. There are many advantages to using block copolymers over other routes for producing nanoporous membranes (i.e. track etching of polymers). In block copolymer systems, pore size and spacing can be precisely controlled since feature sizes are directly related to molecular weight, the pores that form are highly ordered and in our system, the resulting material is a ceramic. For such an application, minority etchable network component double gyroid and cylinder microdomain samples have the most utility as nanoporous membranes. One advantage of the double gyroid structure is that the redundancy of the interconnected pathways significantly decreases the likelihood of the membrane being clogged by the filtrate. (Kinning 1987) Moreover, the ability to form continuous conformal coatings with high specific surface area ($\sim 40\ m^2/g$) presents opportunities for novel catalytic applications.

6.3.2 : The "Inverse" Double Gyroid : PI-P(PMDSS)-PI, 44K-168K-112K

For the PI-DG sample, unstained ozone etched microtomed sections were difficult to image because upon soaking in deionized water, the thin section broke apart since only P(PMDSS) networks were left behind which were fragile due to the small thickness of the film. However, by using a clam-shell TEM grid, it was possible to preserve part of the section, as shown in **Figure 6.6.** The tortuous P(PMDSS) network that is left behind after ozonolysis is evident in the negative image of **Figure 6.6b.**

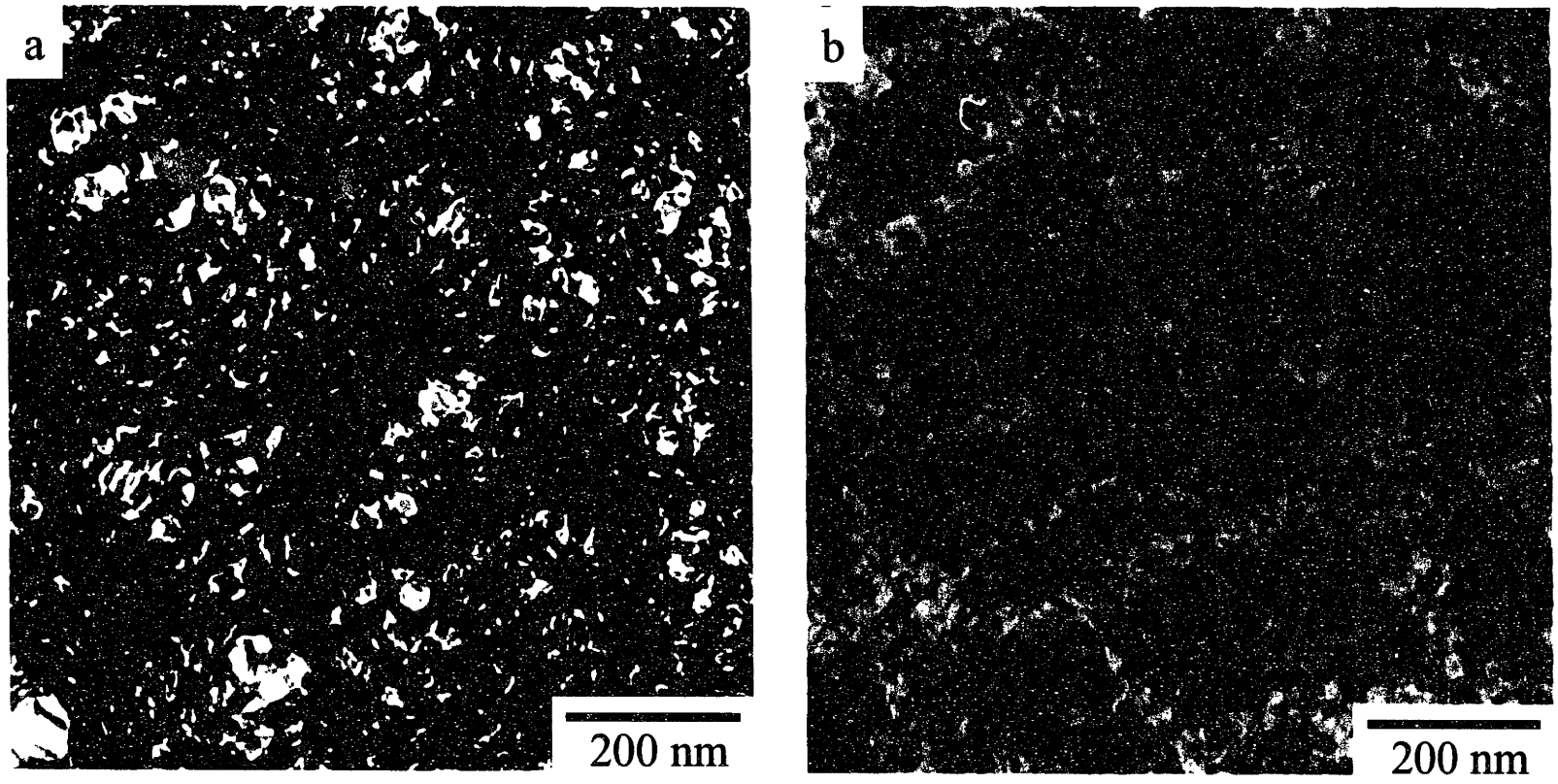

Figure 6.6: Bright field TEM image of PI-DG after ozone etching. a) The positive of the image. The PI matrix has been preferentially removed leaving P(PMDSS) networks which appear dark among the air channels. b) The negative image of Figure 6.6a. Here, the networks appear light and the matrix which has been removed is now dark. The 3-D nature and tortuosity of the networks is more apparent to the eye in the negative image. As indicated by the red arrow, the triple points of the structure are evident.

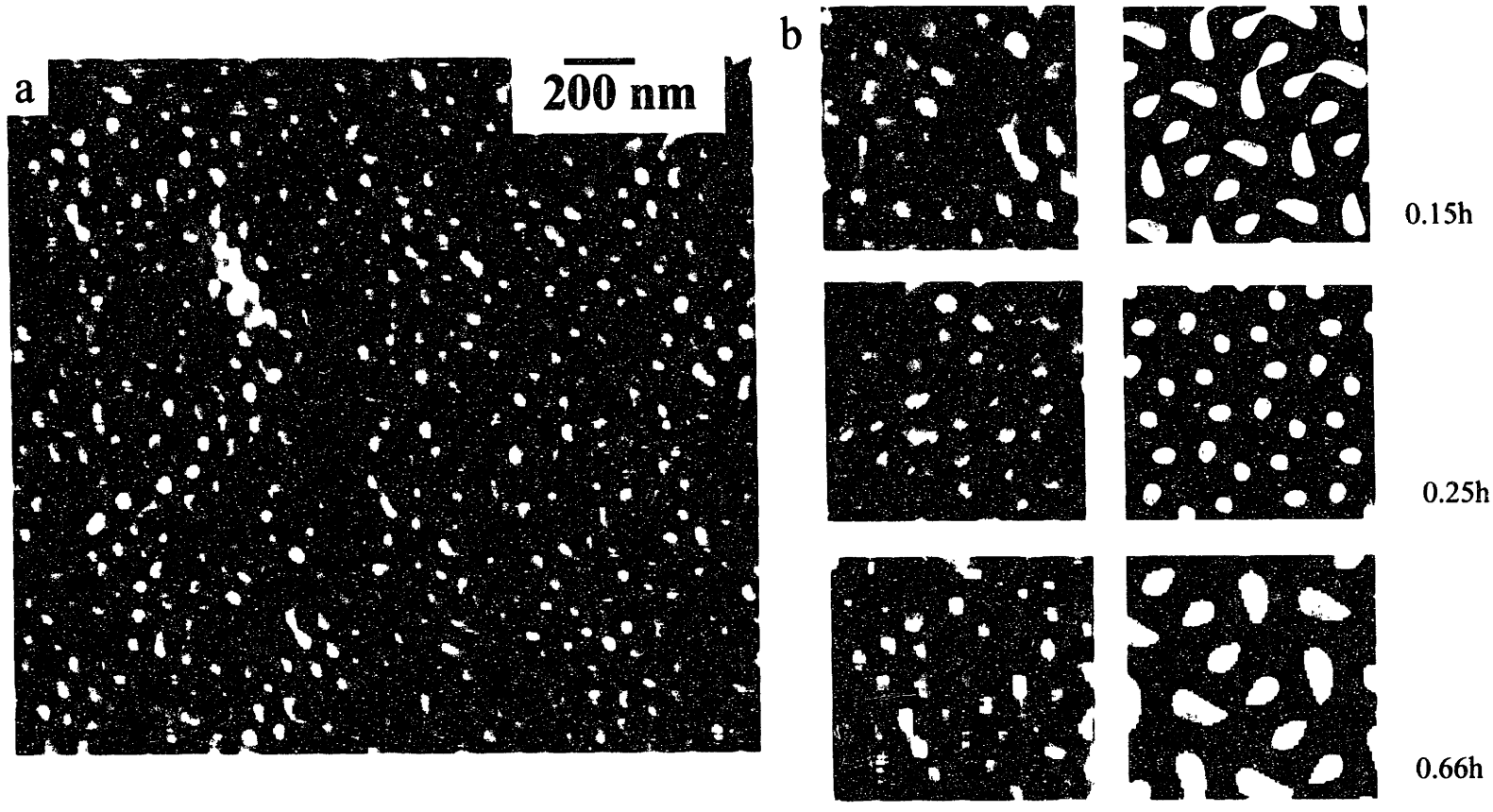

Figure 6.7: (a) AFM image of surface topography of PI-DG after ozonolysis and uv exposure. The PI matrix has been removed leaving behind silicon oxycarbide networks. The highest regions are white and the lowest dark. The maximum z height in this image is 10 nm. (b) Enlargements of selected regions within Figure 4a. At the right are volume rendered surfaces of the double gyroid morphology with silicon oxycarbide strut networks. The uppermost features are white. All simulations are [112] views of the DG silicon oxycarbide network structure with the surface at various heights within the cell (refer to Figure 2a where $h=\sqrt{6}a$). The matrix is made transparent to enable viewing of the networks.

The spincoated PI-DG sample was exposed to ozone + uv and studied by atomic force microscopy (AFM) using intermittent contact mode. In the PI-DG sample, the PI matrix is selectively removed leaving silicon oxycarbide network struts to be imaged as seen in **Figure 6.7a.** This results in an inversion in the height contrast as compared to **Figure 6.5** since the networks rather than the matrix remain. Various areas of the relief double gyroid silicon oxycarbide networks correlate well with simulated surface regions having slightly different levels within the unit cell (**Figure 6.7b**). Spincoating of the block copolymer does not result in a completely uniformly flat surface and as a result, the surface that is imaged consists of slightly different heights along the [112] direction. This can be seen from the good correlation from the simulated image to the real data.

In this case, where the PI matrix has been removed by the oxidation process, a significant amount of air is left behind resulting in a highly porous silicon oxycarbide nanostructure. Because of the incorporation of this significant amount of air, the material has the potential to be used in interconnects due to its low dielectric constant, high temperature stability and the inherent etch selectivity of this material to photoresist. (Hendricks, 1995)

6.5 Conclusions

In the search for routes to nanostructured materials, the process reported here is significant not only because of the type of materials that are attainable but because of the simplicity and versatility of the method: large area, conformable and continuous films/coatings can be produced, the precursor is an easily processible polymer, the nanostructures form by self-assembly without the need for a template and the oxidation is done at room temperature with inexpensive equipment (Chan, US and PCT patent applications). The resulting class of materials could be used for applications where high temperature stability and /or solvent resistance is required.

With this processing method, it is possible that these materials will have important applications in the areas of high temperature membranes, low dielectric constant materials and with the periodic and interconnected high dielectric/low dielectric SiO_x/air structures as potential photonic band gap materials (Joannopoulos 1995, Urbas 1999).

Chapter Seven
Summary of Thesis Work and Suggested Future Directions

7.1 Summary

In this thesis, nanoporous and nanorelief ceramic structures have been produced from a silicon-containing block copolymer precursor, P(PMDSS)-PI. To accomplish this a monomer system was selected, various block copolymers synthesized anionically and volume fractions determined which would yield both the double gyroid and inverse double gyroid morphologies. The silicon-containing homopolymer was processed by different oxidative routes (namely ozonolysis, uv in air, uv+ozone) in order to screen the conversion of this material to a ceramic. It was found that the best route is to expose the block copolymer t ozone and uv for one hour at room temperature, allowing the PI to be preferentially removed and the P(PMDSS) converted to a ceramic stable to temperatures of up to 400°C in nitrogen.

The thesis can be separated into three parts: 1) the design, synthesis and characterization of the materials, 2) the conversion of the P(PMDSS) homopolymer to a ceramic by ozonolysis, uv and oxygen reactive ion etching, 3) the formation of nanoporous and nanorelief ceramics from the P(PMDSS)-PI block copolymers.

In the first part, which corresponds approximately to the content of Chapters Two and Three, the silicon-containing polymer system was carefully designed so that it would be possible through oxidation to selectively remove the hydrocarbon block and convert the inorganic containing block to a ceramic. For this reason, P(PMDSS), a high T_g, silicon containing polymer with more than 10 wt% silicon was selected for the inorganic containing block and PI chosen for the hydrocarbon block since its low T_g would facilitate processing and the presence of double bonds in the backbone would allow for its degradation by ozone and RIE. Once the material system with the desired properties was designed, the polymers were synthesized by both living free radical polymerization and anionic polymerizations. The block copolymers which were synthesized anionically were then static cast, cryo-microtomed and their morphologies characterized by TEM and SAXS. Using SAXS, d-spacings were calculated and with TEM the microdomain morphologies documented. In the process, an asymmetric morphology diagram was discovered in this ABA triblock polymer system although the reasons behind this asymmetry require further investigation. Out of the eight polymers synthesized, two were found

to form the double gyroid morphology. In these two samples, PI formed the networks of one and the matrix of the other. These two polymers are the focus of this thesis.

In the second part of the thesis, Chapters 4 and 5, the oxidation of P(PMDSS) was studied both chemically and morphologically. Chemically, it was found that when P(PMDSS) is exposed to ozone at room temperature, very little oxygen is incorporated into the structure and the majority of the material consists of hydrocarbons. In order to form a stable ceramic, the P(PMDSS) needs to be exposed to uv in air or uv in ozone. In all cases, residual carbon was present but through FTIR and XPS studies, it appears as if a complex silicon oxycarbide has formed since Si-O, Si-C and C-O bonds are identified. Depth profiling of the P(PMDSS) exposed to uv in air and uv plus ozone by AES shows that the composition is relatively constant throughout the thickness of the film, contrary to what was found by Koberstein *et al.* In the case of O_2-RIE, the P(PMDSS) forms a surface oxide which is 10% of the total film thickness as determined by AES. When these samples were annealed to 400°C in a nitrogen atmosphere, it was found that the samples which had been exposed to uv in air, uv and ozone and O_2-RIE were stable since the refractive index did not change with temperature. Morphologically, it was found that when the P(PMDSS) is exposed to O_2-RIE, a reticulated morphology forms on the surface when the temperature of the sample is not regulated. This reticulation was believed to have formed due to dewetting of the polar species that form when the surface is oxidized. By cooling the backside of the substrate, this reticulated structure did not form.

In the final part of the thesis, the two triblock copolymers that form the double gyroid and inverse double gyroid morphologies were used to form nanorelief and nanoporous structures. Through the selective removal of the PI, either nanoporous or nanorelief materials could be made with a predicted interfacial area of 40 m^2/g.

In order to achieve this, both microtomed thin sections of bulk-cast materials and spuncast materials were studied. In the case of the microtomed thin sections, TEM showed the selective removal of the PI by ozonolysis, resulting in the inversion in the image contrast as compared to specimens where the PI had been preferentially stained with OsO_4. When the thin sections were exposed to O_2-RIE, the PI could not be completely removed which is likely due to the directionality of oxygen plasmas which makes etching around corners difficult. It is likely that it is possible to produce nanoporous or nanorelief structures using an oxygen plasma,

through the optimization of the vast parameter space available in O_2-RIE. However, since ozonolysis was successful this was not pursued further in this dissertation.

In addition to thin sections of the bulk cast materials, the two double gyroid morphologies were also spuncast and the thin films exposed to ozone coupled with uv. The resulting structures were characterized by AFM. Comparison of images simulated using the mathematical program TEMsim were in good correspondence with the AFM data in both cases.

The present work demonstrates that block copolymers are promising candidates as high tech materials. It is envisioned that these materials will be useful for many different applications due to their high interfacial areas, tailorable pore sizes, high temperature stability and ordered low dielectric/high dielectric constant structures.

7.2 Future Studies

7.2.1 Extension of the Thesis Work

Material limitations restricted the extent of experimentation that was performed. For the P(PMDSS)-DG sample, 0.6 g of the polymer was synthesized while in the case of the PI-DG sample, there was 1.5 g of polymer. Ideally, if more material is synthesized, then the formation of *bulk* nanoporous and nanorelief double gyroid structures could be studied. From this, interfacial areas could be measured through nitrogen adsorption in order to confirm the high interfacial area that is predicted. It would also be useful to measure the mechanical properties of the resulting nanoporous and nanorelief ceramics to ascertain the technology utility of these materials in commercial applications.

It would also be interesting to see whether or not the reactive ion etching parameters could be optimized such that a porous or relief double gyroid could be made through RIE. As discussed in **Chapter Six,** this could be done by either using lower bias voltages, higher gas pressures or using a plasma asher. In addition, two step processes could be studied where ozonolysis could first be done to remove the polyisoprene component and RIE subsequently done to convert the remaining silicon containing block to silicon dioxide.

Extended temperature stability should could also be done on the converted homopolymer to determine its stability in air and to higher temperatures. The examination of the temperature stability to 400°C and in a nitrogen atmosphere was with the intent to utilize this material for dielectric applications where such temperature stability is necessary. However, this material

should be significantly more stable than 400°C since silicon oxycarbide is formed. It would also be interesting t examine the utility of this material as high temperature coatings for fibers. This could be done by dipcoating fibers with the P(PMDSS) homopolymer or the P(PMDSS)-PI block copolymer and examining the mechanical integrity of the converted coating. Is the coating ductile or brittle, are there problems with delamination, is the microstructure able to conform to the curvature of the fiber?

In addition, the use of these nanostructure and nanorelief ceramics as high temperature membranes, low dielectric constant materials and photonic band gap materials also should be studied. In the case of high temperature membranes, perhaps a composite membrane could be made where the block copolymer is a coating on top of a mechanical support. With the low dielectric constant materials, ozonolysis coupled with uv would not be an ideal route since the process involves soaking the nanostructure in water which is incompatible with present fabrication lines. For this reason, the process parameters for O_2-RIE should be optimized for the etching of the double gyroid morphology. If the majority of the PI is removed than the resulting material must have an extremely low dielectric constant. In the case of photonic band gap materials, it will be necessary to increase the d-spacing of the block copolymer in order to achieve spacings on the order of 600-1000 Å. To do this, higher molecular weight polymers need to be synthesized or the domain spacings increased by swelling each block with low molecular weight homopolymer.

7.2.2 Elucidation of the Asymmetric Morphology Diagram

Several of the morphologies that were documented in this thesis formed at unexpected volume fractions. Theories have been developed that predict asymmetry phase diagrams as a result of asymmetric architectures (Mayes and Olvera de la Cruz) or due to differences in the Kuhn statistical segment lengths (Vavasour and Whitmore). In order to properly determine the reason behind the asymmetric features of observed the P(PMDSS)-PI block samples I studied, a more systematic study should be carried out. To this effect, a set of triblock copolymers should be synthesized which spans a range of volume fractions. However, all the samples should possess the same degree of asymmetry and the same molecular weight (in order to fix $N\chi$). The morphologies should then be characterized and the order-order and order-disorder boundaries determined.

7.2.3 Synthesis of Silicon Containing Block Copolymers by Living Free Radical Polymerization

The P(PMDSS) homopolymer that was synthesized by living free radical polymerization was found to have an extremely high polydispersity. However, it was also found in this research, although not reported in this thesis, that a random copolymer composed of PDMSS monomer and styrene monomer had a polydispersity of <1.1. As long as the resulting polymer has a critical wt% Si = 10%, these materials could be used to form coherent oxides through reactive ion etching. Since PMDSS contains 24 wt% silicon, in order to maintain the critical 10 wt% of silicon in the random copolymer, up to 75% styrene could be incorporated into the random block. Thus, it could be possible to synthesize silicon-containing block copolymers where the first block is a random copolymer of P(PMDSS) and PS and the second block is a pure PS block. Not only will this allow the decrease in the polydispersity of the silicon-containing polymer but also by using a random copolymer the χ_{AB} of the system can be tailored by varying the feed ratios of the monomers.

7.2.4 Selective Degradation of the Hydrocarbon Block by Non-oxidative Means

In this thesis, the hydrocarbon block was selectively removed through oxidation but it is possible to remove hydrocarbon blocks using non-oxidative routes. For example, it is known that polymethylmethacrylate (PMMA) will undergo chain scission when exposed to an electron beam or when exposed to uv light. Thus, a block copolymer consisting could be made that consists of PMMA with P(PMDSS). The PMMA could then be selectively removed using an e-beam or through uv exposure and in a second step the P(PMDSS) converted to a ceramic. Similarly, one could use a block which depolymerized when heated above the ceiling temperature of the polymer (e.g.. alpha-methylstyrene), which could be removed through acid catalysis (e.g. poly(ethyleneoxide)) or a block copolymer synthesized where the blocks are joined not by a covalent bond but by a group which can be selectively triggered so that the blocks can be disjoined. For example, a block copolymer of PS-PMMA-PEO, where the PMMA midblock is only several repeat units. The PMMA could then be unzipped with radiation and the PEO washed away with water.

7.2.5 Applications of Non-Double Gyroid Morphologies

Although the double gyroid is the focus of this dissertation, there also is great utility in using other morphologies, such as cylinders where parallel nanopores could be produced. For example, with a block copolymer that forms PI cylinders within a P(PMDSS) matrix, the goal would be to remove the PI cylinders and convert the P(PMDSS) matrix to a ceramic. Coupled with proper cylinder orientation, this would result in a high temperature membrane with monodisperse pores, as shown in **Figure 2.3.**

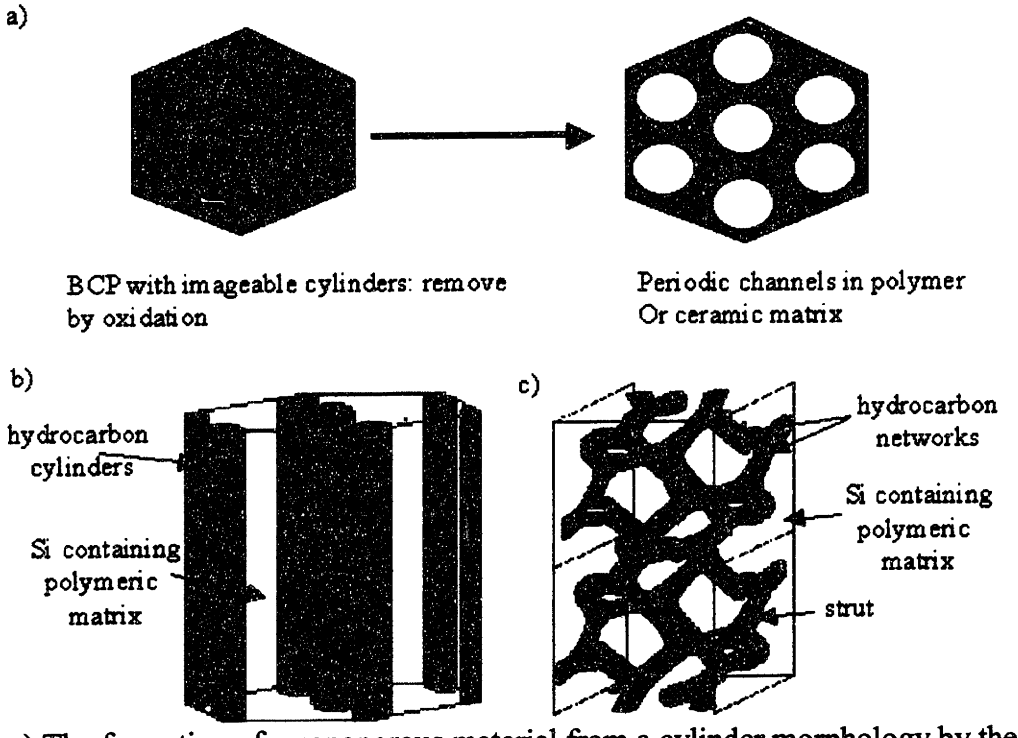

Figure 7.1: a) The formation of a nanoporous material from a cylinder morphology by the oxidation and selective removal of hydrocarbon cylinders. In the formation of high temperature membranes useful morphologies would either be b) hydrocarbon cylinders or c) a double gyroid possessing hydrocarbon networks. In both cases, the minority hydrocarbon component would be removed and the inorganic containing matrix converted to a ceramic. In the case of the double gyroid morphology, the presence of triple points in the networks provides an alternate pathway for filtrates to travel if one of the cylindrical struts were to become clogged.

These nanopores could also be extended to the area of magnetic storage media, where the channels could be electroplated and filled with a magnetic material such as cobalt, as shown in **Figure 7.2.**

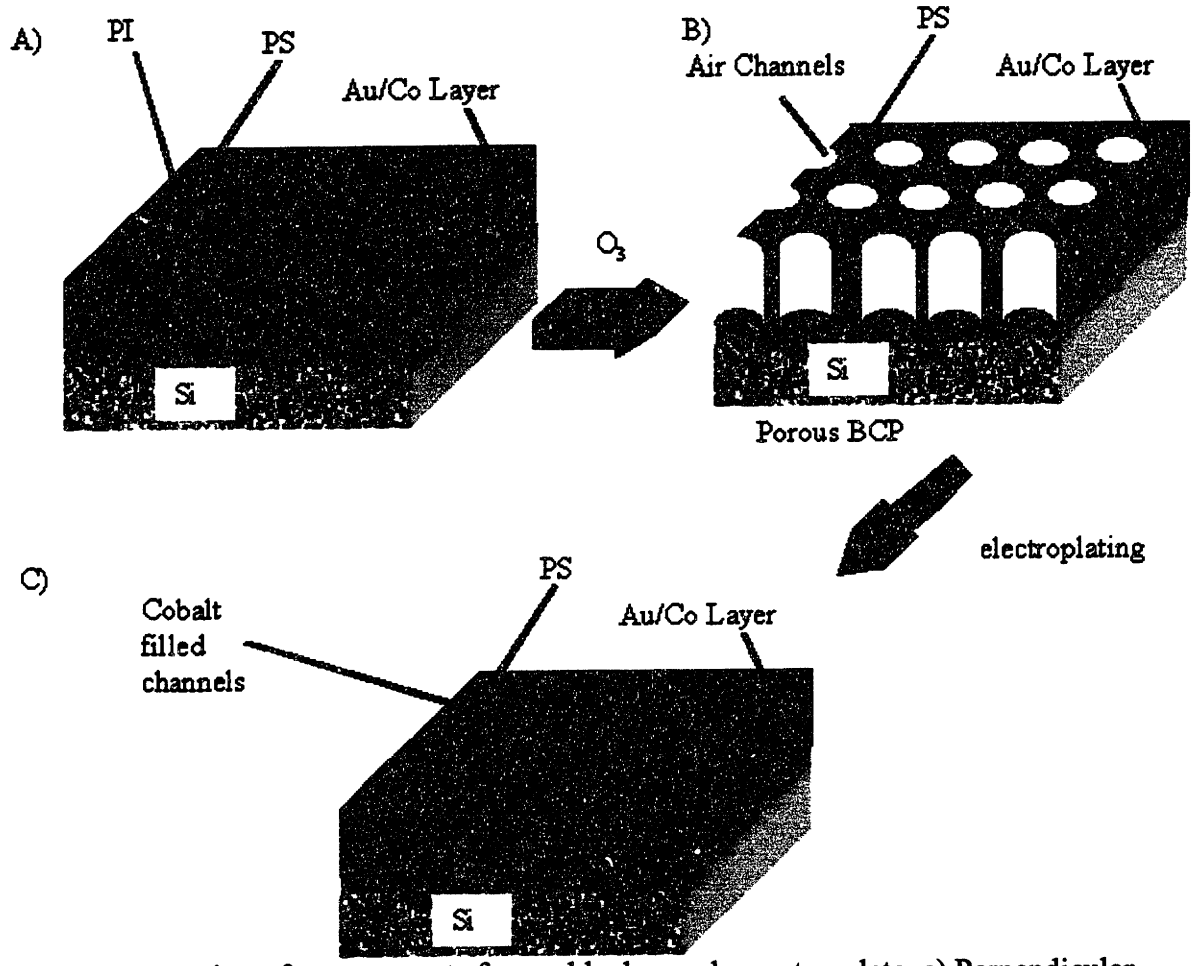

Figure 7.2: Formation of nanomagnets from a block copolymer template. a) Perpendicular cylinders are formed on top of a substrate containing a topmost conducting layer. b) The cylinders are preferentially removed. In this case, the cylinders are comprised of PI and are removed by ozonolysis. c) The pores are backfilled with a magnetic material, such as cobalt, resulting in perpendicularly aligned, precisely and periodically aranged nanomagnets.

This idea will be the basis of the Ph.D. dissertation research of Joy Cheng in Professor Caroline Ross' group in the Department of Materials Science and Engineering at MIT.

Several block copolymers were also synthesized in this thesis which do not form the double gyroid morphology and with all of these block copolymers nanostructures should be able to be formed by O_2-RIE and/or ozonolysis. Using the sphere morphology, one-step lithographic masks can be produced, which was shown in collaboration with Rob Lammertink, (1999) while

with lamellae, switchable diffraction gratings can be realized. For example, the PI could be removed using an oxygen plasma or ozonolysis and the channels backfilled with a liquid crystalline component. The commercial possibilities of these materials are widespread and with some imagination, other ways in which nanoporous or nanorelief ceramics can be utilized can be found.

Appendix A
Small Angle X-ray Scattering Spectra

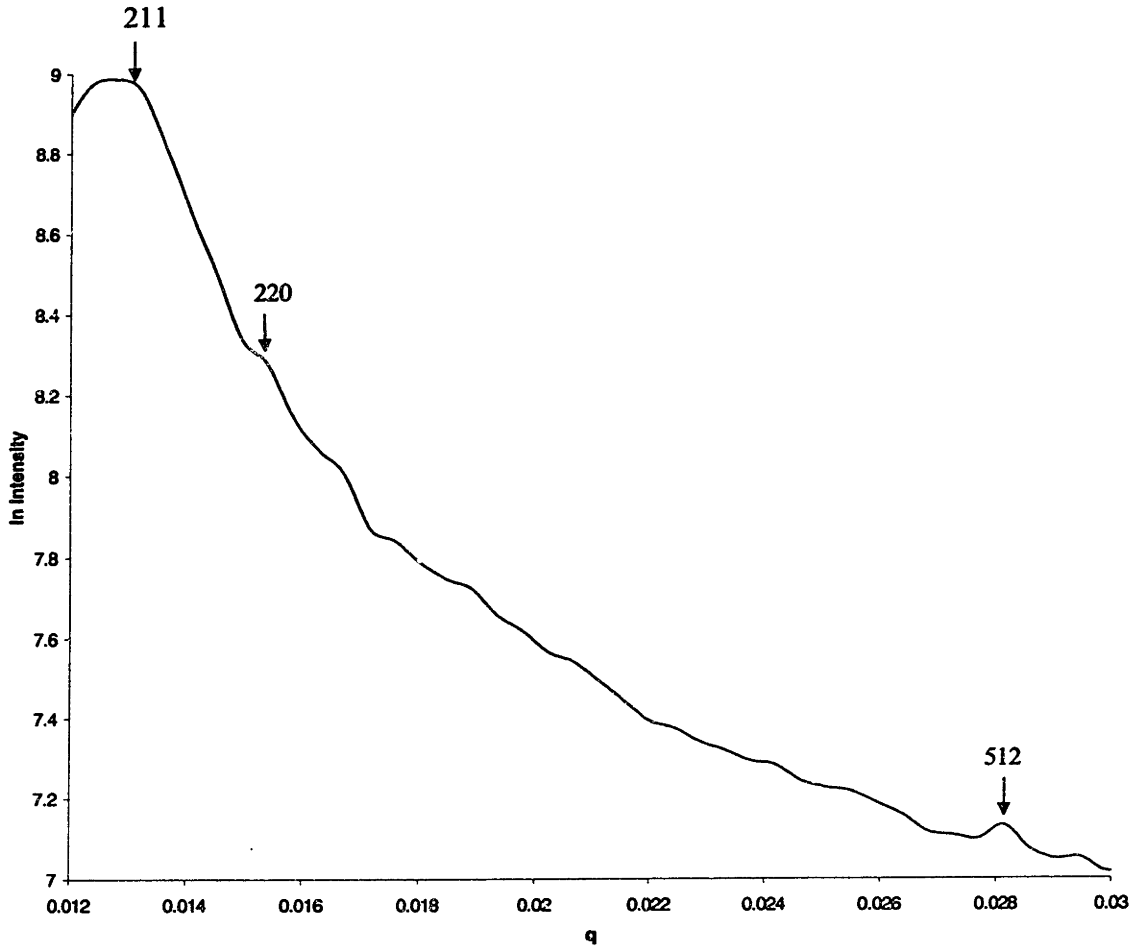

Figure A.1: SAXS pattern for Sample 1, P(PMDSS)-DG. (PI-P(P[illegible]DSS)-PI 24K-98K-26K) taken at 160°C. It can be seen that the scattering pattern is extremely weak for this sample and the only strong peak is the primary beam and the {521} reflection. However, from TEM it is clear that the sample exhibits the double gyroid morphology as evidenced by the clear 2-fold, 3-fold and 4-fold patterns as seen in Figure 3.1.

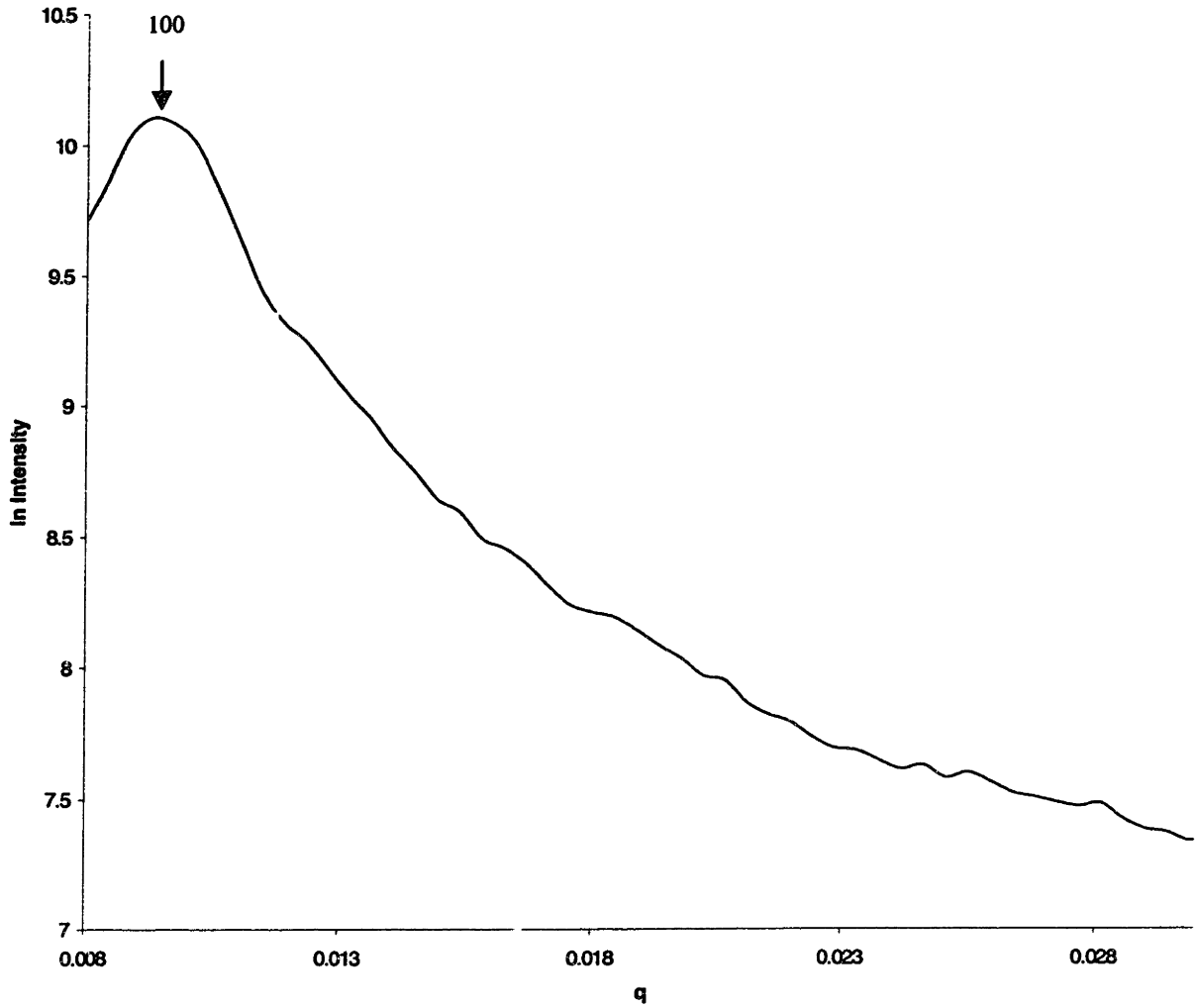

Figure A.2: SAXS Spectra for Sample 5 Cylinders. (P(PMDSS)-PI-P(PMDSS), 44K-148K-120K) taken at room temperature. No peaks other than the primary scattering peak can clearly be identified from the background signal so only a d-spacing was obtained from this spectra. However, by TEM it is clear that this polymer forms cylinders.

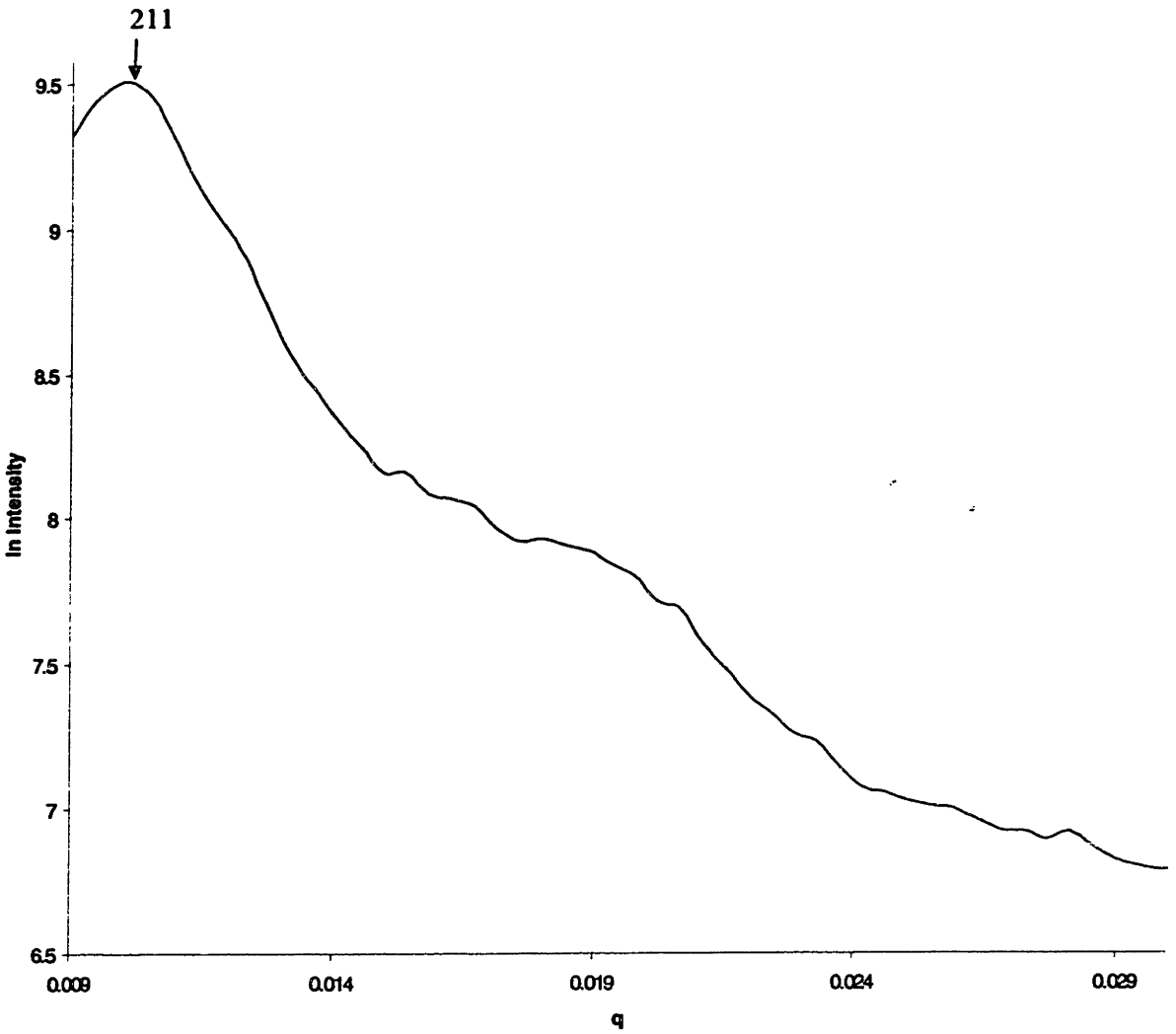

Figure A.3: SAXS Spectra for Sample 6, PI-DG. (P(PMDSS)-PI-P(PMDSS), 44K-167K-112K). taken at room temperature. Only the primary peak is clearly visible but it is shown in Chapter 3 that the sample is clearly double gyroid by TEM.

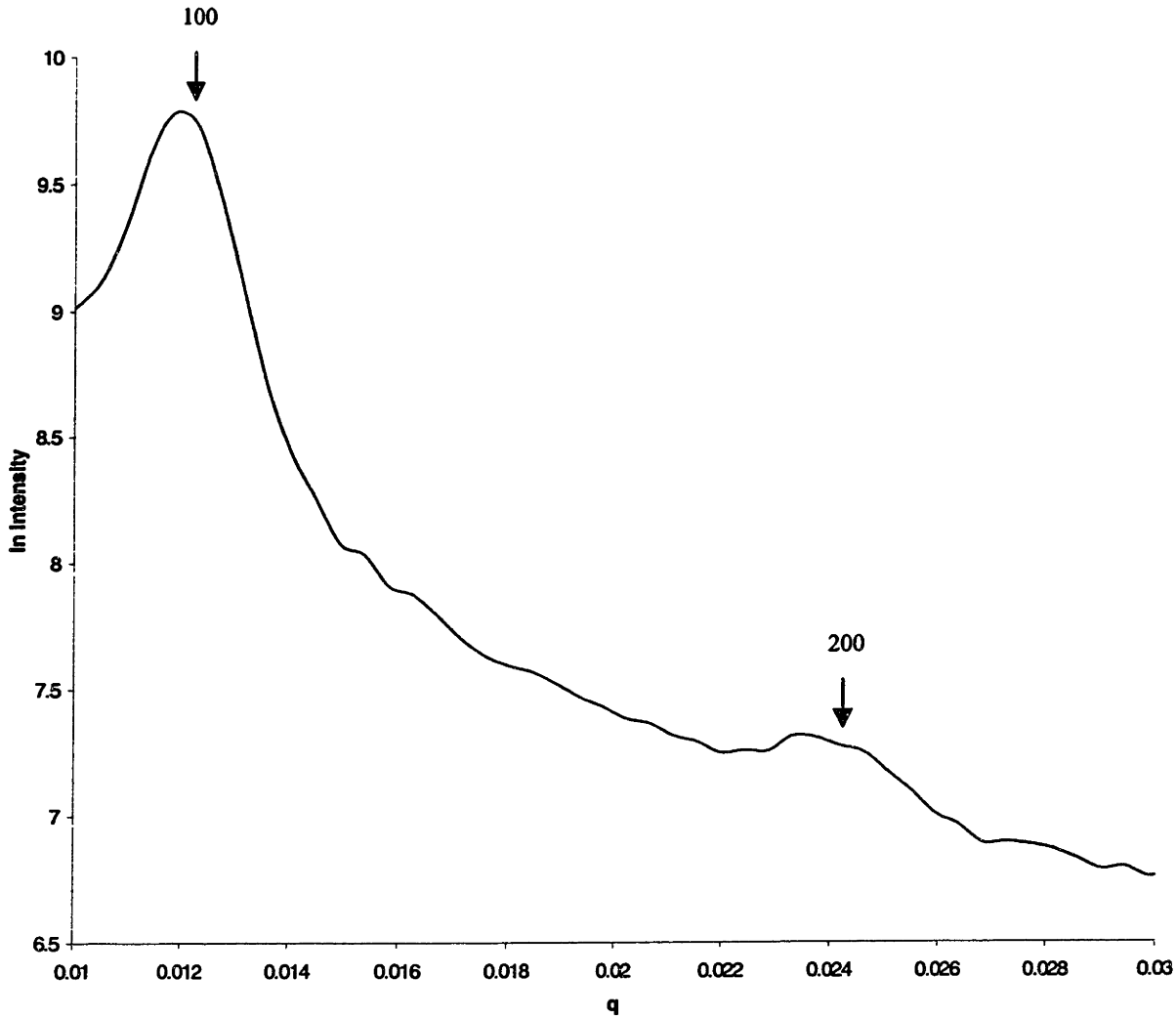

Figure A.4: SAXS Spectra for Sample 7, Lamellae. (P(PMDSS)-PI-P(PMDSS), 44K-167K-46K) taken at room temperature. The scattering pattern from this is the most clear out of the four that were taken for this thesis and lamellae are evident from both TEM and SAXS.

Appendix B

THE BET

Today, Aug. 4, 1997

We hereby declare that if agonolysis works better than plasma etching for removing isoprene than Bob Miller will buy Ned Thomas a case of quality wine. If the reverse is true than Ned Thomas will buy Bob Miller a case of live lobster.

R. D. Miller 8-4-97

N. Thomas 8-4-97

Withessed: Vanessa Kan

Appendix C

Ozone Production : Cautions, Instructions and Concentration Curves

The ozone machine was purchased from Ozone Engineering, Inc. and all the concentration curves were provided by Cindy Slezak. Ozone was generated using a corona discharge gap with a high voltage ceramic dielectric and a titanium counter part. A picture of the ozone machine is shown in **Figure C.1.**

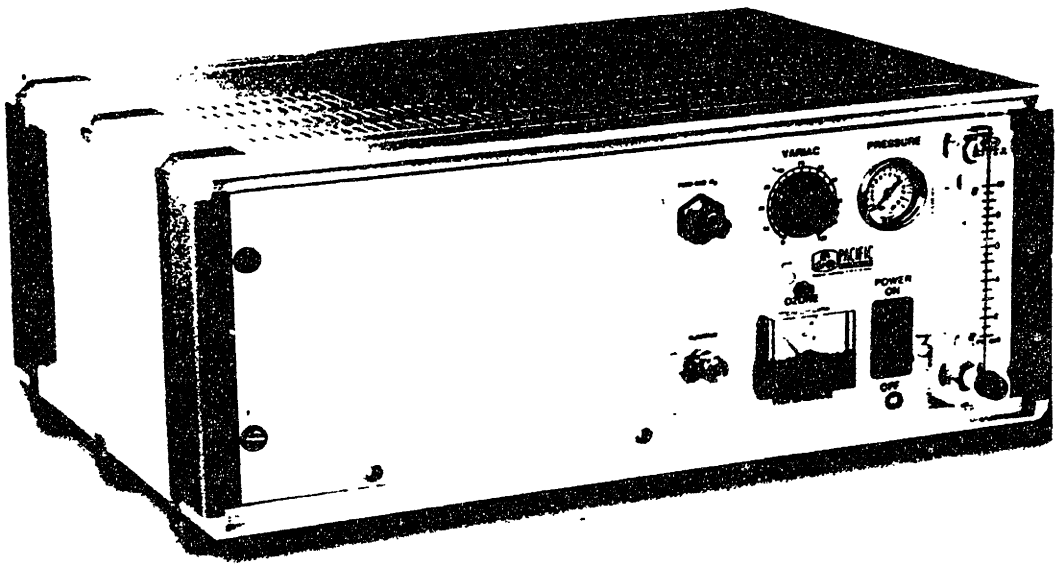

Figure C.1: Picture of the Ozone Generator Model L21.

The ozone which is generated is fed into a glass tube sample chamber with the output bubbled into a potassium iodide solution which forms iodine and turns orange when ozone is produced. The sample chamber is also fitted with a uv lamp (as discussed in **Section 4.2.2.** The spent potassium iodide solution is poured into a waste bottle for disposal after each experiment.

Safety precautions as outlined in the Pacific Ozone technology User Manual are as follows :

1. Oxygen is a fire hazard. It is very dangerous and vigorously accelerates the burning of combustible materials. To avoid fire and/or explosion, oil grease, cotton fibers and any other

combustible material must not be used on or near the Ozone or Oxygen Generators. Smoking, heat and any open flame should be kept at a distance of no less than five feet from any part of the system.

2. OSHA exposure limit to Ozone is 0.1 PPM for a period of 8 hours. The Materials Safety Data Sheet (MSDS) is given in Figure C.2.

3. Ozone is a highly toxic oxidizer. Ozone has a distinctive odor which is easily recognized at very low concentrates. If this odor present itself at any level unplug ghe Generator and contact your installer.

Important operating instructions and schematics are given in Figures A.3-A7 and ozone concentration curves are given in Figures A.8-A.12. These curves were generated by Cindy Slezak and give the concentration of ozone in g/cm^3 for various flow rates as a function of applied power.

Concentration of ozone in g/cm^3 can be converted through the equation :

$$G = C_1\left(\frac{T_1 R}{P_1 M}\right)10^{-4}$$

where G is the weight percentage in the carrier gas, C_1 the concentration of the ozone, M the molecular weight of the gas, R is the international gas constant given as 83,143.3 $cm^3 \cdot mb/g \cdot mol \cdot K$, T is the temperature at which the ozone is produced (usually 298 K) and P is the pressure at which the ozone is produced (usually 1013 mb). For our set-up, this equation becomes :

$$G = 0.07643C_1$$

Material Safety Data Sheet

From Genium's Reference Collection
Genium Publishing Corporation
1145 Catalyn Street
Schenectady, NY 12303-1836 USA
(518) 377-8855

MAR 1 1988 SAFETY OFFICE

No. 34
(Revision B)

Issued: February 1982
Revised: August 1987

SECTION 1: MATERIAL IDENTIFICATION

MATERIAL NAME: OZONE

DESCRIPTION (Origin/Uses): Obtained by passing air between two plate electrodes connected to an alternating current source of several thousand volts. Frequently generated by electronic equipment. Used as an air and water disinfectant; for bleaching textiles, oils, and waxes; and in organic synthesis.

OTHER DESIGNATIONS: Triatomic Oxygen; O_3; NIOSH *RTECS* #RS8225000; CAS #10028-15-6

MANUFACTURER/SUPPLIER: Available from several suppliers, including: PCI Ozone Corp., One Fairfield Crescent, West Caldwell, NJ 07006; Telephone: (201) 575-7052

COMMENTS: Ozone is a severe respiratory hazard.

Not Found

HMIS	
H 1	
F 2	R 1
R 1	I 4
PPE*	S 1
* See sect. 8	K 0

SECTION 2: INGREDIENTS AND HAZARDS

	%	HAZARD DATA
Ozone, CAS #10028-15-6; NIOSH *RTECS* #RS8225000	100	ACGIH Values 1987-88 TLV-TWA: 0.1 ppm, 0.2 mg/m^3* TLV-STEL: 0.3 ppm, 0.6 mg/m^3 OSHA PEL 1986 (29 CFR 1910, Subpart Z) 8-Hr TWA: 0.1 ppm, 0.2 mg/m^3 IDLH** Level: 10 ppm TOXICITY DATA Human, Inhalation, TC_{Lo}: 600 ppb/2 Hrs Human, Inhalation, TC_{Lo}:0.2 ppm/3 Hrs Human, Inhalation, TC_{Lo}: 100 ppm/1 Min Man, Inhalation, TC_{Lo}: 1860 ppb/75 Min

*This TLV-TWA is set to prevent ostensible or manifest injury; yet, sufficiently prolonged continual daily repeated eight-hour exposures may result in premature aging in a manner similar to that from exposure to ionizing radiation.

**Immediately dangerous to life or health.

SECTION 3: PHYSICAL DATA

Boiling Point ... -169.42°F (-111.9°C)
Vapor Pressure ... >1 atm
Water Solubility ... Negligible
Density of Gas (Air = 1) ... 1.6

Melting Point ... -315.4°F (-193°C)
% Volatile by Volume ... 100
Molecular Weight ... 48 Grams/Mole
pH ... Not Listed
Critical Temperature ... 10.22°F (-12.1°C)

Appearance and odor: Blue-colored gas or liquid; characteristic odor often associated with electrical sparks or lightning in concentrations of less than 2 ppm.

COMMENTS: The pungent characteristic odor of ozone is detectable above 0.01 ppm and becomes disagreeable (sulfurlike) above 1 to 2 ppm. CAUTION: Olfactory fatigue develops rapidly, so do not use odor as a preventative warning device.

SECTION 4: FIRE AND EXPLOSION DATA

Flash Point and Method	Autoignition Temperature	Flammability Limits in Air	LOWER	UPPER
Not Available	Not Available	% by Volume	Not Listed	Not Listed

EXTINGUISHING MEDIA: Use large amounts of water spray or fog to put out fires involving ozone. This material increases the intensity of combustion as compared to the burning or exploding of material in air or with a comparable amount of oxygen gas, O_2 (g). Use appropriate fire-fighting techniques to deal with the surrounding material.

UNUSUAL FIRE/EXPLOSION HAZARDS: CAUTION: Ozone is a powerful oxidizing agent, and during fires or heated conditions solutions containing ozone explode when warmed.

SPECIAL FIRE-FIGHTING PROCEDURES: Wear self-contained breathing apparatus with full facepieces operated in a pressure-demand or other positive-pressure mode.

SECTION 5: REACTIVITY DATA

Ozone is not stable. Hazardous polymerization cannot occur.

CHEMICAL INCOMPATIBILITIES: Ozone is chemically incompatible with all oxidizable materials, both organic and inorganic.

CONDITIONS TO AVOID: Avoid ignition sources such as heat, sparks, and open flame. Ozone is unstable at ordinary temperatures because it spontaneously decomposes to oxygen gas. Keep it away from heat, flame, strong reducing agents, and combustible materials such as grease, oils, and fats.

PRODUCTS OF HAZARDOUS DECOMPOSITION: Ozone spontaneously decomposes to oxygen gas even at ordinary room temperatures.

Figure C.2: Material Safety Data Sheet for Ozone.

5.4 Problem Diagnostic Guide

DANGER: High Voltage High Capacitance

Requires qualified electrician for open door problem check

Before opening door unplug Generator power cord from outlet

PROBLEM	POSSIBLE CAUSE	ACTION
1. No green light with power on	a. Plug not seated in outlet b. No power in outlet c. Main fuse in generator d. Door not latched e. Door interlock switch f. Toggle switch g. Loose/corroded connections h. Green 120V. neon light	a. Check plug in outlet b. Check circuit breaker c. Replace fuse d. Close door e. Check switch lever f. Test for proper action g. Replace connector h. Replace light
2. Green light on but red light and DC Volt meter off.	a. Variack Control b. Feed gas flow too low c.Unit not mounted vertical d. PC board fuse blown e. Air flow switch piston Sticking f. Control relay g. Variack	a. Turn control 0 - 100 b. Adjust flow meter 20-50 SCFH c. Remount unit vertical d. DISCHARGE CAPACITORS replace fuse (7 amp max) e. Remove air flow switch & clean f. Check for proper operation g. Check wires
3. Red light will not turn off after feed gas is turned off.	a. Feed gas flow switch piston sticking b. Relay stuck in closed position	a. Clean inside flow switch b. Replace relay
4. High back pressure on PSI gauge. (10 PSIG or more)	a. Obstruction in Ozone outlet tube b. Defective gauge c. Dielectric contaminated	a. Remove obstruction recheck gauge b. replace gauge c. Return unit to factory
5. Cooling fan does not run after 10 minutes.	a. Fan blades jammed against grill b. Fan plug not connected c. Temp switch defective d. Ambient temp below 40 deg. F	a. Remove obstruction fan must turn freely b. Plug in fan c. Replace fan temp switch
6. Red light erratic DC meter not reading steady.	a. Water in dielectric b. Shorted dielectric c. Broken dielectric	a. Remove water run dry air or Oxygen for 8 hours b. Clean Generator enclosure inside c. Return to factory

Figure C.3: Diagnostic guide for problems for the ozone generator, Model L21.

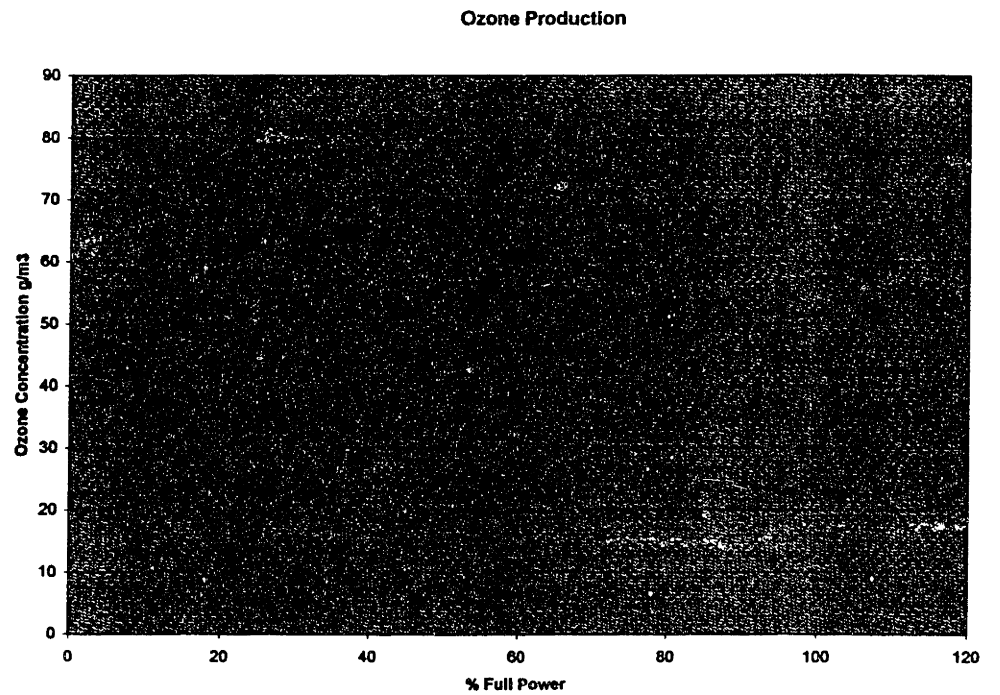

Figure C.4: Ozone production curve for a flow rate of 5 scfh of oxygen.

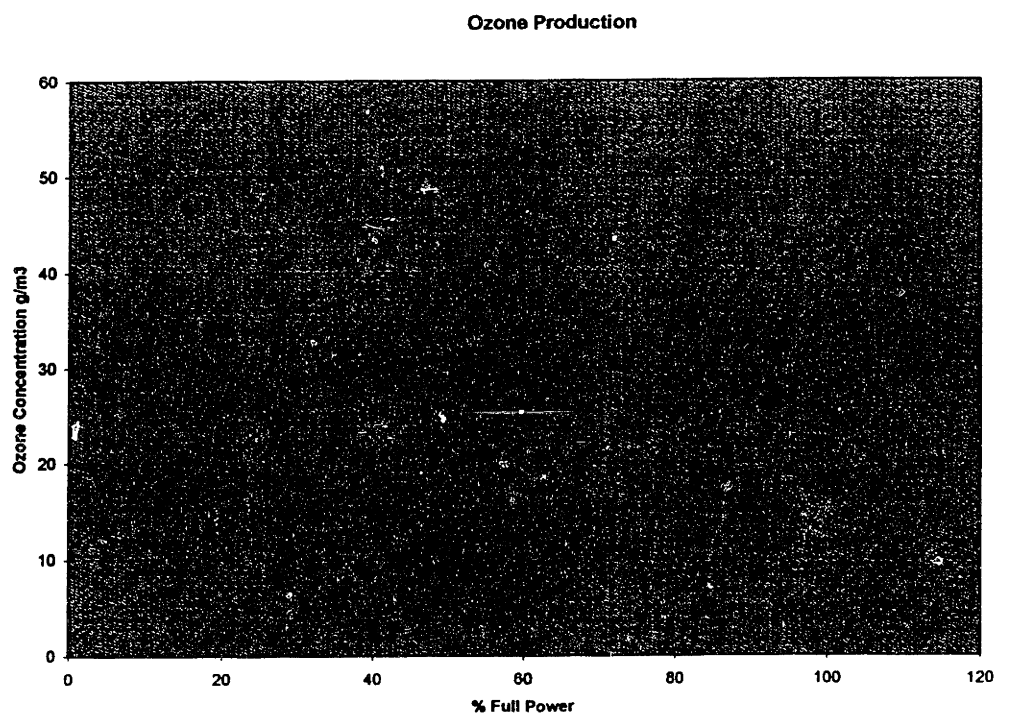

Figure C.5: Ozone production curve for a flow rate of 10scfh of oxygen.

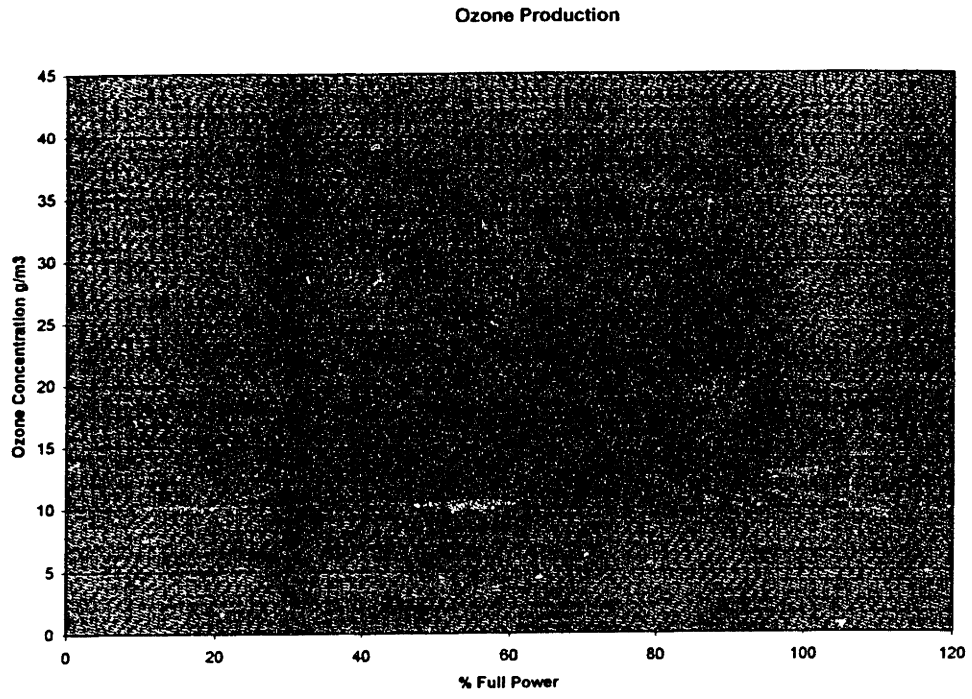

Figure C.6: Ozone production curve for a flow rate of 15 scfh of oxygen.

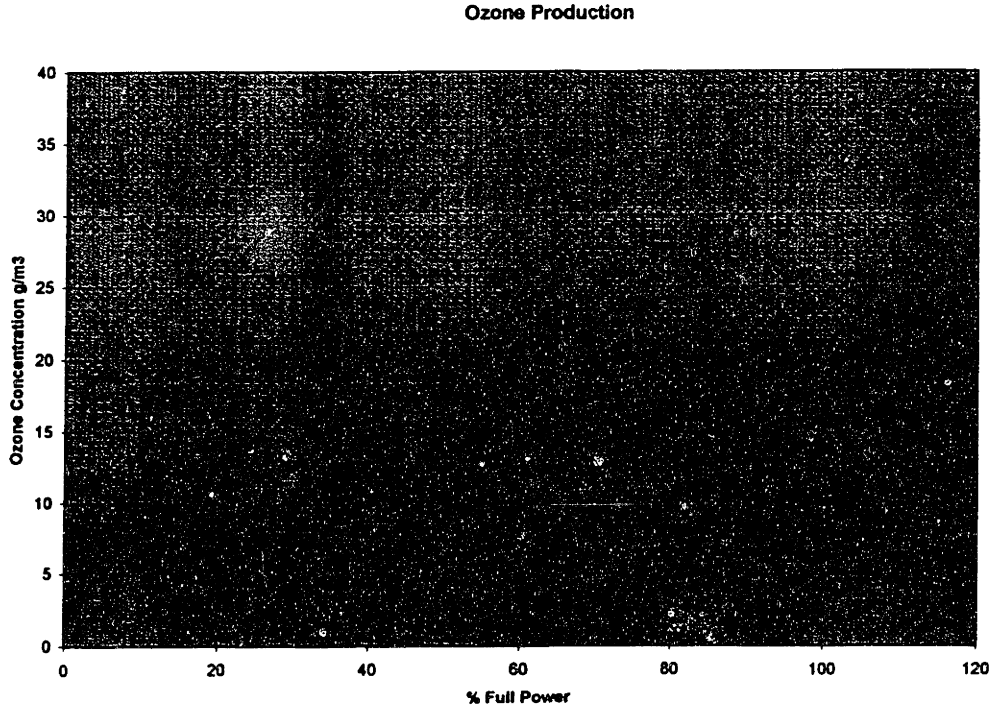

Figure C.7: Ozone production curve for a flow rate of 20 scfh of oxygen.

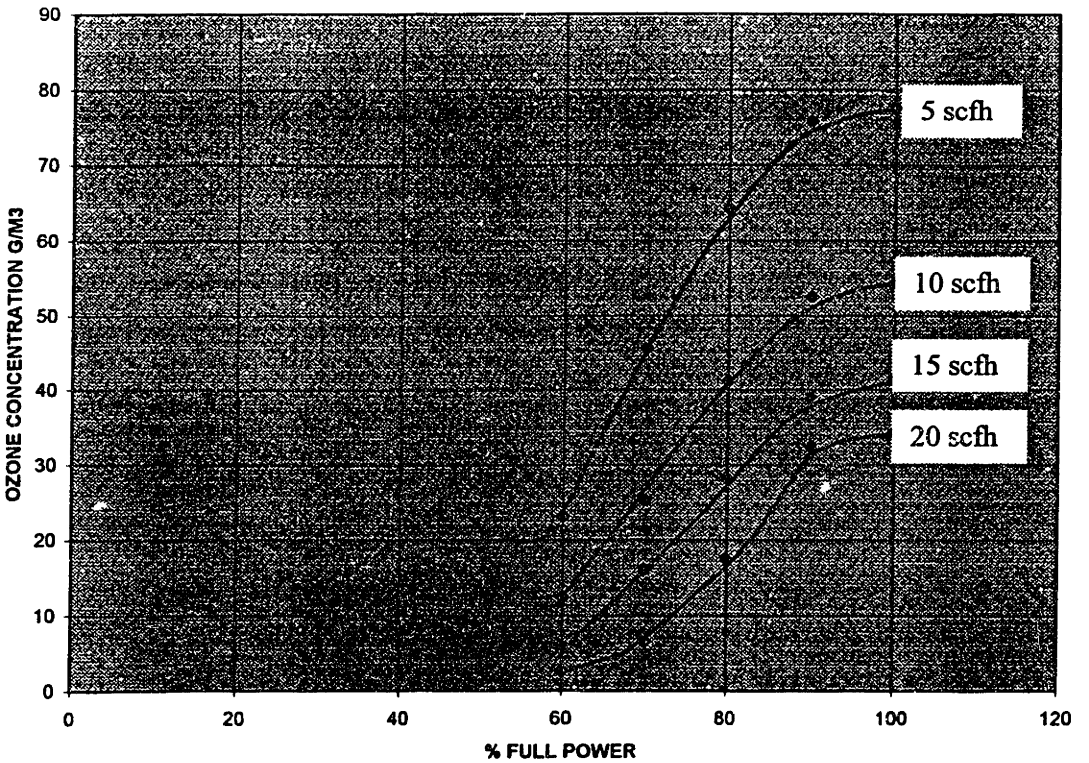

Figure C.8: Ozone concentration as a function of % full power, for a pressure of 6.5 psig for different flow rates, ranging from 5 scfh to 20 scfh. Ozone production begins at 50% full power. It can be seen that the higher the flow rate, the lower the ozone concentration produced.

Appendix D

Determination of Film Stoichiometry through Rutherford Backscattering Spectrometry (RBS) and Forward Recoil Spectrometry (FRES)

RBS and FRES were used to determine stoichiometries for the materials studied in this thesis as explained in **Chapter Four.** Data for RBS were collected at both 3.4 and 2.0 MeV helium beam energies due to the different sensitivities of sample elements at the different beam energies. FRES data was collected at 2.7 MeV. A program named RUMP was then used to determine stoichiometries by simulating data to fit the experimental spectra. To do this, within the program the experimental configuration (such as sample-to-detector angle, beam energy, ion type, etc.) is first specified. Layers are then simulated to match the experimental data. For example, the first layer generated is the silicon substrate, with stoichiometry of Si 1 and an arbitrarily large areal density (e.g. 20000 /cm^2). The silicon substrate provides an accurate internal standard. A second layer is then generated on top of the silicon substrate and the stoichiometry changed until the simulated data matches the collected spectra. In order to match the peak height, the relative amount of one element to another is changed. In order to simulate the peak width, the layer thickness is changed.

With simulations for each sample at both 2 MeV and 3.4 MeV, the stoichiometries of all elements except the hydrogen were able to be correlated by equating the oxygen concentrations in both the 2.0 MeV and 3.4 MeV spectra since the cross-section of oxygen at these two energies is similar. In both the 2.0 MeV and 3.4 MeV the absolute amount of oxygen should be identical for each sample. By equating the oxygen in the two spectra, a ratio could be determined between the simulated amount of oxygen at both 2 MeV and 3.4 MeV. This scaling ratio is given as :

$$\text{Scaling ratio} = \frac{\text{simulated amount of O at 2.0 MeV}}{\text{simulated amount of O at 3.4 MeV}}$$

Thus the amount of silicon at 2.0 MeV could be correlated to the amount of C and O at 3.4 MeV by multiplying the simulated amount of silicon at 2.0 MeV by this scaling ratio.

The amount of stoichiometric hydrogen then had to be correlated to the other elements in the material using the FRES data. In order to do this, the areal density of carbon and hydrogen in the unknown samples needed to be determined.

In order to determine the areal densities of our unknown samples a polystyrene standard with a known C:H ratio of 1:1 was used to normalize the data. Since the ratio of C and H is the same in PS, the atomic density (N) for both C and H are identical and is given by :

$$N = \frac{\rho \times n \times N_A}{MW}$$

where ρ is the density of PS = 1.05 g/cm^3, n the number of H or C atoms in PS = 8, N_A Avagadro's number = 6.022 x 10^{23} atoms/mol and MW the molecular weight of PS = 104 g/mol. Thus, for C and H in PS, the atomic density N calculated to :

$$N_{C,H}^{PS} = 4.864 \times 10^{22} \text{ atoms/cm}^3$$

Using this atomic density, the areal density can be calculated through the equation :

$$\text{Areal density, (Nt)} = \text{atomic density (N)} \times \text{thickness (t)}$$

Areal density is used in the simulations because a sample with a density of X atoms/cm^3 and a thickness of 1000 Å will have the identical backscattering spectrum as a sample with a thickness of 500 Å and a density of 2X atoms/cm^3. Thus, for the PS sample with a measured thickness of 1.4 x 10^{-5} cm, the areal density is determined to be :

$$(Nt)_{PS} = 6.8 \times 10^{17} \text{ / cm}^2$$

For the unknown samples, the areal density of the carbon can be calculated through the relationship :

$$\left(\frac{(Nt)_{PS,C}}{(A/Q)_{PS,RBS}} \right)_{PS,C} = \left(\frac{(Nt)_{unknown,C}}{(A/Q)_{unknown,RBS}} \right)_{unknown,C}$$

where A is the total number of counts and Q the total charge. The counts for both the PS and the unknown sample are obtained by integrating the raw RBS data and the charge is the amount of charge collected by the detector during the experiment. The higher the normalized areal density of the carbon in the unknown sample with respect to charge, the more carbon there is in the sample, so the higher the counts with respect to carbon.

Rearranging yields :

$$(Nt)_{unknown,C} = \left(\frac{(Nt)_{PS,C} \text{ x } (counts / charge)_{unknown, RBS}}{(counts / charge)_{PS, RBS}} \right)$$

Similarly for hydrogen, the areal density can be calculated using the FRES data through the relationship :

$$(Nt)_{unknown,H} = \left(\frac{(Nt)_{PS,H} \text{ x } (counts / charge)_{unknown, FRES}}{(counts / charge)_{PS, FRES}} \right)$$

where the counts for both the PS and the unknown sample are obtained through integration of the raw FRES data and the charge is the amount of charge collected by the detector over the course of the experiment.

For the polystyrene standard, the RBS data was collected at 3.4 MeV for a charge of 10 μC and the counts under the carbon peak determined to be 2200, while the FRES data was collected for a charge of 2 μC resulting in the hydrogen peak counts of 1630.
Thus, for the unknown samples, $(Nt)_C$ is given by :

$$(Nt)_{uknown,C} = \left(\frac{6.802 \text{ x } 10^{17} \text{ x } (counts)_{unknown, RBS}}{220 \text{ x } (charge)_{unknown, RBS}} \right)$$

while $(Nt)_H$ was calculated by :

$$(Nt)_{uknown,\ H} = \left(\frac{6.802 \times 10^{17} \times (counts)_{unknown,\ FRES}}{815 \times (charge)_{unknown,\ FRES}} \right)$$

Once $(Nt)_{unknown,\ C}$ and $(Nt)_{unknown,\ H}$ are known, the ratio of C:H is simply the ratio of the two areal densities, allowing the determination of the relative stoichiometry of the carbon and hydrogen in the sample. Since the amount of carbon was calculated through the simulation of the RBS data, the amount of hydrogen is simply determined through this ratio :

$$\text{Stoichiometric value of hydrogen} = \left(\frac{(Nt)_H}{(Nt)_C} \right) * \text{Stoichiometric value of carbon}$$

With all elemental stoichiometries determined in the thin-film sample, a spreadsheet was created, (**Table D.1.**) to calculate the weight percentage for each element in the sample, as well as a normalized stoichiometry, based on silicon being equal to one.

The normalized stoichiometry was computed by normalizing the elemental stoichiometries for each element and dividing them by the stoichiometry of silicon. The formulas for each sample were then compared and analyzed as discussed in **Section 4.3.**

Table D.1 : Spreadsheet for determining the stoichiometry of the P(PMDSS) thin films before and after oxidation.

Processing	Charge C (μC)[a]	charge H (μC)[b]	O (2.0 MeV) [c]	O (3.4 MeV)[d]	Scaling Ratio [e]	C Gross [f]	H Gross [g]	Si (2MeV) [h]	C (3.4MeV) [i]	Si (norm.)[j]	O [k]	H [l]
UV only in air	20	2.2	10	2	0.200	1262.51	648	5.5	0.4	1.1	2	0.50
ozone only	4	2	0.2	1	5	1427	2047	0.07	4	0.35	1	3.10
ozone + UV	25	2.5	25	0.7	0.028	690.58	324	16	0.4	0.448	0.7	0.51
as-is*	20	1.2	2	0	N/A	4802.55	1887	3	23 (2MeV data)	3	2	40.66

Since there is no oxygen in the as-cast sample, the 2 MeV data was for the calculations.
[a] Charge collected from the 2.0 MeV RBS experiment. [b] Charge collected from the FRES experiment
[c] Stoichiometry determined for O from the 2.0 MeV RBS data. [d] Stoichiometry determined for O from the 3.4 MeV RBS data.
[e] Scaling ratio (d + c) for correlating the 2.0 MeV to the 3.4 MeV data.
[f] Gross integration of the counts for the Carbon peak from the 2.0 MeV data.
[g] Gross integration of the counts for the Hydrogen peak from the 3.4 MeV data.
[h] Stoichiometry determined for Si from the 2.0 MeV RBS data.
[i] Stoichiometry determined for C from the 3.4 MeV RBS data.
[j] Stoichiometry for Si determined from the 2.0 MeV RBS data, normalized to the 3.4 MeV data (h + j)
[k] Stoichiometry determined for O from the 3.4 MeV RBS data.
[l] Stoichiometry for H, determined from the areal density. (see below)

Table D.1 : Spreadsheet for determining the stoichiometry of the P(PMDSS) thin films before and after oxidation. (cont.)

Processing	Nt C (/cm2) [m]	Nt H (/cm2) [n]	C to H Ratio [o]	Sum Total	Si% [q]	C% [r]	O% [s]	H% [t]	Si	C [v]	O [w]	H [x]
UV only in air	1.9517E+17	2.4583E+17	0.7939	68.1	45.2	7.04	46.99	0.74	1	0.36	1.82	0.45
ozone only	1.103E+18	8.5421E+17	1.2913	76.9	12.7	62.4	20.81	4.03	1	11.4	2.86	8.85
ozone + UV	8.5406E+16	1.0816E+17	0.7896	29.1	43.2	16.5	38.55	1.74	1	0.89	1.56	1.13
as-is	7.4243E+17	1.3124E+18	0.5657	433	19.4	63.7	7.396	9.4	1	7.67	0.67	13.55

[m] Areal density of C determined from the 3.4 MeV RBS data. Where N is the atomic density and t thickness.

[n] Areal density of H determined from the FRES data.

[o] Ratio of C to H which gives the stoichiometry of H in the sample. (m + n).

[p] Total "weight" of the sample. Σ(RAM of element * stoichiometry of element) = ((12*i) + (28*j) + (16*k)+(1*l))

[q-t] Weight percentage of element in sample. (RAM of element * stoichiometry of element) / total weight from p

[u-x] Normalized stoichiometry with the stoichiometry of Si set to 1.0.

Appendix E

X-Ray Photoelectron Spectroscopy (XPS), Auger Electron Spectroscopy (AES), Rutherford Backscattering Spectrometry (RBS), Forward Recoil Spectrometry (FRES) and Fourier Transform Infrared Spectra

An outline of these experimental techniques is given in Chapter Four. The data presented here is summarized in Tables 4.3, 4.5 and 4.6. All XPS data reported here is for a sample-to-detector angle of 45° unless otherwise noted. Spectra are interpreted in Chapter Four.

E.1 : Data for As-cast P(PMDSS)

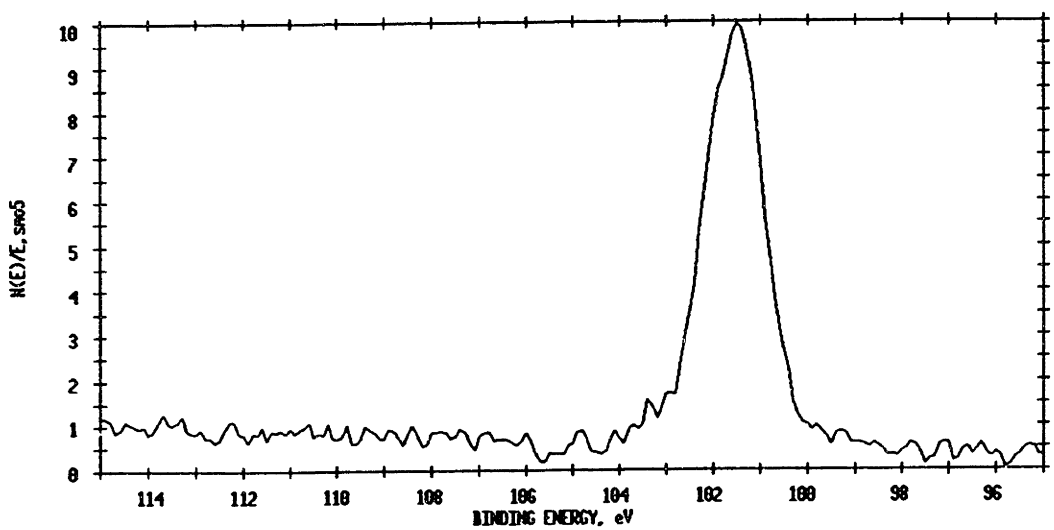

Figure E.1.1: XPS Spectra of the raw Si2p peak for as-cast P(PMDSS).

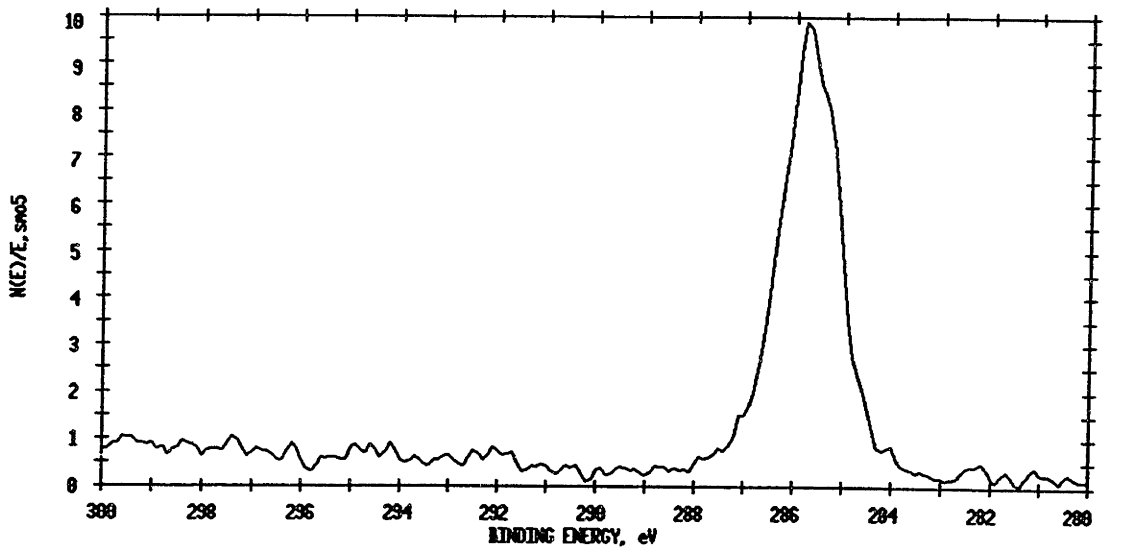

Figure E.1.2: XPS Spectra of the raw C1s peak for as-cast P(PMDSS).

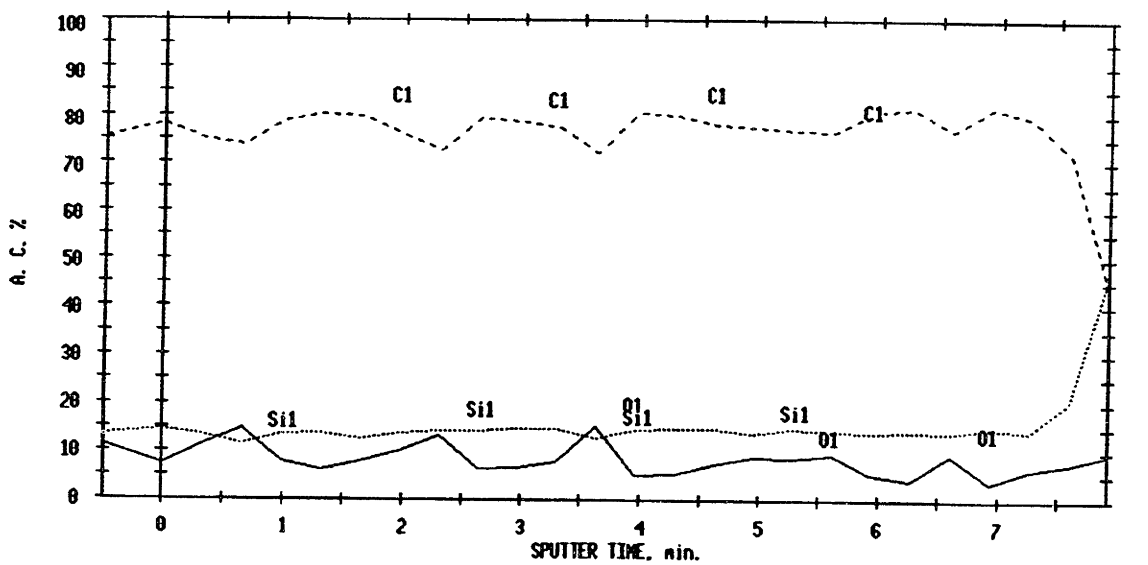

Figure E.1.3: AES depth profile for as-cast P(PMDSS)

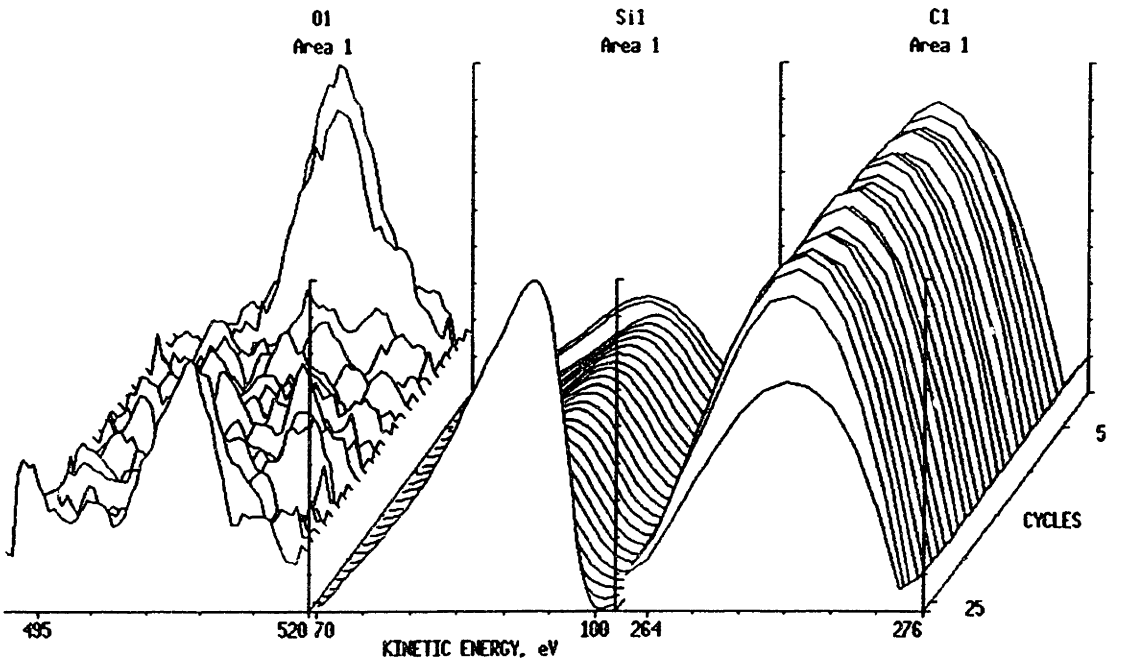

Figure E.1.4: AES composition profile, back view for as-cast P(PMDSS).

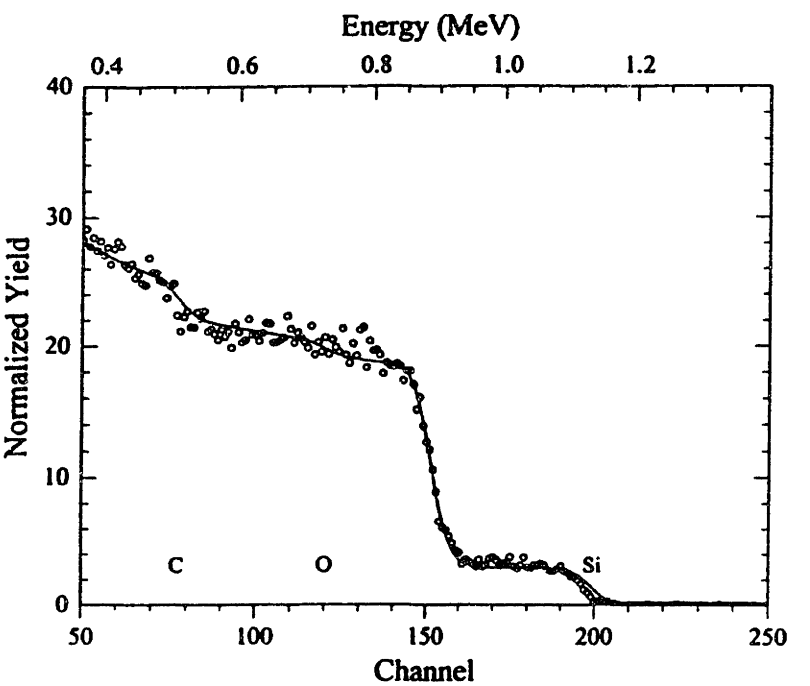

Figure E.1.5: 3.0 MeV RBS spectra for as-cast P(PMDSS).

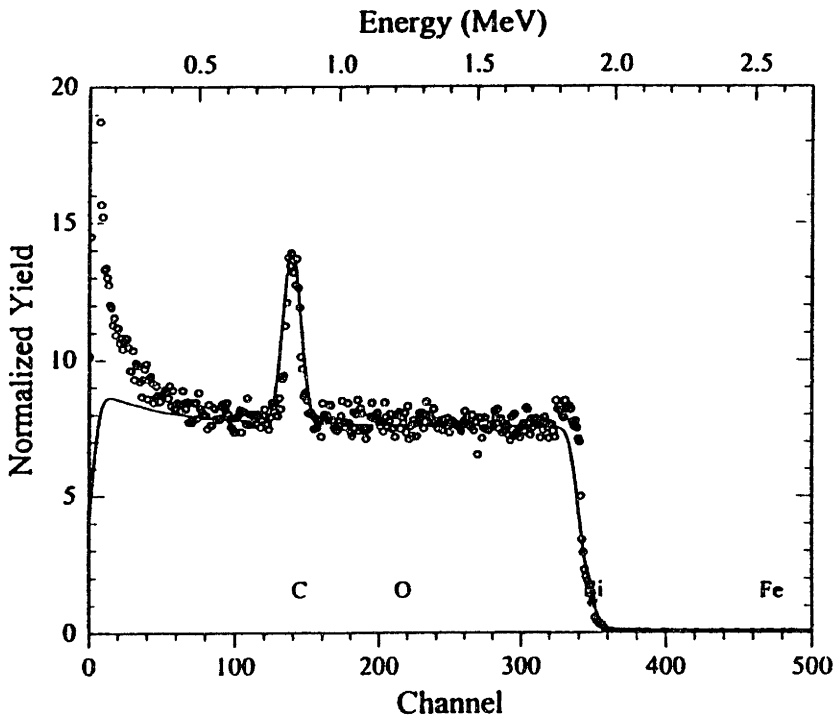

Figure E.1.6: 2.0 MeV RBS spectra for as-cast P(PMDSS).

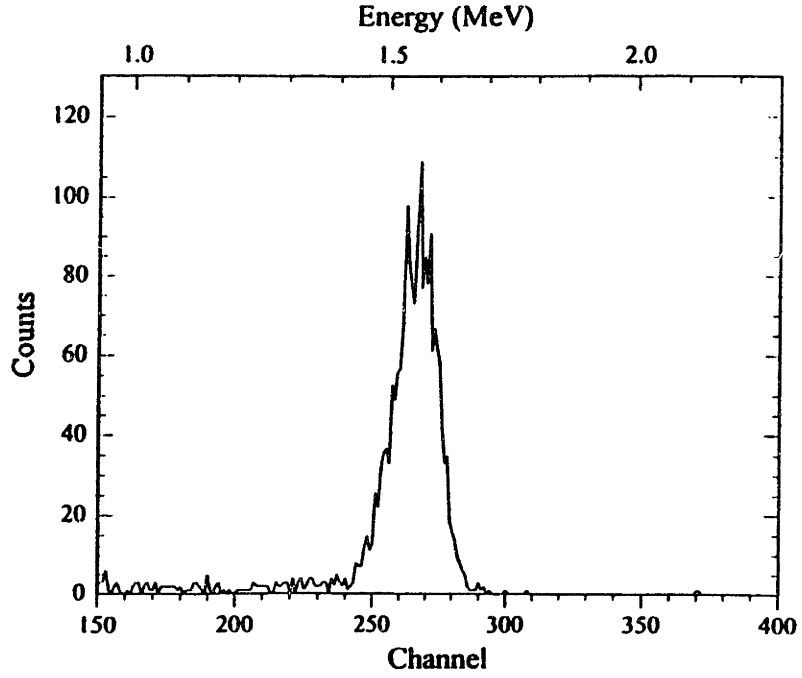

Figure E.1.7: FRES spectra for as-cast P(PMDSS).

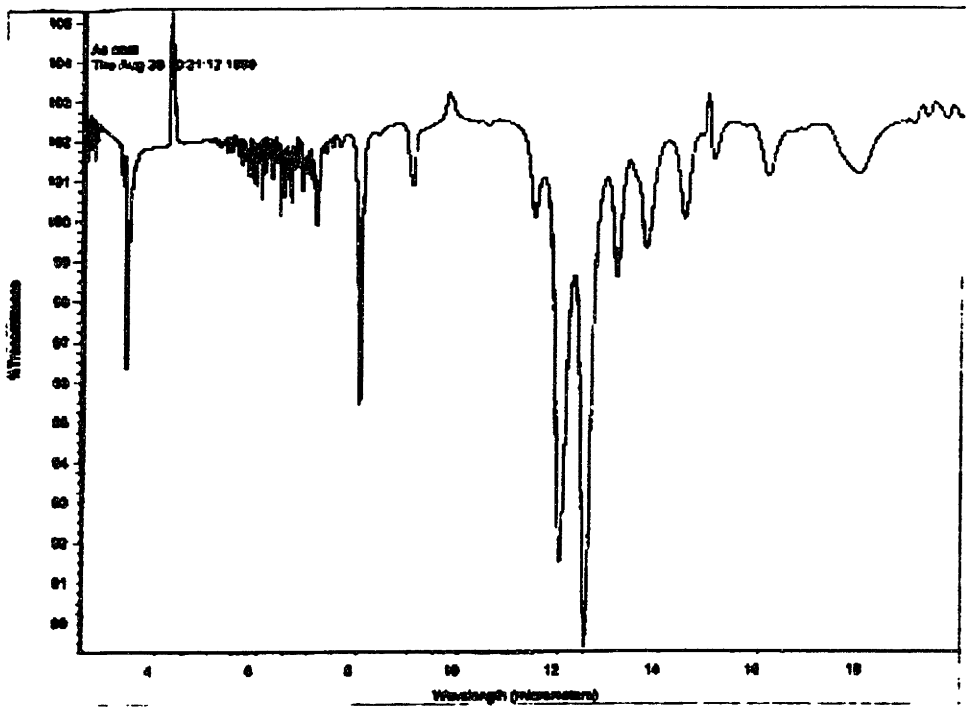

Figure E.1.8: FTIR Spectra for as-cast P(PMDSS).

E.2: Data for P(PMDSS) Exposed to Ozone for One Hour

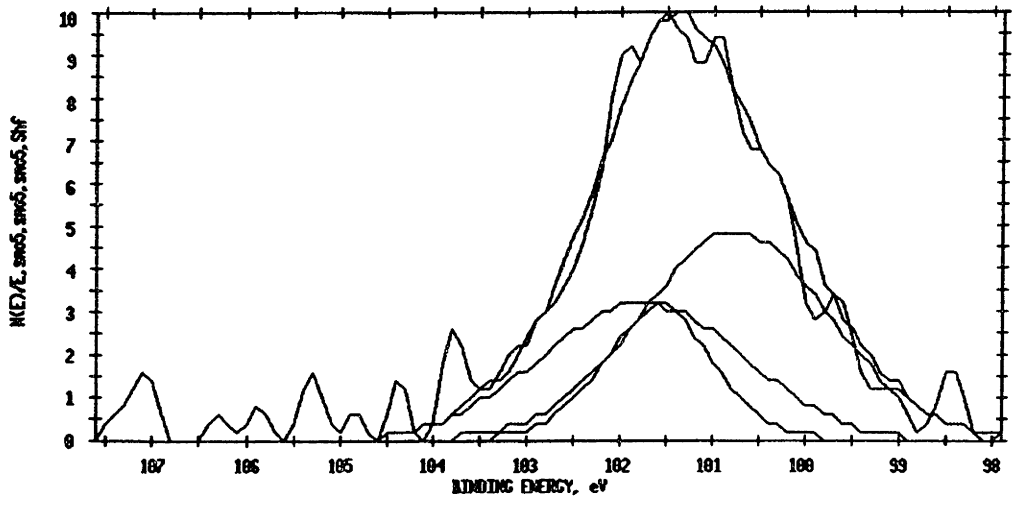

Figure E.2.1: XPS Spectra of the normalized Si2p peak for P(PMDSS) exposed to ozone for one hour.

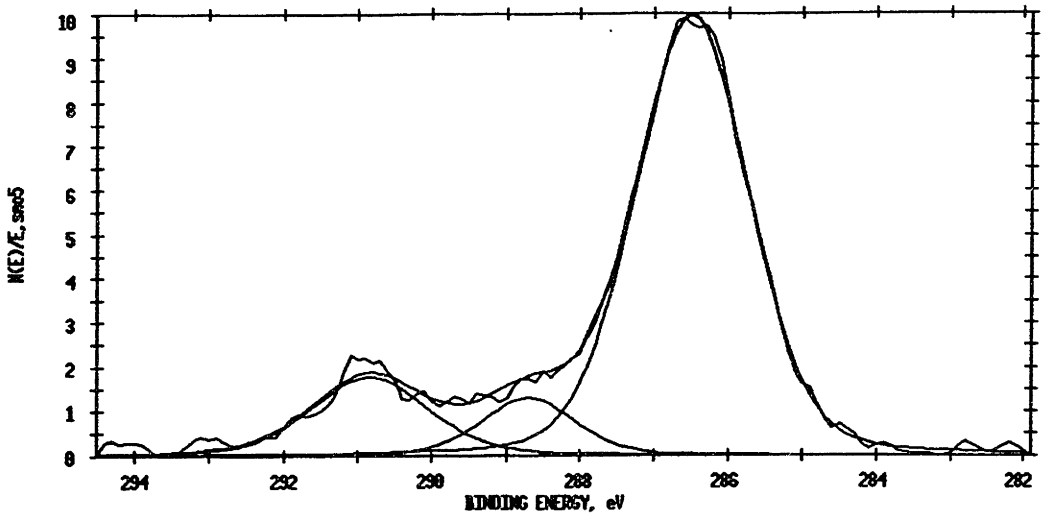

Figure E.2.2: XPS Spectra of the raw C1s peak for P(PMDSS) exposed to ozone for one hour.

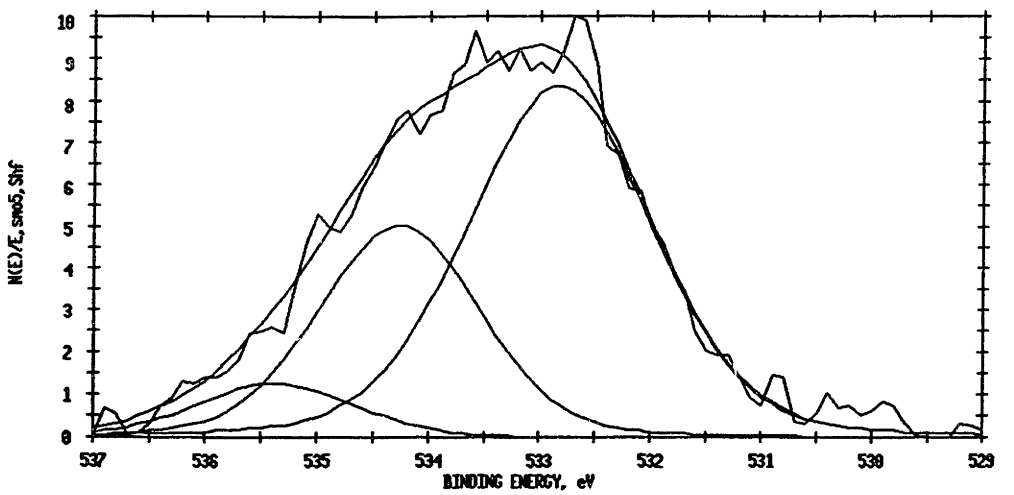

Figure E.2.3: XPS Spectra of the normalized O1s peak for P(PMDSS) exposed to ozone for one hour.

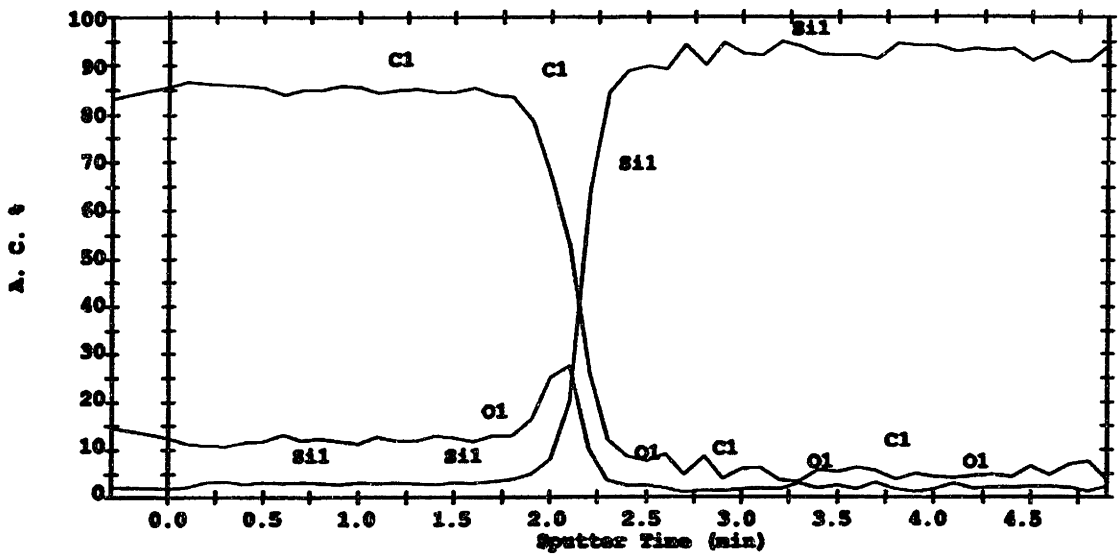

Figure E.2.4: AES depth profile for P(PMDSS) exposed to ozone for one hour.

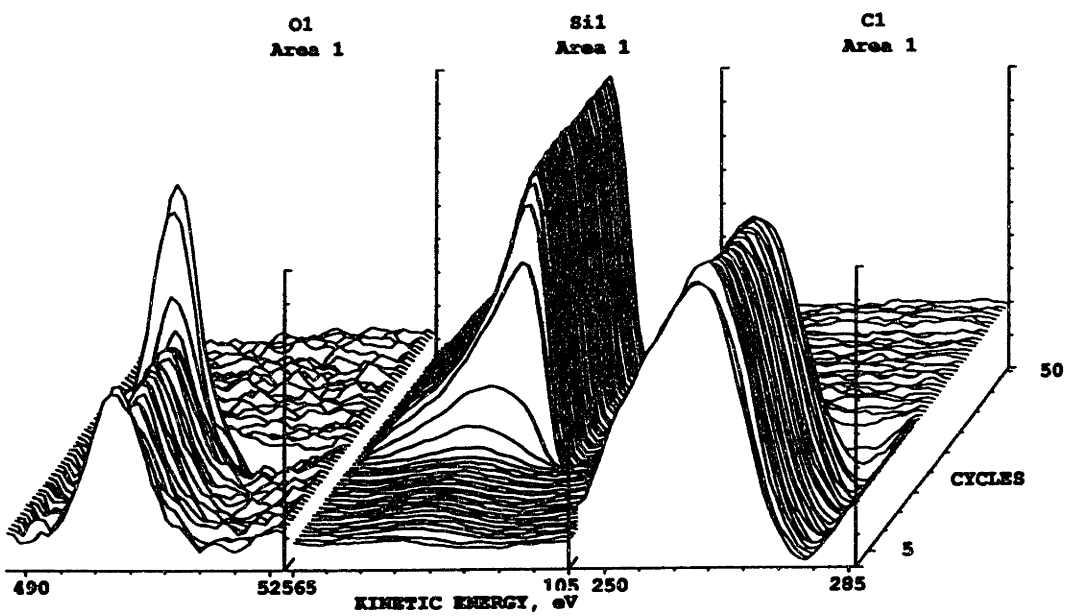

Figure E.2.5: AES composition profile, front view for P(PMDSS) exposed to ozone for one hour.

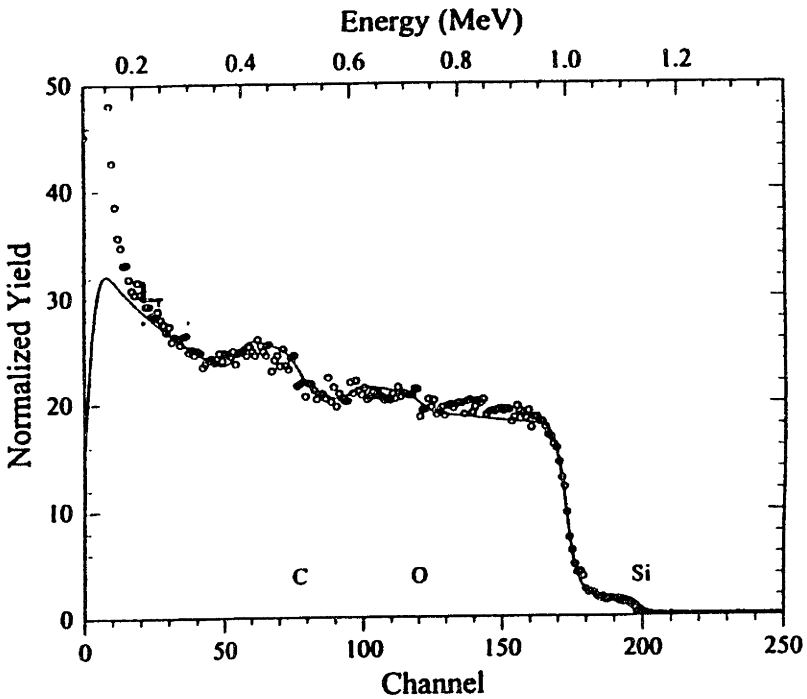

Figure E.2.6: 3.0 MeV RBS spectra for P(PMDSS) exposed to ozone for one hour.

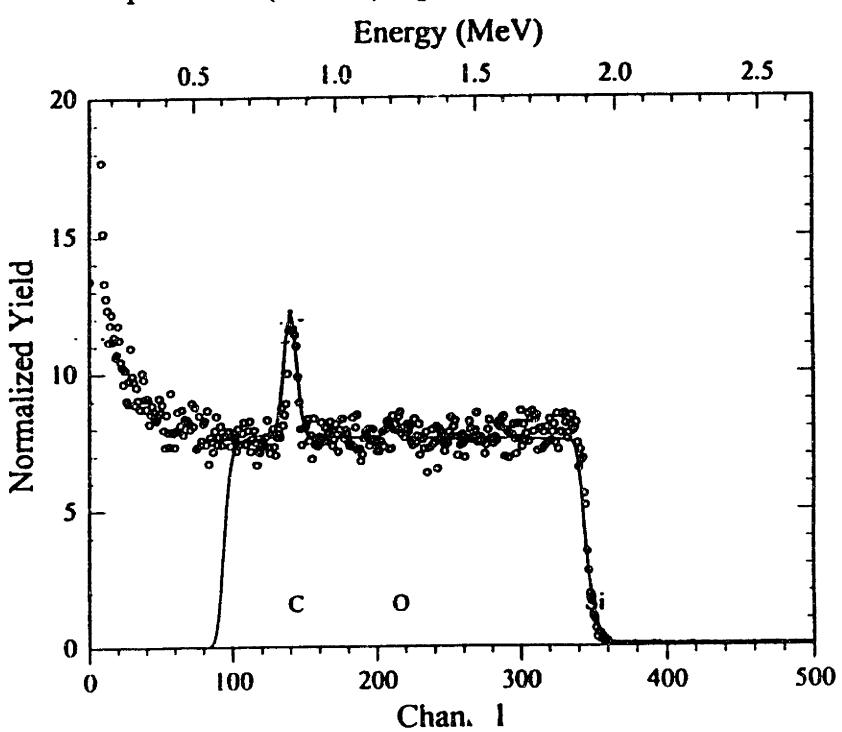

Figure E.2.7: 2.0 MeV RBS spectra for P(PMDSS) exposed to ozone for one hour.

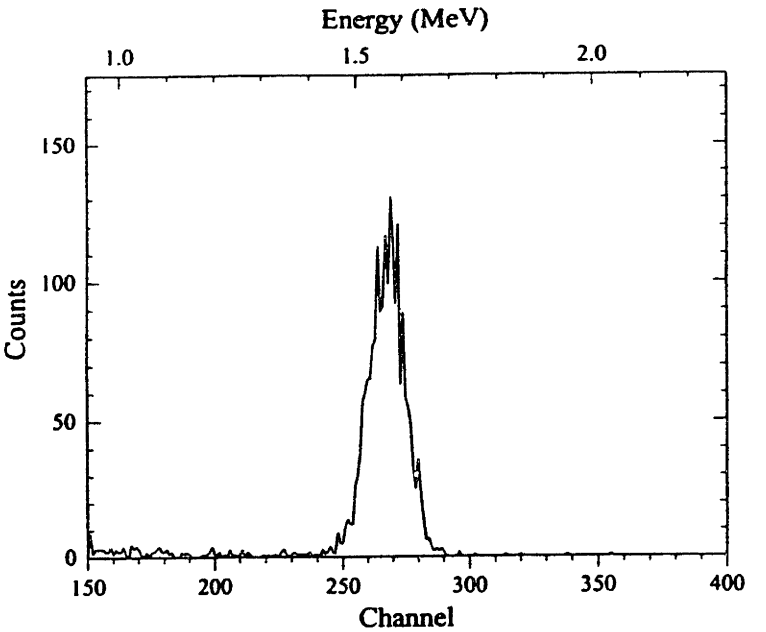

Figure E.2.8: FRES spectra for P(PMDSS) exposed to ozone for one hour.

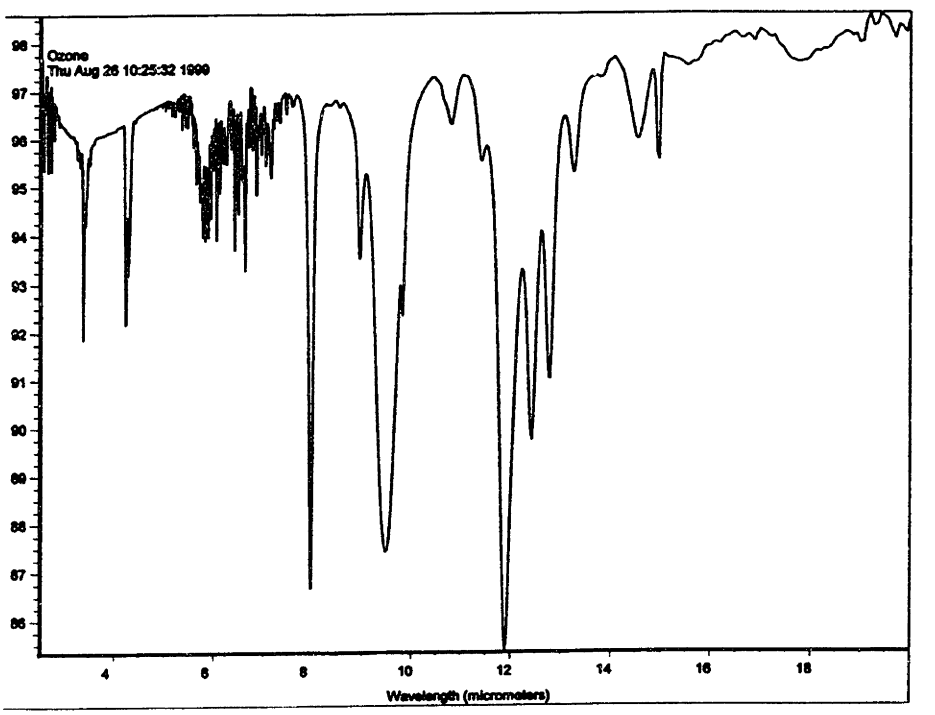

Figure E.2.9: FTIR Spectra for P(PMDSS) exposed to ozone for one hour.

E.3: Data for P(PMDSS) Exposed to Uv in Air for One Hour

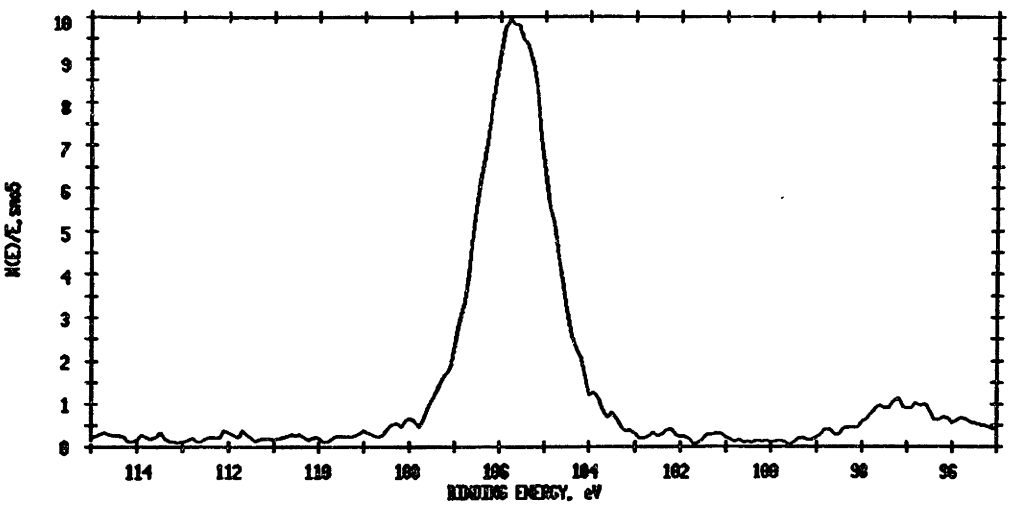

Figure E.3.1: XPS Spectra of the raw Si2p peak for P(PMDSS) exposed to uv in air for one hour.

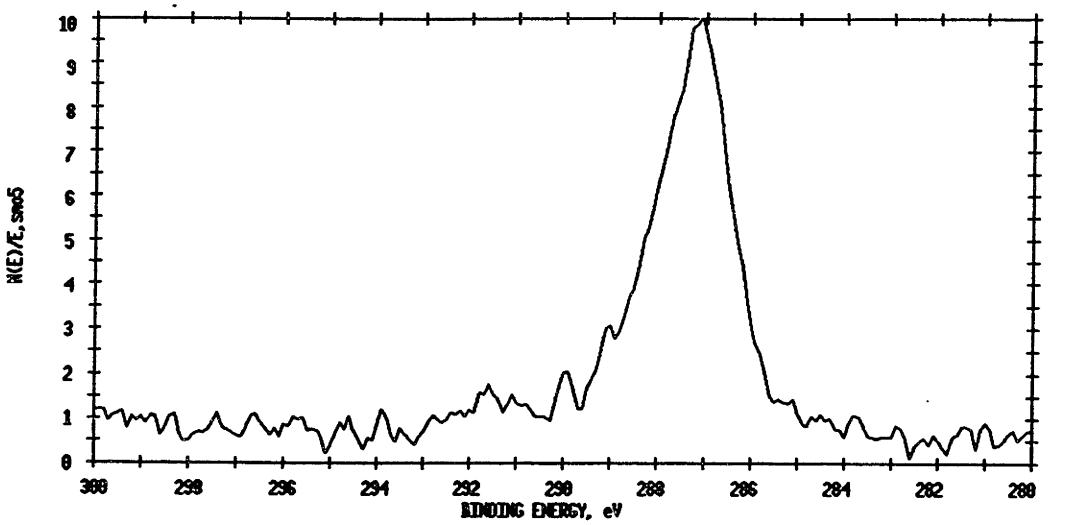

Figure E.3.2: XPS Spectra of the raw C1s peak for P(PMDSS) exposed to uv in air for one hour.

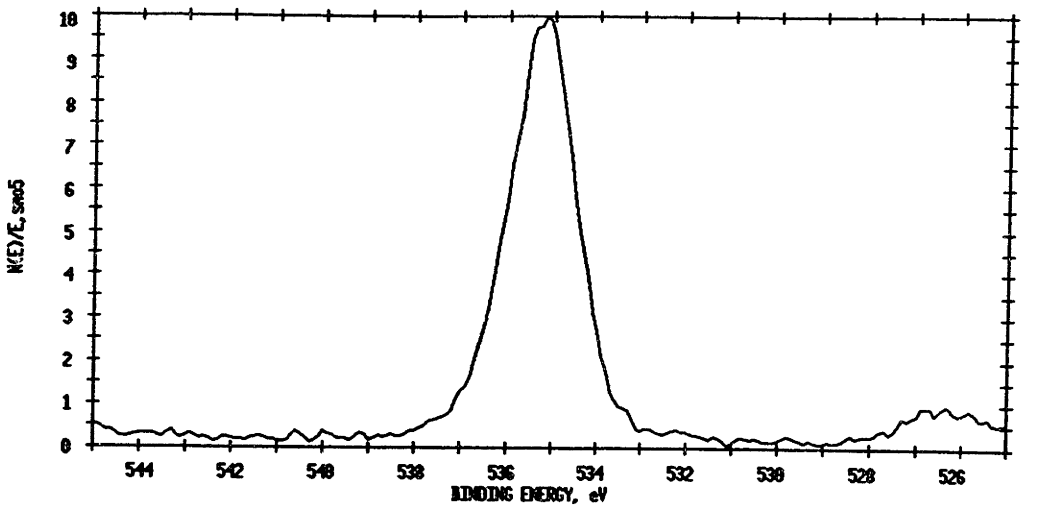

Figure E.3.3: XPS Spectra of the raw O1s peak for P(PMDSS) exposed to uv in air for one hour.

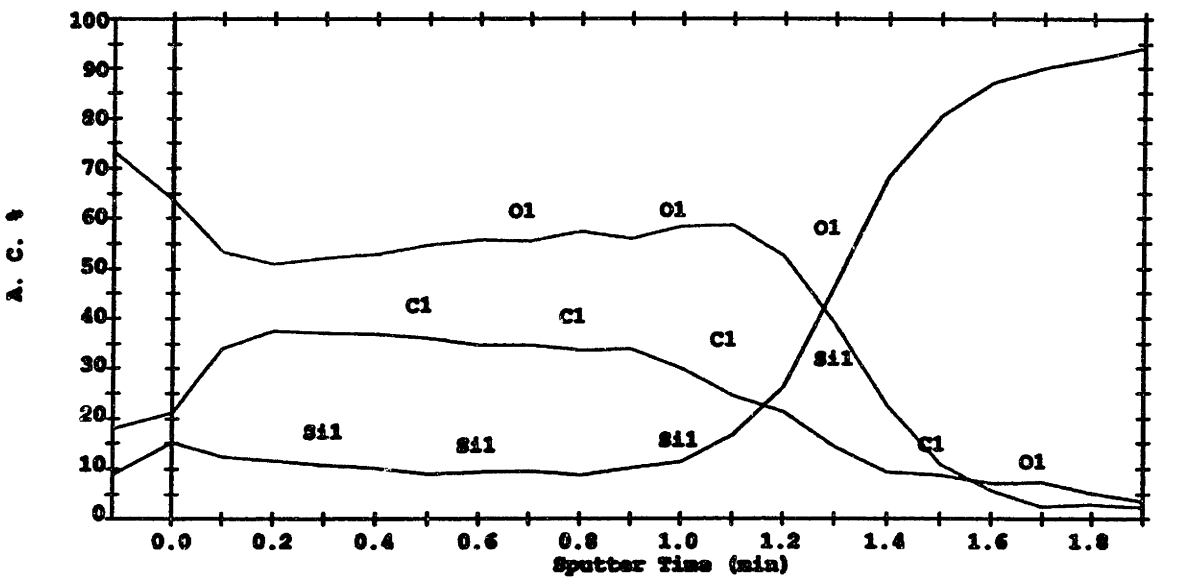

Figure E.3.4: AES depth profile for P(PMDSS) exposed to uv in air for one hour.

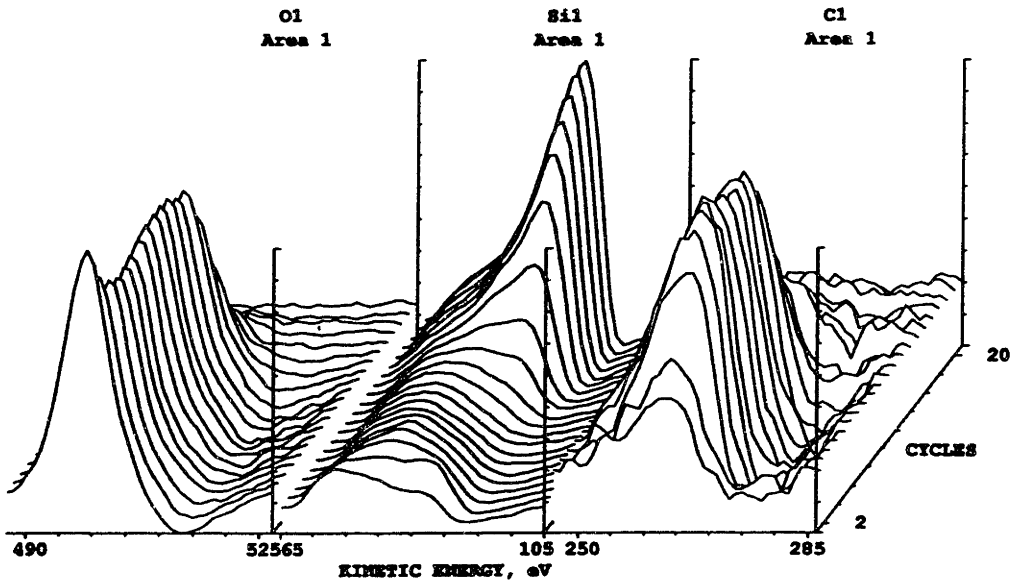

Figure E.3.5: AES composition profile, front view for P(PMDSS) exposed to uv in air for one hour.

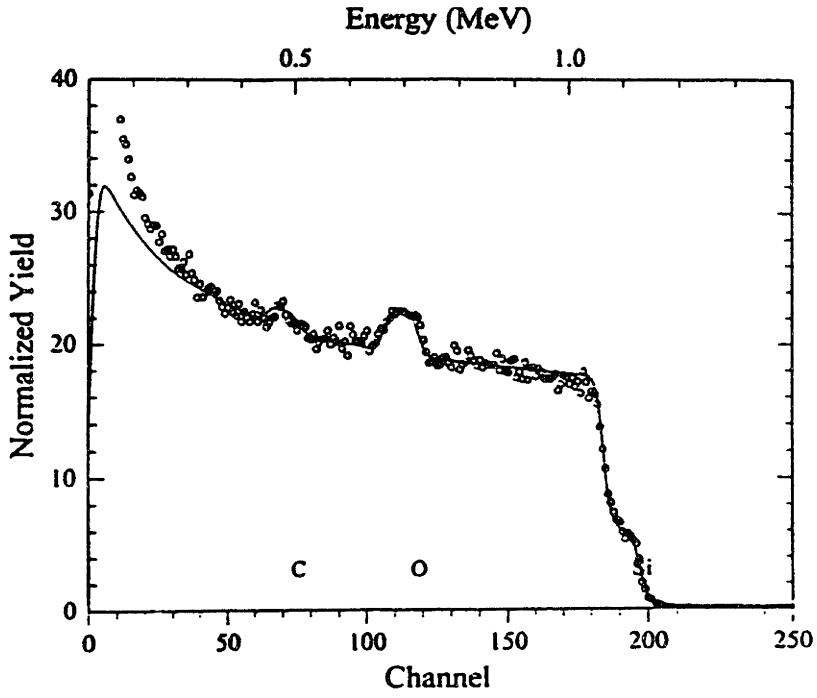

Figure E.3.6: 3.0 MeV RBS spectra for P(PMDSS) exposed to uv in air for one hour.

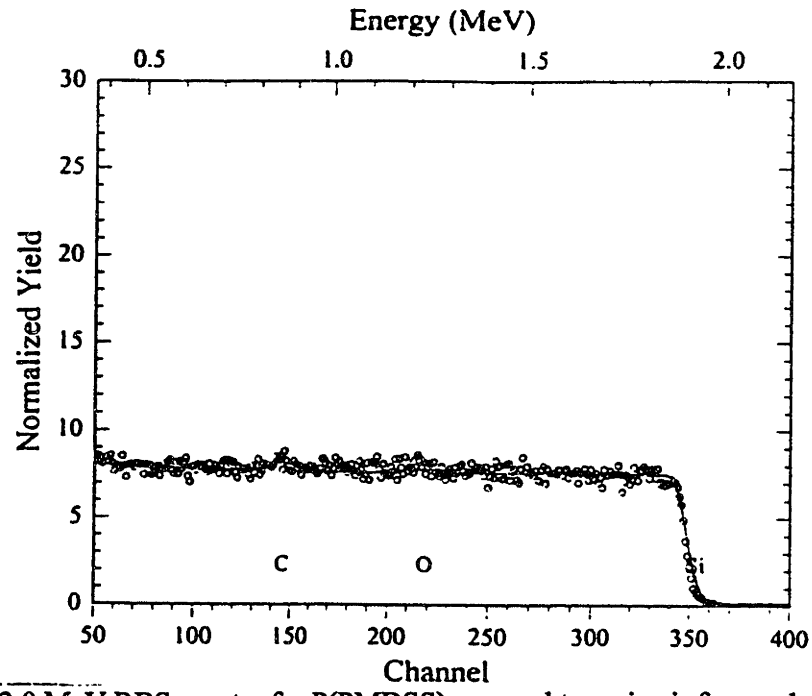

Figure E.3.7: 2.0 MeV RBS spectra for P(PMDSS) exposed to uv in air for one hour.

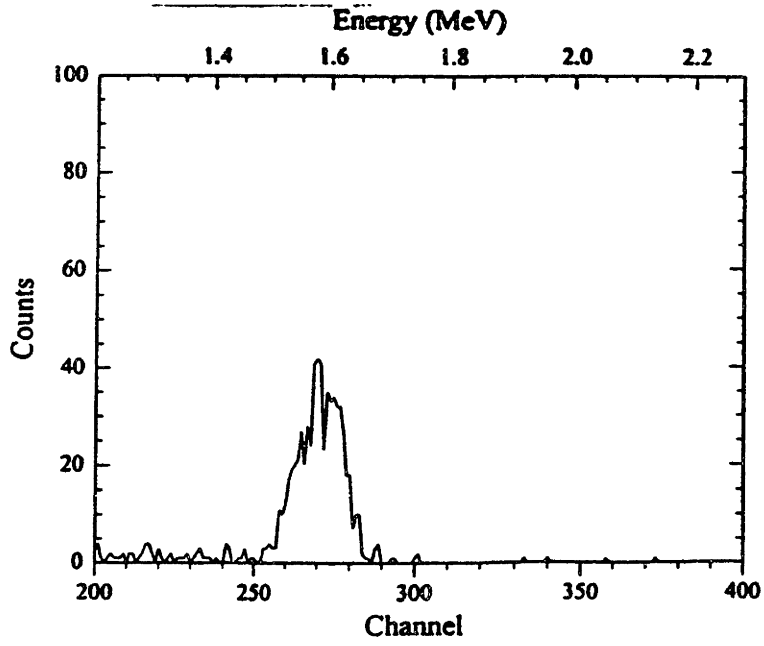

Figure E.3.8: FRES spectra for P(PMDSS) exposed to uv in air for one hour.

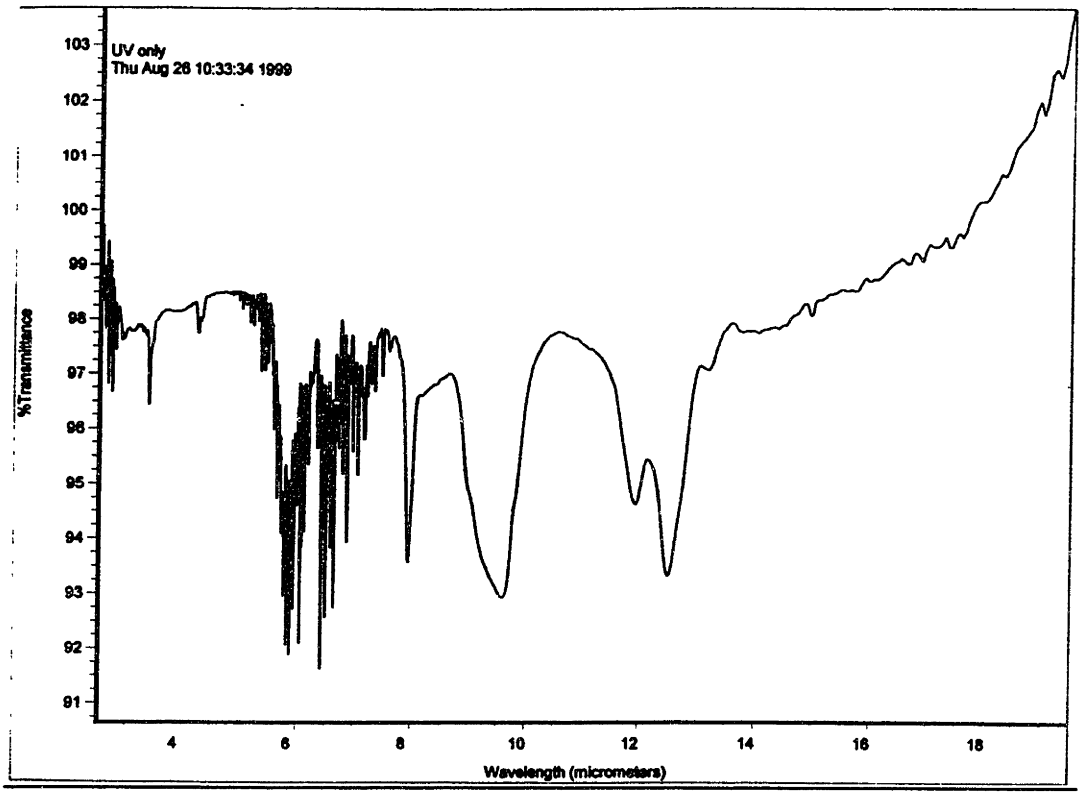

Figure E.3.9: FTIR spectra for P(PMDSS) exposed to uv in air for one hour.

E.4 : Data for P(PMDSS) Exposed to Ozone + Uv for One Hour

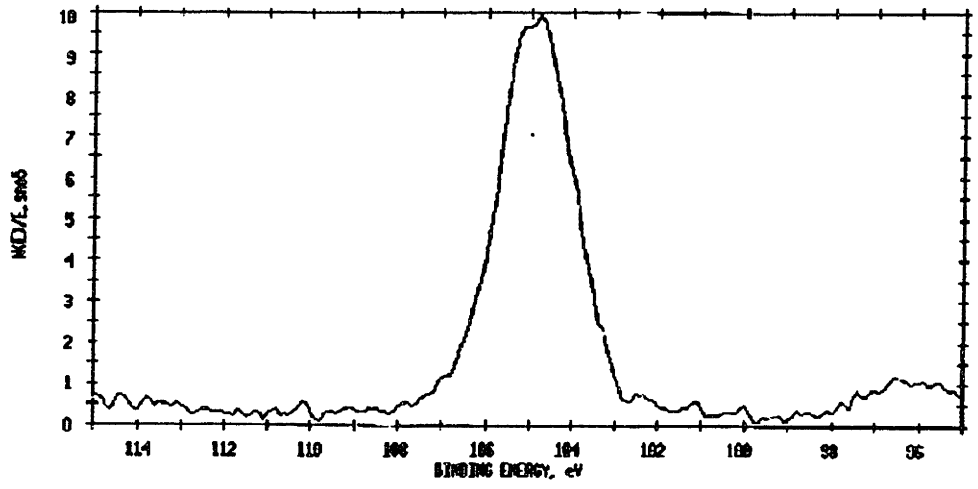

Figure E.4.1: XPS spectra for the raw Si2p peak for P(PMDSS) exposed to ozone and uv for one hour.

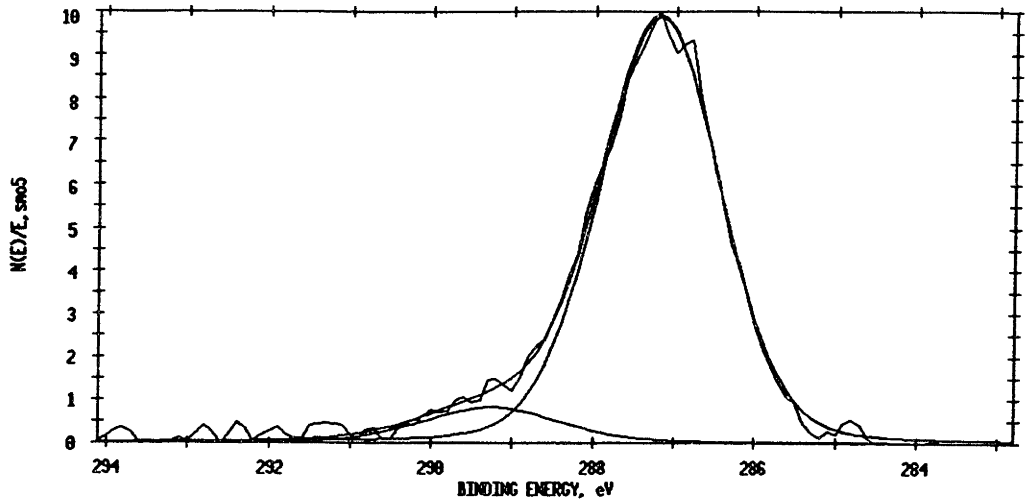

Figure E.4.2: XPS Spectra for the raw C1s peak for P(PMDSS) exposed to ozone and uv for one hour.

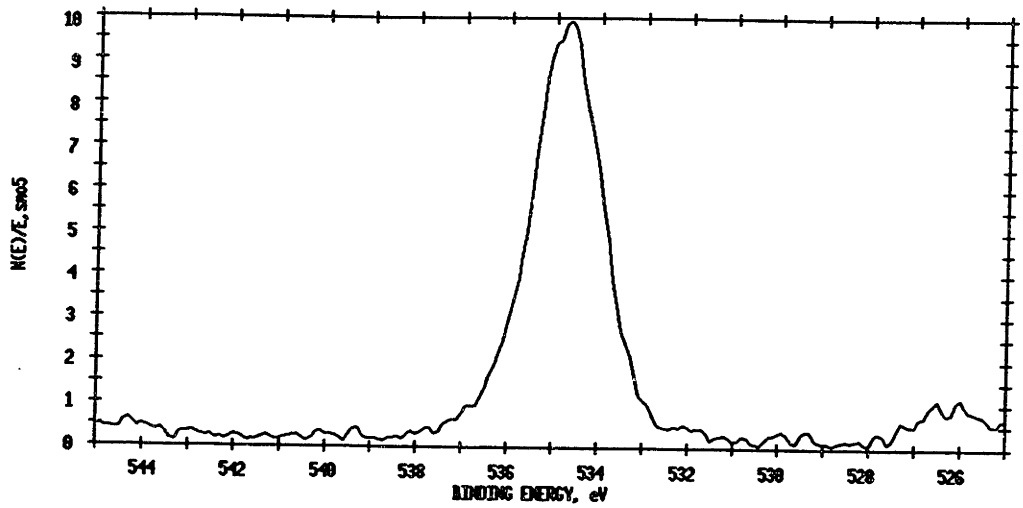

Figure E.4.3: XPS Spectra for the raw O1s peak for P(PMDSS) exposed to ozone and uv for one hour.

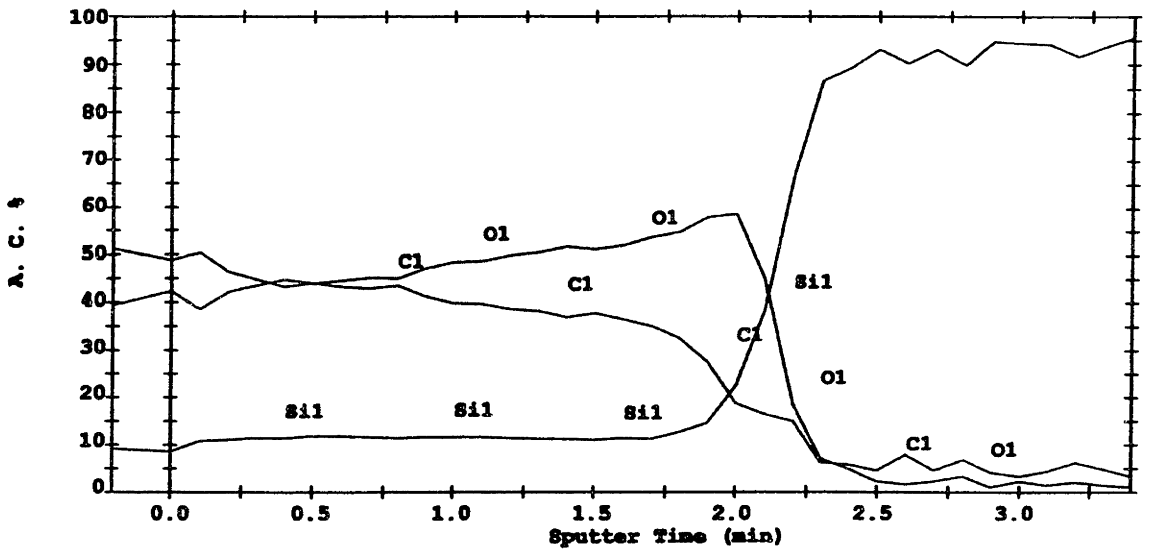

Figure E.4.4: AES depth profile for P(PMDSS) exposed to ozone and uv for one hour.

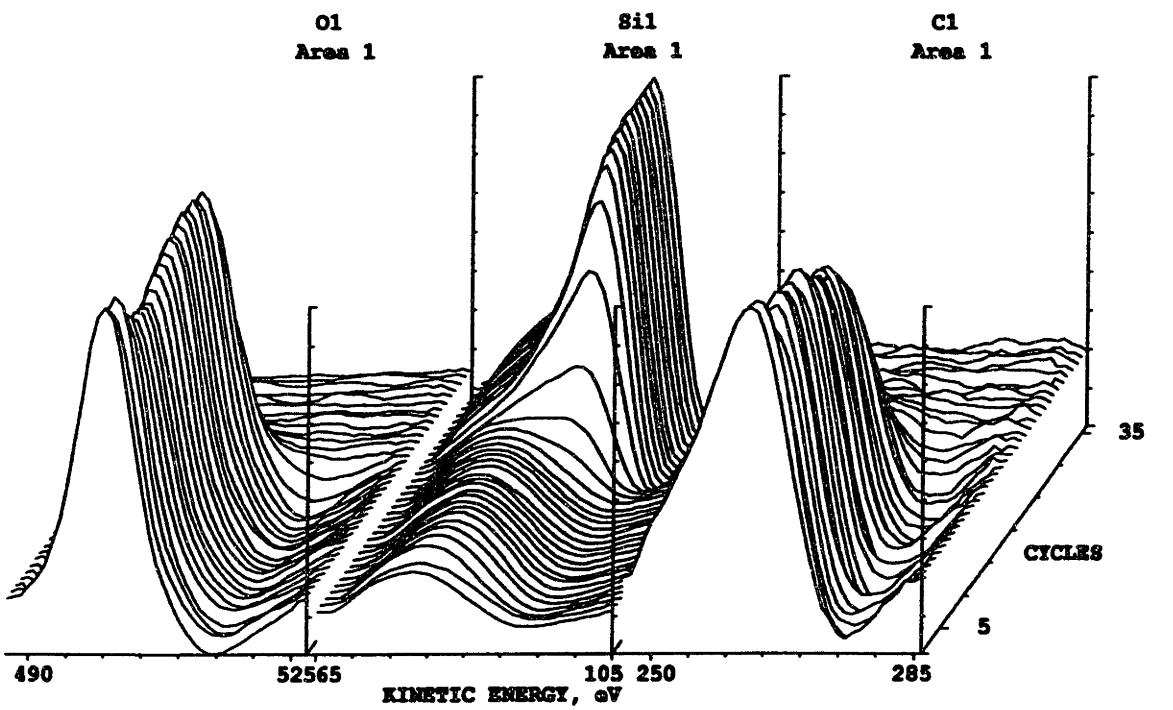

Figure E.4.5: AES chemistry profile for P(PMDSS) exposed to ozone and uv for one hour.

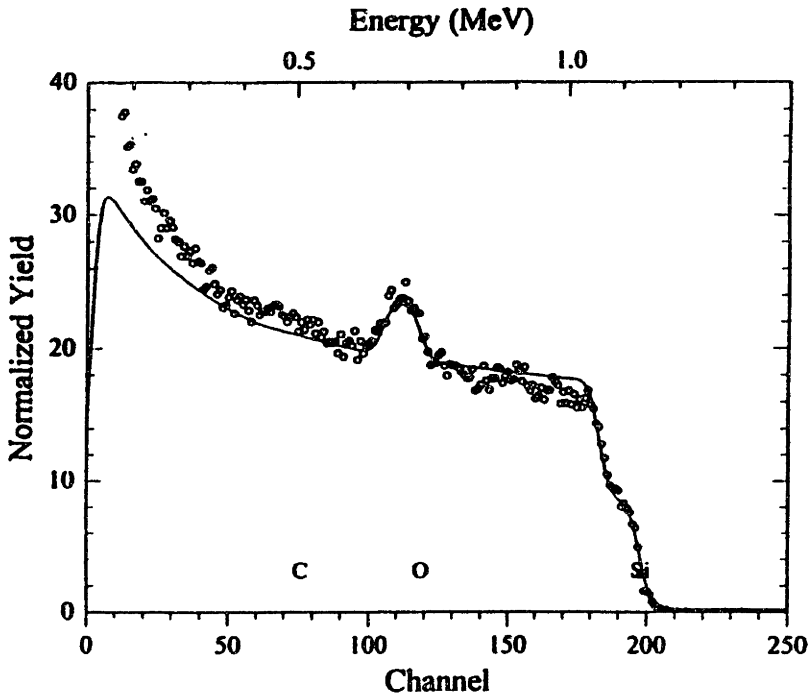

Figure E.4.6: 3.0 MeV RBS spectra for P(PMDSS) exposed to ozone + uv for one hour.

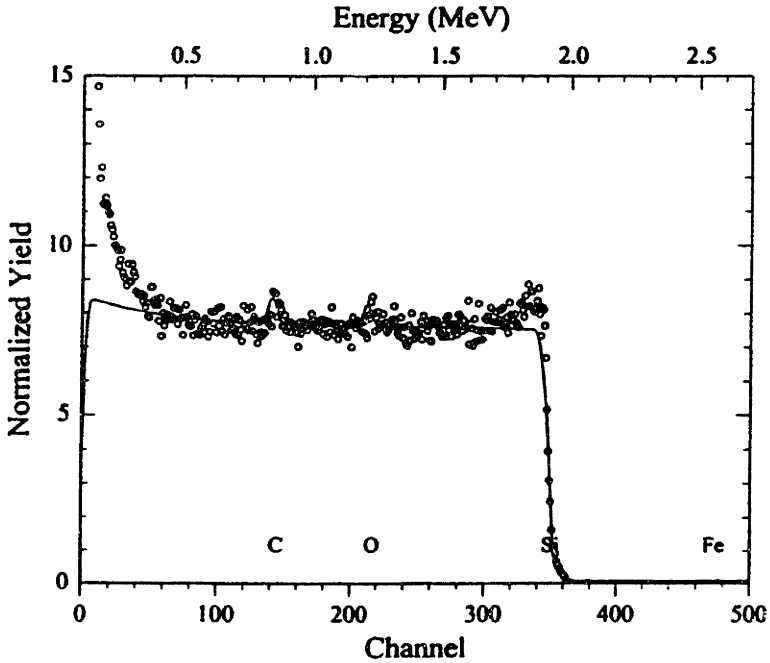

Figure E.4.7: 2.0 MeV RBS spectra for P(PMDSS) exposed to ozone + uv for one hour.

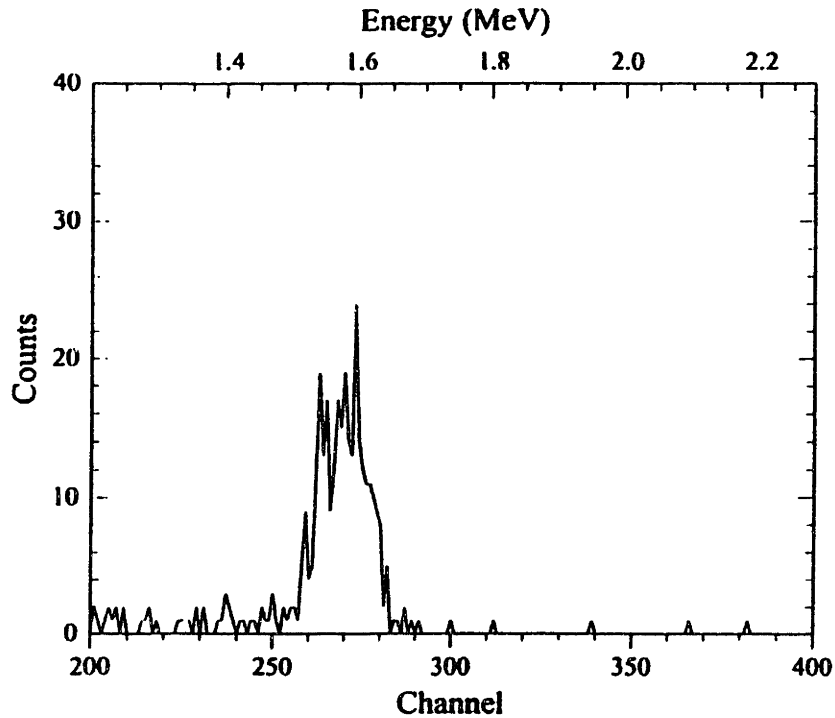

Figure E.4.8: FRES spectra for P(PMDSS) exposed to ozone + uv for one hour.

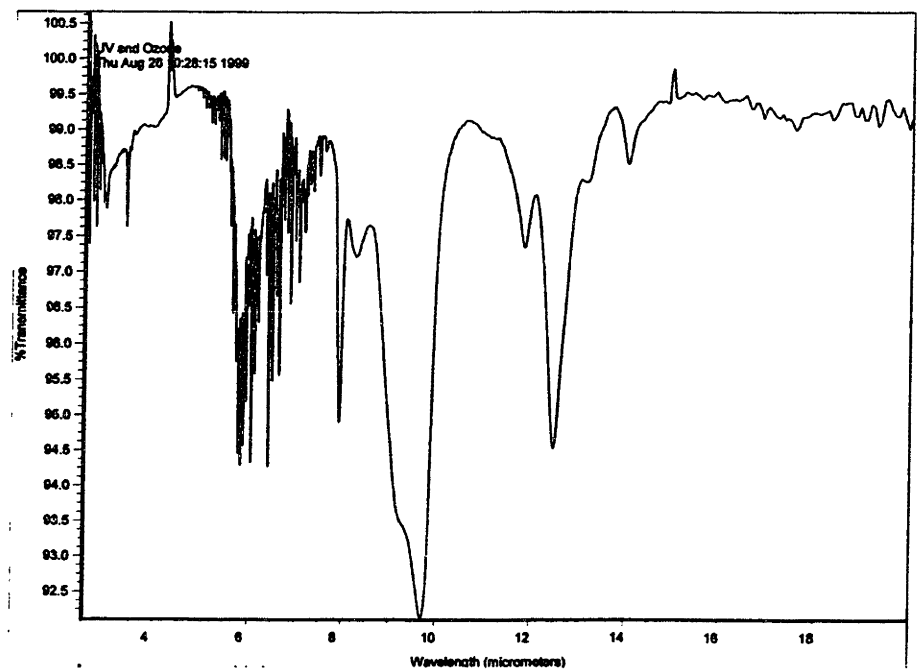

Figure E.4.9: FTIR Spectra for P(PMDSS) exposed to ozone + uv for one hour.

E.5: Data for P(PMDSS) Exposed to O_2-RIE

Data for the P(PMDSS) that was exposed to O_2-RIE was collected at IBM Almaden Research Center. Hence the XPS was taken at a different angle (10° and 60°) as opposed to 45° and a monochromatic x-ray source was used as discussed in **Section 4.2.6.**

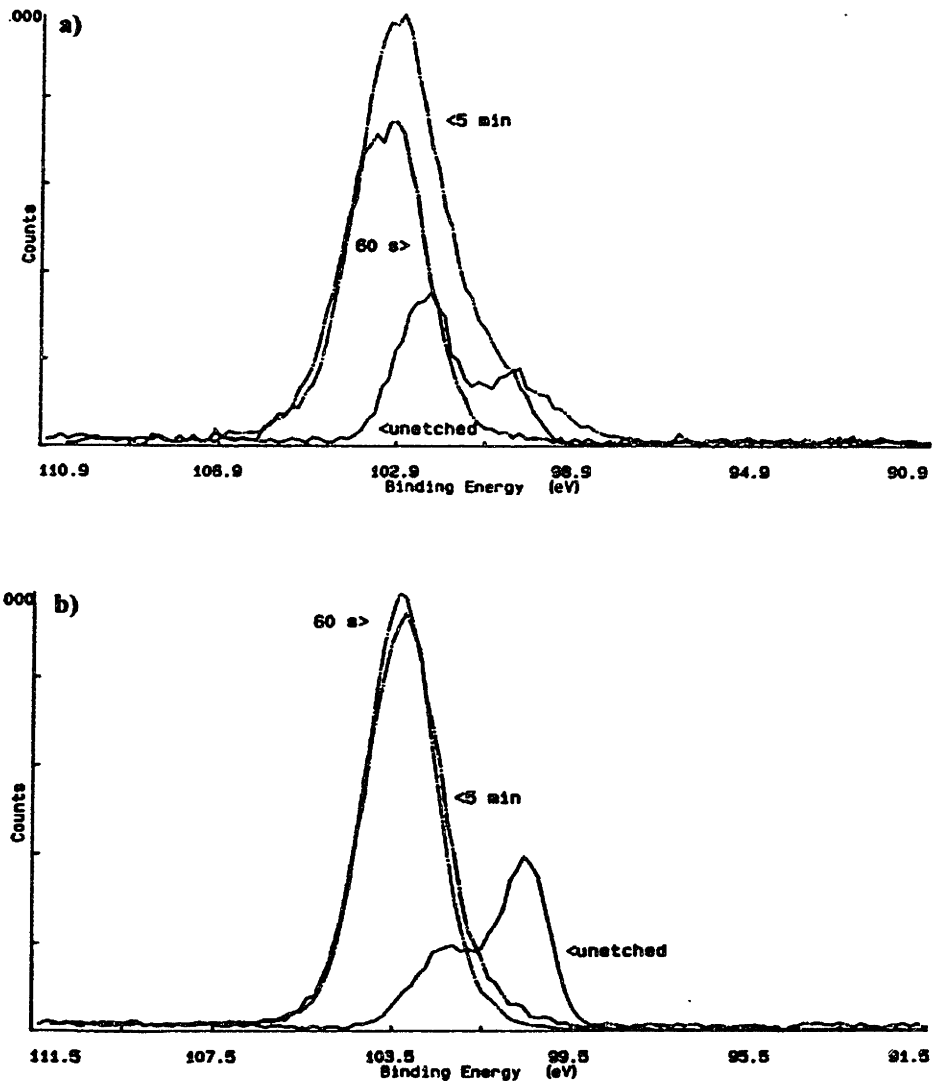

Figure E.5.1: XPS spectra of the raw Si2p peak taken at two sample-to-detector angles a) 10° and b)60° for as-cast P(PMDSS) and P(PMDSS) exposed to O_2-RIE for 60 seconds and 5 minutes. Data were taken at IBM Almaden Research Center.

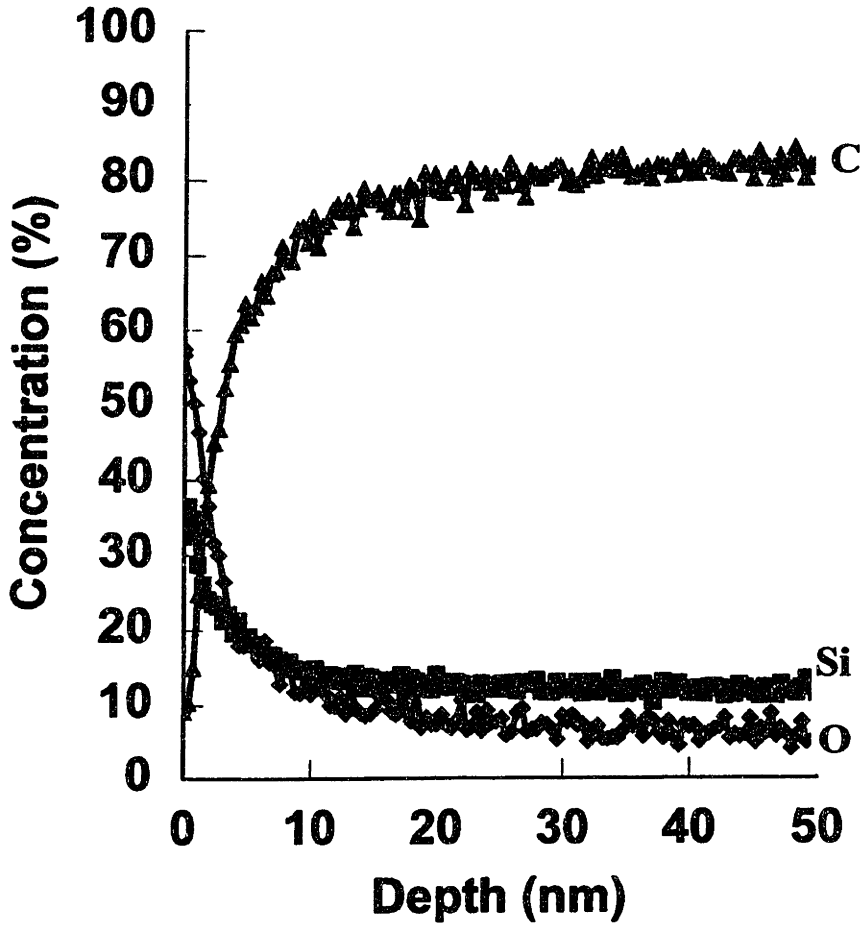

Figure E.5.2: AES depth profile for P(PMDSS) exposed to O_2-RIE for 60 seconds. Data taken at IBM Almaden Research Center.

E.6: P(PMDSS) Exposed to Ozone + Uv for One Hour Annealed to 400°C for One Hour

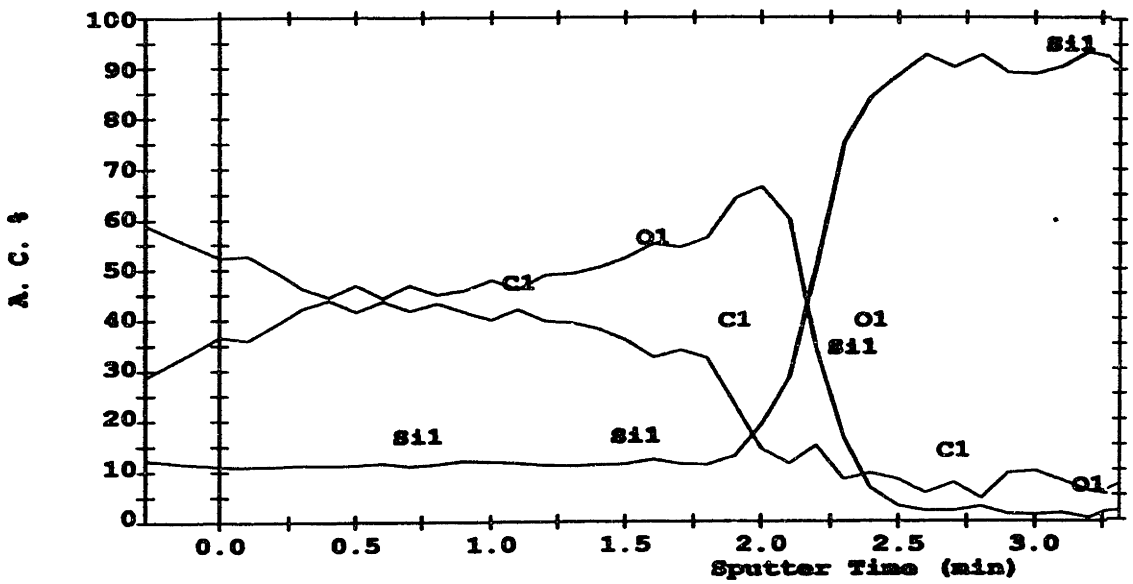

Figure E.6.1: AES depth profile for P(PMDSS) exposed to ozone and uv for one hour, annealed to 400°C for one hour in nitrogen.

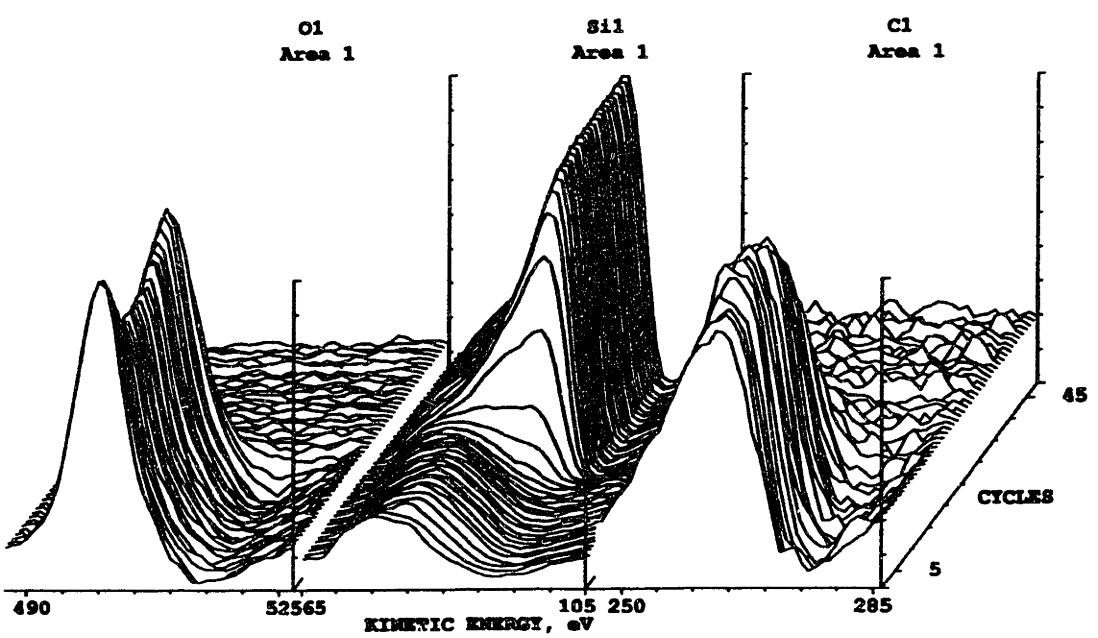

Figure E.6.2: AES chemistry profile for P(PMDSS) exposed to ozone and uv for one hour, annealed to 400°C for one hour in nitrogen.

E.7: P(PMDSS) Exposed to Uv for One Hour Annealed to 400°C for One Hour

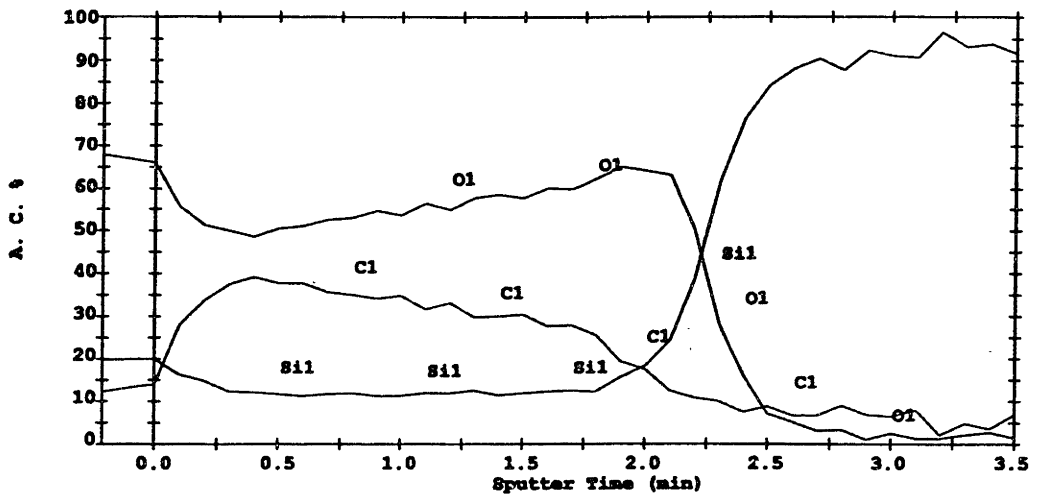

Figure E.7.1: AES depth profile for P(PMDSS) exposed to uv for one hour, annealed to 400°C for one hour in nitrogen.

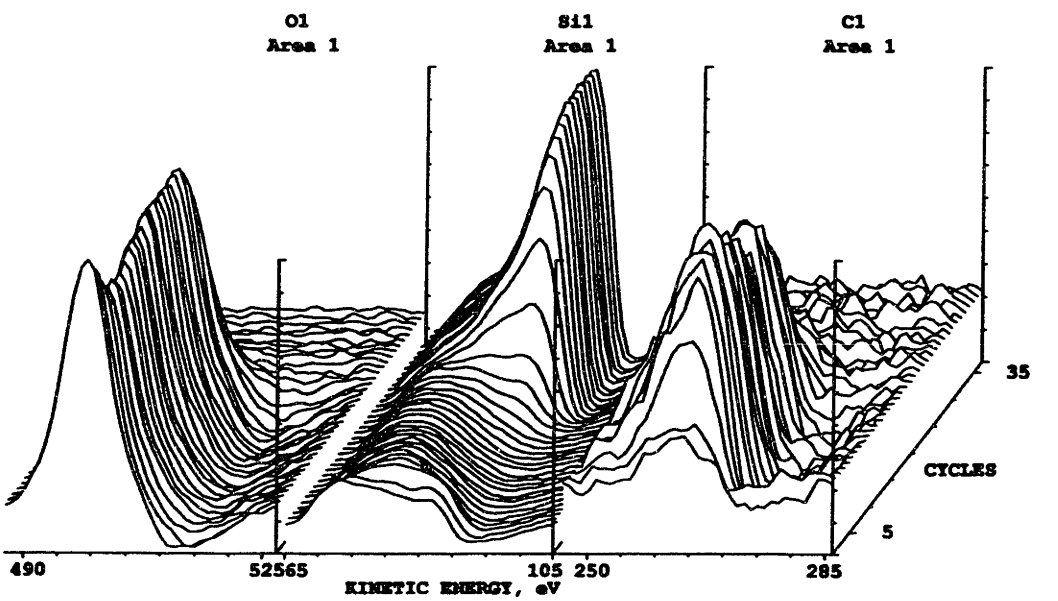

Figure E.7.2: AES chemistry profile for P(PMDSS) exposed to uv for one hour, annealed to 400°C for one hour in nitrogen

Appendix F

Calculation of the Specific Surface for the Double Gyroid Morphology

The d_{211}-spacing for the P(PMDSS)-DG was calculated from SAXS to be 490 Å, which results in a lattice parameter of 1200 Å since for the 211 reflection, $a=\sqrt{6}\, d_{211}$. The volume fraction of PI as calculated from the molecular weight of the polymer is $\phi_{PI} = 0.33$.

Using TEMsim, as discussed in **Section 6.1.4,** Jim Hoffman from the Mathematical Scientific Research Institute (MSRI) at University of California Berkeley, simulated a view along the [110] direction and as seen in **Figure 2.2,** the simulation corresponds well to the experimental data. In this simulation of the level set surface, the volume fraction of the three phases (2 interpenetrating networks and 1 matrix) is set as 0.17 for each of the networks and 0.66 for the matrix, resulting in a volume fraction of the minority phase as $\phi_{minority} = 0.34$. In TEMsim, a mathematical cell is defined from $-\pi$ to π resulting in a volume of the cell of $(2\pi)^3$.

From TEMsim, given this volume fraction and definition of the mathematical unit cell, the area of the crystallographic cell (which corresponds to the surface area of the intermaterial dividing surface, IMDS of the block copolymer) is computed to be 192.21. Thus, for this unit cell, the area to volume ratio is :

$$\frac{\text{Area}}{\text{Volume}} = \frac{190.16}{248.05} = 0.7666$$

In 1997, Grosse-Brauckmann calculated areas and volumes for the gyroid family of triply periodic surfaces with constant mean curvature. He noted that area to volume ratios are strongly dependent on the size of the unit cell. Grosse-Brauckmann suggested using a *dimensionless area*, Area^*. Following Section 5 on "The Normalization Problem", in this paper, the dimensionless surface area to volume ratio is given as:

$$\text{Area}^* = \frac{\text{Area}}{\sqrt[3]{\text{Volume}^2}}$$

This definition allows direct comparisons between surfaces since the dimensionless area is invariant to the definition of the unit cell and is independent of the scaling of the surface.

The crystallographic cell as simulated by TEMsim gives a dimensionless area of :

$$\text{Volume} = 248.05$$

$$\text{Volume}^{2/3} = 39.48$$

$$\text{Area}^{*} = \frac{\text{Area}}{\text{Volume}^{2/3}} = \frac{190.16}{39.48} = 4.82$$

From SAXS, the crystallographic unit cell lattice parameter of the P(PMDSS)-DG is estimated to be 1200 Å. Using the dimensionless area calculated for the double gyroid, the surface area of the P(PMDSS)-DG can be calculated to be :

$$\text{Volume} = (1200\text{Å})^3 = 1.73\text{x}10^9\,\text{Å}^3$$

$$\frac{\text{Area}}{\text{Volume}^{2/3}} = 4.82$$

$$\Rightarrow \text{Area} = 4.82(\text{Volume})^{2/3}$$

$$\text{Area} = 4.82(1.73)^{2/3}\text{x}10^6\ \text{Å}^2$$

$$\text{Area} = 6.95\ \text{x}10^6\,\text{Å}^2$$

Assuming a density, $\rho \sim 1.0$ g/cm^3, the number of unit cells in 1 gram can be calculated as :

$$\text{No. of unit cells in 1 cm}^3 = \frac{1[\text{cm}^3]}{\text{volume of unit cell}[\text{cm}^3]}$$

$$\text{No. of unit cells in 1 cm}^3 = \frac{1\times10^{24}\,\text{Å}^3}{1.73\times10^9\,\text{Å}^3} = 0.58\times10^{15}\,\text{unit cells/cm}^3$$

Since the density is assumed to be 1 gram per cm^3 this translates to 0.58 x 10^{15} unit cells per gram. The total surface area per gram can then be calculated by:

$$\text{Total surface area per gram} = \frac{\text{Surface area per unit cell} * \text{number of unit cells/cm}^3}{\rho\ \text{g/cm}^3}$$

$$\text{Total surface area per gram} = \frac{6.95\times10^{6}\ \text{Å}^2/\text{cell} * 0.58\times10^{15}\ \text{unit cells}}{1\ \text{g/cm}^3}$$

$$\text{Total surface area per gram} = 4.03\times10^{21}\ \text{Å}^2/\text{g}$$

$$\sim 40\ \text{m}^2/\text{g}$$

Similarly, a calculation can be done for the inverse double gyroid. In this case, the P(PMDSS) comprises of the networks and in our material system, the d_{211} spacing as determined by SAXS (see Chapter 3) is 620Å while the volume fraction of the P(PMDSS) = 0.48. Through TEMsim, this corresponds to an area of the crystallographic cell of 213.7. Following this calculation, this corresponds to a surface area: volume ratio of ~36 m^2/g.

Bibliography

"Standard Practice for Describing and Specifying Inductively Coupled Plasma Optical Emission Spectrometers" ASTM E1479-92, *Annual Book of ASTM Standards, American Society for Testing and Materials.*

Albalak R., and Thomas E.L. "Microphase Separation of Block Copolymer Solutions in a Flow Field." *J. Polymer Science: Part B : Polymer Physics* , 31: 37-46, 1993.

Avgeropoulos A., Chan V. Z.-H., Lee V. Y., Ngo D., Miller R.D., Hadjichristidis N., Thomas E.L., "Synthesis and Morphological Behavior of Silicon-Containing Triblock Copolymers for Nanostructure Applications." *Chemistry of Materials,* 10, 8, 2109-2115, 1998...

Avgeropoulos A., Dair B.J., Hadjichristidis N., Thomas E.L., "Tricontinuous Double Gyroid Cubic Phase in Triblock Copolymers of the ABA Type", *Macromolecules*, 30, 9, 5634-5642, 1997.

Belot V., Corriu R.J.P., Leclercq D., Mutin P.H., Vioux A.,, "Thermal Reactions Occurring During Pyrolysis of Crosslinked Polysiloxane Gels, Precursors to Silicon Oxycarbide Glasses", *Journal of Non-Crystalline Solids* , 147&148, 52-55, 1992.

Belot V., Corriu R.J.P., Leclercq D., Mutin P.H. and Vioux A.,, "Organosilicon Gels Containing Silicon-Silicon Bonds, Precursors to Novel Silicon Oxycarbide Compositions", *Journal of Non-Crystalline Solids* , 144, 287-297, 1992.

Belot V., Corriu R.J.P., Leclercq D., Mutin P.H., Vioux A.,, "Silicon Oxycarbide Glasses with Low O/Si Ratio from Organosilicon Precursors", *Journal of Non-Crystalline Solids* , 176, 33-44, 1994.

Bershtein V.A., Egorov V.M., *Differential Scanning Calorimetry of Polymers*, Ellis Harwood, 1994.

Bobbio S.M., Jones S.K., Tessier T.G., Dudley B.W., Cohen B., Russell F.J., Morosoft A., "Etch Resistance of Silicon Containing Polymers in Oxygen Plasma Chemistry", *SPIE,* 1185, 24-33, 1989.

Bouillon E., Lanflais F., Pailler R., Naslain R., Cruege F., Huong P.V., Sarthou J.C., Delpuech A., Laffon C., Lagarde P., Monthioux M., Oberlin A., "Conversion Mechanisms of a Polycarbosilane Precursor into an SiC-Based Ceramic Material", *Journal of Materials Science* , 26, 1333-1345, 1991.

Brandrup J. and Immergut E.H., eds., *Polymer Handbook, 3rd edition,* John Wiley & Sons, New York, V-2, 1989.

Breiner U., Krappe U., Thomas E.L., Stadler R., "Structural Characterization of the "Knitting Pattern" in Polystyrene-block-Poly(ethylene-co-butylene)-block-poly(methylmethacrylate) Triblock Copolymers", *Macromolecules*, 31, 135, 1998.

Burke J.J., Weiss V., eds., *Block and Graft Copolymers*, Syracuse, Syracuse University Press, 1973.

Bushnell, L. P.; Gregor, L. V.; Lyons, C. F., "Multilayer Resist Lithography – Performance and Manufacturability" *Solid State Technology, 29* , 133-138, 1986.

Chan V. Z-H, Avgeropoulos A., Hadjichristidis N. , Lee V.Y. , Miller R.D., Thomas E.L., "Nanoporous Ceramic Structures from Block Copolymers", *PMSE Preprints*, 69, 19-20, 1998.

Chan V.Z-H., Hoffman J., Lee V.Y., Iatrou H., Avgeropoulos A., Hadjichristids N., Miller R.D., Thomas E.L., Ordered Bicontinuous Nanoporous and Nanorelief Ceramics from Self-Assembling Polymer Precursors", accepted to *Science.*

Chan V.Z-H, Rothman JB, Palladino P., Sneddon L.G., Composto R.J., "Characterization of Boron Nitride Thin Films Prepared from a Polymer Precursor", *Journal of Materials Research*, 11, 2, 373-380, 1996.

Chan V.Z.-H., Thomas E.L., Avgeropoulos A., Hadjichristidis N., Lee V.Y., Miller R.D., "Periodic and Relief Nanostructured Articles", US and PCT patent applications pending.

Chan V.Z-H, Thomas E.L., Frommer J.E., Lee V.Y., Ngo D., Miller D.C., Miller R.D., "Curious Morphology of Silicon Containing Polymers Upon Exposure to an Oxygen Plasmas", *Chemistry of Materials*, 1998.

Chaudhry T.M., Ho H., Drzal L.T., Harris M., Laine R.M., "Silicon Oxycarbide Coatings on Graphite Fibers II. Adhesion, Processing and Interfacial Properties", *Materials Science and Engineering*, A 195, 237-249, 1995.

Chaumont P., Beinert G, Herz J., Rempp P., "Synthesis and Characterization of Multiblock Copolymers Containing Poly(dimethyl siloxane) Blocks", *Polymer*, 22, 5, 663, 1981.

Chaumont P., Beinert G., Herz J. E., Rempp P.,"Synthèse et Properiètès du Poly(p-triméthylsilylstyrène)", *Makromoleculare Chemie 183*, 1181, 1982.

Chen J.T., "Influence of a Liquid Crystal Block on the Microstructure and Optical Properties of Block Copolymers", MIT, *Ph.D. Thesis*, 1997.

Chen J.T., and Thomas E.L, "The Use of Force Modulation Microscopy to Investigate Block Copolymer Morphology", *Journal of Materials Science*, 31, 2531-2538, 1996.

Chou N.J., Tang C.H., Paraszcazk J., Babich E., 'Mechanism of Oxygen Plasma Etching of Polydimethylsiloxane Films', *Applied Physics Letters*, 46, 31, 1985.

Chu J.H., Rangarajan P., Adams L.J., Register R.A., "Morphologies of Strongly Segregated Polystyrene-Poly(dimethylsiloxane) Diblock Copolymers", *Polymer*, 36, 8, 1569-1575, 1995.

Chu W.K., Mayer J.W., Nicolet M.A., *Backscattering Spectrometry*, Academic Press, NY, 1978.

Dair B.J., "Characterization, Orientation, and Deformation Behavior of the Double Gyroid Phase in Elastomeric Triblock Copolymers", MIT, *Ph.D. Thesis*, 1999.

Dair B.J., "Characterization, Orientation and Deformation Behavior of the Double Gyroid Phase in Elastomeric Triblock Copolymers", Figures 2.1 and 2.2, pp 29-30, Ph.D. Thesis, MIT 1999.

Dietz P., Hansma P.K., Inacher O., Lehmann H-D. and Herrmann K-H., "Surface Pore Structures of Micro- and Ultrafiltration Membranes Imaged with the Atomic Force Microscope", *Journal of Membrane Science*, 65, 101-111, 1992.

Digital Instruments, "Off-line Analyze Commands", *Nanoscope Command Reference Manual*, Version 4.10.01, pp 12.67, 1996.

Dijkstra J., 'Oxygen Plasma Etching of Silylated Resist in a Top-Imaging Lithographic Process', *SPIE : Advances in Resist Technology and Processing*, 1466, 592-603, 1991.

Durandet A., Joubert O., Pelletier J., Pichot M., 'Effects of Ion Bombardment and Chemical Reaction on Wafer Temperature During Plasma Etching' *Journal of Applied Physics*, 67, 8, 3862-3868, 1990.

Eckert J., Stucky G.D. and Cheetham A.K., "Partially Disordered Inorganic Materials", *MRS Bulletin*, 24, 5, 31-41, 1999.

Fink Y., Winn J.N., Fan S., Chen C., Michel J., Joannopoulos J.D., Thomas E.L., "A Dielectric Omnidirectional Reflector", *Science*, 282, 1679-1682, 1998.

Flory P.J., *Principles of Polymer Chemistry*, Cornell University Press, Ithaca, NY, 1953.

Folkes M.J., ed., *Processing, Structure and Properties of Block Copolymers*, Elsevier Applied Science, London, 1985.

Fritzsche A.K., Arvealo A.R., Moore M.D., Elings V.B., Kjoller K. and Wu C.M., "The Surface Structure and Morphology of Polyvinylidene Fluoride Microfiltration Membranes by Atomic Force Microscopy", *Journal of Membrane Science*, .68, 65-78, 1992.

Fritzsche A.K., Arevalo A.R., Connolly A.F., Moore M.D., Elings V.B., and Wu C.M., "The Structure and Morphology of the Skin of Polyethersulfone Ultrafiltration Membranes: A Comparative Atomic Force Microscope and Scanning Electron Microscope Study", *Journal of Applied Polymer Science*, 45, 1945, 1992.

Fritzsche A.K., Arevalo A.R., Moore M.D., Weber C.J., Elings V.B., Kjoller K. and Wu C.M., "Image Enhancement of Polyethersulfone Ultrafiltration Membrane Surface Structure for Atomic Force Microscopy", *Journal of Applied Polymer Science*, 46, 167, 1992.

Fritzsche A.K., Arevalo A.R., Moore M.D. and O'Hara C., "The Surface Structure and Morphology of Polyacrylonitrile Membranes by Atomic Force Microscopy," *Journal of Membrane Science*, 81, 109-120, 1993

Fukuda T., Terauchi T., "Mechanism of "Living" Radical Polymerization Mediated by Stable Nitroxyl Radicals", *Chemistry Letters*, 293-294, 1996.

Gabor A., Lehner E., Mao G., Schneggenburger L., Ober C., "Synthesis and Lithographic Characterization of Block Copolymer Resists Consisting of Both PS Blocks and Hydrosiloxane Modified Polyisoprene or Polybutadiene Blocks", *Chemistry of Materials*, 6, 927-934, 1994.

Gabor A.H., Ober C.K., "Silicon-Containing Block Copolymer Resist Materials", ACS Symposium Series 614 : Microelectronics Technology, Polymers for Advanced Imaging and Packaging , 281, 1995.

Gaynor S.G., Edelman S., Matyjaszewski K., "Synthesis of Branched and Hyperbranched Polystyrenes", *Macromolecules*, 29, 1079-1081, 1996.

Gobran D.A., "Phase Separation and Morphology of Diblock and Segmented Block Copolymers", *Ph.D. Thesis*, University of Massachusetts, 1990.

Goh M.C., "Atomic Force Microscopy of Polymer Films", In *Advances in Chemical Physics*, ed. Rice S.A. Prigogine I. 1-83. XCI. John Wiley & Sons, Inc., 1995.

Gokan H., Saotome Y., Saigo K., Watanabe F., Ohnishi Y.,. 'Oxygen Ion Etching Resistance of Organosilicon Polymers.' In *ACS Symposium Series : Polymers for High Technology, Electronics and Photonics in* Anaheim, CA, edited by Turner S.R. Bowden M.J., American Chemical Society, 358-368, 1986.

Greiner J.H., "Josephson Tunneling Barriers by rf Sputter Etching in an Oxygen Plasma", *Journal of Applied Physics*, 42, 5151, 1971.

Grosse-Brauckmann K., "On Gyroid Interfaces", *Journal of Colloid and Interface Science*, 187, 2, 418-428, 1997.

Guo, X.; Rempel, G. L., "Catalytic Hydrosilylation of Diene-Based Polymers 2. Hydrosilation of Butadiene Copolymer and Nitrile Butadiene Copolymer" *Macromolecules*, *25*, 883-886, 1992.

Hajduk, D., "Morphological Transitions in Block Copolymers", *Ph.D. Thesis*, Princeton University, Dept. of Physics, 1995.

Hajduk D.A., Harper P.E., Gruner S.M., Honeker C.C., Kim G., Thomas E.L., Fetters L.J., "The Gyroid: A New Equilibrium Morphology in Weakly Segregated Diblock Copolymers", *Macromolecules*, 27, 4063-4075, 1994.

Harris M., Chaudhary T., Drzal L., Laine R.M., "Silicon Oxycarbide Coatings on Graphite Fibers: Chemistry, Processing, and Oxidation Resistance", *Materials Science and Engineering*, A195, 223-236, 1995.

Harrison C., Park M., Chaikin P.M., Register R.A., Adamson D.H., "Lithography with a Mask of Block Copolymer Microstructures", *Journal of Vacuum Science and Technology B*, 16, 2, 544-552, 1998.

Harrison C., Park M., Chaikin P.M., Register R.A., Adamson D.H., "Lithography with a Pattern of Block Copolymer Microdomains as a Positive or Negative Resist", Chapter One, in *Micro- and Nanopatterning Polymers*, eds. Ito H., Reichmanis E., Nalamasu O., and Ueno T., ACS Symposium Series, 214th ACS National Meeting, Vol. 706, 1997.

Harrison C., Park M., Chaikin P.M., Register R.A., Adamson D.H., Yao N., "Layer by Layer Imaging of Diblock Copolymer Films with a Scanning Electron Microscope", *Polymer*, 39, 13, 2733-2744, 1998.

Hartney M.A., Hess D.W., Soane D.S., "Critical Review: Oxygen Plasma Etching for Resist Stripping and Multilayer Lithography", *Journal of Vacuum Science and Technology B*, 7, 1-13, 1989.

Hartney M.A., Novembre A.E., "Poly(methylstyrene-dimethylsiloxane) Block Copolymers as Bilevel Resists", *SPIE Vol. 539 : Advances in Resist Technology and Processing II*, 539, 90, 1985.

Hashimoto T., Tsutsumi K., Funaki Y., "Nanoprocessing Based on Bicontinuous Microdomains of Block Copolymers: Nanochannels Coated with Metals", *Langmuir*, 13, 6869-6872, 1997.

Hawker C.J., "Molecular Weight Control by a "Living" Free-Radical Polymerization Process", *Journal of the American Chemical Society*, 116, 11185-11186, 1994.

Hawker C.J., Barclay G.G., Orellana A., Dao J., Devonport W., "Initiating Systems for Nitroxide-Mediated 'Living' Free Radical Polymerizations : Synthesis and Evaluation", *Macromolecules*, 29, 16, 5245, 1996.

Hawker C.J., Elce E., Dao J., Volksen W., Russell T.P., Barclay G., 'Well-Defined Random Copolymers by a Living Free-Radical Polymerization Process', *Macromolecules*, 29, 7, 2686 - 2688, 1996.

Hedrick J.L., Miller R.D., Hawker C.J., Carter C.K., Volksen W., Yoon D.Y., Trollasas M., "Templating Nanoporosity in Thin-Film Dielectric Insulators", *Advanced Materials*, 10, 13, 1049-1053 , 1998.

Hendricks N.H., "Organic Polymers for Interconnect Intermetal Dielectric Applications", *Solid State Technology*, 177, 1995.

Hirao A., Ando Y., Nakahama S., "Polymerization of Monomers Containing Functional Silyl Groups 12. Anionic Polymerization of Styrene Derivatives Para-Substituted with Pentamethyldisilyl (Si-Si), Heptamethyltrisilyl (Si-Si-Si), and Nonamethyltetrasilyl (Si-Si-Si-Si) groups", *Macromolecular Symposium*, 95, 293-501, 1995.

Hirao A., Nakahama S., "Anionic Living Polymerization of Monomers with Functional Silyl Groups", *Progress in Polymer Science*, 17, 283-317, 1992.

Holden G., Legge N.R., Quirk R.P., Shcroeder H.E., eds., *Thermoplastic Elastomers*, New York, Hanser Publishers, 1996.

Honeker C., "Large Strain Deformation Behavior of Oriented Triblock Copolymer Cylinders", MIT, *Ph.D. Thesis*, 1997.

Horvath M., Bilitzky L., Huttner J., "Chapter 2.3 : Chemical reactions with ozone", *Ozone*, pp 44-55, Akademiai Kiado, Budapest, 1985.

Horvath M., Bilitzky L., Huttner J., "Chapter 2.4: Interaction between Ozone and various substances", *Ozone*, pp 56-58, Akademiai Kiado, Budapest, 1985.

Horvath M., Bilitzky L., Huttner J.," Chapter 3 : Processes for Ozone Generation", *Ozone*, pp 145-256, Akademiai Kiado, Budapest, 1985

http://www.cis.rit.edu/htbooks/nmr/chap-4/chap-4.htm

http://www.msri.org/people/staff/jim

http://www.msri.org/publications/sgp/jim/software/temsim/index.html

http://www.genplot.com/doc/rump.htm

Joannopoulos J., "Photonic Crystals: Molding the Flow of Light", Princeton University Press, Princeton, N.J., (1995).

Johnson S., Ollivier P.J., Mallouk T.E., "Ordered Mesporous Polymers of Tunable Pore Size from Colloidal Silica Templates", *Science*, 283, 963-965, 1999.

Joubert O., Claude R., Pons M., Weill A., Paniez P., "Dry Development of Silylated Resist : Influence of Substrate Temperature", *Advances in Resist Technology and Processing IX; SPIE Vol. 1672;* SPIE : Bellingham, WA, 561-572, 1992.

Joubert O., Fiori C., Oberlin J.C., Paniez P., Pelletier J., Pons M., Vachette T., Weill A., "Resist Degradation Under Plasma Exposure: Synergistic Effects of Ion Bombardment", *Journal of Applied Physics*, 69, 3, 1697-1702, 1991.

Jurgensen C.W., Shugard A., Dudash N., Reichmanis E., Vasile M.J.,, 'Experimental Tests of the Steady-State Model for Oxygen Reactive Ion Etching of Silicon-Containing Polymers', *SPIE, Advances in Resist Technology and Processing V*, 920, 253-259, 1988.

Kawakami Y., Hisada H., Yamashita U., Y. Kawakami, H. Hisada, U. Yamashita, "Polystyrenes with p-ologosiloxane, Silane, Germanosiloxane, Germane or Stannane as p-substituents as Materials for Oxygen Permeable Membranes", *Journal of Polymer Science: Polymer Chemistry*, 26, 1307, 1988.

Kim M.J., Ryoo R., "Synthesis and Pore Size Control of Cubic Mesoporous Silica SBA-1", *Chemistry of Materials*, 11, 487-491, 1999.

Kingery W.D., Bowen H.K. and Uhlmann D.R., *Introduction to Ceramics*, page 3, 2nd ed., John Wiley & Sons, 1976.

Kinning D.J., Thomas E.L., Ottino J.M., "Effect of Morphology on the Transport of Gases in Block Copolymers" , *Macromolecules*, 20, 1129, 1987.

Koberstein J.T., Mirley C.L., "Ultra Thin Silicon Oxide and Metal Oxide Films and a Method for the Preparation Thereof", US Patent 5,661,092, 1997.

Lambert C.A., Radzilowski L.H., Thomas E.L., "Triply Periodic Level Surfaces as Models for Cubic Tricontinuous Block Copolymer Morphologies", *Philosophical Transactions of the Royal Society of London A*, 354, 2009-2023, 1996.

Lammertink R.G.H., Hempenius M.A., van den Enk J.E., Chan V.Z-H., Thomas E.L., Vancso G.J., "Nanostructured Thin Films of Organic-Organmetallic Block Copolymers: One-Step Lithography with Poly(ferrocenylsilanes) by Reactive Ion Etching", accepted to *Advanced Materials.*

Lee J.S., Hirao A., Nakahama S., "Polymerization of Monomers Containing Functional Silyl Groups. 5. Synthesis of New Porous Membranes with Functional Groups", *Macromolecules*, 21, 276-278, 1988.

Lee J.S., Hirao A., Nakahama S., "Polymerization of Monomers Containing Functional Silyl Groups. 7. Porous Membranes with Controlled Micostructures", *Macromolecules*, 22, 2602-2606, 1989.

Leibler L., "Theory of Microphase Separation in Block Copolymers", *Macromolecules*, 13, 1602, 1980.

MacDonald S.A., Steinmann F., Ito H., Lee W.Y., Wilson O.G., "Development of Oxygen Reactive Ion Etch Barriers Based on Poly(trimethylstannylstyrene)", *Proceedings of the American Chemical Society, PMSE*, ACS, Washington DC, 49, 104, 1983.

Maivald P., Butt H.J., Gould S.A.C., Prater C.B., Drake B., Gurley J.A., Elings V.B., and Hansma P.K., *Nanotechnology*, 2, 103, 1991.

Mansky P., Chaikin, P., Thomas, E.L., "Monolayer Films of Diblock Copolymer Microdomains for Nanolithographic Applications", *Journal of Materials Science*, 30, 1987-1992, 1995.

Mansky P., Harrison C.K., Chaikin P.M., Register R.A., Yao N.,, "Nanolithographic Templates from Diblock Copolymer Thin Films", *Applied Physics Letters*, 68, 18, 2586-2588, 1996.

Marsmann H., "Oxygen-17 and Silicon-29", *NMR : Basic Principles and Progress*, eds. Diehl P., Fluck E., Kosfeld, R. pp 210, Springer-Verlag, 1981.

Mathieu H.J., "Chapter 4 : Auger Electron Spectroscopy", In *Surface Analysis : The Principal Techniques*, ed. J.C. Vickerman. 99-133. West Sussex, England: John Wiley & Sons, 1997.

Mayes A. M., Olvera de la Cruz M., "Microphase Separation in Multiblock Copolymer Melts", *J. Chemical Physics*, 91, 11, 7228-7235, 1989.

McNaughton J.L., Mortimer C.T., "Differential Scanning Calorimetry", *Thermochemistry and Thermodynamics"*, H.A. Skinner, Butterworths, London, vol. 10, 1975.

Michlczyk M.J., Farneth W.E., Vega A.J.,, "High-Temperature Stabilization of Cross-Linked Siloxane Glasses", *Chemistry of Materials*, 5, 12, 1687-1689, 1993.

Miller R.D., Michl J., "Polysilane High Polymers", *Chemistry Reviews*, 89, 1359-1410, 1989.

Miller R.D., Wallraff G.M., "Polymeric Silicon-Containing Resist Materials", *Advanced Materials for Optics and Electronics*, 4, 95-127, 1994.

Mirley C.L., Koberstein J.T., "A Room Temperature Method for the Preparation of Ultrathin SiOx Films from Langmuir-Blodgett Layers", *Langmuir*, 11, 4, 1049-1052, 1995.

Monnier A., Schuth F., Huo Q., et al., "Cooperative Formation of Inorganic-organic Interfaces in the Synthesis of Silicate Mesostructures", *Science*, 261, 5126, 1299-1303, 1993.

Morey M.S., Davidson A., Stucky G.D., "Silica-Based, Cubic Mesostructures: Synthesis, Characterization and Relevance for Catalysis", *Journal of Porous Materials*, 5, 195-204, 1998.

Mucha J.A., Hess D.W., Aydil E.S., "Chapter 5: Plasma Etching", *Introduction to Microlithography*, 377-507, 2nd edition, eds Thompson, Willson &Bowden, American Chemical Society, Washington D.C. 1994.

Noshay, A. and McGrath J.E., *Block Copolymers: Overview and Critical Survey.* Academic Press, New York, 17-19, 1977.

Ohnishi Y., Suzuki M., Saigo K., Saotome Y., Gokan H., 'Silicon-containing Resists for Bi-layer Resist Systems', *SPIE Vol. 539 : Advances in Resist Technology and Processing II*, 539, 62, 1985.

Overney, R. et al, "Dewetting Dynamics and Nucleation of Polymers Observed by Elastic and Friction Force Microscopy", *Journal of Vacuum Science and Technology B* 14, 1276 (1996).

Paniez P.J., Joubert O.P., Pons M.J., Oberlin J.-C., Weill A.P., "Dry Development and Plasma Durability of Resists: Melt Viscosity and Self Diffusion Effects" , *Advances in Resist Technology and Processing;* SPIE Vol. 1466; 583-591, 1991.

Park M., Harrison C., Chaikin P.M., Register R.A., Adamson D.H.,, "Block Copolymer Lithography: Periodic Arrays of ~10^{11} Holes in 1 Square Centimeter", *Science*, 276, 1401-1404, 1997.

Patten T.E., Xia J., Abernathy T., Matyjaszewski K., "Polymers with Very Low Polydispersities from Atom Transfer Radical Polymerization", *Science*, 272, 866-868, 1996.

Pattuelli, M., Montalti A., Viola G., Zazzetta A., "Sequence Distribution of Styrene-Butadiene Copolymers by Ozonolysis, High-Performance Liquid Chromatographic and Gas Chromatographic-Mass Spectrometric Techniques", *Journal of Chromatography A*, 665, 117-123, 1994.

Pethica J.B. and Oliver W.C., "Tip Surface Interactions in STM and AFM", *Physica Scripta* T19, pp 61, 1987.

Petri R., Brault P., Vatel O., Henry D., Andre E., Dumas P., Salvan F., 'Silicon Roughness Induced by Plasma Etching', *Journal of Applied Physics*, 75, 11, 7499, 1994.

Ratner B.D., Castner D.G., "Chapter 3 : Electron Spectroscopy for Chemical Analysis", In *Surface Analysis : The Principal Techniques*, ed. J.C. Vickerman. 43-98. West Sussex, England: John Wiley & Sons, 1997.

Razumovskii S.D., Kefeli A.A., Zaikov G.E., "Degradation of Polymers in Reactive Gases", *European Polymer Journal*, 7, 275-285, 1971.

Reichmanis E., Smolinsky G., 'Deep UV Positive Resists for Two-Level Photoresist Processes', *SPIE Vol. 469 : Advances in Resist Technology and Processing*, 469, 38, 1984.

Reichmanis E., Smolinksy G., "Bilevel Resist", US Patent Number US4481049, 1984.

Reiss, H., "Statistical Geometry in the Study of Fluids and Porous Media", *Journal of Physical Chemistry* 96, 12, 4736, 1992.

Renlund G.M., Prochazka S., Doremus R.H.,, "Silicon Oxycarbide Glasses: Part I. Preparation and Chemistry", *Journal of Materials Research*, 6, 12, 2716-2722, 1991.

Renlund G.M., Prochazka S. and Doremus R.H., "Silicon Oxycarbide Glasses: Part II Structure and Properties", *Journal Materials Research*, 6, 12, 2723-2734, 1991.

Sierra L., Lopez B., Gil H., Guth J-L., "Synthesis of Mesoporous Silica from Sodium Silica Solutions and a Poly(ethylene oxide)- Based Surfactant", *Advanced Materials*, 11, 4, 1999.

Sioula S., Hadjichristidis N., Thomas E.L., "Direct Evidence for Confinement of Junctions to Lines in an 3 Miktoarm Star Terpolymer Microdomain Structure", *Macromolecules*, 31, 23, 8429-8432, 1998.

Solomon, D.H., Rizzardo, E. and Cacioli, P., US Patent 4 581 429, 1993.

Soraru G.D., D'Andrea G., Glisenti A.,, "XPS Characterization of Gel-Derived Silicon Oxycarbide Glasses", *Materials Letters*, 27, 1-5, 1996.

Stimm M., in *Advances in Polymer Science*, Springer-Verlag, Berlin,Vol. 100, 357-400, 1992.

Sugita K., Ueno N., "Resists for Microlithography: Present Status and Recent Research Trends", *Progress in Polymer Science*, 17, 319-360, 1992.

Tamayo J., Garcia R., "Effects of Elastic and Inelastic Interactions on Phase Contrast Images in Tapping Mode Scanning Force Microscopy", *Applied Physics Letters*, 71, 16, 2394-6, 1997.

Tanaka Y., Kawahara S., Ikeda T., Tamai H., "Analysis of the Sequence Distribution of 1,2 Units in Polybutadiene by an Ozonolysis-GPC Method", *Macromolecules*, 26, 5253-5255, 1993.

Tanaka Y., Nakafutami Y., Kashiwazaki Y., Adachi J., Tadokoro K., "Sequence Structure of Styrene-Butadiene Copolymer Determined by Ozonolysis-HPLC Method", *Rubber Chemistry and Technology*, 60, 2, 207-216, 1987.

Tanaka Y., Sato H., Adachi J., "Structural Characterization of Diene Block Copolymers by GPC and Ozonolysis-GPC Measurements", *Rubber Chemistry and Technology*, 60, 1, 25-34, 1987.

Taylor G.N. and Wolf T.M., " Oxygen Plasma Removal of Thin Polymer Films", *Polymer Engineering and Science*, 20, 1087-1092, 1980.

Thomas E.L., *The Encyclopaedia of Polymer Science and Engineering*, edited by J.I. Kroschwitz, John Wiley, New York, Vol. 5, pp 644, 1986.

Thomas E.L., Anderson D.M., Henkee C.S., Hoffman D., "Periodic Area-Minimizing Surfaces in Block Copolymers", *Nature*, 334, 598-601, 1988.

Ulrich R., Du Chesne A., Templin M., Wiesner U., "Nano-objects with Controlled Shape, Size and Composition from Block Copolymer Mesophases", *Advanced Materials*, 11, 2, 141-146, 1999.

Urbas A., Fink Y., Thomas E.L., "One-dimensionally Periodic Dielectric Reflectors from Self-Assemble Block Copolymer and Homopolymer Blends", *Macromolecules*, 32, 14, 4748-4750, 1999.

Vavasour J.D., Whitmore M.D., "Self-Consistent Field Theory of Block Copolymers with Conformational Asymmetry", *Macromolecules*, 26, 7070-7075, 1993.

Veregin R.P.N., Odell P., Michalak L.M., Georges M.K., "The Pivotal Role of Excess Nitroxide Radical in Living Free Radical Polymerizations with Narrow Polydispersity", *Macromolecules*, 29, 2746-2754, 1996.

Veregin R.P.N., Odell P.G., Michalak L.M., Georges M.K, "Molecular Weight Distributions in Nitroxide-Mediated Living Free Radical Polymerization: Kinetics of the Slow Equilibria between Growing and Dormant Chains", *Macromolecules*, 29, 3346-3352, 1996.

Wallace et al., "Analytical Methods for Inductively Coupled Plasma Spectrometry", Perkin-Elmer Corp., Norwalk, 1981.

Wang, J-S., Matyjaszewski K., " Controlled/"Living" Radical Polymerization. Halogen Atom Transfer Radical Polymerization Promoted by a Cu(I)/Cu(II) Redox Process", *Macromolecules*, 28, 7901-7910, 1995.

Wang, J-S., Matyjaszewski K., "Controlled/"Living" Radical Polymerization. Atom Transfer Radical Polymerization in the Presence of Transition-Metal Complexes", *Journal of the American Chemical Society*, 117, 5614-5615, 1995.

Watanabe F., Ohnishi Y., 'Oxygen Reactive Ion Etching of Organosilicon Polymers', *Journal of Vacuum Science and Technology, B*, 4, 422-425, 1986.

Wei Y., Jin D., Ding T., Shih W-H., liu X., Cheng S.Z.D., Fu Q., "A Non-Surfactant Templating Route to Mesoporous Silica Materials", *Advanced Materials*, 3, 4, 313-316, 1998.

Yamazaki, N.; Nakahama, S.; Hirao, A.; Shiraishi, Y.; Phung, H. M., "Anionic Polymerization of p-Styrenyl Substituted Derivatives of Silicon, Germanium and Tin", *Contemporary Topics in Polymer Science 4*, 379, 1984.

Zhao D., Feng J., Huo Q., Melosh N., Fredrickson G.H., Chmelk B.F., Stucky G.D., "Triblock Copolymer Syntheses of Mesoporous Silica with Periodic 50 to 300 Angstrom Pores", *Science*, 279, 548-552, 1998.

Ziegler J.F., *Helium Stopping Powers and Ranges in All Elemental Matter*, Pergamon Press, New York, 1977.

Biographical Note

Education

Massachusetts Institute of Technology, Cambridge, MA **Fall 1994-Fall 1999**
Ph.D., in Polymers through the Materials Science and Engineering department, February 2000.
Thesis: Research on the formation of ceramic nanostructures from self-assembling silicon containing block copolymers through oxidation techniques.

University of Pennsylvania, Philadelphia, PA **Fall 1991-Spring 1994**
Bachelor of Science in Engineering, **Magna Cum Laude**, May 1994 (completed in 3 years)
Major: Materials Science and Engineering Minor: Mathematics
Cumulative GPA: 3.72/4.00 GPA in Major: 3.82/4.00

Experience

Universität Ulm, Dept. of Chemistry, Ulm Germany **Fall 1999-Fall 2000**
Advisor: Professor Martin Möller
Post-doctoral Fellow. Awarded NSF International Research Opportunity Fellowship to study "Growth and Patterning of Biological Materials on Functionalized Surfaces". Fellowship awarded based on proposal reviewed by NSF panel. Research will be on the replication of nanosized patterns into the extracellular matrix of cells.

MIT, Dept. of Materials Science and Engin., Cambridge, MA **Fall 1994-Fall 1999**
Advisor: Professor Edwin L. Thomas
Full-time graduate student. Currently developing way to utilize inorganic containing block copolymers to produce nanoporous ceramic structures. This work is in collaboration with research groups at the University of Athens (Prof. Nikos Hadjichristidis) and University of Twente (Prof. Julius Vancso). Work involves understanding the oxidation of polymers by ozone and oxygen plasmas, characterizing morphology of block copolymers in both thin film and in the bulk and orienting block copolymers by roll casting. Utilized clean room facilities at the Nanostructures Laboratory (with Prof. Hank Smith) and performed TEM, SEM, XPS, AES, AFM, RBS and FRES

IBM Almaden Research Center, San Jose, CA **1 year period between 1995-1998**
Mentor: Dr. Robert D. Miller
Visiting Researcher. Research trips ranging in time from 6 weeks to 4 months were taken during this period in order to use equipment and technology not accessible at MIT. Synthesized silicon containing polymers by living free radical polymerization with guidance from Dr. Craig Hawker. Investigated oxidation of polymers by oxygen plasmas and ozone by AFM with Dr. Jane Frommer and utilized XPS and AES.

MIT Dept. of Materials Science and Engineering, Cambridge, MA **Spring 1999**
Lecturer for 3.063. Undergraduate class in "Polymer Physics". Topics include mechanical properties of polymers, viscosity of polymer solutions and characterization techniques of polymers.

MIT Dept. of Materials Science and Engineering, Cambridge, MA **Spring 1999**
Undergraduate Research Opportunity Research Advisor. Supervised undergraduate research project of sophomore student, Ms. Jennifer Wagner. Research was on using the computer program RUMP to obtain stoichiometries from RBS and FRES data obtained at the University of Pennsylvania.

MIT, Dept. of Materials Science and Engineering, Cambridge, MA **Spring 1996**
Organizer of 3.911 Graduate Class: "Professional Development of Engineers" (26 students enrolled). Purpose was to broaden the scope of graduate students beyond traditional science by inviting speakers from industry to talk on subjects including starting a technological company, patent law and negotiation.

Cytotherapeutics, Cambridge, MA **Spring 1996**
Consultant. Investigated the morphology of polymer membranes for implantation into the spine of human beings for pain prevention. Performed SEM and AFM on membranes provided by company.

AT&T Bell Laboratories, Murray Hill, NJ **Summer 1994**
Advisor: Dr. Mihal Gross
Summer Researcher. Investigated effects of deposition conditions on morphology by AFM, composition by XPS and electrical properties of CVD tantalum nitride thin films on silicon.

University of Pennsylvania, Philadelphia, PA **September 1992-May 1994**
Advisor: Professor Russell Composto
Undergraduate Researcher. Independently investigated the synthesis and characterization of boron nitride thin films on silicon substrates via a polymer precursor route. Characterized the materials using RBS, FRES and cross-sectional SEM.

University of Pennsylvania, Philadelphia, PA **June-August 1992**
Advisor: Professor Charles McMahon
Summer Researcher. Independently researched for Merlin Metalworks the effects of oxygen contamination from the welding process on titanium bike tubes by optical microscopy and hardness testing. Report was used by company to improve their welding process.

Patents and Publications

1. "Magnetic Nanostructures from Block Copolymer Templates", V.Z-H Chan, E.L. Thomas, C.A. Ross, patent pending.
2. "Periodic Porous and Relief Nanostructured Articles", V. Z-H Chan, E.L. Thomas, V. Lee, R.D. Miller, A. Avgeropoulos, N. Hadjichristidis, patent pending.
3. "Oxidation of Silicon Containing Homopolymers", V.Z-H Chan, J. Wagner, E.L. Thomas, H. Wang, R J. Composto, in prep.
4. "Ordered Bicontinuous Nanoporous and Nanorelief Ceramics from Self-Assembling Polymer Precursors", V.Z-H Chan, J. Hoffman, V.Y. Lee, H. Iatrou, A. Avgeropoulos, N. Hadjichristidis, R.D. Miller, E.L. Thomas, accepted to *Science.*

5. "Nanostructured Thin Films of Organic-Organometallic Block Copolymers: One-Step Lithography with Poly(ferrocenylsilanes) by Reactive Ion Etching", R.G.H. Lammertink, M.A. Hempenius, V.Z-H Chan, E.L. Thomas, G.J. Vancso, accepted to *Advanced Materials.*
6. "Curious Morphology of Silicon Containing Polymers After Exposure to an Oxygen Plasma", V. Z-H Chan, E.L. Thomas, J. Frommer, D. Sampson, R. Campbell, V. Lee, C. Hawker, D. Miller, R.D.Miller, *Chemistry of Materials*, 10, 3895-3901, (1998).
7. "Nanoporous Ceramic Structures from Block Copolymers", V.Z-H Chan, A. Avgeropoulos, N. Hadjichristidis, V. Lee, R. D. Miller, E.L. Thomas, *PMSE Preprints*, 69, 19-20 (1998).
8. "Synthesis and Morphological Behavior of Triblock Copolymers for Nanostructure Applications", A. Avgeropoulos, V. Z-H Chan, V.Y. Lee, D. Ngo, R.D. Miller, N. Hadjichristidis, E.L. Thomas, *Chemistry of Materials*, 10, 2109-2115 (1998).
9. "Extending Spatial-Phase-Locked Electron-Beam Lithography to Two Dimensions", J.G. Gooderblet, J. Ferrera, M. Farhoud, V. Z. Chan, H.I. Smith, *Japanese Journal of Applied Physics, Part 1*, 36, 7557-9 (1997).
10. "Synthesis and Characterization of Boron Nitride Thin Films Prepared by a Polymer Precursor Route", V. Z-H Chan, P. Palladino, R.J. Composto, J. B. Rothman, L. Sneddon, *Journal of Materials Research*, 11, 373-380 (1996).

Presentations

1. *Invited Talk:* "Self-assembling Nanostructures : Magnetic Storage Media to 3D Membranes", V.Z-H Chan, Materials Processing Center, MIT, October 1999.
2. "Ceramic Coated Nanostructures from Block Copolymers", V.Z-H Chan and E.L. Thomas, American Physical Society Conference, Atlanta, GA, April 1999.
3. *Invited Talk:* "Ceramic Nanostructures from Block Copolymer Precursors", V.Z-H Chan, Program in Polymer Science and Technology, MIT, March 1999.
4. *Invited Talks:* "Ceramic Coated Nanostructures from Silicon Containing Block Copolymers", V. Z-H Chan, Presented at : Univ. of Groningen, Holland ; Univ. of Twente, Holland; CNRS Paris, France; ELF, Normandy France ; MPI Mainz, Germany; University of Freiburg, Germany; Oct 9-29, 1998.
5. "Formation of Nanoporous Structures from Polymer Precursors", V.Z-H Chan, E.L. Thomas, CCMM Conference , Bayreuth, Germany, Oct. 1998.
6. *Invited Talk:* "Characterizing New Microdomain Morphologies in Block Copolymer Systems", E.L. Thomas, V.Z-H Chan, presented at the Chemistry and Characterization of Mesophase Materials Workshop, Bayreuth, Germany, Oct. 1998.
7. "Nanoporous Ceramic Coated Structures from Polymers", V.Z-H Chan, A. Avgeropoulos, N. Hadjichristidis, V.Y. Lee, R.D. Miller, E.L. Thomas, presented at the American Chemical Society, Boston, MA, Aug. 1998.
8. "Oxidation of Silicon Containing Polymers", V.Z-H Chan, A. Avgeropoulos, N. Hadjichristidis, V.Y. Lee, R.D. Miller, E.L. Thomas, presented at the Polymer Physics Gordon Conference, Newport, RI, Aug. 1998.
9. "Synthesis and Characterization of Boron Nitride Thin Films Prepared by a Polymer Precursor Route", V.Z-H Chan, R.J. Composto, J. Bruce, L. Sneddon, presented at the Materials Research Society, Boston, MA, Nov. 1994.
10. "Characterization of Tantalum Nitride Thin Films Prepared by CVD", V.Z-H Chan and M. Gross, presented at the Materials Research Society, Boston, MA, Nov. 1994.

Awards

1. National Science Foundation International Research Opportunity Fellowship, 1999-2000.
2. IBM Co-operative Research Fellowship, 1998-1999.
3. IBM Almaden Research Center Fellowship, 1997-1998.
4. National Science Foundation Graduate Research Fellowship, 1994-1997.
5. Finalist in the Frank J. Padden, Jr. Graduate Research Award for "Excellence in Polymer Physics", 1999 Annual Meeting of the American Physical Society.
6. First place in graduate student competition, CCMM conference, Germany, Oct. 1998.
7. Sigma Xi: National Science Honors Society, MIT, Fall 1997.
8. Alpha Sigma Mu: Materials Science Honors Society, MIT, Fall 1996.
9. Recipient of the *Rose Award*: Awarded to four students at the University of Pennsylvania in recognition of outstanding research projects, June 1994.
10. Recipient of the *University of Pennsylvania Appreciation Award*, for service to the University as an undergraduate, June 1994.
11. Dean's List, University of Pennsylvania, 1992-1993, 1993-1994.
12. Tau Beta Pi: National Engineering Honor Society, Univ. of PA, Jan. 1994.
13. National Science Foundation Summer Undergraduate Research Fellowship and University Scholars Grant, Summer 1993.
14. ASM Scholar: National Award for outstanding MSE students, Philadelphia, PA, 1993.
15. University Scholar: Honors Program, University of Pennsylvania, 1992-1994.

From: *The Tech,* April 19, 1996.

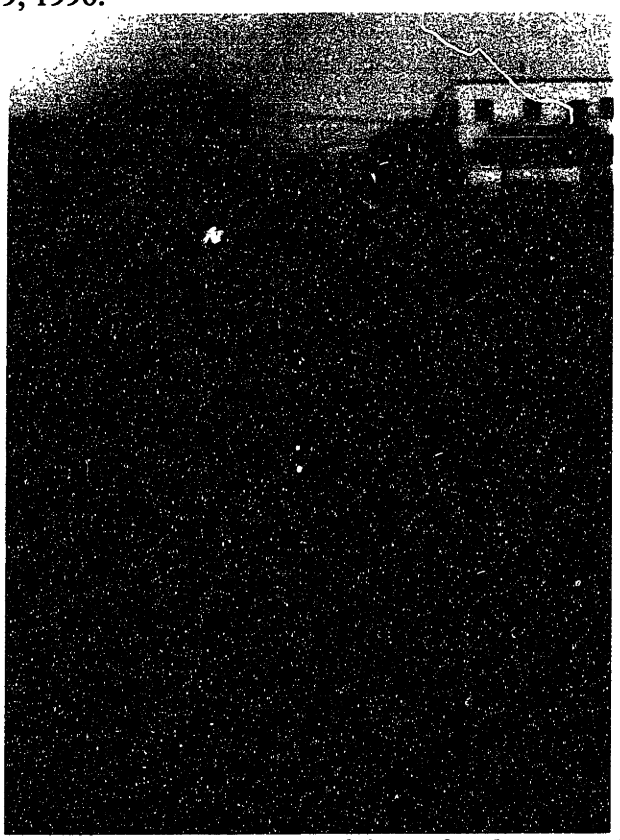

Caption: *Vanessa Z. Chan G evades the clutches of the Tufts players on her way to scoring her second try. MIT won, 22-3.* Picture by Indranath Neogy.

THESIS PROCESSING SLIP

FIXED FIELD: ill. _____ name _____

index _____ biblio _____

▶ COPIES: (Archives) Aero Dewey Eng Hum

Lindgren Music Rotch (Science)

TITLE VARIES: ▶☐ _____

NAME VARIES: ▶☐ _____

IMPRINT: (COPYRIGHT) _____

▶ COLLATION: 238 l

▶ ADD: DEGREE: _____ ▶ DEPT.: _____

SUPERVISORS: _____

NOTES:

cat'r: date:

page: F47

▶ DEPT: Materials

▶ YEAR: 2000 ▶ DEGREE: Ph.D.

▶ NAME: CHIN, Vanessa Zee-Haye